Self-oscillating clouds in magneto-optical traps

Marius Gaudesius

UNIVERSITÉ CÔTE D'AZUR

ÉCOLE DOCTORALE
SCIENCES FONDAMENTALES ET APPLIQUÉES

THÈSE DE DOCTORAT

Nuages auto-oscillants dans des pièges magnéto-optiques

Marius Gaudesius

Institut de Physique de Nice (INPHYNI)

Présentée en vue de l'obtention du grade de docteur en Physique

de l'Université Côte d'Azur

Dirigée par : Robin Kaiser / Guillaume Labeyrie

Soutenue le : 21 Avril 2021

Devant le jury, composé de :

Bruno Marcos, Maître de Conférences, Université Côte d'Azur

Caroline Champenois, Chargée de Recherche CNRS, Université d'Aix-Marseille

Daniel Hennequin, Directeur de Recherche CNRS, Université de Lille

Gian Luca Lippi, Professeur, Université Côte d'Azur

Guillaume Labeyrie, Directeur de Recherche CNRS, Université Côte d'Azur

José Tito Mendonça, Professeur, Institut Supérieur Technique de Lisbonne

Robin Kaiser, Directeur de Recherche CNRS, Université Côte d'Azur

Thorsten Ackemann, Professeur, Université de Strathclyde

ColOpt

cnrs

Nuages auto-oscillants dans des pièges magnéto-optiques

JURY :

Président
Gian Luca Lippi, Professeur, Université Côte d'Azur

Rapporteurs
Caroline Champenois, Chargée de Recherche CNRS, Université d'Aix-Marseille
Daniel Hennequin, Directeur de Recherche CNRS, Université de Lille

Examinateurs
José Tito Mendonça, Professeur, Institut Supérieur Technique de Lisbonne
Thorsten Ackemann, Professeur, Université de Strathclyde

Invité
Bruno Marcos, Maître de Conférences, Université Côte d'Azur

Directeur de Thèse
Robin Kaiser, Directeur de Recherche CRNS, Université Côte d'Azur

Co-directeur de Thèse
Guillaume Labeyrie, Directeur de Recherche CNRS, Université Côte d'Azur

Self-oscillating clouds in Magneto-Optical Traps

by
Marius Gaudesius

Supervisor: Dr. Robin Kaiser
Co-supervisor: Dr. Guillaume Labeyrie

A thesis for the Doctoral degree in
Physics

Université Côte d'Azur
Institut de Physique de Nice (INPHYNI)
Nice, France
2021

Résumé

Marius Gaudesius. Nuages auto-oscillants dans des pièges magnéto-optiques.

Dans cette Thèse, nous étudions les aspects fondamentaux des nuages atomiques auto-oscillants dans un grand piège magnéto-optique (MOT, de l'anglais Magneto-Optical Trap) équilibré. Ces instabilités présentent des analogies avec des systèmes astrophysiques tels que les étoiles variables (Céphéides), dont les auto-oscillations dépendent de la pression de radiation et de la gravitation, ainsi que des systèmes technologiques tels que les plasmas confinés, où des auto-oscillations peuvent survenir en raison des interactions entre les particules de plasma et le champ magnétique de confinement. Nous commençons par une étude expérimentale des instabilités dans un MOT équilibré, en étudiant d'abord le comportement du seuil d'instabilité par rapport à divers paramètres du MOT, y compris le gradient de champ magnétique, le nombre d'atome et l'intensité laser. Nous procédons ensuite à l'étude des propriétés spatio-temporelles du régime instable et identifions des régimes d'instabilité distincts. Différentes techniques d'analyse sont employées qui permettent d'identifier les modes d'oscillation du nuage dans chacun de ces régimes. Nous étudions également le comportement des distributions des tailles des structures spatiales qui se développent dans le nuage. Dans une approche théorique, nous développons un modèle cinétique 3D pour le MOT en prenant en compte les interactions entre atomes et l'utilisons avec succès dans des simulations numériques de nos instabilités. Nous trouvons des accords qualitatifs avec les seuils d'instabilité issus des expériences et prédisons les régimes d'instabilité obtenus expérimentalement. Nous étudions l'impact des ingrédients physiques de notre modèle sur les instabilités, afin de faciliter la compréhension de la physique complexe à l'œuvre. Enfin, nous montrons un résultat numérique préliminaire pour une instabilité dans un MOT désaligné, observée expérimentalement, démontrant ainsi que notre outil numérique peut être utilisé au-delà du MOT équilibré.

Mots-clés : piège magnéto-optique (MOT), simulations 3D du MOT, atomes froids, auto-oscillations, instabilités.

Abstract

Marius Gaudesius. Self-oscillating clouds in Magneto-Optical Traps.

In this Thesis, we study the fundamental aspects of self-oscillating atomic clouds in a large, balanced Magneto-Optical Trap (MOT). These instabilities bear analogies with astrophysical systems such as Cepheid variable stars, whose self-oscillations depend on radiation pressure and gravity, as well as technological systems such as confined plasmas, where self-oscillations may arise due to interactions between the plasma particles and the confining magnetic field. We begin with an experimental study of self-oscillating balanced MOT instabilities, investigating first the instability threshold behavior versus various MOT parameters, including magnetic field gradient, atom number and laser intensity. We proceed then investigating the spatio-temporal properties of the unstable regime and identify distinct instability regimes. Different analysis techniques are employed that allow us to learn about the oscillation modes of clouds of these regimes as well as the size distribution of the structures developing in clouds of these regimes. In a theoretical approach, we develop a kinetic 3D model for the MOT, with many-atom effects included, and successfully use it in numerical simulations of our instabilities. We find qualitative agreements with the instability thresholds from the experiments as well as predict experimentally obtained instability regimes. We investigate the impact of our model's physical ingredients on the instabilities, to aid the understanding of the complex physics at work. Finally, we show a preliminary simulated result for a self-oscillating instability in the misaligned MOT, known to experimentally exist, in that way demonstrating that our developed numerical tool can be employed beyond the balanced MOT.

Keywords: Magneto-Optical Trap (MOT), 3D simulations of the MOT, cold atoms, self-oscillations, instabilities.

Contents

General introduction

Self-oscillation is a phenomenon referring to the maintenance of an oscillation under a stimulus that lacks any corresponding periodicity. Other commonly used names for self-oscillation include e.g. *autonomous*, *spontaneous*, *self-sustained*, *-excited* and *-induced* vibration [1]. There are numerous examples in nature where self-oscillations occur. Our own hearts are self-oscillators, whose period is regulated by abrupt switching at thresholds by the so-called pacemaker current [2]. Another example is Cepheid variable stars, whose self-oscillations arise from the variations in the rate at which the radiation escapes the star as it expands and contracts due to respectively radiation pressure and gravity [3]. On the technological side, everyday clocks and advanced systems such as confined plasmas are self-oscillators. Clocks, electronic or spring-driven, use positive feedback to self-oscillate: a power source amplifies the vibration that is fed back to the source for the clock to be driven in phase with the velocity of the oscillation [4]. Confined plasmas may exhibit self-oscillations as a consequence of interactions between the plasma particles and the confining magnetic field [5]. Unwanted types of self-oscillation often plague technology and thus are immensely relevant to study for technological improvements [6, 7, 8]. Studying self-oscillations is of high fundamental interest, too [9, 10, 11]. At times, though, one is faced with extreme challenges to do an adequate study. For instance, systems can be massive (and distant), such as Cepheid variable stars, or technologically intricate, such as confined plasmas. In the case of these systems, analogies have fortunately been suggested to exist between them and a relatively simple device, the Magneto-Optical Trap (MOT), thus offering a great opportunity to investigate the hard-to-tackle systems [39]. Self-oscillations existing in the MOT are at the core of the work of this Thesis.

Self-oscillations are in general, and not only in the MOT, labeled as instabilities. This is related to the fact that self-oscillations appear as growing solutions to some equations of motion by small perturbations around an equilibrium [1]. In case the equations of motion are linear, the self-oscillations keep growing in time. However, real physical processes are nonlinear, and thus nonlinear equations of motion are required to correctly describe them. It is by having nonlinearities included that the oscillations can be prevented from growing indefinitely. However, the theoretical challenge then magnifies and it usually becomes true that general solutions to the problems no longer exist. The MOT is conceptually simple but highly nonlinear: to understand its deep inner workings and self-oscillations on a theoretical basis one thus often opts for simulations.

Apart from self-oscillations, other instabilities that exhibit oscillations in the MOT are resonant phenomena. Resonant phenomena differ from self-oscillations, as a periodic stimulus is applied to maintain periodic motion. Self-oscillations exist in three of the four different configurations of the MOT, while resonant phenomena exist in the remaining one. Oscillating MOT instabilities have been studied to a fairly good extent in the past, and this Thesis will include a synthesis of their studies. Instabilities that we study in detail exist in the

so-called balanced MOT configuration, and these are self-oscillating. The past research on self-oscillating instabilities in this configuration described in Ref. [40] has mentioned similar types of unstable motion to appear in the discussion of a broad range of applications, including swarm dynamics, propagation of waves or dissipative solitons in reaction-diffusion systems, and grain motion in dusty plasmas. We do not, however, concentrate on the technological prospects of balanced MOT instabilities, but rather on their fundamental aspects. The work here includes both experiments and simulations. There are three main Chapters in this Thesis, and their main contents are as follows.

Chapter 1 concerns basic working principles of the device behind our experiments (Chapter 2) and numerical simulations (Chapter 3), being the MOT, as well as a presentation of different regimes of MOT operation.

Chapter 2 concerns experiments of instabilities using our balanced MOT. New experimental knowledge about balanced MOT instabilities is achieved, and the known analytical instability-models are assessed.

Chapter 3 concerns balanced MOT instability simulations in 3D. A kinetic 3D model based on a 2-level atom is first described and discussed, which is then used in the development of the $F = 0 \rightarrow F' = 1$ model, being the kinetic model employed in our simulations. The balanced MOT simulation results are compared with results of our experiments (Chapter 2). Qualitative agreements are obtained. Original studies on how the instabilities depend on implemented physical ingredients are also performed.

The important contributions of the Author are as follows, with comments. The Author participated in the experiments; the setup was already built upon the arrival by Guillaume Labeyrie. For the simulation part, the Author worked in a collaboration with Thomas Pohl and Yong-Chang Zhang. The Author made the theoretical derivations for the simulation model. The Author devised a new numerical method - the tube method (section 3.3.3). The Author wrote the simulation code. This code was put on a computer cluster at Aarhus University and run by Yong-Chang Zhang; the running parameters were selected by the Author.

The work has yielded the publications in Refs. [72] and [73].

Chapter 1

The Magneto-Optical Trap and its regimes

Local table of contents

This Chapter concerns basic working principles of the device behind our experiments (Chapter 2) and numerical simulations (Chapter 3), being the Magneto-Optical Trap (MOT), as well as a presentation of different regimes of MOT operation.

This Chapter is organized as follows. We start with an introduction to the MOT and provide an elementary picture of its main function. Then, we present regimes of MOT operation that are governed by single- and many-atom physics, known respectively as the temperature-limited regime and the multiple-scattering regime, and, finally, present the unstable regime of the MOT.

1.1 Basics of the Magneto-Optical Trap (MOT)

In this section, we introduce to the MOT and provide an elementary picture of its main function. The basics of laser cooling are covered, followed up by a description of a 1D model of the MOT.

What is the MOT ?

Realized first in 1987 by S. Chu and coworkers [12], the MOT is a device that has its main function to cool and confine a gas of neutral atoms in a tight region of space. As sketched in Fig. 1.1, it consists of three mutually orthogonal pairs of counter-propagating laser beams having appropriate circular helicities and meeting at the center of the MOT, plus a pair of anti-Helmholtz coils producing a quadrupole magnetic field that is zero at the center. To gain an elementary picture of the cooling and confinement in this arrangement, one may do so by considering the *radiation pressure forces* stemming from the laser beams (a more complete picture will be provided in Chapter 3). In what follows, we will first explain the basic physics behind the radiation pressure forces and show how these forces lead to the atom cooling by examining a situation where two beams counter-propagate each other. We will then show how by adding a magnetic field the radiation pressure forces lead furthermore to the atom confinement.

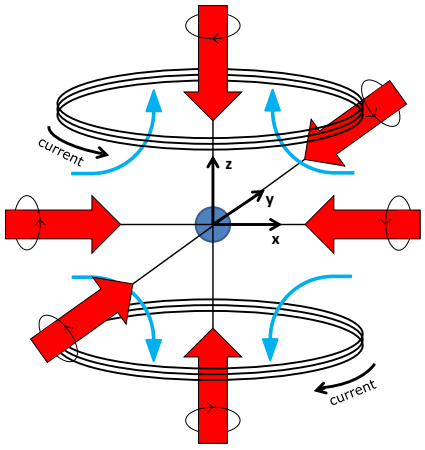

Figure 1.1: Sketch of the Magneto-Optical Trap (MOT). The MOT consists of three mutually orthogonal pairs of counter-propagating laser beams having appropriate circular helicities (right-handed for the z-axis beams and left-handed for the x- and y-axis beams) and meeting at the center of the MOT, plus a pair of coils with opposite current (anti-Helmholtz coils) giving rise to a quadrupole magnetic field that is zero at the center. The curved blue arrows are drawn to indicate the direction of the magnetic field lines produced by the coils.

Laser radiation pressure and cooling

The basic physics behind the laser radiation pressure can be understood by considering the simple situation in Fig. 1.2, depicting the pressure's effect on a 2-level atom. During the absorption event the photon momentum $\mathbf{p} = \hbar\mathbf{k}$ is, according to the law of momentum conservation, preserved both in magnitude and direction, resulting in the atom receiving a kick of momentum $M\mathbf{v} = \hbar\mathbf{k}$ (Fig. 1.2(a.1-2)). Here $\hbar$ is the reduced Planck constant, M is the atom mass, $\mathbf{v}$ is the atom velocity, and $\mathbf{k}$ is the wavevector of the photon, with $|\mathbf{k}| = k_L = 2\pi/\lambda$ being the photon wavenumber and λ being the photon wavelength. A single momentum kick thus provides the atom the recoil speed $v_{rec} \equiv \hbar k_L/M$. For Rb-87, which is the atomic species used in our experiments (Chapter 2), $v_{rec} \approx 6$ mm/s, assuming one considers the $\lambda = 780$ nm Rb-87 D2 line ($5^2S_{1/2} \rightarrow 5^2P_{3/2}$), being the optical transition utilized in our experiments. Indeed, this recoil speed of approximately 6 mm/s is tiny compared to the mean thermal speed v_{th} of Rb exceeding 300 m/s at room temperature [13], but nevertheless, many momentum kicks can be provided in short successions as absorption is followed up by spontaneous emission, which in the case of Rb-87 D2 line has a natural lifetime of approximately 26 ns [14]. For the 2-level atom, as the spontaneous radiation is considered isotropic, the recoil velocity (vector quantity) due to spontaneous emission processes will on average cancel out, and thus the net momentum change will solely be due to processes of absorption (Fig. 1.2(b)). The mean force acting on this atom will hence point in the direction of the laser beam.

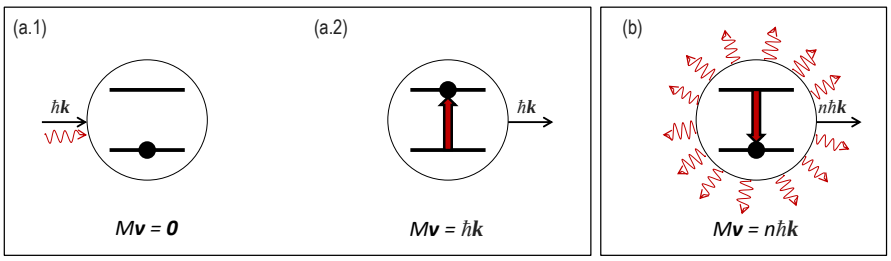

Figure 1.2: Depiction of the laser radiation pressure's effect on a 2-level atom. (a.1) A photon (wavy arrow) carrying momentum (straight arrow) approaches a resting 2-level atom in the ground state; (a.2) an absorption event occurs, where the atom is put in the excited state, and the photon's momentum is transferred to the atom. (b) After many absorption-spontaneous emission cycles, the recoil momentum due to emitted photons will average to zero, and the atom will gain momentum in the direction of n absorbed photons.

Next, let us concentrate on what happens to the 2-level atom when it is put in a counter-propagating beam arrangement in 1D. We consider the beam traveling in the positive direction of the arrangement to have the wavevector $+\mathbf{k}$ and the beam traveling in the negative direction - the wavevector $-\mathbf{k}$. Taking $\mathbf{v}$ to be the atom velocity with respect to the beam sources of frequency ω_L, the

atom will see the beams with the Doppler shifted frequency

$$\omega_D = \omega_L \mp \mathbf{k} \cdot \mathbf{v} \tag{1.1}$$

where "$-$" case is for the beam traveling in the positive direction, and "$+$" for the beam traveling in the negative direction. If the atomic transition frequency $\omega_0 = \omega_D$, the atom will be at resonance with the given beam, resulting in photon absorption.

Tuning ω_L below ω_0, we observe from Eq. 1.1 that ω_D of the beam counter-propagating with the atom is closer to ω_0 than of the beam's co-propagating with the atom, and so the probability of photon absorption is increased for the counter-propagating beam while decreased for the co-propagating beam. Thus, the atom will be under an asymmetric influence by the laser beams determined by the direction of its motion and will be slowed down by the radiation pressure. We note that the idea of using counter-propagating beam arrangement to cool atoms was first suggested in 1975 by T. W. Hänsch and A. L. Schawlow [15].

Adding together the laser radiation pressure forces stemming from each of the two beams, one obtains an expression for the cooling force known as the Doppler cooling force. Denoting the force by $\mathbf{F}_D$, we have

$$\mathbf{F}_D(v_\mathbf{z}) = \hbar\mathbf{k}\Gamma_D^+(v_\mathbf{z}) - \hbar\mathbf{k}\Gamma_D^-(v_\mathbf{z}) \quad , \quad \Gamma_D^\pm(v_\mathbf{z}) = \frac{\Gamma}{2}\frac{s_0}{1 + s_0 + 4\frac{(\delta \mp k_L v_\mathbf{z})^2}{\Gamma^2}} \tag{1.2}$$

where the term $\hbar\mathbf{k}\Gamma_D^+$ is the radiation pressure force of the beam traveling in the positive direction, while $-\hbar\mathbf{k}\Gamma_D^-$ is the radiation pressure force of the beam traveling in the negative direction, with Γ_D^+ and Γ_D^- being the corresponding photon scattering rates. Regarding the remaining quantities, Γ is the natural linewidth of the transition, $s_0 = \frac{I_L}{I_{sat}}$ is the on-resonance saturation parameter, with I_L being the intensity of each laser beam and I_{sat} being the saturation intensity of the transition, and $\delta = \omega_L - \omega_0$ is the laser detuning from resonance; with these quantities, we write the saturation parameter $s = \frac{s_0}{1+\frac{4\delta^2}{\Gamma^2}}$. Observe that δ is in Eq. 1.2 shifted by $\mp k_L v_\mathbf{z}$ - this is exactly due to the Doppler effect with $\mathbf{v} = v_\mathbf{z}\hat{\mathbf{z}} = \mathbf{v_z}$ (see Eq. 1.1). Note that the Doppler cooling theory is valid only in the low-intensity limit, where $s_0 \ll 1$.

In the limit of small velocities, $|v_\mathbf{z}| \ll \Gamma/k_L \;\&\; |\delta|/k_L$, the Doppler cooling force is a friction force with the friction coefficient γ:

$$\mathbf{F}_D(v_\mathbf{z}) \approx -\gamma\mathbf{v_z} \quad , \quad \gamma = s_0\frac{-8\hbar k_L^2\delta\Gamma^3}{(\Gamma^2 + \Gamma^2 s_0 + 4\delta^2)^2} \tag{1.3}$$

where γ is positive for $\delta < 0$, such that cooling is achieved, and negative for $\delta > 0$, such that heating is achieved (i.e. the atom velocities increase). Because of the feature that for slow atoms $\mathbf{F}_D$ exhibits damping behavior when γ is positive, the cooling technique involving counter-propagating beams has been called the Optical Molasses (OM) technique.

In Fig. 1.3, we plot the Doppler force of Eq. 1.2 for different $\delta < 0$, in order to visualize important features of the force. Here we first observe that the atom will be subject to a positive force if it has a negative velocity, hence slowing it, and that it will be subject to a negative force if it has a positive velocity, again slowing it. The atom will not be subject to the force only if it is motionless, implying overall that a moving atom should eventually be slowed down to zero velocity. The slowing down to zero velocity cannot, however, be achieved, and the reason for that we will come back to shortly.

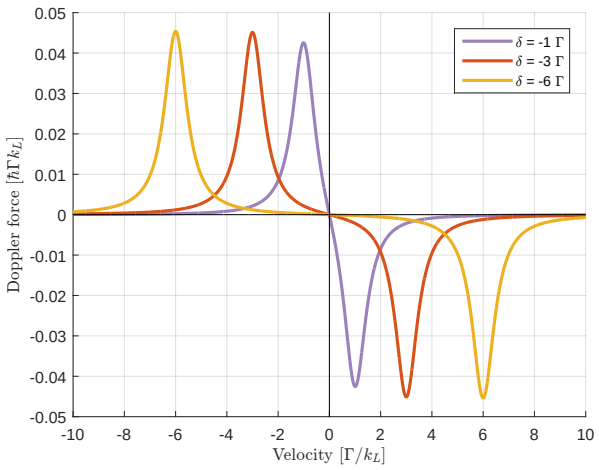

Figure 1.3: Doppler cooling force (Eq. 1.2) plots for different $\delta < 0$. $I_L = I_{sat}/10$ is used. The positive and negative Lorentzian peaks are centered at $\approx \pm\frac{\delta}{\Gamma}$ on the velocity-axis.

Fig. 1.3 shows that the Doppler force is strongest around the positive and negative Lorentzian peaks. The capture range of velocities is defined to be the interval between the two peaks. As we can observe, this interval includes the region around $v_z = 0$, where the linearized Doppler force of Eq. 1.3 is applicable ($\delta < 0$). We can observe also that the velocity capture range becomes narrower as the laser frequency ω_L approaches the atomic transition frequency ω_0, i.e. as $\delta \to 0$. Differentiating Eq. 1.2 with respect to v_z, we may find that the peaks occur at $\approx \pm\frac{\delta}{k_L}$ (corresponding to $\approx \pm\frac{\delta}{\Gamma}$ seen in Fig. 1.3). As an example, for the Rb-87 D2 line ($\Gamma = 2\pi \cdot 6.07$ MHz), this gives the approximate velocity capture range of $[-2.4; 2.4]$ m/s for $\delta = -\Gamma/2$, and implies that only slowly moving atoms can be cooled efficiently with this method (compare to v_{th} of Rb exceeding 300 m/s at room temperature).

In the treatment of laser cooling above, we are led to zero-velocity atoms. This is because we are neglecting fluctuations involved in the cooling. The fluctuations arise due to variations in photon absorption as well as randomness in the direction of spontaneously emitted photons. These two effects together contribute to the momentum diffusion coefficient D, which is responsible for the diffusive heating of the atoms.

In the equilibrium between the diffusive heating and Doppler cooling processes, the finite limit temperature T_{lim} achievable with Doppler cooling is related to D and γ via the following expression

$$k_B T_{lim} = \frac{D}{|\gamma|} \tag{1.4}$$

where k_B is the Boltzmann constant. This expression can be shown to give [49]

$$k_B T_{lim} = \frac{\hbar}{8} \frac{\Gamma^2 + 4\delta^2}{|\delta|} \tag{1.5}$$

For $\delta = -\Gamma/2$, we obtain the lowest temperature achievable with Doppler cooling, called the Doppler temperature T_D:

$$k_B T_D = \frac{\hbar\Gamma}{2} \tag{1.6}$$

The Doppler temperature for Rb-87 is approximately 146 μK, given we consider the D2 line. The Doppler temperature is, however, not the lowest temperature that actually can be achieved in the OM arrangement. Experiments with Rb-87 atoms have measured the temperatures to be as low as 3 μK [16], and also for many other atomic species the temperatures have been reported to be lower than what is set by the Doppler cooling limit [17, 18, 19]. The discrepancy happens because Rb-87 and other kinds of atoms used in cold atom experiments possess usually multi-level substructures in both the excited and ground levels of the cooling transition. Such multi-level character of the atoms leads to sub-Doppler cooling mechanisms, most notably Sisyphus cooling, also known as polarization gradient cooling [20]. We comment that Sisyphus cooling also appears in the context of 2-level atoms: here one relies on working in the high-intensity limit, which is where the Doppler cooling theory breaks down [49]. We mention very briefly now the implications of the sub-Doppler cooling mechanisms.

In Fig. 1.4, taken from Ref. [21], one compares the Doppler and sub-Doppler forces, respectively concerning a 2-level atom and a multi-level atom (with 3 ground and 5 excited Zeeman sub-levels). As can be seen, the important deviation between the two forces happens around the zero-velocity region, where the gradient of the sub-Doppler force is much steeper than of the Doppler force, implying that the sub-Doppler cooling mechanisms are much more efficient at interacting with the very slowly moving atoms than the Doppler cooling counterpart. The momentum diffusion coefficient obtainable for the present case multi-level atom is such that its ratio with the increased friction coefficient leads to a smaller temperature than for Doppler cooling (Eq. 1.5) [50].

Now, whilst the OM arrangement provides an efficient way of decelerating neutral atoms, with the velocity damping time $M\gamma^{-1}$ typically well-below a millisecond, it does not provide means of confining them in a tight region of space. To achieve the confinement, one can do so by making the radiation pressure force a position-dependent force that would push the atoms to the trap center. In the following, we will discuss how the radiation pressure force can be made position-dependent by exposing the atoms to an external magnetic field.

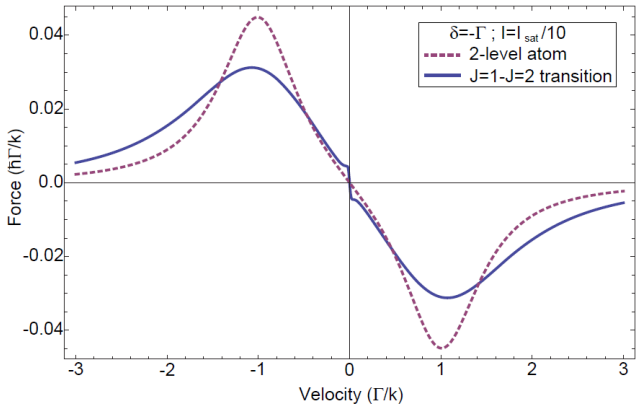

Figure 1.4: Comparison of the Doppler cooling force (dashed line) versus the sub-Doppler cooling force (thick line). **Source:** [21].

Spatial confinement

To gain an insight on how the spatial confinement of atoms can be achieved using radiation pressure, let us consider the 1D model of the MOT depicted in Fig. 1.5(a). In this model, an atom with the hyperfine transition $F = 0 \rightarrow F' = 1$ is put in a counter-propagating beam arrangement, with the two beams having polarizations that are respectively right- (σ^+) and left-hand circular (σ^-), and a linearly increasing magnetic field $\mathbf{B}(z) = B'z\hat{\mathbf{z}}$ is applied, with B' being the positive gradient along the arrangement's z-axis. The Zeeman interaction between the atomic total angular momentum operator $\hat{\mathbf{F}}$ and the field $\mathbf{B}(z)$ lifts the three-fold degeneracy of the excited $F' = 1$ level, such that we may write the transition frequency between the ground Zeeman sub-level $|F = 0, m = 0\rangle$ and the excited Zeeman sub-levels $|F' = 1, m'\rangle$ as

$$\omega'(m') = \omega_{0\rightarrow 0} + m'\mu B'z \tag{1.7}$$

where $m = 0$ and $m' = 0, \pm 1$ are the magnetic quantum numbers corresponding to respectively the ground level with the total angular momentum quantum number $F = 0$ and the excited level with the total angular momentum quantum number $F' = 1$, $\omega_{0\rightarrow 0}$ is the constant transition frequency between $|F = 0, m = 0\rangle$ and $|F' = 1, m' = 0\rangle$, and $\mu = g_F\mu_B/\hbar$ is the gyromagnetic ratio, with g_F being the hyperfine Landé g-factor and μ_B being the Bohr magneton.

As implied by the light coupling scheme in Fig. 1.5(b), the selection rules of orbital angular momentum tell us that the σ^+ polarization carrying laser induces transitions only between $m = 0$ and $m' = +1$, whereas the σ^- laser only between $m = 0$ and $m' = -1$. Because of the particular way the excited sub-levels are shifted in energy (Fig. 1.5(a) and Eq. 1.7), the (red-detuned) laser coming from the left (σ^+ polarization) is closer to the transition $m = 0 \rightarrow m' = +1$ for $z < 0$ than compared to $z > 0$, whereas the laser coming from the right (σ^- polarization) is closer to the transition $m = 0 \rightarrow m' = -1$ for $z > 0$ than compared to $z < 0$, meaning overall that the atom will experience a stronger force pushing it to the center of the trap, and so the confinement will be achieved.

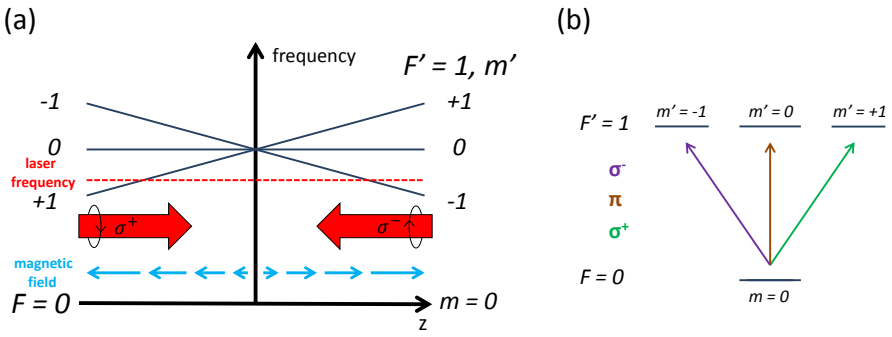

Figure 1.5: (a) 1D scheme of the MOT for an atom with the hyperfine transition $F = 0 \rightarrow F' = 1$. The linearly increasing magnetic field causes the Zeeman splitting of the excited $F' = 1$ level, and the two red-detuned, counter-propagating laser beams with the respective σ^+ and σ^- polarizations provide a force driving the atom towards the zero-point of the magnetic field (i.e. the trap center). (b) Light coupling scheme for the hyperfine transition $F = 0 \rightarrow F' = 1$. The Zeeman transition $m = 0 \rightarrow m' = -1$ is induced only by left-hand circular (σ^-) polarized light, $m = 0 \rightarrow m' = +1$ only by right-hand circular (σ^+), and $m = 0 \rightarrow m' = 0$ only by linear (π).

Let us consider now obtaining an equivalent 1D MOT model as previously but with a 2-level atom in mind. As the Zeeman effect does not exist for such an atom, we consider assuming that the beams *themselves* are shifted in frequency according to where the atom is situated in the *fictive* 1D MOT arrangement. Observing Eq. 1.7, we introduce the shifts $-\mu B' z$ and $+\mu B' z$ for respectively the positively and negatively directed beam. Recalling the discussion surrounding Fig. 1.5, it is clear that with these shifts, the confinement of the 2-level atom in the fictive 1D MOT arrangement will be achieved.

Observing Eq. 1.2, we continue constructing the force that a moving 2-level atom will experience due to radiation pressure forces in the fictive 1D MOT arrangement. We refer to this force as the trapping force and denoting it by $\mathbf{F}_{tr}$, we have

$$\mathbf{F}_{tr}(z, v_z) = \hbar\mathbf{k}\Gamma^+_{tr}(z, v_z) - \hbar\mathbf{k}\Gamma^-_{tr}(z, v_z) \quad , \quad \Gamma^{\pm}_{tr}(z, v_z) = \frac{\Gamma}{2}\frac{s_0}{1 + s_0 + 4\frac{(\delta \mp k_L v_z \mp \mu B' z)^2}{\Gamma^2}} \tag{1.8}$$

where the term $\hbar\mathbf{k}\Gamma^+_{tr}$ is the radiation pressure force of the beam traveling in the positive direction, while $-\hbar\mathbf{k}\Gamma^-_{tr}$ is the radiation pressure force of the beam traveling in the negative direction, with Γ^+_{tr} and Γ^-_{tr} being the corresponding photon scattering rates. Observe that δ is in Eq. 1.8 shifted by $\mp k_L v_z$ and $\mp\mu B' z$ - this is respectively due to the Doppler effect with $\mathbf{v} = v_z\hat{\mathbf{z}} = \mathbf{v_z}$ (see Eq. 1.1) and the *ad hoc* Zeeman effect (see the above discussion).

In the limit of small velocities, $|v_z| \ll \Gamma/k_L$ & $|\delta|/k_L$, and for positions close to the trap center, $|z| \ll \Gamma/(\mu B')$ & $|\delta|/(\mu B')$, the trapping force describes a harmonic oscillator with the friction coefficient γ and the spring constant κ:

$$\mathbf{F}_{tr}(z, v_z) \approx -\gamma \mathbf{v_z} - \kappa \mathbf{z} \quad , \quad \kappa = \frac{\mu B'}{k_L}\gamma \tag{1.9}$$

with γ defined in Eq. 1.3. We observe here that the trapping force is written as a sum of the friction force $-\gamma \mathbf{v_z}$ and the restoring force $-\kappa \mathbf{z}$. For negative detunings ($\delta < 0$) γ is positive, such that the friction force cools the atoms, and likewise κ is positive, such that the restoring force pushes the atoms to center of the trap, giving rise to the confinement. Indeed, in this way the MOT can provide us with both cooled and confined atomic samples.

In Fig. 1.6, we plot the trapping force of Eq. 1.8 for a motionless atom ($v_z = 0$) for different $\delta < 0$. As can be seen, Fig. 1.6 is analogous to Fig. 1.3 where the Doppler force of Eq. 1.2 was plotted: if the atom is situated at negative/positive positions it will be subject to a positive/negative force, pushing it towards the trap center, and the atom will not be subject to the force only if it is positioned exactly at the trap center. The last point does not imply that there is no limit to how dense atomic clouds can become, although the existence of such limit cannot be explained by the presence of the diffusive heating, which is a single-atom effect. As more and more atoms get trapped, many-atom effects start to become significant, and it is their presence that puts a limit to how dense atomic clouds can become. In the next section, different regimes of the MOT will be introduced, and we will see how such limit arises due to many-atom effects as well as how important the role of these effects can be in a broader range of MOT physics.

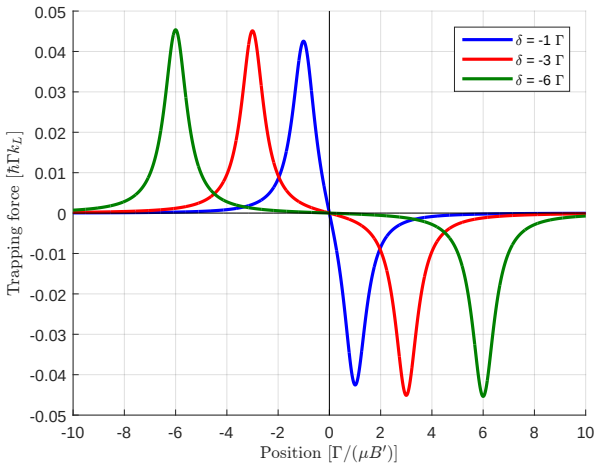

Figure 1.6: Trapping force (Eq. 1.8) plots for a motionless atom ($v_z = 0$) for different $\delta < 0$. $I_L = I_{sat}/10$ is used. The positive and negative Lorentzian peaks are centered at $\approx \pm\frac{\delta}{\Gamma}$ on the position-axis. Note the analogy with Fig. 1.3.

1.2 Different regimes of the MOT

We begin this section by describing regimes of MOT operation that are governed by single- and many-atom physics, known respectively as the temperature-limited regime and the multiple-scattering regime. Cloud size scaling laws characterizing these two regimes are provided, and change to the cloud temperature as the atom number gets large is discussed. Finally, the unstable regime of the MOT is presented.

1.2.1 The temperature-limited regime

For optical depths $b \ll 1$, higher than first-order scattering events are negligible in the MOT[1], and the cloud dynamics are governed by single-atom physics. Such optical depths are typically obtained in clouds with atom numbers $N \lesssim 10^5$ and densities $\rho \lesssim 10^{11}$ cm^{-3} [30].

As the cloud dynamics are governed by single-atom physics, the equipartition theorem can be applied to predict the root-mean-square (RMS) size of the cloud. Within the simplified treatment of trapping provided in section 1.1, the equipartition theorem tells us that the mean of the trapping potential $U_{tr} = \frac{1}{2}\kappa z^2$, found from Eq. 1.9 with $v_z = 0$ ($\mathbf{F}_{tr} \approx -\frac{dU_{tr}}{dz}\hat{\mathbf{z}}$), is equal to $\frac{1}{2}k_B T_{lim}$, with T_{lim} being the limit temperature given by Eq. 1.5:

$$\frac{1}{2}\kappa\langle z^2\rangle = \frac{1}{2}k_B T_{lim} \tag{1.10}$$

From the above equation we find the RMS size of the MOT cloud, $\Delta z = \sqrt{\langle z^2\rangle}$, to be

$$\Delta z = \sqrt{\frac{k_B T_{lim}}{\kappa}} \tag{1.11}$$

from which we observe that the size is limited by the temperature and does not depend on the atom number. Accordingly, the regime here is known as the temperature-limited regime.

As reported in Ref. [30], MOT clouds in the temperature-limited regime were experimentally observed to form a small sphere with a diameter that remained constant at approximately 0.2 mm as the atom number was increased. The density of this sphere had a Gaussian distribution and grew linearly in proportion to the number of atoms, as one would have expected for an ideal gas in a harmonic trapping potential.

In Ref. [22], MOT cloud temperatures were studied in the temperature-limited regime, and these were found to be similar to the sub-Doppler temperatures in the OM arrangement. The similarity was explained by the fact that in the temperature-limited regime, the atoms remained confined close to the trap

[1] The optical depth b can be expressed as $b = l/\ell$, where l is the length of the scattering medium, and ℓ is the mean free-path in this medium. b can thus be interpreted to measure the number of scatterings made by light before escaping the medium.

center, where the magnetic field was approximately zero, and thus the conditions were similar to those in the OM arrangement. The authors mentioned that at sufficiently high cloud densities an increase in temperature was observed. As we will understand from the next subsection, such increase in temperature can be explained by many-atom effects becoming relevant.

1.2.2 The multiple-scattering regime

When optical depths $b \sim 1$, second-order scattering events become important in the MOT, and the cloud dynamics are affected by many-atom physics. Such optical depths are typically obtained in clouds with larger atom numbers and larger densities than in the temperature-limited regime (where $N \lesssim 10^5$ atoms, $\rho \lesssim 10^{11}$ cm^{-3}). The new regime here is known as the multiple-scattering regime, first described by a model introduced in 1991 by C. E. Wieman and coworkers [30]. This *Wieman* model relies on the Doppler description of the trapping force and takes into account many-atom effects known as the shadow effect and the rescattering. In what follows, we explain the basics of respectively the shadow effect and the rescattering, and then explain how these effects are incorporated in the Wieman model for predicting a finite cloud density as well as an atom number dependent scaling law for the cloud size. The cloud temperature change that occurs due to atom-atom interactions is also discussed.

The shadow effect

Prior to the introduction of the Wieman model in 1991, the MOT beams were known to expose the atomic cloud to an additional compressional effect, called the shadow effect, first described in 1988 by J. Dalibard in Ref. [23]. As understood from Fig. 1.7, it is caused by an intensity imbalance created in the cloud due to the attenuated beams. The attenuation is due to the light being scattered by the atoms as it traverses through the cloud. The compressional effect goes by the name of the shadow effect because each atom in the laser field is imagined to be casting a shadow, with an area of a laser scattering cross-section. We derive next an *illustrative* expression for the force describing this effect.

In the following derivation, we consider the limit of linear attenuation and the atoms at rest as well as the magnetic field turned off[2]. With these considerations, the intensities of the beams traveling in the positive and negative direction of the z-axis can be respectively written as

$$I_z^+(z) = I_L e^{-\sigma_L \rho(l+z)} \simeq I_L[1 - \sigma_L \rho(l+z)] \tag{1.12a}$$

$$I_z^-(z) = I_L e^{-\sigma_L \rho(l-z)} \simeq I_L[1 - \sigma_L \rho(l-z)] \tag{1.12b}$$

[2]The limit of linear attenuation ($b \ll 1$) is not correct in the context of the multiple-scattering regime (entered when $b \sim 1$), and the atom velocities as well as the magnetic field cannot simply be neglected in the MOT. All these considerations in the derivation of the force describing the shadow effect are made for illustration purposes.

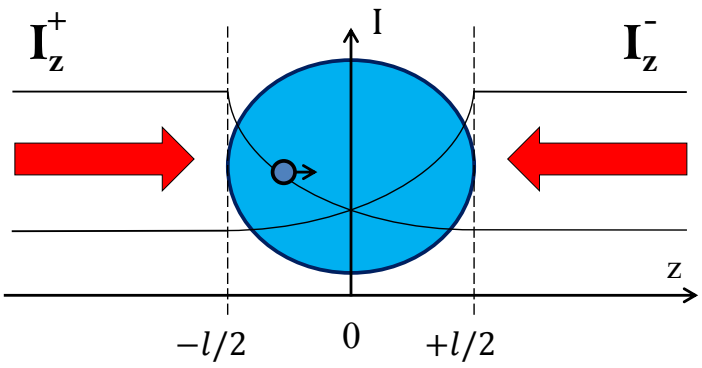

Figure 1.7: Depiction of the mechanism behind the shadow effect. As the positively and negatively directed beams with the respective intensities I_z^+ and I_z^- travel through the MOT cloud they become attenuated, giving rise to an intensity imbalance in the cloud. This imbalance results in a compressional effect of the cloud, i.e. the so-called shadow effect.

where l is the length of the cloud, and

$$\sigma_L = \frac{\sigma_0}{1 + s_0 + 4\frac{\delta^2}{\Gamma^2}} \tag{1.13}$$

is the laser scattering cross-section, with $\sigma_0 = \frac{3\lambda^2}{2\pi}$ being the on-resonance scattering cross-section.

Adding together the radiation pressure forces stemming from the corresponding beams with the respective intensities I_z^+ and I_z^- seen in Eqs. 1.12(a, b), we can find the following force that the atom will experience due to the shadow effect:

$$\mathbf{F}_{shw}(z) = -\frac{2I_L\sigma_L^2\rho}{c} z\hat{\mathbf{z}} \tag{1.14}$$

where c is the speed of light. We refer to the force $\mathbf{F}_{shw}$ as the shadow force. As can be seen from the above (illustrative) expression, if the atom is off-centered, at $z < 0$ or $z > 0$, then the shadow effect will push it in the direction of the center, whereas if the atom is exactly at the center, then it will not be exposed to the pushing effect. Overall, the cloud will be compressed, with the compression directed towards the center.

Although the shadow effect is a compressional effect by which the cloud density will increase, it will be countered by the repulsive effect of the rescattering, introduced to next.

The rescattering

The rescattering is responsible for the atoms repelling each other in the MOT [30]. As understood from Fig. 1.8, it is caused by atoms rescattering the photons that the surrounding atoms scatter due to the laser light. We derive next a basic expression for the force describing this effect, in the situation with two atoms exposed to one laser beam. As in Fig. 1.8, we let atom 1 be the atom that scatters light and atom 2 - the atom that rescatters the scattered light.

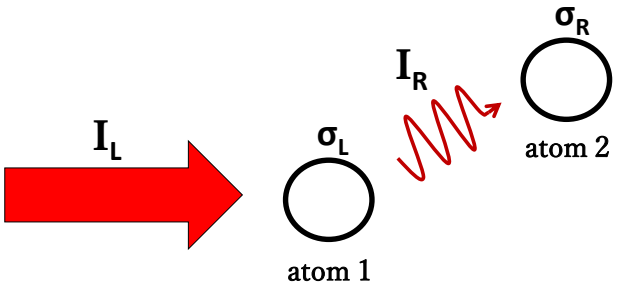

Figure 1.8: Depiction of the mechanism behind the rescattering. Laser light of intensity I_L is scattered by atom 1. This scattered light is then rescattered by atom 2. The rescattered light has the intensity I_R determined by the inverse-square law of propagation. σ_L is the laser scattering cross-section of atom 1, and σ_R is the rescattering cross-section of atom 2. σ_L and σ_R determine respectively the power scattered and rescattered.

We observe first in Fig. 1.8 laser light of intensity I_L being scattered by atom 1. The power that atom 1 will scatter from the laser will be

$$P_L = I_L \sigma_L \tag{1.15}$$

where σ_L is the laser scattering cross-section of atom 1.

The power rescattered by atom 2 will be, analogously to Eq. 1.15,

$$P_R = I_R \sigma_R \tag{1.16}$$

where I_R is the intensity rescattered by atom 2, and σ_R is the rescattering cross-section of atom 2.

The intensity I_R will be diminished according to the inverse-square law of propagation:

$$I_R = \frac{P_L}{4\pi |\mathbf{r}_{1,2}|^2} \tag{1.17}$$

where it is assumed that the scattering is isotropic. $\mathbf{r}_{1,2} \equiv \mathbf{r}_2 - \mathbf{r}_1$ defines the vector pointing from atom 1, at $\mathbf{r}_1$, to atom 2, at $\mathbf{r}_2$.

With help of Eqs. 1.15-1.17, we write down the following force that atom 2 will experience due to the rescattering:

$$\begin{aligned}\mathbf{F}_{rsc}(\mathbf{r}_2) &= \frac{P_R(\mathbf{r}_2)}{c}\hat{\mathbf{r}}_{1,2} \\ &= \frac{I_L\sigma_L\sigma_R}{4\pi c}\frac{\hat{\mathbf{r}}_{1,2}}{|\mathbf{r}_{1,2}|^2}\end{aligned} \tag{1.18}$$

where $\hat{\mathbf{r}}_{1,2} = \frac{\mathbf{r}_{1,2}}{|\mathbf{r}_{1,2}|}$ is the unit vector corresponding to $\mathbf{r}_{1,2}$. We refer to the force $\mathbf{F}_{rsc}$ as the rescattering force. From the above expression, this force is seen to be proportional to the inverse-square of the distance between the atoms, implying that it has a Coulomb-like force character.

The rescattering cross-section σ_R is found by evaluating an overlap integral between (i) the emission spectrum that atom 1 produces when illuminated by the laser light (of intensity I_L) and (ii) the absorption spectrum of atom 2 when illuminated by the laser light and also in presence of the weak perturbing field (of intensity I_R). We will not consider writing down an expression for σ_R at the moment (it will be done in Chapter 3) but note that in the Wieman model discussed next, we will see that σ_R is larger than σ_L, such that the repulsion becomes larger than the compression, and the cloud expands when the atom number is increased.

The Wieman model

In the Wieman model [30], one considers a situation where the rescattering force within the MOT cloud balances the trapping force. The trapping force is here written as a sum of the restoring force and the shadow force, and, for the sake of simplicity, it is assumed that the cloud is spherically symmetric. In the balance of the model's forces, one predicts the uniform cloud density

$$\rho_n = \frac{\kappa c}{2I_L\sigma_L^2(\sigma_R/\sigma_L - 1)} \tag{1.19}$$

where $\kappa > 0$ (corresponds to damping), and $\sigma_R/\sigma_L > 1$ (corresponds to $|\mathbf{F}_{shw}| < |\mathbf{F}_{rsc}|$). If $\sigma_R/\sigma_L \leq 1$ (corresponds to $|\mathbf{F}_{shw}| \geq |\mathbf{F}_{rsc}|$) instead, the cloud compresses, and Eq. 1.19 is invalid.

From Eq. 1.19 we see that the Wieman model's predicted density is determined by the inequality $\sigma_R/\sigma_L > 1$ and does not dependent on the atom number. This inequality relies critically on inelastic scattering in the cloud [30].

The radius R_n of the cloud (uniform and spherical) is found using the volume formula $V = \frac{4}{3}\pi R_n^3 = \frac{N}{\rho_n}$, and is given by

$$R_n = \left(\frac{3}{4\pi}\frac{N}{\rho_n}\right)^{1/3} \tag{1.20}$$

from which we see that the cloud expands when the atom number is increased, according to $R_n \propto N^{1/3}$.

The fact the cloud here is of uniform density and expands with the atom number contrasts the temperature-limited regime case (refer to section 1.2.1).

The original Ref. [30] of the Wieman model reported a good agreement with the $R_n \propto N^{1/3}$ law for $N < 5 \cdot 10^7$ atoms and observed a steeper increase for a larger amount of atoms - see Fig. 1.9, taken from Ref. [30]. The explanations for the steeper increase included the effect of the magnetic field gradient, multiple-level character of the atoms and higher-order (> 2) scattering events inside the MOT clouds. Later experiments described in Ref. [24] (2014), surrounding scaling behavior of large MOT clouds (using our MOT), yielded the scaling law $R_n \propto N^{0.39}$ in the atom number range of $2 \cdot 10^7 \lesssim N \lesssim 10^{11}$ (with the reported cloud size increase from 0.3 to 9 mm). The deviation from the $R_n \propto N^{1/3}$ law was in Ref. [24] linked to the complex behavior of the cloud density profiles as the atom number was increased: (a) for $N \lesssim 10^8$ atoms the density profiles were observed to be close to Gaussian, similarly to what has been observed in the temperature-limited regime as described in Ref. [30]; (b) when increasing to roughly $N = 10^9$ atoms, the profiles resembled flat-tops, corresponding to the prediction of the Wieman model; (c) then, increasing N further, the profiles were observed to gradually round off, where for $N \gtrsim 10^{10}$ atoms a development of a central feature with enhanced density was observed - such development of the central feature was linked in Ref. [24] to the MOT entering the so-called two-component regime [25], which is characterized by the density of the cloud core being enhanced as it is subject to a highly restoring sub-Doppler trapping force, while the remaining part of the cloud remains of lower density as it is subject to a regular Doppler-like trapping force. We will not be elaborating on the two-component regime but only mention that it is a regime that the MOT can enter when the cloud surpasses a certain cloud radius (refer to Eq. 21 in Ref. [25]). In Ref. [24], to calculate the density of the clouds the authors made use of an assumption that the clouds were axially symmetric and had a Gaussian density distribution, and it was found that the densities in the mentioned N range of $2 \cdot 10^7 \lesssim N \lesssim 10^{11}$ were $\sim 2 \cdot 10^{11}$ cm^{-3} - largely independent of N, in agreement with the Wieman model.

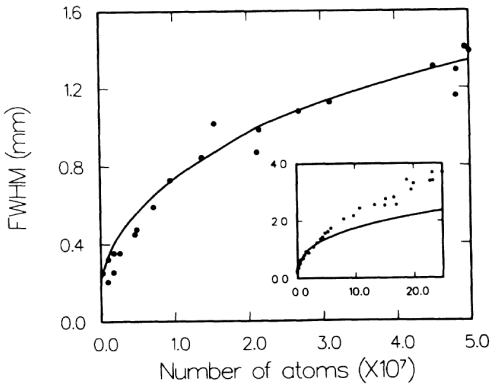

Figure 1.9: The full-width at half-maximum (FWHM) size of the MOT cloud versus the number of atoms in the cloud. The dots are the experimental results, and the solid lines correspond to the Wieman model's prediction of size $\propto N^{1/3}$. **Source:** [30].

Temperature change due to atom-atom interactions

To end this subsection, we discuss briefly the MOT cloud temperature change that occurs due to atom-atom interactions.

Previously, in section 1.1, we have mentioned about the spontaneous emission contributing to the momentum diffusion coefficient D, which is responsible for the diffusive heating of the atoms. Naturally, as the scattered photons get rescattered, additional heating will be produced that is similar to the heating caused by the spontaneous emission in the usual laser cooling.

The temperature increase caused by the rescattering can be predicted by considering a 2-level atom case, where the additional contribution to the diffusion in the limit of high detuning (absolute value) is found to be proportional to the cloud's optical depth [26], which for a constant cloud density (as is characteristic to the multiple-scattering regime) reads as $\sigma_L \rho_n R_n$. Using Eq. 1.20 result telling us that $R_n \propto N^{1/3}$, and the fact that the momentum diffusion coefficient is proportional to the temperature of the cloud (see Eq. 1.4), the temperature excess due to the rescattering thus should scale as $N^{1/3}$. Such temperature scaling has indeed been verified by several experiments [27, 28, 29].

1.2.3 The unstable regime

The unstable regime of the MOT is characterized by the cloud behavior where the spatial density distribution of the clouds evolves with time. Certainly, even in apparently stationary clouds the positions of the individual atoms evolve continuously due to the diffusion; however, in these situations the density remains stationary on spatial scales that are tiny compared to the cloud size, and thus such clouds are deemed as stable.

In this subsection, a synthesis of past results on different kinds of unstable behavior observed in the MOT is made, categorized by the configuration of the MOT. We present instabilities existing in the configurations that are respectively misaligned, retro-reflected, balanced and parameter-modulated. In the first three configurations the considered instabilities are of self-oscillatory nature, while in the last configuration the considered instabilities are resonant phenomena. Note that this Thesis has concentrated on studying self-oscillating instabilities in the balanced MOT. Results have been acquired also for self-oscillations occurring in the misaligned MOT but have been mentioned only briefly, as part of the Thesis outlook.

1.2.3.1 Instabilities in the misaligned MOT

Virtually every MOT has some degree of beam misalignment, but not every such MOT can be considered to be in the misaligned configuration. In the misaligned MOT, the degree of misalignment is great enough (explained shortly) for very specific cloud structures to appear that can be either stable or unstable. The misaligned MOT cloud structures were first described by C. E. Wieman and coworkers in 1991 in the same paper that introduced to the Wieman model,

Ref. [30]. Since then, the misaligned MOT was studied extensively and by various authors, e.g. in Refs. [31, 32, 33]. In the following, we make a synthesis of the research described in Refs. [30]-[33].

The original study seen in Ref. [30] reported observations of misaligned MOT structures with atoms in an orbit, in a regime governed by many-atom physics, with $\sim 10^8$ atoms loaded into the MOT, for different degrees of misalignment in the horizontal-plane, i.e. the xy-plane. Fig. 1.10, taken from Ref. [30], illustrates the main experimental findings, where in (a) a uniform density sphere (characteristic to the multiple-scattering regime) is seen, obtained with well-aligned beams, and in (b) and (c) an orbiting clump around a core and a stable ring around a core respectively are seen, obtained with misaligned beams. The cloud switched into the unstable structure (a rotating clump around a core) when the misalignment at the trap region was between $\frac{1}{6}$ and $\frac{1}{4}$ of the beam waist diameter and into the stable structure (a ring with a core) for the misalignment between $\frac{1}{4}$ and $\frac{1}{2}$ of the waist diameter. Additionally, as the misalignment grew further (beyond $\frac{1}{2}$ of the waist diameter), a stable ring without a core was formed and, eventually, for too large misalignment, the cloud would escape the trap. When the misalignment was introduced to the vertical (z-axis) trapping beams, the plane of rotation could be tilted up to 20 °, but no stable orbits were observed in the vertical direction; Ref. [30] speculated that this was due to the asymmetry of the MOT's trapping force, where the gradient is twice as large in the vertical direction compared to the horizontal plane (refer to Chapter 3 for the 3D MOT theory). The used theoretical model showed that the rescattering was necessary to explain the existence of the orbits. The model could not, however, explain the dynamical features of the unstable structure. It was speculated that such features were indicative of nonlinear interactions that could stem from e.g. the intensity attenuation, being an effect that was excluded from the model.

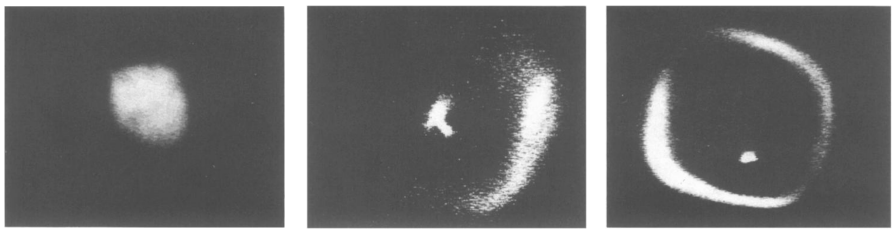

(a) **(b)** **(c)**

Figure 1.10: Snapshots of trapped atoms. In (a) the cloud is a uniform density sphere, obtained when the MOT beams are well-aligned. In (b) and (c) the beams are misaligned, where in (b) a clump of atoms that rotates around a core is observed, and in (c) a stable ring of atoms around a core is observed. Horizontal scale for (b) is 0.8 cm, and for (a), (c) it is 1 cm. **Source:** [30].

After the original paper in Ref. [30], the misaligned MOT experiments described in Ref. [31] from 1993 by a group of V. S. Bagnato showed that stable ring structures could be obtained in the temperature-limited regime. Such ob-

servation indicated that many-atom physics was not needed to explain them, contrary to what was suggested in Ref. [30]. The theoretical model developed in Ref. [31] excluded the rescattering and was able to predict the stable structures. The model was based on a coordinate-dependent vortex force induced by the beam misalignment. As explained in Ref. [31], the atoms were accelerated by the vortex force until their velocity became large enough such that it was balanced by the friction force, and the stabilization of ring orbits was achieved. A new instability study, shown below, used a model based on the vortex force.

Two years later, in 1995, the study in Ref. [32] by a group of V. S. Bagnato reported a second variant of an unstable structure in the misaligned MOT - a double-ring structure displayed in Fig. 1.11, taken from Ref. [32]. The structure was obtained when the beam misalignment at the trap region was around $\frac{1}{2}$ of the waist diameter and high beam intensity was used (the Rabi frequency much larger than the trapping detuning), and it would collapse into a single-ring structure, with or without a core, in times on the order of one second. A similar theoretical model as in Ref. [31] was used that was based on the vortex force and excluded the rescattering, and it could predict the static features of the new structure, although not the dynamical ones. However, the follow-up study from 1999 on the new unstable structure, in Ref. [33], by a group of V. S. Bagnato used another theoretical model to show that the prediction of this structure in Ref. [32] was actually due to the over-simplicity of the model in Ref. [32] rather than a real fact and that the inclusion of the rescattering was necessary for its prediction. The model in Ref. [33] nevertheless could not reproduce the observed unstable behavior of this structure. In Ref. [33], new experimental details also emerged surrounding this structure, where it was shown that it appeared in a regime governed by many-atom physics, with $N > 10^6$ atoms loaded into the MOT, and that it would collapse into a single-ring structure and then oscillations between the two structures would occur (note that while the collapse was reported in Ref. [32], the oscillations were, however, not). It was speculated in Ref. [33] that the oscillations were caused by the presence of atom number loss mechanisms that were not included in the newest model; as mentioned in Ref. [33], the loss mechanisms might reduce the atom number after cloud shape variations, giving rise to the observed oscillating behavior.

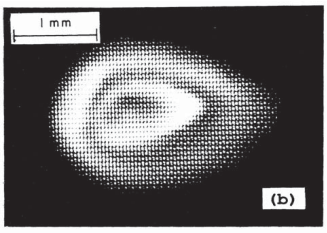

Figure 1.11: Snapshot of trapped atoms showing an unstable double-ring structure in the misaligned MOT. The structure collapses into a single-ring structure, with or without a core. **Source:** [32].

As seen from the above synthesis, no research has yet been able to fully address the two different kinds of unstable structures in the misaligned MOTs, i.e. a clump of atoms orbiting around an atomic core and a double-ring structure oscillating between single- and double-ring structures. In the Thesis outlook, we will show preliminary simulation-results that we were able to obtain on the unstable regime of the misaligned MOT and mention the physical ingredients needed to enter it.

1.2.3.2 Instabilities in the retro-reflected MOT

In the retro-reflected MOT, a given counter-propagating beam pair is formed by retro-reflecting a beam on a mirror. The incident beams in this MOT configuration are referred to as the *forward* beams, whereas the beams that are formed by the retro-reflection are referred to as the *backward* beams. Because of the attenuation due to light scattering by the atoms, the backward beams have lower intensity than the forward beams, and it is in this asymmetry of intensities the instabilities can be generated. Instabilities occurring in the retro-reflected MOT were first described by D. Wilkowski et al. in 2000 in Ref. [34] and then further studied in a same group (of D. Hennequin) in Refs. [35]-[38]. In the following, we make a synthesis of the research described in Refs. [34]-[38].

To start, we mention that Refs. [36] and [37] from 2004 presented extensive studies on the dynamics of retro-reflected MOT instabilities. These studies respectively dealt with types of the dynamics deemed as *stochastic* and *deterministic* by the previous respective studies in Refs. [34] and [35]. To explain all the existing observations on the dynamics, Refs. [36, 37] used the theoretical model developed in Ref. [35]. We will first consider Refs. [34, 35], and then Refs. [36, 37]. Afterwards, the remaining study, in Ref. [38], will be considered, which is on the spatial properties of instability dynamics.

The first study to have dealt with retro-reflected MOT instabilities, in Ref. [34], reported the instabilities to consist of fluctuations of the center-of-mass (COM) location z_{com} and the atom number N of the cloud. The instabilities appeared in a regime governed by many-atom physics, with more than 10^8 atoms loaded into the MOT, but only in limited ranges of parameters (for example, at the fixed intensity of 4.4 mW/cm^2 per forward beam and the fixed coil-axis magnetic field gradient of 14 G/cm, the instabilities would occur for δ between $-1.3\,\Gamma$ and $-0.9\,\Gamma$). The behavior of z_{com} appeared as an erratic signal that at times would be interrupted by almost periodic oscillations of large amplitude, typically $\sim$30 μm peak-to-peak, for a 1 mm sized cloud. The frequency spectrum of z_{com} exhibited a peak centered at a high-frequency, which depended on the MOT parameters (but typically between 10 and 100 Hz). The spectrum also possessed a low-frequency component (below 5 Hz), which was responsible for the displacement of the cloud along the first bisector of the three forward beams. The behavior of N was very different. It was erratic, with the frequency spectrum containing only low frequencies (below 5 Hz). A throughout analysis of the behavior of N did not evidence any order, and thus the behavior of N was concluded as being stochastic. Even though the behaviors of N and z_{com}

were very different, they were nevertheless found to be correlated when the high-frequency components were filtered. The theoretical model developed in Ref. [34] could successfully explain the observations. It identified the intensity attenuation as responsible for the nonlinearity associated with the instability (as it appeared in a limited parameter-range), and that its dynamics were driven by noise and presented stochastic resonance-like[3] characteristics. Such characteristics were responsible for the enhancement of an eigenfrequency in the system, consequently producing the high-frequency peak in the spectrum of z_{com}. The results of the model in Ref. [34] were later confirmed in Ref. [36], with help of another model developed in Ref. [35].

The next study in Ref. [35] from 2003 reported a new type of retro-reflected MOT instabilities, characterized by large amplitude self-oscillations that were either periodic or erratic, depending on the parameters. The oscillation amplitudes could be more than 100 times greater than those reported in Ref. [34] (up to several millimeters versus tens of micrometers), while the main change with respect to the experiment in Ref. [34] was that a larger beam intensity was used (up to 20 mW/cm^2). The important observations were as follows. Far from resonance, the cloud was stable. As one came close to the resonance, giant oscillations were observed, and they would change in character the closer to the resonance one got. Two different kinds of giant oscillations were found to occur. The first kind ($\delta = -1.7\,\Gamma$, for the forward beam intensity of 20 mW/cm^2 and the coil-axis magnetic field gradient of 13 G/cm) were periodic and asymmetric, with both z_{com} and N observed to first slowly grow and then suddenly drop (the characteristic times of the growth and loss stages would differ by more than one order of magnitude). Closer to the resonance ($\delta > -0.8\,\Gamma$), the behavior of z_{com} and N was still cyclic with asymmetric growth and loss stages, but the periodicity was gone. Finally, when getting very close to the resonance ($\delta > -0.55\,\Gamma$), the cloud would be again stable. The model developed in Ref. [35] could successfully be used in explaining the observed instabilities. It identified the intensity attenuation as responsible for the nonlinearity associated with the instabilities and allowed these to be deemed of deterministic origin, due to the appearance of giant oscillations not requiring addition of a random component in the model. Note that the erratic-kind giant oscillations (lost periodicity) appeared due to the oscillations being affected by noise, as explained by this kind exploring the region close to the edge of the beam waists, where sensitivity to noise was increased. Also note that an important difference between the previous model in Ref. [34] and the one in Ref. [35] was that in the former model, the attenuation was taken into account by considering the cloud to be a point object, whereas in the latter one, that was done by considering the cloud to posses a finite extent. The finite extent was considered in the latter model, as one kept in mind that the experimentally observed giant oscillations could approach distances beyond the edge of the beam waist, where the trap was empty, such that the edge could

[3]Stochastic resonance is a phenomenon, where the frequencies in the white noise corresponding to the system's natural frequencies resonate with each other, amplifying the system's oscillations while not amplifying the rest of the noise and thereby increasing the signal-to-noise ratio.

affect the cloud in stages, in proportion to the number of atoms beyond this edge. (To take into account the noise produced by the edge effects, Ref. [35] added noise artificially in the model.)

The following year, in 2004, Refs. [36] and [37] presented extensive studies on the dynamics of respectively stochastic and deterministic retro-reflected MOT instabilities. New kinds of stochastic and deterministic dynamics including those already investigated in Refs. [34] and [35] were reported, with the theoretical model of Ref. [35] employed in explaining the observations. All the instabilities appeared in a regime governed by many-atom physics, with more than 10^8 atoms loaded into the MOT, and the detuning range in which the stochastic- or deterministic-type would appear depended critically on the beam intensity, with the stochastic-type being progressively replaced by the deterministic-type as the intensity was increased. Ref. [36] reported a new kind of stochastic instability, with the main difference compared to the old one being that the z_{COM} frequency spectrum did not possess the high-frequency peak, such that only low-frequency components were significant, and so the dynamics essentially were along the first bisector of the three forward beams. The employed theoretical model was used in reproducing both kinds of the stochastic instabilities: in a certain detuning range, noise (artificially added in the model) was efficient at enhancing oscillations at the system's natural frequency, leading to the appearance of a peaked high-frequency component for the z_{COM} behavior, as was characteristic to the old instability; outside that detuning range, noise's efficiency of the excitation was diminished, leading to the flat resonance observed in the case of the new instability. Now, moving on to Ref. [37], a new kind of deterministic instability was reported, which not only had the periodicity gone in its (giant) oscillations, but secondary fast oscillations during the growth stage would appear and also the amplitude of the oscillations would change in time. The employed theoretical model was used in showing that these features of the (deterministic) instability were due to the instability being affected by noise, as explained by it exploring the region close to the edge of the beam waists, where sensitivity to noise was increased; the oscillations of the new instability were more erratic than of the old instability where only the periodicity was effected, due to the new one being affected by greater edge effects (modeled by having more noise artificially added in). The appearance of the deterministic instabilities with erratic features allowed Ref. [37] to confirm that noise plays a crucial role in the cloud dynamics.

Finally, more than a decade later, in 2016, Ref. [38] reported a study on the spatial properties of retro-reflected MOT instability dynamics. Ref. [38] studied the instability observed originally in Ref. [34], and focused on understanding how the instability was located in the cloud as well as what spatial modes the instability dynamics consisted of. Temporal Fourier analysis (TFA) as well as principal component analysis (PCA) were employed as the two complementary methods in the analysis. Experiments described in Ref. [38] involved recording the temporal evolution of the 2D projection of the cloud's fluorescence, and the methods were illustrated for a single, fixed set of MOT parameters. By applying TFA to each point of the (recorded) cloud, it was found that the dynamics of

the instability were localized in a limited area of the cloud, typically 10% of the whole cloud, while the remaining part of the cloud was stable. Nonetheless, for different recording sequences, there would be changes in how the instability was distributed in the cloud: the location of the local instability maxima, their number as well as the overall shape were observed to differ. PCA could complement the results of TFA by identifying the different spatial modes that the dynamics consisted of. PCA uncovered that for different recording sequences the first mode accounted for 50-80 % of the statistical fluctuations and the second mode accounted for 5-25 % of the statistical fluctuations. Thus, one single mode appeared to dominate all the dynamics, but with the weight of the second mode being non-negligible. The major difference between the two methods, i.e. TFA and PCA, was that in the former, a wide variety of shapes were obtained, whereas in the latter, the results were more homogeneous, with one set of modes accounting for the majority of the statistical fluctuations. From the results of the two complementary methods, Ref. [38] was able to conclude that spatial and temporal unstable behaviors could not be separated, such that, to gain a deeper physical interpretation of the observed behavior, models that relied exclusively on temporal description of the instabilities, like in Refs. [36, 37], had to be abandoned in favor of spatio-temporal models. As proposed in Ref. [38], one of such spatio-temporal models could be the *photon bubble* model [42]. In the next sub-subsection, where balanced MOT instabilities will be considered, the photon bubble model will be described.

1.2.3.3 Instabilities in the balanced MOT

In the balanced MOT, the laser beams are independent and of the same intensities before entering the cloud. However, instabilities still appear in this MOT configuration and require a new kind of theory to be explained. Instabilities occurring in the balanced MOT were first mentioned to exist by D. Wilkowski et al. in 2000 in the concluding remarks of Ref. [34] (that dealt with instabilities in the retro-reflected MOT), but the first observation of balanced MOT instabilities was done only years later, in 2006, by G. Labeyrie et al. in Ref. [39]. Further research was done in a same group (of R. Kaiser) as well as by different authors in collaboration with this group, in Refs. [40]-[44]. In the following, we make a synthesis of the research described in Refs. [39]-[44].

The original study seen in Ref. [39] reported an observation of self-oscillations in a balanced MOT, containing up to 10^{10} atoms, in a regime governed by many-atom physics. The precise shape of the oscillations varied with the cloud region being monitored. The instability threshold behavior was investigated by varying the trapping detuning and the magnetic field gradient, with the outcome shown in Fig. 1.12, where the black squares are the experimental results, while the solid red line indicates the theoretical prediction of the *1-zone* model, to be covered shortly. As Fig. 1.12 displays, the unstable behavior was observed when the trapping laser frequency was within roughly one natural linewidth from the resonance, with the instability threshold depending weakly on the magnetic field gradient. The cloud size and the atom number varied naturally with the control

parameters in Fig. 1.12 (variation of a factor of 2 for the size and a factor of 5 for the atom number). The fluctuations of the atom number as the MOT operated in the unstable regime were found to be negligible (below 2 %, as in the stable regime) and indicated that for a given set of control parameters the unstable cloud would oscillate at a fixed atom number. Note that this is in contrast to the retro-reflected MOT case (section 1.2.3.2), where fluctuations of the atom number were an intrinsic part of the instability dynamics.

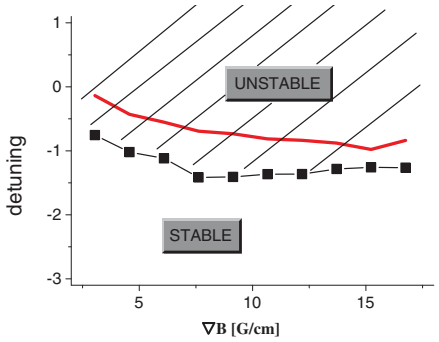

Figure 1.12: Phase diagram for balanced MOT instabilities. The trapping detuning is in units of Γ, and the magnetic field gradient (∇B) is along the MOT's coil-axis. The black squares are the experimental results, and the solid red line indicates the theoretical prediction of the 1-zone model (see text). The solid black line connecting the black squares is drawn to display the separation between the stable and unstable regimes. **Source:** [39].

In order to explain the appearance of the instabilities, the authors Ref. [39] extended the Wieman model to account for larger optical depths, due to the great atom numbers involved. The extended model was called the 1-zone model, and it showed that for large enough MOT clouds the edge of the cloud would experience a negative friction, such that the edge atoms would be accelerated away from the trap center, instead of being pushed towards it (as otherwise is the case for stable clouds). The passage from a positive to negative friction at the cloud's edge was marked by the following instability threshold condition:

$$\delta + \mu B' R_c = 0 \tag{1.21}$$

where R_c denotes the so-called critical radius, deemed to be the largest radius that the cloud could have before unstable cloud motion was induced. The theoretically predicted instability threshold in Fig. 1.12 (solid red line) was drawn according to the instability threshold condition of Eq. 1.21 by using the radii of the stable clouds just below the threshold and letting the gyromagnetic ratio $\mu = g_F \mu_B/\hbar = 2\pi \times 1.4 \times 10^6$ Hz/G, where $g_F = 1$. A comparison of the behaviors of the experimental and theoretical instability thresholds suggested a qualitative match. We note that in Chapter 2, we will do our own assessment of the 1-zone model, by making comparisons of our experimentally obtained results with the corresponding predictions of Eq. 1.21.

Shortly after the original study in Ref. [39], in the same year of 2006, Ref. [40] by T. Pohl et al. described simulations of balanced MOT instabilities. The numerical model was based on a 2-level atom in the Doppler picture, with the ingredient forces being the trapping force and the rescattering force, with intensity attenuation incorporated in these forces. The simulations were quasi-1D in nature: spherical cloud symmetry was assumed, which effectively reduced the dimension to 1D while also preventing COM motion of the clouds. In the stable regime, the simulations could reproduce the $N^{1/3}$ cloud size scaling law (the Wieman model's prediction). Most importantly, Ref. [40] was successful in simulating unstable behavior and to provide some interpretations. It was stated that the critical radius R_c of the cloud was uniquely determined by the instability threshold condition of Eq. 1.21 (as predicted by Ref. [39]). Just below the instability threshold the cloud radius would exhibit underdamped oscillations, and in the unstable regime the cloud radius would exhibit driven oscillations. It was shown that beyond R_c a finite active region (positive total force) would be formed that fed the oscillatory dynamics of the unstable MOT. These oscillatory dynamics were observed to be triggered by the outer fraction of the atoms that gained energy as they moved in and out of the active region. The higher-energetic atoms deposited their energy to the region with radii smaller than R_c, and a density wave would form that propagated towards the trap center. During the propagation, this density wave flattened, indicating that it was losing energy (which was mostly due to the damping by the lasers). At the same time, the outer atoms were gaining energy from the active region, and the whole process would then repeat itself. As concluded in Ref. [40], a number of different effects, such as the intensity attenuation, the rescattering as well as the position dependence of σ_R were *all* necessary in explaining the appearance of the instabilities. We note that in Chapter 3, we will present simulations of balanced MOT instabilities in a full-blown 3D environment and see how our results compare to those in Ref. [40].

Later, in 2010 and 2012, balanced MOT instabilities were treated theoretically in respectively Ref. [41] by H. Terças et al. and Ref. [42] by J. T. Mendonça and R. Kaiser. The theoretical models developed in these references were based on fluid descriptions of atomic medium and proposed new instability mechanisms. The mechanism proposed in Ref. [41] was driven by the coupling between the modes that resulted from the restoring force and the collective forces (i.e. the shadow and rescattering forces), respectively responsible for the COM oscillations of frequency ω_{COM} and the breathing oscillations of frequency ω_P (the notation ω_P was used, as the breathing mode was also referred to as the effective plasma mode). Ref. [41] considered assuming a balance between the restoring and collective forces, such that a relation between ω_{COM} and ω_P could be established ($\omega_{COM} = \omega_P/\sqrt{3}$), after which stability criteria could be established for the resulting dynamics of the system, as described by a Mathieu type of equation. Then, a phase diagram could be obtained that was similar to the one seen in Ref. [39] (Fig. 1.12 above). This *Mathieu equation* model, however, predicted different stability zones, which did not happen in the 1-zone model of Ref. [39]. The discrepancy was explained by Ref. [41] to rely on the

fact that the new model did not depend on the size of the cloud, and, as a consequence, the edge atoms were not required to contribute to the dynamics of the system. Regarding the mechanism proposed in Ref. [42], it allowed for the formation of oscillating and purely growing photon bubbles that were suggested to provide a source for the unstable spatio-temporal density structures as predicted by Ref. [40]. The collective forces were required to be present for the photon bubble formation. Although Ref. [42] considered the photon bubbles only theoretically, the scientific pre-print in Ref. [43] from 2016 by J. D. Rodrigues et al. made an experimental investigation on these structures. It was claimed that, as the beams were tuned very close to the atomic resonance ($\delta = -0.5\,\Gamma$, for the coil-axis magnetic field gradient of 9 G/cm), the observed unstable cloud contained signatures of photon bubbles. Such a claim was based on the fact that the power spectrum of the unstable cloud density fluctuations displayed a k^{-4} scaling at large wavenumbers, being a scaling that was theoretically predicted by Ref. [43] to characterize a particular type of dipolar-shaped photon bubbles. This theoretical prediction of Ref. [43] followed after power spectrum derivations using the photon bubble model described in Ref. [42]. We note that in Chapter 2, we will do our own assessment of the two instability models presented here, i.e. the Mathieu equation model and the photon bubble model, by using our experimentally obtained results.

We would like to lastly mention the publication in Ref. [44] from 2018 that studied synchronization of balanced MOT instabilities. A kind of hybrid situation was considered in the study, as the described experiment involved a balanced MOT instability, and a weak sinusoidal modulation was applied to the trapping detuning, technically making the MOT a parameter-modulated MOT (talked about in the next sub-subsection). One considered working just above the instability threshold, where the cloud's motion was monochromatic; deeper in the unstable regime, more diverse oscillations would occur. One observed that synchronization frequencies were slightly asymmetric around the natural oscillation frequency, and that the synchronization frequency range increased with the forcing amplitude. One compared the observations to what could be predicted using the 1-zone model formalism. The prediction yielded symmetrically distributed synchronization frequencies around the natural oscillation frequency and wider synchronization range for very weak modulations. Nevertheless, the experimental result was deemed to agree well with theory when considering the real-world limitations, with noise being an important component. Ref. [44], moreover, investigated phase differences between the oscillator and the modulating drive, and it was found that phase coherence between the two was achieved when in the synchronization region. In conclusion, the authors were able to confirm that synchronization of the cloud to an external modulation establishes control over the frequency and phase of the self-oscillations.

1.2.3.4 Instabilities in the parameter-modulated MOT

In the parameter-modulated MOT, a parameter, such as beam intensity, magnetic field gradient or trapping detuning, is periodically modulated. In this MOT configuration, unstable cloud motion can be induced that depends on the external modulation and is no longer self-sustained, which otherwise is the case for the instabilities existing in all the previously mentioned MOT configurations. Instabilities occurring in the parameter-modulated MOT were first described by K. Kim et al. in 2003 in Ref. [45] and then further studied in a same group (of W. Jhe), with the collection of their main results published in 2017 in Ref. [46]. A six-independent-beams MOT was used in the studies. In the following, we make a synthesis of the research described in Ref. [46].

As reported in Ref. [46], by periodically modulating the intensity of the coil-axis trapping beams with the controlled phases, one could realize two kinds of nonlinear oscillators - the parametrically driven Duffing oscillator (PDDO) and the resonantly driven Duffing oscillator (RDDO). For the PDDO, one used the modulation frequency $\omega_F \approx 2\omega_{tr}$, where $\omega_{tr} = \sqrt{\kappa/M}$ is the MOT's trapping frequency, and the relative phase difference between the beams as $\Delta\phi = 0$; for the RDDO, one used $\omega_F \approx \omega_{tr}$ and $\Delta\phi = \pi$. These instabilities could be obtained in a regime governed by single-atom physics, with $\sim 10^6$ atoms loaded into the MOT, and, as one entered a regime governed by many-atom physics, with $\gtrsim 10^6$ atoms loaded into the MOT, they exhibited respectively the collective phenomena such as the spontaneous symmetry breaking (SSB) and the kinetic phase transition (KPT). We will first consider showing the obtained results in the single-atom physics regime and then the many-atom physics regime. Lastly, we will consider showing the investigation on the system's behavior as one instead modulated the magnetic field gradient or the trapping detuning.

In Fig. 1.13, taken from Ref. [46], the vibrational amplitudes of the oscillators versus the modulation frequency normalized to the trapping frequency are seen to be plotted for different values of the modulation amplitude ϵ. The solid and dashed curves correspond to respectively the stable and unstable solutions, predicted by a theoretical model developed in Ref. [46] that was based on a trapping force, with the intensity modulation included. The upper part of Fig. 1.13 shows the snapshots (experimental) of the PDDO and RDDO that occupy the stable vibrational states for the largest values of ϵ ($\epsilon = 0.9$ for the PDDO and $\epsilon = 0.3$ for the RDDO). Concentrating on Fig. 1.13(a) with the PDDO, two atomic packets are seen to appear in the modulation region I, as explained by the model predicting that the PDDO is invariant under a discrete-time translation, implying existence of two identical out-of-phase stable states that vibrate symmetrically around the trap center (the middle between the packets). In the modulation region II, a central feature between the two atomic packets appears, which is attributed to the fact that in this region, a zero-amplitude stable state exists (notice the solid red line at the zero-level in Region II). Moving on to Fig. 1.13(b) with the RDDO, only a single distinct atomic packet is seen to appear in regions I and III, because unlike in the case for PDDO, the RDDO does not posses the time-translational symmetry, implying existence of only one stable

state in these regions. In the modulation region II, two atomic packets appear for the RDDO, as in this region an additional stable state exists (refer to the plot); the amplitude of this state is not zero, contrary to the case of the PDDO. For the RDDO, the state in region I was called the large-amplitude state (LS), the state in region III - the small-amplitude state (SS), while the (stable) states in region II - the coexisting dynamical states (CS), treated as a collection of the LS and SS states. As explained in Ref. [46], multiple stable states would become populated at once for the experimentally observed PDDO and RDDO due to noise caused by the finite temperature present in the studied system. As also explained and to be covered next in more detail, when atom-atom interactions came into play, changes occurred in the behavior of the oscillators.

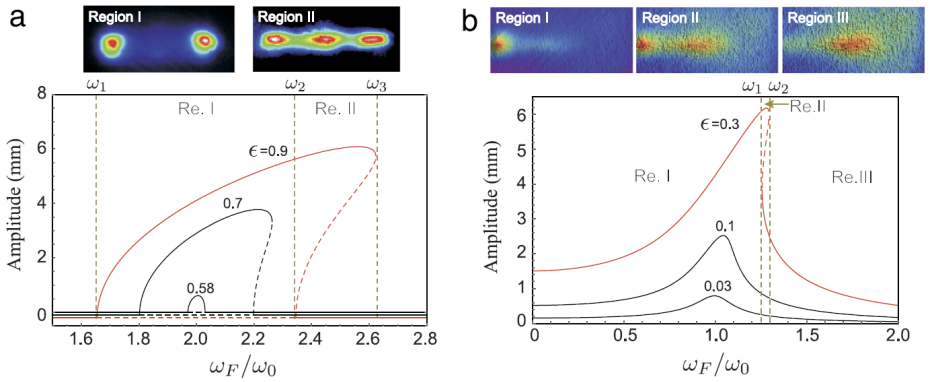

Figure 1.13: The vibrational amplitude versus the modulation frequency normalized to the trapping frequency, ω_F/ω_0 (in the text, ω_0 is ω_{tr}), depending on the modulation amplitude ϵ for (a) the parametrically driven Duffing oscillator (PDDO) and (b) the resonantly driven Duffing oscillator (RDDO). The solid and dashed curves correspond to respectively the stable and unstable solutions. Each curve is drawn with a small offset to distinguish each other. The frequencies ω_1, ω_2 and ω_3 separate the different modulation regions (Re.). The upper pictures show the snapshots (experimental) of the PDDO and RDDO that occupy the stable vibrational states for the largest displayed values of ϵ (red curves). When atom-atom interactions come into play, changes occur in the behavior of the oscillators (see text). **Source:** [46].

When atom–atom interactions came into play (with increased atom number), one could observe the collective phenomena such as the SSB and the KPT. Starting with the PDDO, when the atom number increased and surpassed a certain critical atom number, the SSB occurred between the two symmetrical vibrational states, such that the atoms became populated preferentially in one of the two states, as seen in Fig. 1.14. Since below the critical atom number the system was invariant under each discrete-time translation set by the modulation period τ_F, above this critical number the system was invariant under the discrete-time translation set by $2\tau_F$. The RDDO, on the other hand, did not posses the SSB property, but instead, as the atom number increased, a shift occurred to the KPT boundary, i.e. the boundary in the ω_F - ϵ phase-space where

the population in LS and SS was equal, resulting in the behavior displayed in Fig. 1.15. As can be seen from Fig. 1.15, the RDDO that was initially prepared in SS changed its state to LS while passing through the region with CS, when the atom number was increased. Ref. [46] was able to successfully predict the SSB and KPT phenomena by adding intensity attenuation into the previously used model.

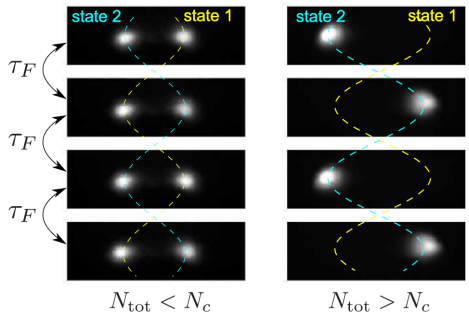

Figure 1.14: Snapshots of the PDDO taken for each modulation period τ_F at the positions where the two vibrational states are spatially separated the most. The left (right) panel is for the total atom number N_{tot} smaller (larger) than the critical atom number N_c. The dashed curves indicate the trajectories of each vibrational state. **Source:** [46].

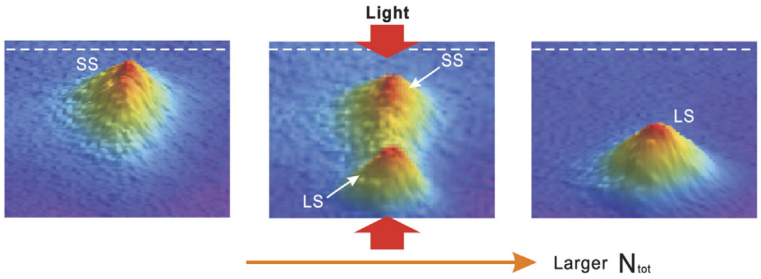

Figure 1.15: Snapshots of the RDDO showing the differences in the atomic population with the total atom number N_{tot}. The RDDO initially prepared in the small-amplitude state (SS) changes its state to the large-amplitude state (LS) in a unidirectional way while passing through the region with the coexisting dynamical states (CS; a collection of the LS and SS states), when N_{tot} is increased. The white dashed line indicates the trap center. **Source:** [46].

Finally, we mention that Ref. [46] argued that the modulation of the magnetic field gradient or the trapping detuning would lead to stronger nonlinear oscillations, such that more diverse complex dynamic behaviors could be investigated when either of these two parameters were modulated. As an example, it was demonstrated that modulating either of the two parameters at large values of ϵ ($\epsilon = 0.8$ and $\epsilon = 0.9$ for respectively the gradient and detuning case) could lead to chaotic motion.

Chapter 2

Balanced MOT instability experiments

Local table of contents

This Chapter concerns experiments of instabilities using our balanced, six-independent-beams Rb-87 MOT. New experimental knowledge about balanced MOT instabilities is achieved, and the known analytical instability-models (section 1.2.3.3) are assessed.

This Chapter is organized as follows. We begin by presenting our experimental setup and introducing to the different types of instability experiments that were conducted. Next, we investigate the instability threshold behavior versus respectively the magnetic field gradient ∇B, the atom number N and the intensity I per MOT beam. Then, we study the spatio-temporal properties of the unstable regime using various techniques, including eight-sector analysis (ESA), principal component analysis (PCA) and spatial Fourier analysis (SFA). By using ESA for analyzing the spatio-temporal distribution of clouds we are able to distinguish unique instability regimes, whose boundaries we draw in a phase-space diagram of the trapping detuning δ and ∇B. Using PCA we learn about the oscillation modes of clouds of these regimes, while using SFA we learn about the size distribution of the structures developing in clouds of these regimes. Finally, this Chapter is closed with some remarks where we summarize our assessment of the known analytical instability-models, employed in carrying out explanations of our observations, and provide motivation for the next course of action.

2.1 The experimental setup

In this section, we introduce first to the atomic species used in our experiments. Then, we describe the lasers involved in our setup, how they are prepared, as well as how our MOT is operated. Finally, the details of the applied cloud-monitoring techniques are explained.

We note, for overview purposes, Figs. 2.2 and 2.4 represent diagrammatically our experimental setup: Fig. 2.2 shows the laser preparation stage of the setup, while Fig. 2.4 shows the MOT assembly with the different detectors employed. A picture of the MOT assembly from our laboratory is seen in Fig. 2.5.

2.1.1 Rb-87

The atomic species used in our experiments is Rb-87. The Rb-87 atoms enter the experimental MOT chamber in a vapor form from a reservoir that contains a chunk of natural Rb atoms[1] held at room temperature[2]. The MOT chamber's volume is 22 cm^3, and it operates under ultra-high vacuum pressure. As reported in Ref. [24], surrounding experiments done with our MOT, the background Rb-87 pressure is $\sim 3 \cdot 10^{-9}$ Torr. Rb-87 is also contained within the vapor cells utilized in the saturation absorption spectroscopy measurements, which form an important part of the laser preparation that is covered in the following subsection.

2.1.2 The lasers

The Rb-87 atoms inside our MOT chamber are exposed to light stemming from the six MOT beams, with each beam being a superposition of trapping laser light and repump laser light. As seen in Fig. 2.1(a), we use the D2 line of Rb-87, i.e. the transition $5^2S_{1/2} \rightarrow 5^2P_{3/2}$. The trapping laser is red-detuned from the hyperfine transition $F = 2 \rightarrow F' = 3$ by δ at a fixed value in the range from $-8.0\,\Gamma$ to $-0.7\,\Gamma$; this is the main laser used for cooling and confining the atoms. The repump laser is tuned to near-resonance with the transition $F = 1 \rightarrow F' = 2$; the role of this laser is to bring the atoms out of the ground $F = 1$ level so to maintain them in the interaction with the trapping laser. The repump light intensity I_{rep} is typically a few percent of the trapping light intensity I_L. Although very weak compared to the trapping laser, the repump laser is still relevant, as we keep in mind that it is possible to off-resonantly excite the transition $F = 2 \rightarrow F' = 2$ with the trapping laser, and from $F' = 2$ the atoms can decay to $F = 1$. We use the notation I to denote the intensity per MOT beam (equal to $I_L + I_{rep}$). Shown in Fig. 2.1(a) there is also a probe laser that is red-detuned from the transition $F = 2 \rightarrow F' = 3$ by δ_{pr}; this laser

[1] Natural Rb consists mainly of the isotopes Rb-85 and Rb-87, with Rb-85 accounting for $\sim$72 % and Rb-87 for $\sim$28 % of the total [14]. The respective atom masses are $1.410 \cdot 10^{-25}$ kg and $1.443 \cdot 10^{-25}$ kg [14].

[2] Natural Rb melts at 39.30 °C under atmospheric pressure [14].

is used in the measurements of the atom number N in stable clouds, as will be covered in section 2.1.4, surrounding the cloud-monitoring techniques.

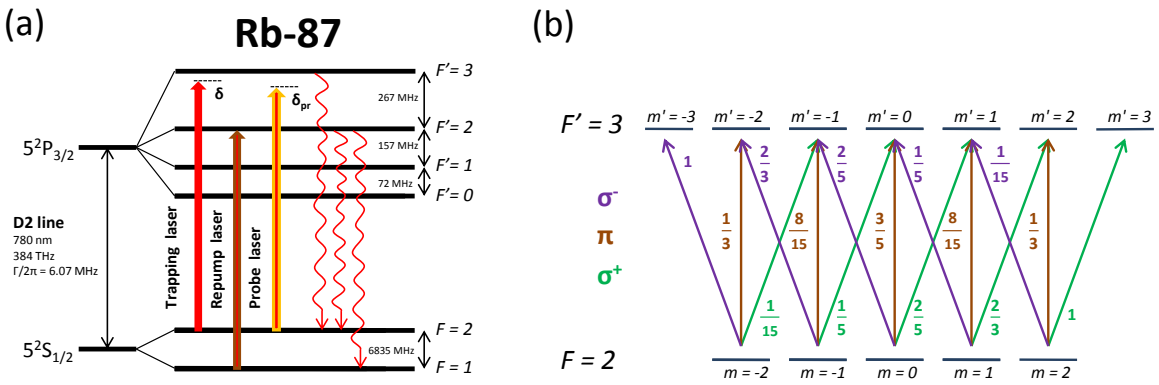

Figure 2.1: (a) Hyperfine energy level scheme for the Rb-87 D2 line. The trapping and probe lasers are red-detuned from the hyperfine transition $F = 2 \rightarrow F' = 3$ by respectively δ and δ_{pr}, and the repump laser is tuned to near-resonance with the hyperfine transition $F = 1 \rightarrow F' = 2$. The wavy lines correspond to the electric dipole allowed decay channels from respectively $F' = 2$ and $F' = 3$. The energy levels are not to scale. (b) Light coupling scheme for the hyperfine transition $F = 2 \rightarrow F' = 3$ with shown squared absolute values of the Clebsch-Gordan coefficients for all the possible Zeeman transitions $m \rightarrow m'$. The Zeeman transitions satisfying $\Delta m \equiv m - m' = -1$ are induced only by left-hand circular (σ^-) polarized light, $\Delta m = +1$ only by right-hand circular (σ^+), and $\Delta m = 0$ only by linear (π).

We concentrate now on the laser preparation stage, diagrammatically represented in Fig. 2.2. There are two laser sources in our setup. Both of them are distributed feedback laser diodes from Toptica, with 60 mW power output and 3 MHz linewidth. The trapping and probe laser beams stem from a common laser source, whereas the repump laser beam stems from its own separate laser source. With help of two respective saturation absorption spectroscopy (SAS) setups (implied by the arrows in Fig. 2.2 pointing to SAS), the laser sources are first frequency locked. The trapping/probe laser source is locked at a cross-over peak in the middle between the $F = 2$ and $F' = 3$ levels, and the repump laser is locked at a cross-over peak in the middle between the $F = 1$ and $F' = 2$ levels. The beam stemming from the trapping/probe laser source is seen in Fig. 2.2 to be split by a polarizing beam-splitter (PBS) into two beams - one being the trapping beam and another one being the probe beam. These two beams then have their frequencies shifted in the respective double-pass acousto-optical modulator (AOM) configurations (involving "AOM, tr" and "AOM, pr" in Fig. 2.2). The repump beam has its frequency also shifted in a separate double-pass AOM configuration (involving "AOM, rep" in Fig. 2.2). After the trapping and repump beams have their frequencies shifted by the respective AOMs, we

observe that the beams are collected together by a PBS. The collected beam travels through a tapered amplifier (TA), amplifying the beam's power. The TA is from Sacher Lasertechnik and provides up to 2.5 W output power. After the TA, the collected beam gets frequency shifted by a switch AOM ("AOM, MOT switch" in Fig. 2.2) and next gets injected into a fiber beam-splitter (FBS) that splits this beam into the six MOT beams. The FBS is from OZ Optics, and the fibers that we use are polarization-maintaining. Coming back to the probe beam, after its frequency gets shifted in the double-pass AOM configuration, this beam travels into the part of the setup where its frequency again gets shifted, this time by a switch AOM ("AOM, pr switch" in Fig. 2.2), afterwards which the beam is sent to the MOT through a polarization-maintaining fiber. Note that when a given switch AOM is switched off, the corresponding beam does not enter the fiber and into the MOT. In summary, the respective detunings for the trapping laser, the repump laser and the probe laser are

$$\delta = \omega_{2\to3} + 2\omega_{aom,tr} - \omega_{aom,MOTsw} \tag{2.1a}$$

$$\delta_{rep} = \omega_{1\to2} + 2\omega_{aom,rep} - \omega_{aom,MOTsw} \tag{2.1b}$$

$$\delta_{pr} = \omega_{2\to3} + 2\omega_{aom,pr} - \omega_{aom,prsw} \tag{2.1c}$$

$\omega_{2\to3}$ and $\omega_{1\to2}$ are the frequencies of respectively the trapping/probe and repump laser sources after the frequency locking is performed with help of SAS. $\omega_{aom,tr}$, $\omega_{aom,rep}$ and $\omega_{aom,pr}$ are the frequency shifts induced by respectively "AOM, tr", "AOM, rep" and "AOM, pr" seen in Fig. 2.2; note that these AOMs are passed twice, ergo the multiplication by 2 is required. $\omega_{aom,MOTsw}$ and $\omega_{aom,prsw}$ are the frequency shifts induced by respectively "AOM, MOT switch" and "AOM, pr switch" seen in Fig. 2.2. The particular plus and minus signs appearing on the right-hand side of Eqs. 2.1(a-c) are explained by Fig. 2.3, depicting how the different AOMs induce the frequency shifts after the frequency locking of the laser sources is performed. We note that a given light beam must pass two separate AOMs (with one of the AOMs passed twice) in order to achieve the required detuning, because our AOMs shift frequencies in a limited frequency range. The signals controlling the AOMs are generated by a computer board, which is controlled by a graphical user interface (GUI) created with MATLAB. In this GUI, we type in the detunings δ, δ_{rep}, δ_{pr}, and the AOMs adjust themselves in an automated way. The GUI used is quite versatile, and in the next subsection (2.1.3) as well as the next section (2.2) we will be seeing its other functionalities that are important for us.

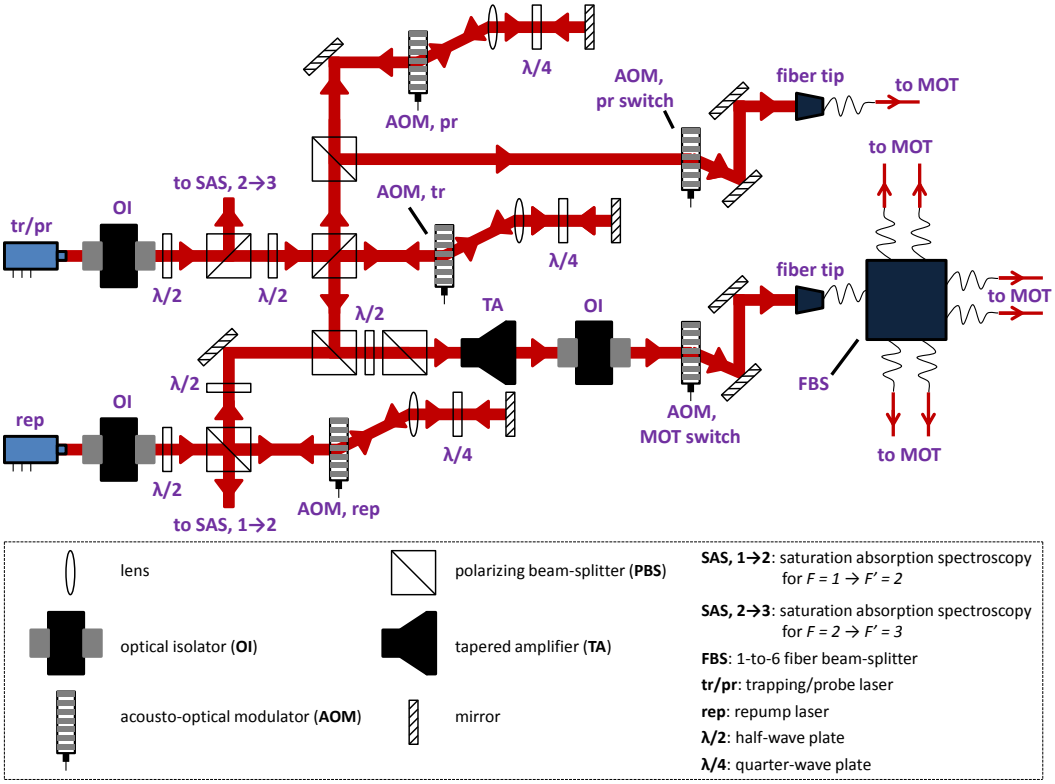

Figure 2.2: Diagrammatic representation of the laser preparation stage of our experimental setup.

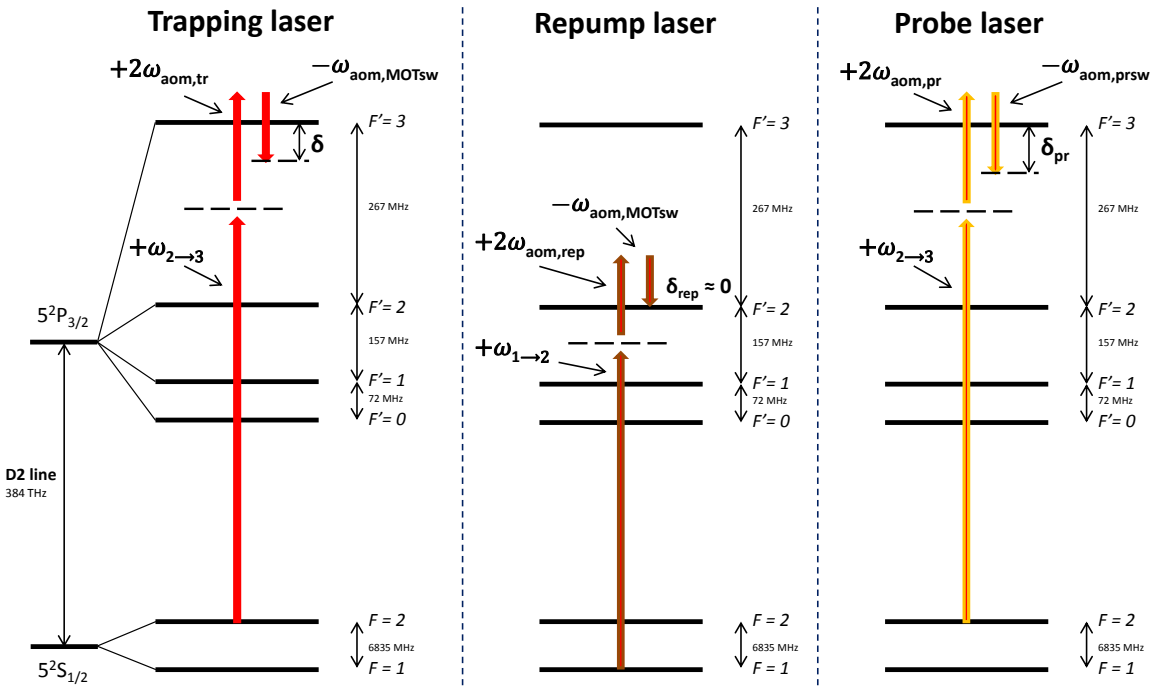

Figure 2.3: Depiction showing how the AOMs in our experimental setup induce the frequency shifts after the frequency locking of the laser sources is performed with help of saturation absorption spectroscopy. Using the scheme, the detunings δ, δ_{rep} and δ_{pr} of the respective lasers are set. For the remaining definitions of the frequencies refer to Eq. 2.1. The energy levels are not to scale.

2.1.3 The MOT assembly

After having explained the laser preparation stage, we concentrate now on our MOT assembly and clarify how the MOT beams as well as the probe beam propagate in this assembly, and describe the magnetic field coil system used in our MOT. Note that the real life picture of the assembly is shown in Fig. 2.5.

Let us observe the sketch of our MOT assembly, Fig. 2.4, and start with the MOT beams. As they exit the fibers, the beams pass first through collimators attached to the fiber tips. The intensities of the beams are balanced using the half-wave plate and PBS assemblies; calibrated photodiodes (not shown in Fig. 2.4) give the intensity measurements. The beam polarizations are then made circular with help of quarter-wave plates. Finally, before entering the MOT chamber, the beams are expanded using afocal telescopes (made by lenses L1 and L2 in Fig. 2.4) with the magnification of 6. The waist size of the MOT beams is 3.4 cm. Note that we check that the beams indeed are overlapping with help of masks, with the aperture diameter of 5 mm, that we place on the large lenses (L2 in Fig. 2.4) of the afocal telescopes; the lenses themselves have a diameter of 94 mm. Now, in the case of the probe beam, it diverges as it exits the fiber, because there is no collimator attached to the fiber tip. After diverging the right amount, the probe beam passes through a lens (L3 in Fig. 2.4), which collimates the beam. The waist size of the probe beam is 2.2 cm. After passing through the MOT chamber, the probe beam passes through an afocal telescope (made by lenses L4 and L5 in Fig. 2.4), after which it gets collected by the charge-coupled device (CCD) camera called CCD3, providing us with an intensity profile with help of which we can, when using the procedure covered in the next subsection, give an estimate for the atom number N in stable clouds. We note that we turn on the probe beam only when the MOT beams are turned off (achieved by switching on "AOM, pr switch", with "AOM, MOT switch" switched off; see Fig. 2.2).

Next, we describe the magnetic field coil system we use in our MOT. On the outside of the MOT chamber there are four magnetic field coil pairs. One of the pairs is an anti-Helmholtz coil pair (shown in Fig. 2.4). Its coil-axis is the MOT's z-axis, which we note to have referred to as *the* coil-axis. This pair produces an approximately linearly increasing magnetic field gradient through the intersection of the beams, i.e. where the magnetic field is finely tuned to be zero by using the Helmholtz coil pairs, being the three remaining coil pairs (not shown in Fig. 2.4). The calibration of the magnetic field is done using a calibrated Hall probe. The coil-axes of the Helmholtz coil pairs are the respective MOT's x-, y- and z-axes. These pairs produce a compensating magnetic field with help of which we can adjust the position of the zero of the magnetic field. All the coil pairs have their own separate current sources. The current through the anti-Hemholtz coils is manually-controlled, but can be turned on and off with help of the GUI. The current through the Helmholtz coils is, on the other hand, fully GUI-controlled. The coil-axis magnetic field gradient produced by the anti-Helmholtz coils (due to the current) is set in the range from 1.2 to 12 G/cm, with the corresponding uncertainty going down from 10 to 1 % (as set by the increment of the current). Note that due to the nature of the anti-Helmholtz magnetic field, its gradient is two times weaker in the MOT's horizontal plane (xy-plane). We use the notations ∇B and B' interchangeably to denote the coil-axis magnetic field gradient and, for simplicity, just call it the magnetic field gradient.

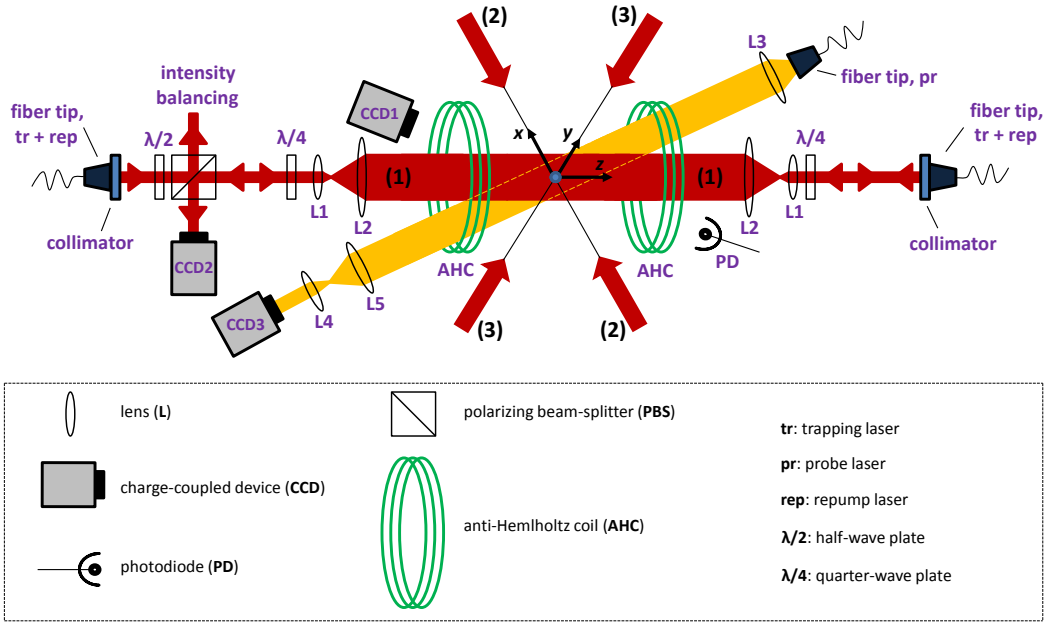

Figure 2.4: Diagrammatic representation of our MOT assembly. All the detectors employed are shown (CCD1, CCD2, CCD3 and PD1). The probe beam (yellow) is only turned on when the MOT beams (red) are turned off. The MOT beam pairs (2) and (3) are identical to the beam pair (1).

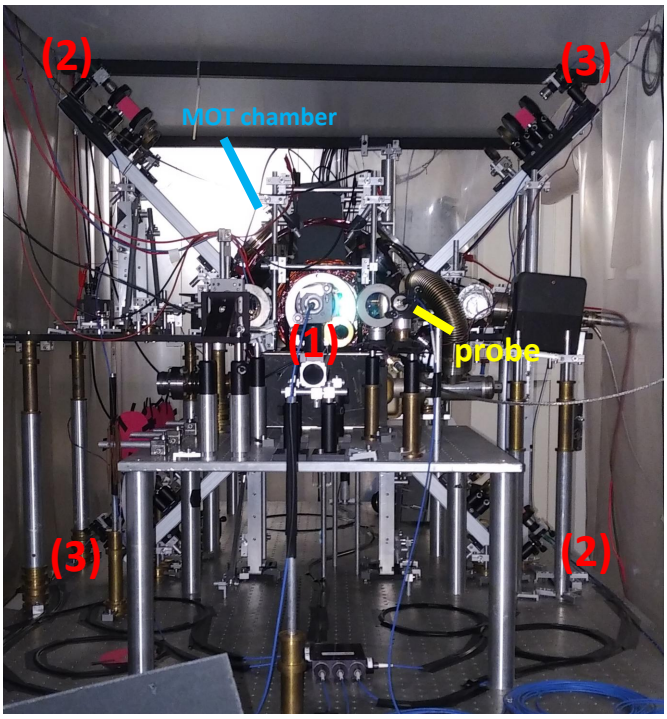

Figure 2.5: A picture of the MOT assembly from our laboratory. The fiber tips from which the probe beam and the MOT beam pairs (1), (2) and (3) stem from are indicated. Behind the MOT chamber, which is also indicated, there is the fiber tip of one of the beams belonging to the pair (1).

2.1.4 The cloud-monitoring techniques

The two cloud-monitoring techniques that we use are fluorescence imaging and absorption imaging. When fluorescence imaging is done the cloud's fluorescent light is picked up by a detector, and when absorption imaging is done a detector picks up direct laser light whose intensity depends on how much it has been absorbed by the cloud. The detectors employed in the monitoring are specified next, after which we describe the two techniques in better detail.

There is a total of four detectors employed in the monitoring, as shown in Fig. 2.4, with the sketch of our MOT assembly. Two of the detectors are the fluorescence imaging detectors: the charge-coupled device (CCD) camera called CCD1 as well as the photodiode called PD. The remaining detectors are the absorption imaging detectors: the CCD cameras called CCD2 and CCD3. All the CCD cameras monitor in the xy-plane (the lines of sight for the CCD1 and CCD3 are at small angles with the z-axis, respectively at $\sim 10\,^\circ$ and $\sim -10\,^\circ$). The CCD1 is either (a) MIKROTRON's MotionBLITZ Cube7 with 1696×1710 pixel resolution and 523 frame rate per second, or (b) Point Grey Scorpion 20SO with 1600×1200 pixel resolution; the option (a) is used when we are making continuous recordings and the option (b) when we are triggering to obtain single-shot recordings. The CCD2 and CCD3 are Point Grey Grasshopper GRAS-20S4M with 1600×1200 pixel resolution; these CCD cameras are triggered. The PD is from Hamamatsu with the photo-sensitive area of 1 cm^2.

Fluorescence imaging

We use fluorescence imaging in studying the cloud dynamics. With fluorescence imaging done with the CCD1, we can obtain 2D images of the 3D spatial density of clouds, integrated along the line of sight. However, in optically-thick clouds, the spatial distribution of the fluorescence light and that of the cloud density are two different quantities due to the multiple-scattering [24]. We minimize the distortion due to the multiple-scattering by using far-detuned light (by $-8\,\Gamma$) during the image acquisition, as detailed in the next section. The total fluorescence, as obtained from the PD, can be used to infer the relative atom number N_{rel} as the parameters are varied; in the upcoming part, surrounding absorption imaging, we will explain the usage of N_{rel}.

To extract stable cloud sizes from the 2D density images, we make use of 2D Gaussian fitting, as Fig. 2.6 exemplifies. The used fitting function can be written as $f(x,y) = Ae^{-(a(x-x_0)^2+b(y-y_0)^2+c(x-x_0)(y-y_0))}$, where A is the amplitude, $(x_0,\, y_0)$ are the center coordinates, $a = \frac{cos^2(\theta_\circlearrowleft)}{2\sigma_{G,1}^2} + \frac{sin^2(\theta_\circlearrowleft)}{2\sigma_{G,2}^2}$, $b = \frac{sin^2(\theta_\circlearrowleft)}{2\sigma_{G,1}^2} + \frac{cos^2(\theta_\circlearrowleft)}{2\sigma_{G,2}^2}$, $c = -\frac{sin(2\theta_\circlearrowleft)}{4\sigma_{G,1}^2} + \frac{sin(2\theta_\circlearrowleft)}{4\sigma_{G,2}^2}$, with $\theta_\circlearrowleft$ being the clockwise rotational angle, and $\sigma_{G,1}$ and $\sigma_{G,2}$ being the RMS widths. The mean of $\sigma_{G,1}$ and $\sigma_{G,2}$ yielded by the fit we define as the radius of a stable cloud. We pick Gaussian fitting because the stable clouds in our described experiments typically possess Gaussian features as well as because of its simplicity.

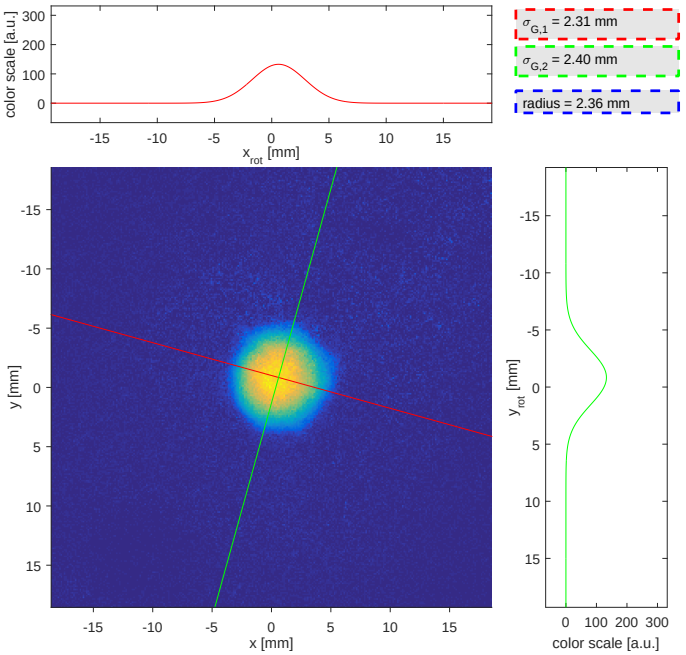

Figure 2.6: 2D Gaussian fitting applied to the stable cloud fluorescence image. The image represents the cloud density integrated along the line of sight. The measurement was done at $\delta = -3.4\,\Gamma$, for $\nabla B = 9.6$ G/cm and $I = 5$ mW/cm^2. The fitted 2D Gaussian (rotated; abbrev. rot) has the RMS widths $\sigma_{G,1}$ and $\sigma_{G,2}$ of the 1D Gaussians seen in the plots respectively above and to the right of the image. These 1D Gaussians follow the (correspondingly colored) solid lines in the image that are tilted by the rotational angle of the 2D Gaussian. The mean of $\sigma_{G,1}$ and $\sigma_{G,2}$ is the radius of the cloud.

Absorption imaging

We use absorption imaging in determining a stable cloud's optical depth, its size and its *absolute* atom number N. Regarding finding N in the unstable regime, this will be explained in the next section. Now, with the CCD2 we can measure the cloud's optical depth as seen by a MOT beam when in presence of the other MOT beams, while with the CCD3 we can measure the cloud's optical depth as seen by the probe beam after turning off the MOT beams. The optical depth measurements by the CCD3 can be used to find the cloud size and N in the cloud. The optical depth measurements by the CCD3 are done as follows (an analogous procedure is used for the CCD2). We begin by recording two images: first an image in the presence of the atoms and then an image in the absence of the atoms. These images are then used to determine the probe transmission profile $T_{pr}(x,y) = \frac{I_{pr}(x,y)}{I_{pr,0}(x,y)}$, where $I_{pr}(x,y)$ and $I_{pr,0}(x,y)$ denote the intensity profiles shown in the images respectively with and without the atoms. Once $T_{pr}(x,y)$ is determined, the cloud's optical depth profile as seen

by the probe beam, $b_{pr}(x,y)$, can be found from $b_{pr}(x,y) = -ln\left(T_{pr}(x,y)\right)$. The result for $b_{pr}(x,y)$ is used in finding N as follows. Given that we can write $N = \int dx'\, dy'\, dz'\, \rho(x',y',z')$, where ρ is the cloud density, together with the fact that $b_{pr}(x,y)$ can be expressed by $b_{pr}(x,y) = \int_{-\infty}^{+\infty} dz' \sigma_{pr}(x,y,z')\rho(x,y,z')$, we have, when assuming the scattering cross-section σ_{pr} of the atoms exposed to the probe field is constant, that $N = \frac{1}{\sigma_{pr}} \int dx'\, dy'\, b_{pr}(x',y')$. We approximate this N integral by assuming that b_{pr} takes a 2D Gaussian shape and obtain

$$N \approx 2\pi b_{pr}^{max} \sigma_{G,1} \sigma_{G,2} / \sigma_{pr} \tag{2.2}$$

where $\sigma_{G,1}$ and $\sigma_{G,2}$ are the RMS widths of the 2D Gaussian that we fit to b_{pr}, and b_{pr}^{max} is the probe's maximal optical depth, which is equal to the maximum of the fitted 2D Gaussian. We assume σ_{pr} to be given by

$$\sigma_{pr} = g \times \frac{\sigma_0}{1 + 4\frac{\delta_{pr}^2}{\Gamma^2}} \tag{2.3}$$

We have $g = \frac{7}{15}$, which is the degeneracy factor of the cooling transition $F = 2 \rightarrow F' = 3$. g is equal to the average value of the squared absolute values of the Clebsch-Gordan coefficients for all possible transitions between the Zeeman states of $F = 2$ and $F' = 3$, shown in Fig. 2.1(b). g appears, as we assume a uniform Zeeman sub-level population in the ground $F = 2$ level. Next, the term $\frac{\sigma_0}{1+4\delta_{pr}^2/\Gamma^2}$ is the laser scattering cross-section of a 2-level atom, where the Doppler effect as well as the Zeeman effect have been neglected and we have taken into account that experimentally the probe intensity $I_{pr} \ll I_{sat}$, with $I_{sat} = 3.58$ mW/cm^2 being the saturation intensity for Rb-87 for the case it has a uniform Zeeman sub-level population in the ground $F = 2$ level [14]. The Doppler effect can be neglected for the following reason. As reported in Ref. [47] that described experiments with our MOT, clouds that contained $\sim 10^{10}$ atoms (a typical number in our experiments) had temperatures in the range of 100 μK, which would correspond to Doppler widths as small as $\sim \frac{1}{30}\,\Gamma$. Considering that we set the probe detuning δ_{pr} at a fixed value in the typical range from $-7\,\Gamma$ to $-3\,\Gamma$, it is therefore very reasonable for the Doppler effect to be neglected. We note to rely on the temperature measurements reported in the previous study with our MOT because temperature measurements have not been done in our experiments. Regarding the Zeeman effect, it can be neglected because in our typical experimental conditions the Zeeman width is comparatively smaller than $|\delta_{pr}|$ (for example, for the edge atoms as in Fig. 2.6, the Zeeman width can be estimated to be $\mu \nabla B \cdot (radius) \approx 0.5\,\Gamma$, where $\mu = 2\pi \times 1.4 \times 10^6$ Hz/G as in section 1.2.3.3).

In Fig. 2.7, we can observe the optical depth profile of the stable cloud displayed in Fig. 2.6. As can be seen in Fig. 2.7, the 2D Gaussian fitting procedure has been applied to yield the RMS widths $\sigma_{G,1}$ and $\sigma_{G,2}$, and Eq. 2.2 has been made use of to find N in the cloud (see the figure text). Notice that the radius of the cloud as obtained using fluorescence imaging (2.36 mm) is very close to the radius obtainable using absorption imaging (2.33 mm), thanks to

the experimental procedure (next section) applied for fluorescence imaging that minimizes the distortion caused by the multiple-scattering. We finally note that, for a given set of parameters, the statistical fluctuations of N (shot to shot) as measured by absorption imaging are $\sim 3\,\%$.

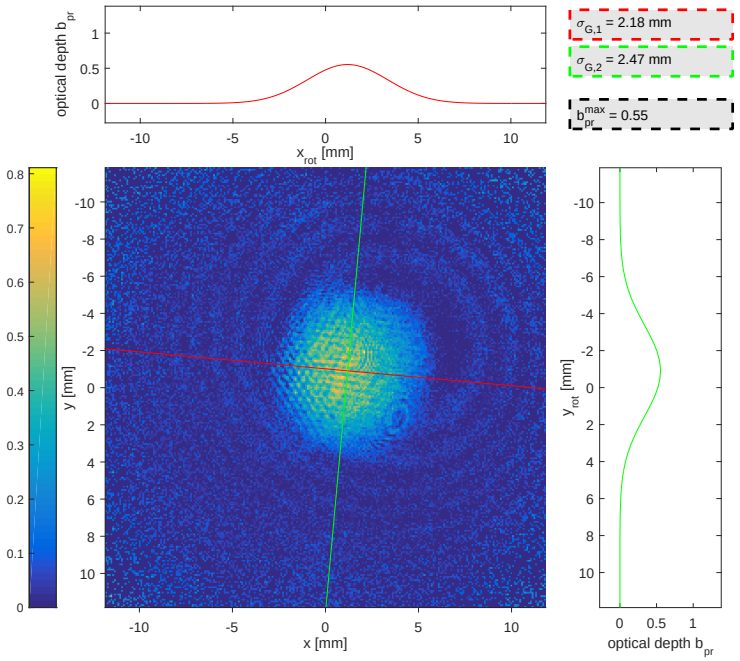

Figure 2.7: 2D Gaussian fitting applied to the optical depth profile of the stable cloud displayed in Fig. 2.6. The fitting procedure is similar to what is seen in Fig. 2.6. The maximal optical depth as seen by the probe beam, b_{pr}^{max}, is equal to the maximum of the fitted 2D Gaussian. The cloud contains $1.5 \cdot 10^{10}$ atoms, found using Eq. 2.2, with $\delta_{pr} = -5.2\,\Gamma$. The colorbar shows the optical depth b_{pr}.

2.2 The different types of instability experiments

In this section, we introduce to the two different types of instability experiments that were conducted - the steady-state type and the pulsed type.

2.2.1 The steady-state experiment type

In a steady-state experiment, the control parameters δ, ∇B and I are held fixed during the whole measurement sequence. If we choose to move to another set of values for the control parameters, the atom number N will naturally vary. The purpose of such experiment type is to study the temporal dynamics of the cloud. The cloud monitoring is done using the fast CCD1 (the CCD1 option

(a); refer to section 2.1.4). We have conducted a single steady-state experiment and will present its results in section 2.4.2.

To achieve control over N, the experiment type that is pulsed has been devised, although at a price, as will be seen next.

2.2.2 The pulsed experiment type

As we wish to study the instability threshold behaviors at a fixed N as well as the unstable regime behavior, also at a fixed N, we have devised the experiment type that is pulsed. In an experiment of this type, N is held fixed as different measurements are performed, and, to achieve this, the temporal sequence seen in Fig. 2.8 is employed that is continuously cycled, or, in other words, is pulsed. In the next paragraph, we concentrate on explaining this sequence.

There are three phases involved in the temporal sequence in Fig. 2.8, all of which are GUI-controlled. In the first phase, which is the MOT loading phase that typically lasts 2 s, the trapping detuning δ is set to the detuning δ_{load}. The value of δ_{load} is typically in the range from $-7\,\Gamma$ to $-4\,\Gamma$; the cloud is stable at δ_{load}. Next, in the instability phase, δ is changed to the detuning δ_{inst}. The value of δ_{inst} is typically in the range from $-4\,\Gamma$ to $-0.8\,\Gamma$. Jumping from δ_{load} to δ_{inst} makes the cloud atoms to start readjusting their positions. There is an initial readjustment period that is set by the position damping constant of the trap, and after this period is over, the post-transient cloud dynamics at the parameters in the instability phase are produced. 100 ms are experimentally checked to be long enough for the initial readjustment period to be over and, at the same time, short enough to keep N constant. Finally, in the imaging phase, δ is changed to the fixed detuning $\delta_{img} = -8\,\Gamma$. The period of the last phase is 1 ms, such that the atom position readjustment caused by the detuning jump (δ_{inst} to δ_{img}) is insignificant. By jumping the detuning to $\delta_{img} = -8\,\Gamma$, the distortion due to the multiple-scattering is minimized; see the study in Ref. [24]. During the last phase, two things are done. One thing is that the single-shot CCD1 (the CCD1 option (b); refer to section 2.1.4) is triggered to take a snapshot image, displaying a random instance of the post-transient cloud dynamics at the parameters in the instability phase. Another thing is that the PD gives us the total fluorescence signal that can be used as a reference for the relative atom number N_{rel}. The signal for N_{rel} stemming from the PD is read out on an oscilloscope and, by keeping this signal constant during the imaging phase, we maintain N fixed in the experiment (to know the actual value of N, absorption imaging is done, as explained in section 2.1.4).

Now, although by pulsing we achieve control over N, it comes at a price of losing the possibility of studying the temporal dynamics of the cloud. Thus, the pulsed experiment type is regarded as being complementary to the steady-state experiment type. We have conducted three pulsed experiments and will present their results in sections 2.3 and 2.4, to be concentrated on next.

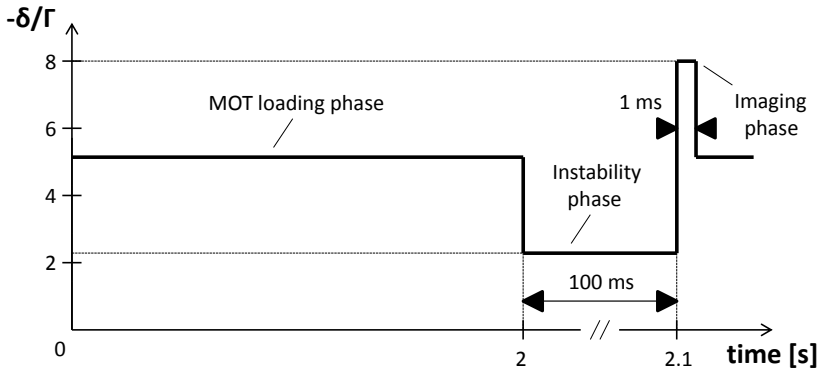

Figure 2.8: Temporal sequence employed in the pulsed type of experiments. The sequence consists of three different phases that are continuously cycled: (i) the MOT loading phase, (ii) the instability phase, (iii) the imaging phase. See the text for the details on each phase.

2.3 The instability threshold behaviors

In this section, we investigate the instability threshold behavior versus respectively the magnetic field gradient ∇B, the trapped atom number N and the intensity I per MOT beam. We explain the general procedure used for finding instability threshold in the first subsection (surrounding threshold versus ∇B). We note that in Chapter 3, the threshold behaviors investigated here will be compared with the corresponding simulated behaviors.

Before we start, we bring into attention that to study the threshold behaviors, we have performed experiments of the pulsed type (section 2.2.2), in that way achieving control over N during the measurements. Also, as we saw in section 1.2.3.3 introducing to balanced MOT instabilities, only a single experimental study has ever been done on instability threshold [39], where its behavior versus ∇B was examined, and, contrary to us, the experiment was of the steady-state type (section 2.2.1), where N was not controlled.

2.3.1 Instability threshold versus ∇B

In this subsection, we start by explaining the details of our experiment for studying the impact of the magnetic field gradient ∇B on the instability threshold behavior. We then explain the general procedure used for finding instability threshold and, finally, present the experimental threshold versus ∇B. A discussion of the results is provided. We note that results seen here are part of the publication in Ref. [72].

The details of the experiment considered here are as follows. The peak intensity per MOT beam was fixed at $I = 5$ mW/cm^2. Using the pulsed scheme described previously (section 2.2.2), the atom number N was maintained at $1.5 \cdot 10^{10}$ atoms and cloud fluorescence images were acquired during the different measurements. The measurements were performed at ∇B values of 1.2, 1.8, 2.4,

3, 3.6, 4.8, 6, 7.2, 9.6 and 12, all in units of G/cm, where for each ∇B value we varied the value of the trapping detuning δ at the instability phase (see Fig. 2.8) from $-4\,\Gamma$ to $-0.8\,\Gamma$ in a step of $0.2\,\Gamma$.

To understand how we find instability threshold, we start with a comment on the previous study in Ref. [39], where the detuning at threshold, δ_{thr}, was used to mark the point before the onset of the instability. Per this choice, we naturally also use δ_{thr} to mark the point before the onset of the instability.

The general procedure we use for extracting the instability threshold detuning δ_{thr} involves first quantifying the amount of cloud spatial fluctuation. Such quantification is done as follows: (i) start with a set of fluorescence images acquired from a given measurement, (ii) pick all the unique pairs of images from this set, (iii) subtract the images in these pairs from each other, (iv) find the total intensity in the absolute-valued difference-images, (v) normalize it by the total intensity contained in the sum of the two images in the corresponding pair, and, (vi) finally, sum all the normalized results and divide by the amount of the unique pairs. After the division, a single number quantifying the amount of cloud spatial fluctuation is obtained. The number is in the interval from zero to one. The number is zero if there is no difference between the images, and the closer the number is to one, the less overlap there is between the images; the number is one if there is no similarity between the images. We note that, because in our pulsed experiments we typically acquired $n = 50$ images from a given measurement, then the total of unique image pairs in each set of images was $\frac{n(n-1)}{2} = 1225$.

In Fig. 2.9, we plot the cloud spatial fluctuation over the complete experimental range of δ, i.e. $-4\,\Gamma \leq \delta \leq -0.8\,\Gamma$, for three values of ∇B. As can be observed, after a certain point in δ, the cloud spatial fluctuation begins to grow larger and exhibits a clear threshold behavior. The detuning points in the initial growth are used in a linear extrapolation of the δ value at the constant level, being the level set by all the detuning points before the points in the initial growth. This extrapolated δ is the threshold detuning δ_{thr} that marks the point before the onset of the instability - the clouds at detunings smaller than or equal to the extrapolated δ_{thr} are considered as stable, and the clouds at detunings larger than the extrapolated δ_{thr} are considered as unstable. By employing our procedure for extracting δ_{thr}, a distinction between the stable and unstable regimes is evidently made, with a sudden rise of fluctuations above the threshold. This is reproducible with whichever parameter we vary, thus deeming our procedure as well-suited for the threshold determination.

In Fig. 2.10, we plot the measured δ_{thr} values versus ∇B (see the black dots). It is observed that δ_{thr} decreases with ∇B, with the linear slope of $-0.13\,\Gamma$ per 1 G/cm (see the solid black line). In the inset of the figure, we plot the experimental threshold in log-log scale and do a comparison with the threshold found with help of the 1-zone model's condition of Eq. 1.21 (see the brown plus-signs). We here define the critical radius R_c to be twice the cloud radius just below the threshold, r_{thr}, and, similarly to what was done in Ref. [39], let the gyromagnetic ratio $\mu = 2\pi \times 1.4 \times 10^6$ Hz/G. We are

free to choose R_c as any multiple of r_{thr} because R_c is a free parameter in the model, due to the cloud edge being ill-defined. Nevertheless, as we switch to log-log scale, the slope behavior becomes independent of the multiplicative factor in front of r_{thr}, and we thus can clearly see that there is qualitative mismatch between the experiment and the 1-zone model prediction. We may therefore conclude that the physical mechanism behind the instabilities is more involved than of the 1-zone model's, where the instabilities are induced by the cloud's edge passing from a positive to negative friction. Alternatively, we could therefore turn to the two analytical models apart from the 1-zone model that have been used in explaining balanced MOT instabilities (section 1.2.3.3): (i) the Mathieu equation model, where the instability mechanism is driven by the coupling between the COM and breathing modes [41], (ii) the photon bubble model, where photon bubble structures provide a source for the unstable motion [42]. We recall that the Mathieu equation model has been used in obtaining a phase diagram similar to the one presented in Ref. [39]. We will, however, not consider applying this model to study threshold behavior; to assess this model, we took a different route as seen in the next section. Regarding the photon bubble model, it has not been devised with a goal of predicting instability threshold and therefore further theoretical work would be required to see if the model could yield predictions of such kind; in the next section we will nevertheless make an assessment of this model. To understand the threshold behavior versus ∇B, we have turned to simulating it, and in Chapter 3 we will see that we obtain a qualitative match with the experiment; comments will there be provided.

To compare our experimental threshold to that of Ref. [39] (Fig. 2.10 versus Fig. 1.12), we observe that our threshold detunings are much smaller (around $-2.5\,\Gamma$ instead of $-1\,\Gamma$) as well as that our threshold's variation with ∇B is stronger. We attribute the first discrepancy to N being larger in our case and the second one to the variation of N (with δ and ∇B) that naturally occurred in the steady-state scheme employed in the experiment in Ref. [39]. These explanations for the discrepancies are validated by the results in the next subsection, surrounding the impact of N on the threshold behavior.

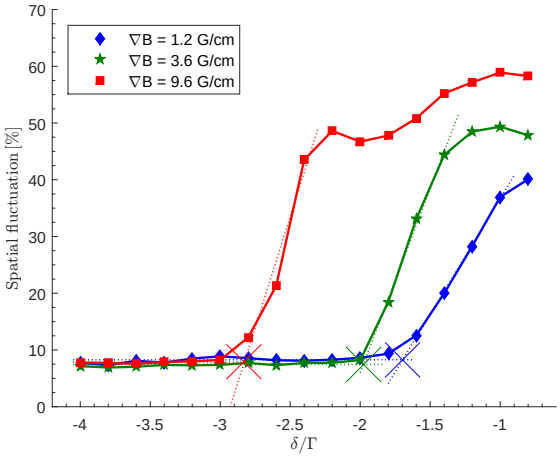

Figure 2.9: Determination of the instability threshold detuning δ_{thr}. The cloud spatial fluctuation (in %) is plotted versus the trapping detuning δ (in units of Γ) for three values of the magnetic field gradient: $\nabla B = 1.2$ G/cm (blue diamonds), $\nabla B = 3.6$ G/cm (green stars), $\nabla B = 9.6$ G/cm (red squares). In the experiment, the peak intensity per MOT beam was 5 mW/cm^2 and the atom number was $1.5 \cdot 10^{10}$ atoms. Linear fits are done to the initial growth (sloped dotted lines), and extrapolation is performed at the constant levels (horizontal dotted lines), yielding δ_{thr}/Γ (crosses) at the different values of ∇B.

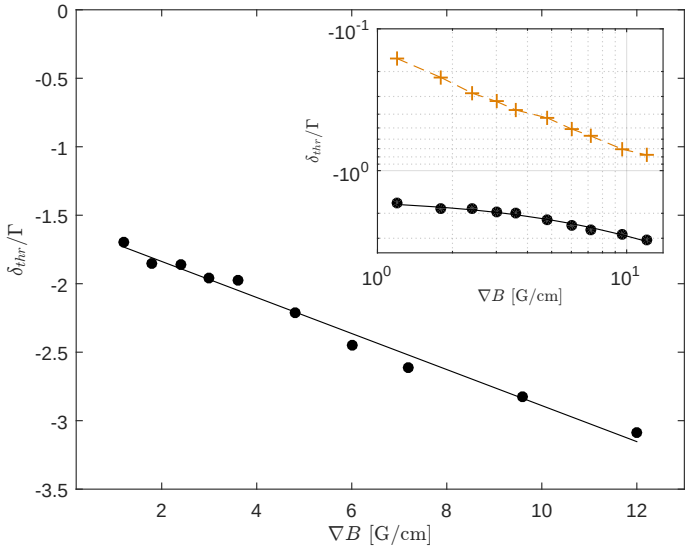

Figure 2.10: The threshold detuning δ_{thr} in units of Γ versus the magnetic field gradient ∇B, displayed in linear scale (main figure) and log-log scale (inset). The black dots are the experimental results, and the brown plus-signs are the theoretical results of the 1-zone model. In the experiment, the peak intensity per MOT beam was 5 mW/cm^2 and the atom number was $1.5 \cdot 10^{10}$ atoms. The solid black line is a linear fit to the experimental data-points, while the dashed brown line connecting the theoretical data-points is drawn as a visual aid.

2.3.2 Instability threshold versus N

In this subsection, we study the impact of the atom number N on the instability threshold behavior. The experimental details are first explained, followed up by a presentation of the results with their discussion. We note that results seen here are part of the publication in Ref. [72].

The details of the experiment considered here are as follows. The peak intensity per MOT beam was fixed at $I = 5$ mW/cm^2, and the magnetic field gradient was fixed at $\nabla B = 7.2$ G/cm. We used the pulsed scheme described previously (section 2.2.2), but with an additional ingredient to vary N over a wide range. Following the technique described in Ref. [24], we truncated the MOT beams using circular apertures of different diameters, to vary the trapping volume. The range of N values we worked with is from $8.4 \cdot 10^8$ to $1.2 \cdot 10^{11}$ atoms.

In Fig. 2.11, we plot the measured δ_{thr} values versus N in log-log scale (see the black dots). A power law fit made to the data-points (see the solid black line) yields the scaling of -0.17. Very roughly, this scaling tells us that δ_{thr} decreases by one Γ when N increases by one order of magnitude. To confirm the previous conclusion that the physical mechanism behind the instabilities is more involved than of the 1-zone model's, we plot in the figure the δ_{thr} values found with help of Eq. 1.21 (see the brown plus-signs). Like in the case of the experimental data, we make a power law fit to the theoretical data (see the solid brown line). This fit yields the slope of -0.37 (independent of the multiplicative factor in front of r_{thr} in the definition of R_c), which is very different from the experimental one and thus confirms our previous conclusion. To understand the threshold behavior versus N, we have turned to simulating it, and in Chapter 3 we will see that we obtain a qualitative match with the experiment; comments will there be provided.

To be used in other parts of this Thesis, we show additionally the measurement results in Fig. 2.12, for the maximal optical depth b_{MOT}^{max} as seen by a MOT beam when in presence of the other MOT beams versus N, for the stable clouds just below the threshold. We note that this outcome has a diminished quality, and so we stick to a discussion involving only its general features. As can be seen, the b_{MOT}^{max} values consistently stay above the value of 1 and on average are almost twice as large. This tells us that we are in a regime of strong attenuation. The attenuation is here no longer linear, which is one assumption of the Wieman model. Moreover, whereas in the Wieman model second-order scattering (rescattering) is taken into account, understanding this regime would in principle require taking into account third-order scattering (re-rescattering). The fact the beams are strongly attenuated will help us to fully justify the inclusion of the intensity attenuation, as described in Chapter 3, surrounding our simulations. We note that in Chapter 3, we will show the simulated b_{MOT}^{max} behavior and see how it can help us gain more insight on the instability physics.

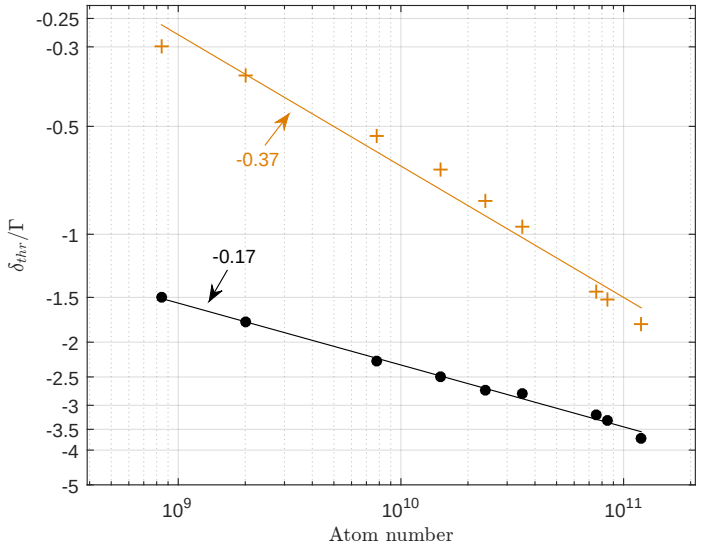

Figure 2.11: The threshold detuning δ_{thr} in units of Γ versus the atom number N, displayed in log-log scale. The black dots are the experimental results, and the brown plus-signs are the theoretical results of the 1-zone model. In the experiment, the peak intensity per MOT beam was 5 mW/cm^2 and the magnetic field gradient was 7.2 G/cm. The solid black and brown lines are the power law fits to the corresponding data-points. The numbers next to the arrows are the scaling exponents of the corresponding power law fits.

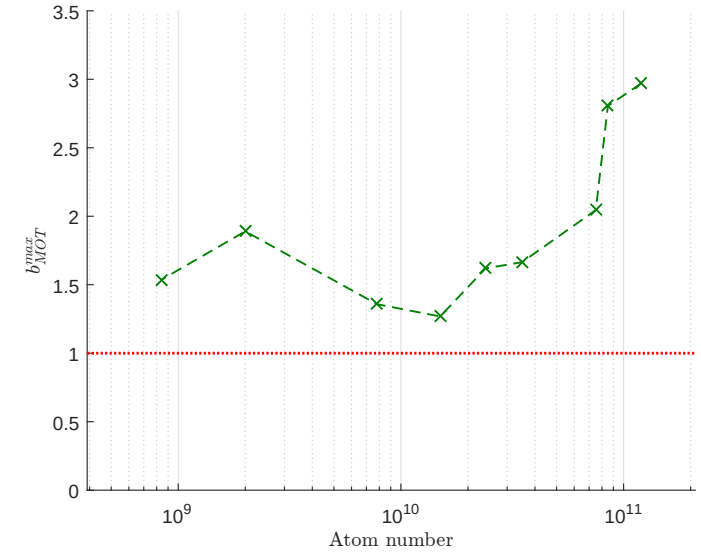

Figure 2.12: The maximal optical depth b_{MOT}^{max} as seen by a MOT beam when in presence of the other MOT beams versus the atom number N, for the stable clouds just below the threshold. The same experiment as in Fig. 2.11. The green crosses are the experimental results, and the dashed line connecting them is drawn as a visual aid. The horizontal dotted line indicates the rough boundary near which the multiple-scattering regime occurs.

2.3.3 Instability threshold versus I

In this subsection, we study the impact of the MOT beam intensity I on the instability threshold behavior. This study is motivated by the consideration of the fact that in the Wieman model, the inelastic scattering is critical for the repulsion to win over the compression in the cloud (refer to section 1.2.2). Thus, it is natural to ask how the instabilities will depend on the intensity, and, especially, whether they appear at very low intensities, where the elastic scattering dominates over the inelastic scattering - refer to Appendix A, where expressions for elastic and inelastic scattering rates can be found (Eqs. A.1(a, b)), together with a graphical representation of these expressions (Fig. A.1). We first explain the experimental details and then present as well as discuss the results.

The details of the experiment considered here are as follows. We performed three separate measurement rounds at fixed magnetic field gradients of respectively $\nabla B = 2.4$ G/cm, $\nabla B = 4.8$ G/cm and $\nabla B = 9.6$ G/cm. We used the pulsed scheme described previously (section 2.2.2) to maintain the value of the atom number N at $5.5 \cdot 10^{10}$, $8.7 \cdot 10^{10}$ and $4.5 \cdot 10^{10}$ at the respective ∇B values. For each ∇B value, we performed our typical threshold determination measurements at different values of the peak intensity per MOT beam, I, in the range from 0.17 to 5.24 mW/cm^2.

In Fig. 2.13, we plot the measured δ_{thr} values versus I for $\nabla B = 2.4$ G/cm, $\nabla B = 4.8$ G/cm and $\nabla B = 9.6$ G/cm (see resp. the blue diamonds, green dots and red squares). We observe first of all that the instabilities persist over the complete range of I. The most interesting part of this observation is that the I value as low as $\sim$0.2 mW/cm^2 is reached. It is surprising the instabilities occur in this region, as here $s \ll 1$, such that the elastic scattering completely dominates over the inelastic scattering (see Fig. A.1), which goes against our feeling that the inelastic scattering is important. Secondly, we observe that the threshold behavior versus I is non-monotonous and divided into two regimes: first a sharp decrease at lower I, with a slower increase at higher I (note the log horizontal-axis). The I value marking the boundary between these regimes is seen to increase with ∇B (see the vertical dotted lines). The third observation that we make is that the threshold shifts closer to the resonance as the ∇B value is decreased. This observation is consistent with our threshold versus ∇B (see Fig. 2.10), as the variation in N (with ∇B) rather weakly affects the threshold (see Fig. 2.11). To understand the threshold behavior versus I, we have turned to simulating it, and in Chapter 3 we will see that we obtain a qualitative match with the experiment; comments will there be provided.

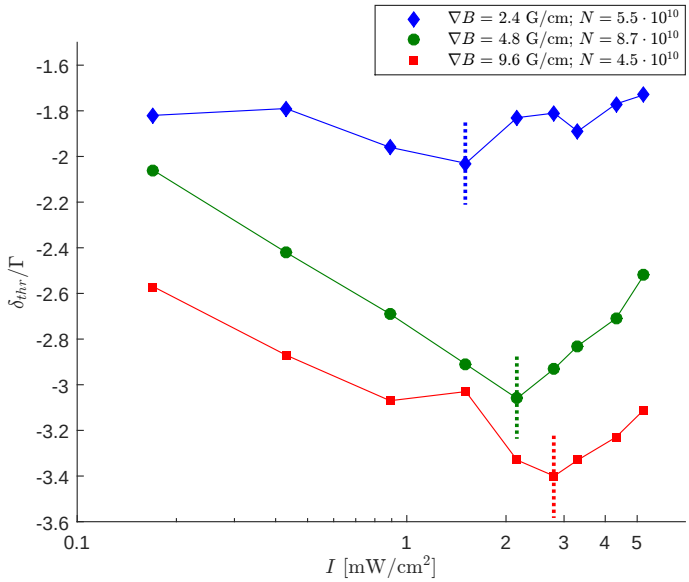

Figure 2.13: The threshold detuning δ_{thr} in units of Γ versus the peak intensity per MOT beam, I. The blue diamonds, green dots and red squares are the experimental results for the respective magnetic field gradient ∇B and atom number N values shown in the legend. The solid lines connecting the data-points are drawn as a visual aid. The vertical dotted lines mark the points of the smallest δ_{thr} values for the corresponding experimental sequences.

2.4 The spatio-temporal properties of the unstable regime

In this section, we go beyond investigations of the threshold behaviors and perform a study on the spatio-temporal properties of the unstable regime. Various techniques are employed, including eight-sector analysis (ESA), principal component analysis (PCA) and spatial Fourier analysis (SFA). By using ESA for analyzing the spatio-temporal distribution of clouds we are able to distinguish unique instability regimes, whose boundaries we draw in a δ-∇B phase-space diagram. Using PCA we learn about the oscillation modes of clouds of these regimes, while using SFA we learn about the size distribution of the structures developing in clouds of these regimes. We note that in Chapter 3, the ESA technique will be applied in studying simulated unstable clouds.

Before we start, we bring into attention that in all of the upcoming subsections (these are devoted to the analysis with the mentioned techniques), we use data from the pulsed experiment where we varied δ and ∇B (section 2.3.1), and in the last of these subsections (where PCA is performed), we as well consider treating data from an experiment of the steady-state type where we also varied δ and ∇B (section 2.2.1 covers the basics of this experiment type).

2.4.1 δ-∇B phase-space instability diagram

In this subsection, we start by describing the tool of eight-sector analysis (ESA) and employ it to analyze the spatio-temporal distribution of clouds from the experiment where we varied δ and ∇B (section 2.3.1). We explain how the analysis is able to distinguish unique instability regimes, whose boundaries we draw in the δ-∇B phase-space diagram seen at the end of this subsection. A discussion of the results is provided. We note that results seen here are part of the publication in Ref. [73].

Eight-sector analysis (ESA)

ESA is a computational technique that allows us to retrieve some information on the dynamics as well as symmetry of our clouds. It is an extension of four-quadrant analysis, which is an experimental technique where a four-quadrant photodiode is used in e.g. detecting the position of a laser beam. Closer to our topic, the experiments of retro-reflected MOT instabilities (section 1.2.3.2) employed four-quadrant analysis to monitor the position of the cloud COM. We make use of an extended version of the technique as our analysis requires increased sensitivity.

We perform ESA as follows. For a given pair of δ and ∇B values, we start with a set of 50 fluorescence images. A circle is cropped out from a given image and divided into eight angular sectors of equal size, with the center set to the COM of the average image of the stable cloud just below the threshold at a considered ∇B value; see Fig. 2.14(a) displaying such average image together with the sectors for one of the ∇B values (out of a total of ten). The circle's radius is fixed and is large enough to encompass the largest cloud deformations. The reason for the particular choice of the circle's center is because we would like it to be as close as possible to the MOT center for the unstable clouds (in the plane of view), with the MOT center being the natural reference point in the MOT. The circle's center is adjusted for each ∇B value to account for the experimental drift of the MOT center with ∇B. In Fig. 2.15, we display the COM radial drift for (a) the clouds just below the threshold, with respect to the cloud just below the threshold at $\nabla B = 1.2$ G/cm, and (b) the clouds below the threshold, with respect to the cloud just below the threshold, for different respective values of ∇B. This figure tells us that for increased ∇B the drift is small, yet non-negligible - on average $\sim$4 % of the image-dimension (5.3 cm), and that the drift gradually increases as $|\delta|$ is increased at a given ∇B value, but is at most $\sim$2 % of the image-dimension (see the $\nabla B = 1.2$ G/cm result). The origin for this drift we, however, do not know and choose to refrain from speculation. As the drift with $|\delta|$ is gradual as well as less pronounced than with ∇B, we expect the circle's center for the unstable clouds to be near the MOT center. We note that another viable option for picking the circle's center is to let it coincide with the COM of the average image for each single pair of δ and ∇B values. However, the reason this option is not picked is due to some unstable

clouds possessing highly anisotropic average envelopes (to be seen soon), which we believe have their COM further from the MOT center than determined by the current procedure. Now, moving on to the next step of the analysis, the intensity in each sector is found (i.e. by summing the values of every pixel in a sector) and divided by the total intensity inside the circle. Histograms are finally constructed, giving us the statistics on the intensity fractions in each sector for our set of 50 images. Two important quantities that are obtained from the histograms are the histogram-width and the histogram-mean. To be precise with their definitions, we take (i) the histogram-width to be defined as the difference between the largest and the smallest value of the data used in the construction of the histogram, and (ii) the histogram-mean to be defined as the mean of the data used in the construction of the histogram.

Applying ESA, it is easy to see that for a motionless, isotropic cloud the histograms for all the sectors would be infinitely narrow and centered at 1/8. The widths of the histograms can in some sense tell us how much movement a cloud exhibits, with greater widths indicating greater movement, and thus could be used in determining instability threshold. However, such method of using histogram-widths in determining instability threshold is not as robust as compared to the one we have been using (section 2.3.1). For instance, in a case where the cloud undergoes breathing oscillations, the histograms would obviously be infinitely narrow, deeming the cloud, incorrectly so, as stable. Let us proceed considering the result of ESA in Fig. 2.14(b), for the stable cloud in Fig. 2.14(a). As can be observed, there are histograms that possess residual width (see S3 and S7) and the mean of the histograms is not exactly at 1/8. The respective results are namely due to the cloud possessing a tiny amount of movement and not being perfectly isotropic. Generally speaking, the widths of the histograms tell us about the breadth of intensity variations in the sectors, whereas the means of the histograms tell us about the average of these variations. In the next part, we will apply ESA to the unstable clouds and use the dispersion of histogram-widths as a criterion to distinguish between isotropic and anisotropic modes of cloud deformation. The ability to distinguish such modes will aid us in the construction of a δ-∇B phase-space instability diagram that will mostly agree with visual inspection.

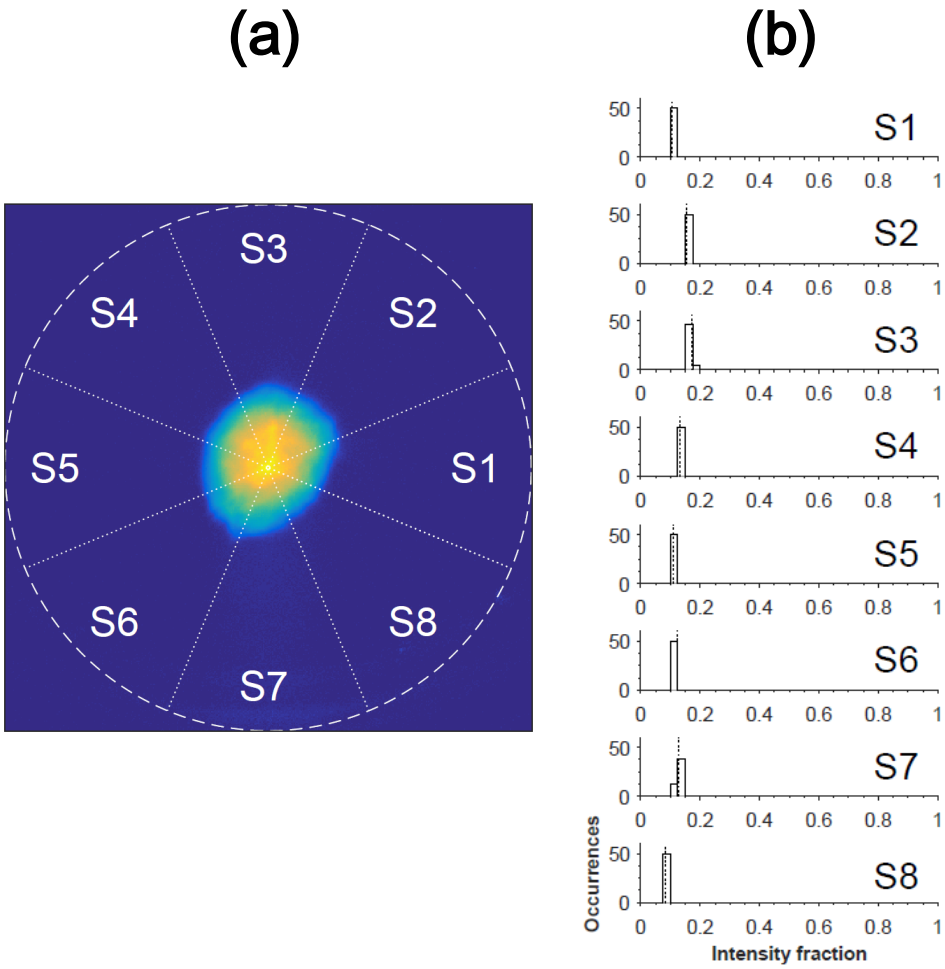

Figure 2.14: (a) Average image of the stable cloud at the trapping detuning $\delta = -2.6\,\Gamma$ and the magnetic field gradient $\nabla B = 6$ G/cm from the experiment where δ and ∇B were varied (section 2.3.1). 50 images are used in the average. A circle (dashed white line), whose center is the COM of this image, encloses the area where ESA is performed; the placement of the eight sectors is shown (S1-8, separations with dotted white lines). The field of view is 5.3×5.3 cm^2. (b) The ESA result for the cloud in (a). The histograms show the statistics on the intensity fractions in each sector. The vertical dotted lines indicate the means of the data used in the construction of the corresponding histograms.

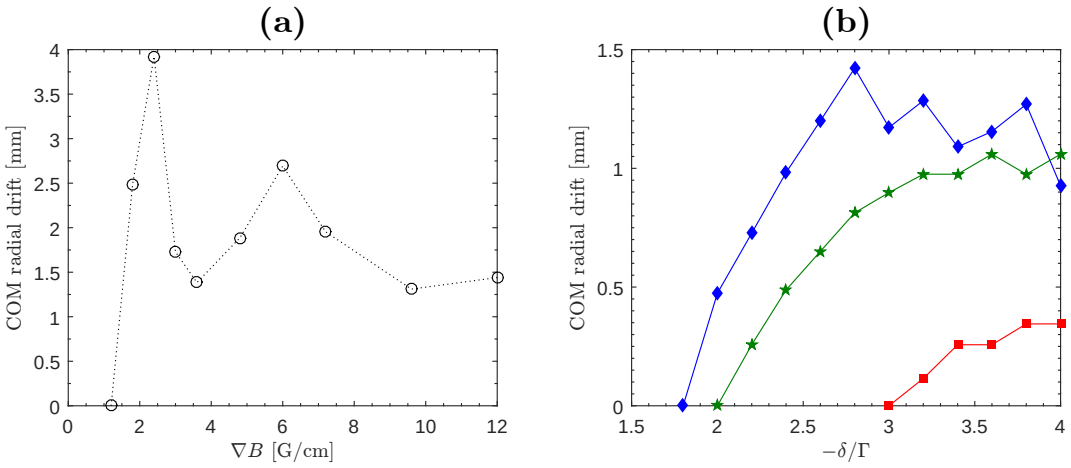

Figure 2.15: The average image COM radial drift for (a) the clouds just below the threshold, with respect to the cloud just below the threshold at $\nabla B = 1.2$ G/cm, and (b) the clouds below the threshold, with respect to the cloud just below the threshold, for $\nabla B = 1.2$ G/cm (blue diamonds), $\nabla B = 3.6$ G/cm (green stars), $\nabla B = 9.6$ G/cm (red squares). 50 images are used in each average. The lines connecting the data-points in (a) and (b) are drawn as a visual aid.

δ-∇B phase-space instability diagram

Here we start by presenting imagery of clouds that we have visually identified to belong to distinct instability regimes in the δ-∇B phase-space and afterwards provide the results of ESA for these clouds. Then, we devise criteria for separating the instability regimes from each other, and, as the final step, present a δ-∇B phase-space diagram showing the boundaries of these regimes.

In Fig. 2.16, we display imagery of clouds that we have visually identified to belong to distinct instability regimes in the δ-∇B phase-space. The three different example cases, at $[\delta, \nabla B] = [-0.8\,\Gamma,\ 1.2\ \mathrm{G/cm}]$, $[-2.2\,\Gamma,\ 9.6\ \mathrm{G/cm}]$ and $[-1.4\,\Gamma,\ 12\ \mathrm{G/cm}]$, are respectively referred to as A, B, and C. We observe that the case-A cloud possesses complex-looking, filamentary structures fluctuating inside a roughly fixed envelope. The case-B cloud is seen to exhibit intermittent elongations along beam directions, nearly corresponding to diagonals in the images. For the case-C cloud, we observe large deformations in arbitrary directions but on average roughly isotropically distributed around the trap center.

In Fig. 2.17, we display the histograms obtained using ESA for the unstable clouds in Fig. 2.16. Starting with the case-A cloud, we observe that the histograms have similar, rather small width of $\sim$0.2 and are centered at $\sim$1/8. This tells us that the cloud undergoes small anisotropic deformations that are on average almost isotropically-distributed, as may also be judged from its single-shot and average images in Fig. 2.16. In case B, the situation is quite different compared to case A. We first of all observe the histogram-widths increase in comparison to case A: they are from $\sim$0.15 to $\sim$0.6, with the average of $\sim$0.3. The great dispersion in the histogram-widths implies that some cloud parts undergo much greater anisotropic deformations than other parts. The histogram-means are observed to also vary by a lot, from $\sim$0.05 to $\sim$0.25, and imply anisotropic cloud distribution on average. We take notice of the double-peak/bimodal structure appearing for one of the sectors, S8. This structure indicates that the cloud jumps between two preferred spatial distributions, one of which is highly anisotropic, since it corresponds to $\sim$50 % of the atoms in that sector. Such intermittent behavior may also be discerned from the single-shot images of the cloud in Fig. 2.16. Now, considering case C, we observe that it presents us with the third distinct case. The widths of the histograms are larger than in case B: they are from $\sim$0.3 to $\sim$0.7, with the average of $\sim$0.5. This implies the largest cloud deformations of all the cases. All the histograms are centered at $\sim$1/8, implying, similarly to case A but differently from case B, that the average cloud envelope is almost equally distributed among each sector. Also, like in case A, there are no signs of intermittent behavior as exhibited by case B. Case C is nevertheless different from case A, because the deformations do not happen within an envelope that is roughly stationary, and, instead, there are occurrences where a major part of the cloud is brought to a single sector. Overall, the case-C cloud undergoes large anisotropic deformations that are on average almost isotropically-distributed, as may also be judged from its single-shot and average images in Fig. 2.16.

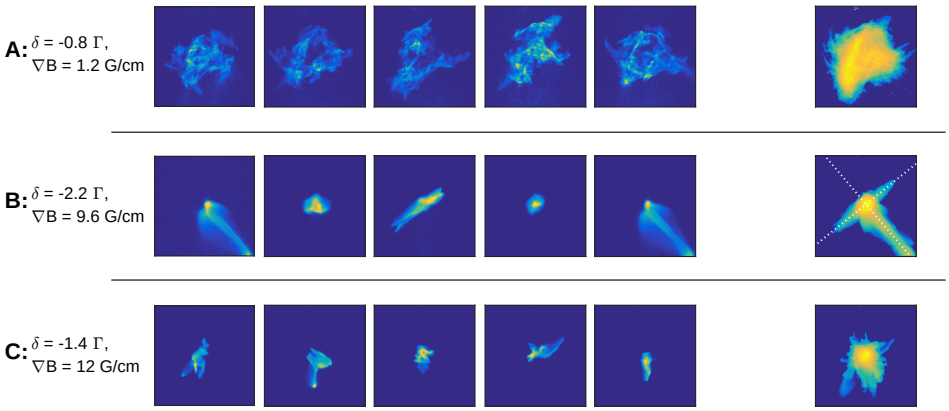

Figure 2.16: Display of images of clouds belonging to the distinct instability regimes discussed in the text. Each image in the five leftmost columns is a single-shot image showing a random instance of the cloud dynamics, and each image in the rightmost column is a log-scaled average of 50 single-shot images. 10 % of the lowest intensity has been removed from the single-shot images in the construction of each average image (for display purposes only). The dotted white lines in the average image of the second row indicate the directions of two pairs of MOT beams. The field of view is 5.3×5.3 cm^2.

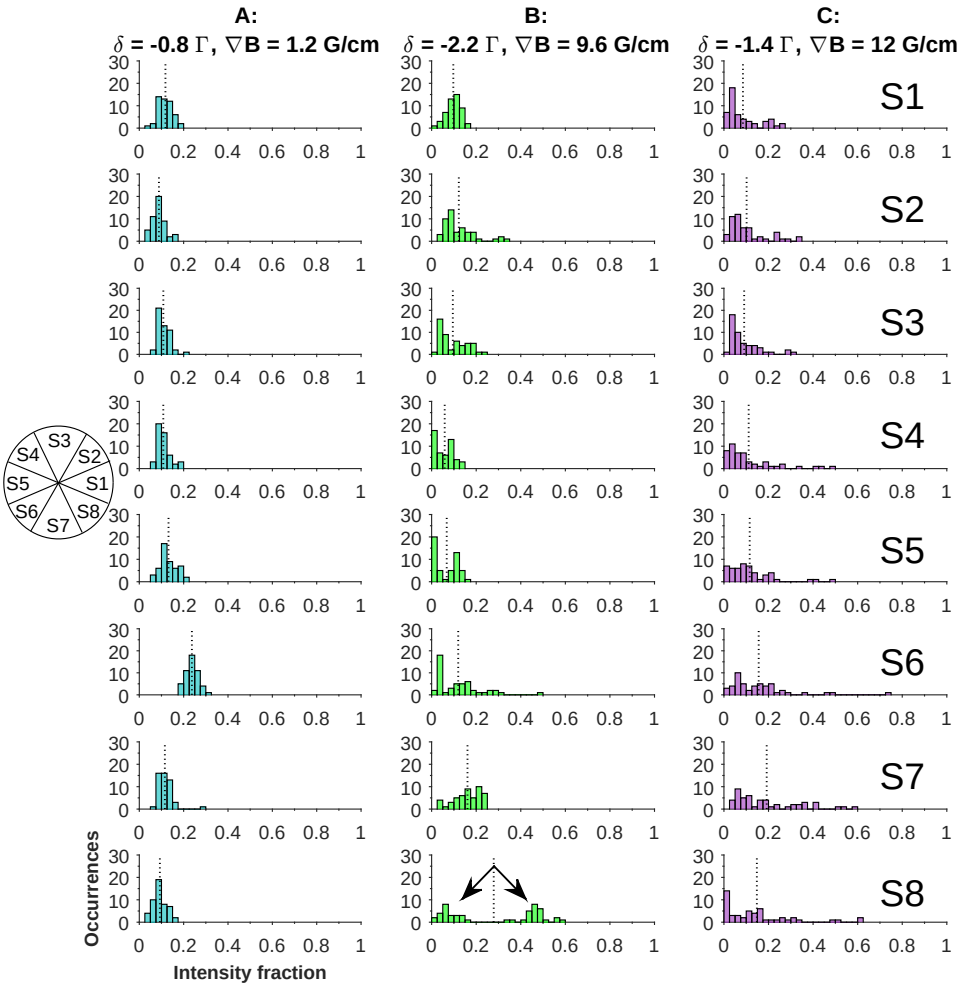

Figure 2.17: The ESA results for the unstable clouds in Fig. 2.16. The histograms show the statistics on the intensity fractions in each sector (S1-8, rows). The arrows reflect intermittent behavior of one of the clouds as discussed in the text. The vertical dotted lines indicate the means of the data used in the construction of the corresponding histograms.

Our next step is to devise criteria for separating from each other the different instability regimes. Based on the observations made in the previous paragraph we note down first the following important facts. Cases A and C discern themselves from one another by having very different average widths of the histograms - case A having rather small average width ($\sim$0.2), and case C having very large average width ($\sim$0.5). The average width of the histograms of case B lies in-between those of A and C ($\sim$0.3); however, the main reason case B discerns itself is rather because it presents great dissimilarities among the individual widths of the histograms (0.15 to 0.6) and the individual means of the histograms (0.05 to 0.3), as due to the intermittent behavior that is otherwise not present in cases A and B. Sticking to usage of histogram-widths only, we provide thus the colormaps seen in Figs. 2.18(a, b), which for the complete set of δ and ∇B values in the unstable regime show (a) the average histogram-width and (b) the average of the largest-to-individual histogram-width ratios[3]. These figures are commented on in the proceeding paragraphs.

From Fig. 2.18(a) we take notice of the stand-out region for high ∇B values ($\nabla B \geq 9.6$ G/cm), where the average histogram-width exceeds 1/3, indicative of the clouds undergoing sizable anisotropic deformations, as for the case-C cloud. The existence of this stand-out region will be taken into account when devising the instability criteria seen shortly. As a further comment, note that the particular color-order in Fig. 2.18(a) seems to related to the one implied by our previous result in Fig. 2.9, where cloud spatial fluctuation is plotted for different δ and ∇B values, and a similar kind of trend is observed - the spatial fluctuation grows as the ∇B value gets larger and the closer to the resonance-level one gets. Nevertheless, we point out that no such order should *a priori* be expected, as the result in Fig. 2.18(a) relies most importantly on the kind of deformations the clouds undergo for different parameter values.

From Fig. 2.18(b) we take notice of the stand-out region for intermediate and high ∇B values ($\nabla B \geq 6$ G/cm), where the average of the largest-to-individual histogram-width ratios exceeds 1.8 and implies that some cloud parts undergo much greater anisotropic deformations than other parts, as for the case-B cloud. The instability criteria devised next will take into account the existence of this stand-out region.

Using the results of Figs. 2.18(a, b) combined with visual inspection of cloud images (commented on shortly) we proceed writing down the following simple criteria for separating the boundaries of the case-A, -B and -C clouds:

1. Case-B clouds have the average of the largest-to-individual histogram-width ratios of ≥ 1.8.
2. Case-C clouds simultaneously have the average of the largest-to-individual histogram-width ratios of < 1.8 and the average histogram-width of $> 1/3$.
3. Case-A clouds simultaneously have the average of the largest-to-individual histogram-width ratios of < 1.8 and the average histogram-width of $\leq 1/3$.

[3] As an example, for a set of three histogram-widths with values 0.6, 0.5, 0.3, the average of the largest-to-individual histogram-width ratios will be $\frac{0.6/0.6+0.6/0.5+0.6/0.3}{3} = 1.4$.

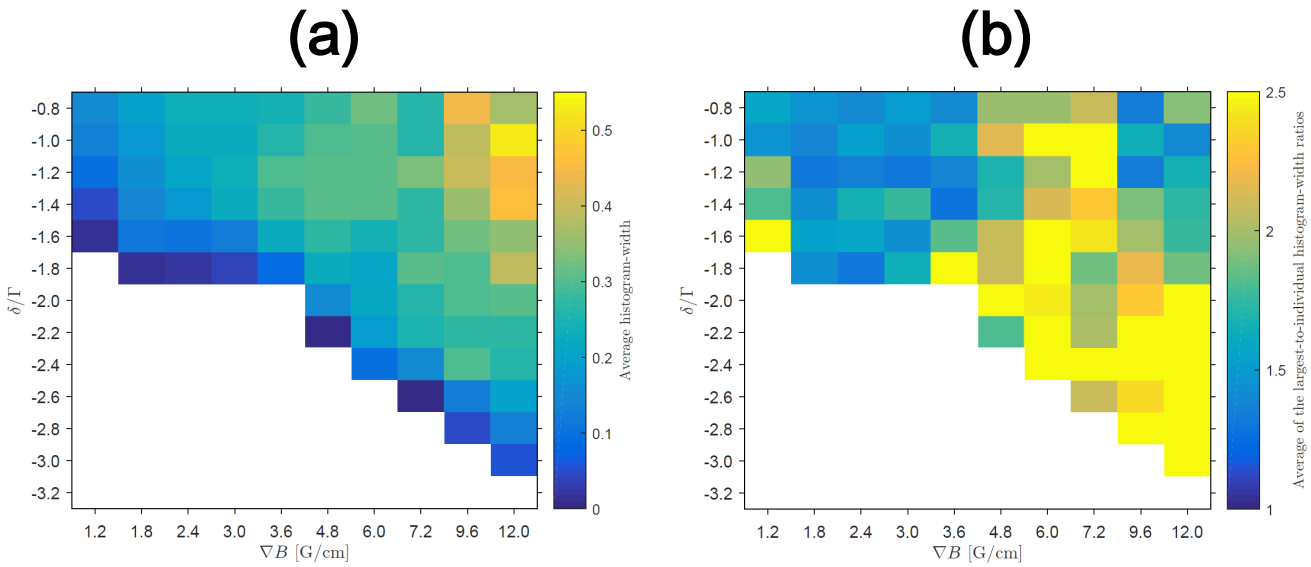

Figure 2.18: δ-∇B phase-space colormaps showing (a) the average histogram-width and (b) the average of the largest-to-individual histogram-width ratios, calculated from ESA. White color is used for stable clouds, determined by the experimental result in Fig. 2.10.

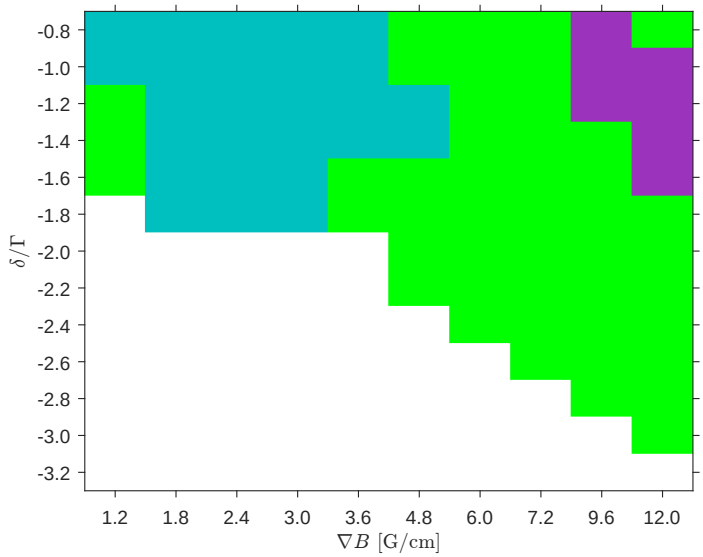

Figure 2.19: δ-∇B phase-space colormap diagram that is drawn according to the instability criteria seen in the text. The following color code is used for the unstable clouds: blue, green and purple for respectively the case-A, -B and -C clouds. White color is used for stable clouds, determined by the experimental result in Fig. 2.10. Note that this diagram is used in drawing the instability regime boundaries in the δ-∇B phase-space diagram seen in Fig. 2.20.

In Fig. 2.19, we show the δ-∇B phase-space colormap diagram that is drawn according to the devised criteria above. The following color code is used to indicate the different kinds of unstable clouds: blue, green and purple for respectively the case-A, -B and -C clouds. We make use of the result of Fig. 2.19 in drawing the boundaries separating the different instability regimes as seen in Fig. 2.20, which is our final instability diagram. It includes unstable cloud imagery from which features characteristic to each regime can be observed. Starting with the case-A regime (blue enclosure), we observe that the average features are mostly similar to those of the example case-A cloud at [$\delta = -0.8\,\Gamma$, $\nabla B = 1.2$ G/cm], as roughly isotropic distribution of deformations can be discerned. Note that some clouds at $\nabla B = 1.2$ G/cm ($-\delta/\Gamma = 1.2$, 1.4, 1.6), which do not fall into the case-A category and make the diagram look patchy, resemble visually case-A clouds. This kind of patchiness and the overall quality of the diagram will be commented on as we finish discussing the individual regimes. Moving on to the case-B regime (green enclosure), we observe that the vast majority of the clouds are elongated along beam directions (almost diagonals in the images). We report that nearly all the clouds here, like the example case-B cloud at [$\delta = -2.2\,\Gamma$, $\nabla B = 9.6$ G/cm], show the same kind of intermittency, where the cloud undergoes elongations along beam directions, thus breaking the symmetry of the trap in a very striking fashion. One may wonder whether such kind of symmetry-breaking behavior is indeed possible in the balanced MOT or is it due to some experimental artifact, e.g. residual intensity imbalance. As will be seen in the simulation Chapter (3), where a similar instability diagram will be provided and compared with the one here, we obtain simulated clouds that can posses symmetry-breaking behavior of such kind, thus providing strong evidence to the fact that what we observe is not due to experimental imperfections. Regarding the case-C regime (purple enclosure), visual inspection of the average features confirms that isotropic distribution of deformations is present, much like for the example case-C cloud at [$\delta = -1.4\,\Gamma$, $\nabla B = 12$ G/cm]. The deformations here can be very large, with the majority of the cloud shifting away from the MOT center, as opposed to the case-A regime, where the deformations happen in an envelope that is roughly stationary. Also, the case-C regime, similarly to the case-A regime, does not exhibit intermittent behavior as the case-B regime. We report additionally that large deformations of the case-B and -C clouds have been observed to occur primarily in the xy-plane (the image-plane in Fig. 2.20), with the possible reason being the asymmetry of the MOT's trapping force (the gradient is twice as strong along the z-axis compared to the xy-plane). Note that there is a cloud at $\nabla B = 12$ G/cm ($\delta = -0.8\,\Gamma$) which resembles a case-C cloud, although falls outside of that category. This patchiness together with the one noted to occur at $\nabla B = 1.2$ G/cm can be attributed to experimental drifts, limited sampling of the dynamics as well as insufficient precision of the ESA technique and insufficient robustness of the criteria for separating the different regimes. Using more advanced methodology it is entirely possible that the placement of the different regime boundaries would be changed and some patchiness eliminated, although, at the same time, no profound differences should be expected to occur, as visual inspection mostly

agrees with the result of our current (and simple) approach. We note that in the remaining subsections, we will be examining the identified regimes using other tools of analysis, to see what complementary information can be gathered about these regimes.

We would like to close this subsection by giving names to the instability regimes according to their most characteristic features observed in Figs. 2.16 and 2.20. The case-A regime, due to the clouds possessing complex-looking, filamentary structures, we call it the *filament-like* regime. The case-B regime, due to the clouds breaking the symmetry of the trap in a striking fashion by intermittently elongating themselves along beam directions, we call it the *asymmetric* regime. The case-C regime, due to the remarkably symmetrically distributed deformations around the trap center, we call it the *symmetric* regime.

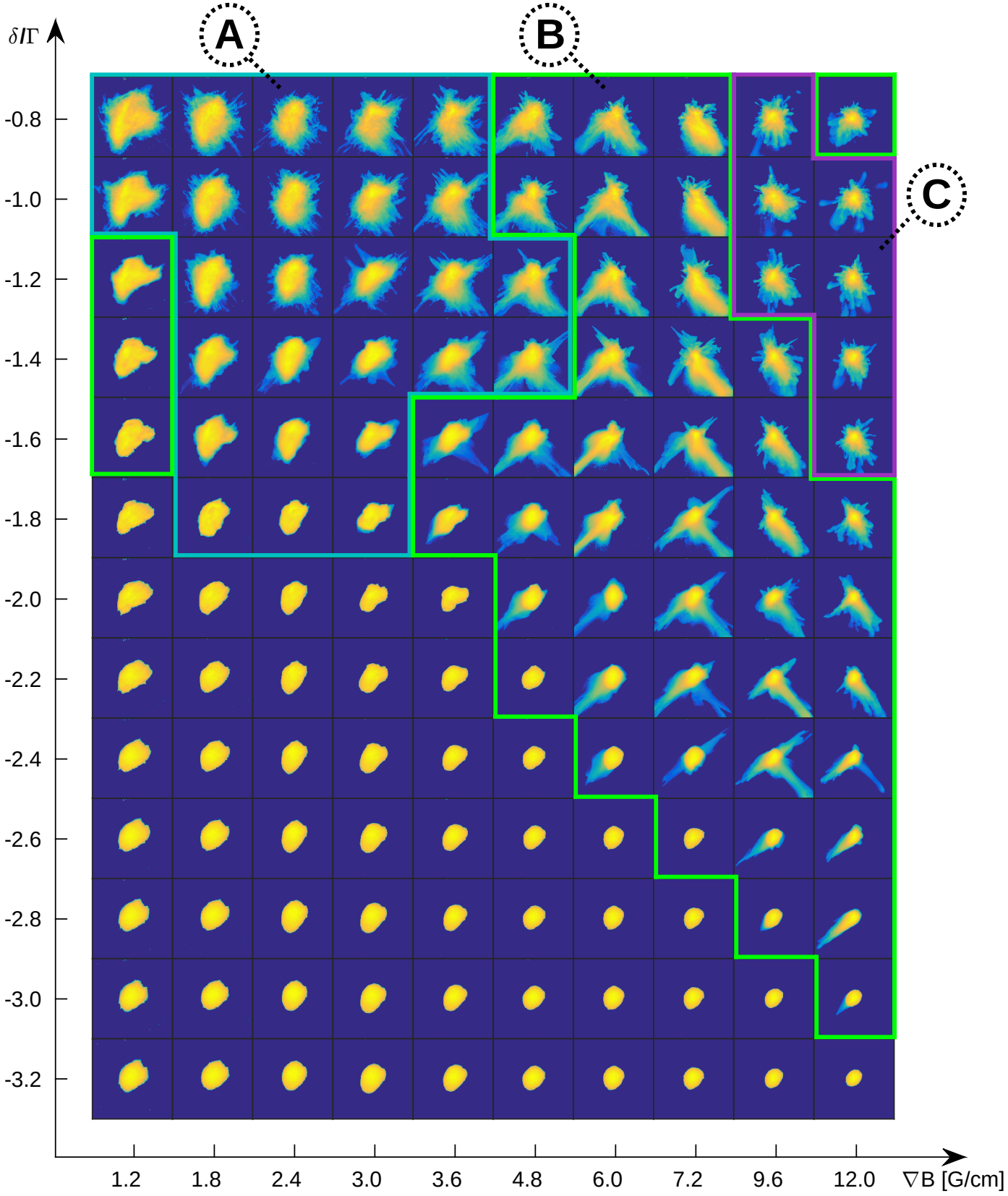

Figure 2.20: δ-∇B phase-space instability diagram. Each image is the log-scaled average of 50 single-shot images, which had 10 % of their lowest intensity removed (for display purposes only). The blue, green and purple lines are drawn according to the colormap seen in Fig. 2.19 and enclose respectively the filament-like (A), asymmetric (B) and symmetric (C) regimes. The diagonals in the images nearly correspond to the directions of two pairs of MOT beams (see Fig. 2.16 for these directions). The field of view is 5.3×5.3 cm^2.

2.4.2 Analysis of the dynamics with principal component analysis (PCA)

In this subsection, we perform principal component analysis (PCA) on fluorescence images from two experiments: (i) the same experiment treated previously, i.e. the pulsed experiment where we varied δ and ∇B (section 2.3.1), (ii) a steady-state experiment where we recorded movies of stable and unstable clouds at different ∇B values in the range from 1.2 to 9.6 G/cm. We start by describing the tool of PCA and motivating its use, followed up by a discussion of our performed analysis on data from the two experiments.

Principal component analysis (PCA)

PCA is a generic method of signal analysis that allows us to separate a series of spatial distributions (images) into a superposition of uncorrelated spatial modes. PCA can be applied on both temporal and non-temporal data, and similar results can be obtained (examples will be given). Thus, we may treat our previous pulsed experiment data (non-temporal) and directly provide complementary information on the different instability regimes (filament-like, asymmetric and symmetric). However, the main drawback of using non-temporal data is that the time evolution of the different modes cannot be accessed, which is otherwise important to us as that allows us to relate our findings to the Mathieu equation model (section 1.2.3.3), being a candidate model for shedding light on the mechanism behind our instabilities. Thus, to learn about the time evolution of the modes we will be considering treating also our steady-state experiment data (temporal). We note that in the past, PCA was applied to Bose-Einstein condensate (BEC) clouds to unveil their collective excitations and to detect the noise components [48]. Closer to our topic, we recall from section 1.2.3.2 that PCA was employed in studying the oscillation modes of retro-reflected MOT instabilities [38].

Following Ref. [48] we explain how PCA proceeds. We begin with a data set containing 50 images in the case of the pulsed experiment, or 200 images in the case of the steady-state experiment[4]. First, the mean image of the data set is found and subtracted from all the images, such that an ensemble of mean-centered images is obtained. The pixel values of the centered images are then stored in a single data matrix, either row-wise or column-wise. The data matrix is next used to construct a covariance matrix that is real and symmetric. The diagonal elements of the covariance matrix contain the variances of the pixels, and the off-diagonal elements contain covariances between the pixels; these covariances quantify correlations between the pixels. Finally, eigendecomposition of the covariance matrix is performed, yielding eigenvalues and eigenvectors of

[4] In the steady-state experiment we have more images at our disposal compared to the pulsed experiment (200 versus 50), and that helps us in minimizing the finite sample size induced errors in PCA. PCA can nevertheless be noted to be quite robust, as in Ref. [48] dealing with BEC excitations, when only one out of ten of the original 152 images used was kept, PCA still was able to produce high-fidelity results.

the covariance matrix. The normalized eigenvectors are called the principal components (PCs). The PCs are uncorrelated, as the covariance between the PCs is zero. The amount of elements in each PC (vector) is equal to the amount of pixels in each image, and by resizing the PCs to the dimensions of the images one gains access to the 2D shapes of movement patterns that may represent e.g. excited fundamental oscillatory modes and fluctuations associated with the sources of noise. Because the PCs are uncorrelated, the noise sources will be associated with different PCs. The eigenvalues of the respective PCs are equal to the variances of the respective PCs. By ranking the PCs in order of their eigenvalues, from highest to lowest, one obtains the PCs in the order of their significance. We note that when dealing with n images, there will be n PCs and n eigenvalues associated with the respective PCs; the eigenvalues may not necessarily be distinct.

Before presenting the results of PCA on cloud images stemming from our experiments, we illustrate first PCA with some simple and relevant examples. In Figs. 2.21(a.1-4), we display these examples, where a numerically generated Gaussian cloud is seen to (a.1) perform an oscillation across the screen, (a.2) breathe, (a.3) perform an oscillation across the screen while breathing, (a.4) do the same as last but randomly shuffled. In Figs. 2.21(b.1-4), we display the outcome of PCA for the respective examples. The PCs are labeled by the letters from "b" to "e" and are sorted in the order of their significance; the sequence's mean image is labeled by "a". Notice the dark (blue) and bright (yellow) zones in the PCs - these zones correspond respectively to the loss and gain of atoms. We comment now on the individual PCA results. Starting with Fig. 2.21(b.1), we observe first of all that the shapes in the PCs are in the line of the cloud's movement. As this line is rotated, translated or shortened, the shapes in the PCs respond in the same manner (i.e. rotate, translate or shorten). We observe that the first PC, "b", resembles a dipole mode, corresponding to the side-to-side-shifting oscillation of the cloud, while the remaining PCs ("c" to "e") resemble compressional modes, whose appearance can be surprising but occur because PCA per definition determines all the uncorrelated movement patterns that can possibly be obtained from the available cloud imagery. As will be seen from PCA of the last example, this is indeed the reason why similar PCA results are produced when randomly shuffling the image data. Next, in Fig. 2.21(b.2), we observe that the first PC, "b", resembles a monopole mode, corresponding to the breathing of the cloud, while the remaining PCs resemble higher-order monopole modes, which correspond to higher-order breathing patterns. Notice that the first PC accounts for the completely dominant part of all the variations ($\sim$98%), such that the higher-order breathing patterns can be considered to be irrelevant. Next, in Fig. 2.21(b.3), the appearance of the dipole mode is expected, because the cloud exhibits side-to-side oscillation, but there is no presence of the monopole mode which would correspond to the cloud's breathing. (Overall, the PCs resemble closely those seen in Fig. 2.21(b.1).) The non-presence of the monopole mode is linked to the fact that PCA per definition does not exclude any part of the cloud imagery in the determination of a given movement pattern. We report that as the path of the cloud's oscillation

is shortened, the patterns get more compact and, as expected, monopole modes start to emerge. Finally, in Fig. 2.21(b.4), the same modes as in Fig. 2.21(b.3) expectedly appear, with the minor difference being that the order of the dark and bright regions is switched for some of the PCs. The same modes are expected to appear because, as mentioned earlier, PCA per definition determines all the uncorrelated movement patterns that can possibly be obtained from the available cloud imagery. Since the rows of the data matrix (or the columns, if the data is stored column-wise) is randomly shuffled, the order of the dark and bright regions can, however, switch for a given PC, corresponding to a switched order of respectively the atomic loss and gain in the movement pattern that the PC represents.

Note that the main purpose of the last example was to illustrate that similar movement patterns can be obtained even with non-temporal data, like we have gathered in our pulsed experiment. In what follows next, we will be discussing PCA on experimental data, first pulsed and then steady-state.

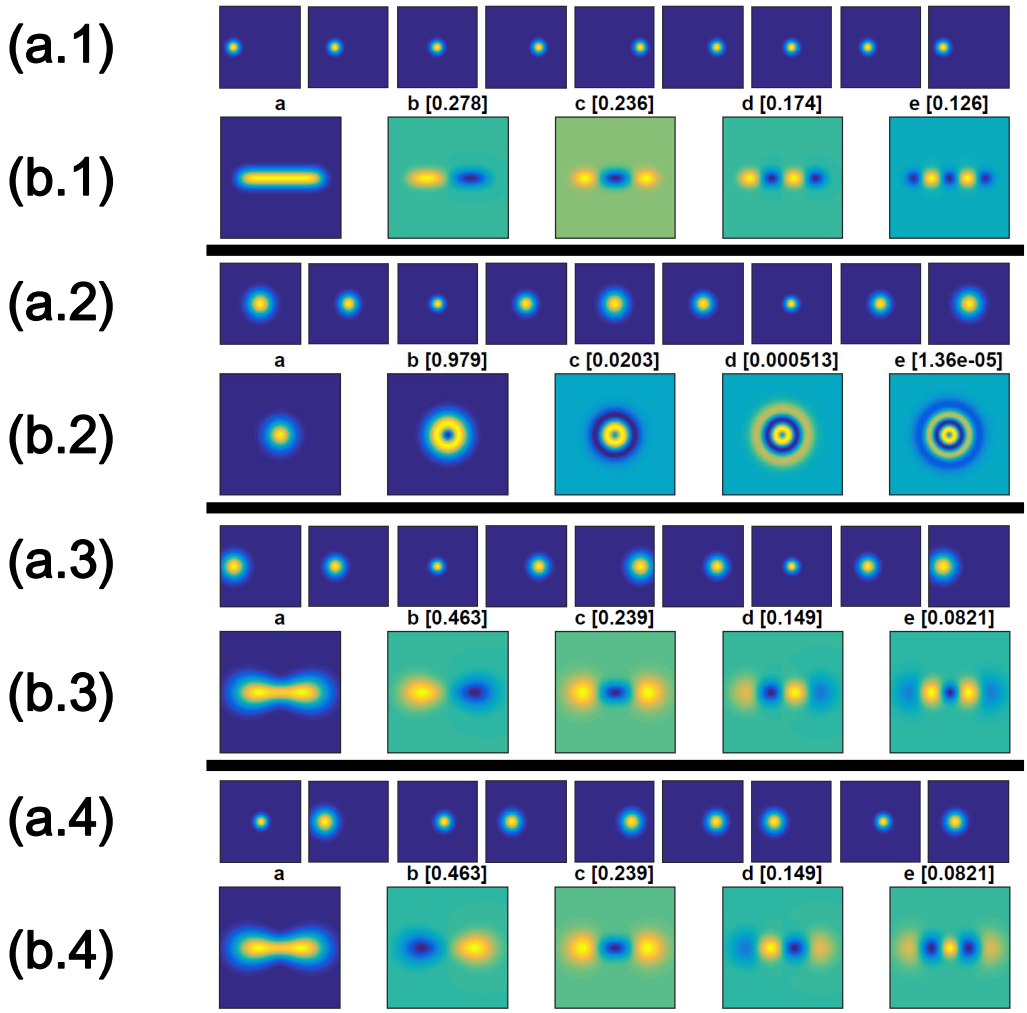

Figure 2.21: (a.1-4) A regularly-spaced sequence of 9 out of a total 200 images (with the 1st and 9th being respectively the 1st and last of the image set) showing a numerically generated Gaussian cloud (1) perform an oscillation across the screen, (2) breathe, (3) perform an oscillation across the screen while breathing, (4) do the same as last but randomly shuffled. (b.1-4) The mean image ("a") and the first 4 PCs ("b" to "e") of the respective sequence in (a.1-4). The number between the brackets is the corresponding PC eigenvalue, showing the significance of the PC. The eigenvalue is written as a fraction of the total variance. For (a.1-4) and (b.1-4), the color scale is arbitrary for each image.

PCA on cloud images from the pulsed experiment

We discuss here the PCA results for a stable cloud and then unstable clouds from our pulsed experiment (section 2.3.1). In discussing the PCA results for the stable cloud, we see what noise sources PCA identifies in our system. In discussing the PCA results for the unstable clouds, we see what complementary information can be provided on the different instability regimes (filament-like, asymmetric and symmetric).

Let us start by commenting on the outcome of PCA seen in Fig. 2.22, where a stable cloud is considered. The first PC, "b", which accounts for around a fifth of all the variations, is seen to have a very similar shape as the mean cloud image, shown in "a". This PC identifies a global variation in the cloud, associated likely with the intensity fluctuation of the lasers. There can be many causes for the intensity fluctuation; for instance, due to the fibers that inject light into the MOT not being perfectly polarization-maintaining, such that fluctuations occur after the intensity balancing stage (refer to Fig. 2.4). The remaining PCs also possess a similar shape as the mean cloud image but are harder to interpret as the atomic depletion (blue) and augmentation (yellow) regions show little order. The weights of these PCs are quite small, of around a quarter of the first PC or lower. These PCs may be reflecting presence of mechanical vibrations during the measurement, such as e.g. tiny jitters of the camera position and even the MOT chamber itself. As we already have learned from before, since PCs are uncorrelated, the movement patterns due to the mechanical vibrations are associated with different PCs.

We proceed now commenting on the outcome of PCA displayed in Figs. 2.23, 2.24 and 2.25, where unstable clouds are considered at respectively $\nabla B =$ 1.2 G/cm, 9.6 G/cm and 12 G/cm. Note that these are the same clouds as seen in Fig. 2.16, which are our example clouds for respectively the filament-like, asymmetric and symmetric instability regimes. It is clearly noticeable that for all these cases the movement patterns are very different from each other, although, at the same time, their interpretation can be difficult. In the case of the filament-like regime cloud (Fig. 2.23), all the movement patters are fairly complex and we cannot really associate them with fundamental oscillatory modes such as the monopole, the dipole, the quadrupole[5], etc. For the asymmetric regime cloud (Fig. 2.24), on the other hand, we can distinguish two kinds of modes: the large deformations along beam directions (e.g. "b" and "c"), and smaller fluctuations within a core (e.g. "e", "f", "i"). The jumps between these two kinds give rise to the intermittent behavior, which can be captured by the double-peak histograms (see Fig. 2.17). For the symmetric regime cloud (Fig. 2.25), we observe that some of the modes faintly resemble the dipole ("b", "d"), the compressional mode ("c"), the quadrupole ("e", "f") and even the hexapole[6] ("g"). The appearance of such modes may not be surprising, considering that

[5]The quadrupole mode is indicative of centro-symmetric compression of two sides of the cloud with centro-symmetric expansion of the remaining two sides in a quadrupole shape.

[6]The hexapole mode is indicative of centro-symmetric compression of three sides of the cloud with centro-symmetric expansion of the remaining three sides in a hexapole shape.

the deformations are symmetrically distributed around the trap center in this regime.

Now, the fact that the modes are clearly different for each considered cloud indicates that PCA has the power of distinguishing instability regimes from each other. However, note that if we were to treat these modes in doing this distinguishing, tools of image analysis would have to be invoked, and thus the PCA approach could become too tortuous and lose its appeal compared to the much simpler ESA approach (section 2.4.1). On the other note, we bear in mind that PCA not only provides us with information on the modes but also their eigenvalues, and those can be used in obtaining complementary information on the identified regimes, as discussed below.

Observing the eigenvalues of the PCs of the different unstable regime clouds (in Figs. 2.23, 2.24, 2.25), we see that they decrease more steeply for the symmetric regime cloud compared to the filament-like regime cloud, and then for the asymmetric regime cloud compared to the symmetric regime cloud. The behavior is illustrated more clearly in Fig. 2.26, where the first 5 PC eigenvalues have been plotted for each of these clouds versus the order of the mode (PC) in log-log scale. As we can see, different scaling exponents are extracted for each different regime cloud: -0.24, -1.81 and -0.59 for respectively the filament-like, asymmetric and symmetric regime cloud. A large exponent translates into a greatly diminished relevance of the high-order modes. For the filament-like regime cloud, in particular, the exponent is relatively small and tells us that there are many modes with almost the same relevance. Coupled with the fact that its modes are complex, this implies a very complicated dynamical structure of this cloud. We note, however, that the knowledge of the exponents cannot really be used in differentiating the regimes, except the asymmetric regime - Fig. 2.27 displays a δ-∇B phase-space colormap showing the exponents, and as it can be observed from the brightness of the colors in this map, no evident distinction between the filament-like and symmetric regimes can be made.

Before proceeding to the next part of our analysis (where we will be considering PCA on cloud images from our steady-state experiment), we note about the result of the study in Ref. [38] (covered in section 1.2.3.2) on the spatial properties of retro-reflected MOT instability dynamics, where it was found that the first two modes dominated all the dynamics. In our case, the results of Figs. 2.23, 2.25 and 2.27 on the filament-like and symmetric regime clouds tell us that for these clouds the first two modes cannot account for even a half of all the variations. On the other hand, the results of Figs. 2.24 and 2.27 on the asymmetric regime clouds tell us conversely that the first two modes account for the majority of the fluctuations, similarly to the retro-reflected MOT instability case. Of course, although the same amount of modes is needed to explain the variations in both the retro-reflected and asymmetric cases, this does not imply that the two are equally dynamically complex, as that would be determined by the complexity of the modes themselves. For instance, if we were to obtain similar mode-eigenvalues for our filament-like and symmetric regime clouds (Figs. 2.23, 2.25), the symmetric regime would be deemed as less dynamically complex, due to its modes being the relatively simpler fundamental oscillatory modes.

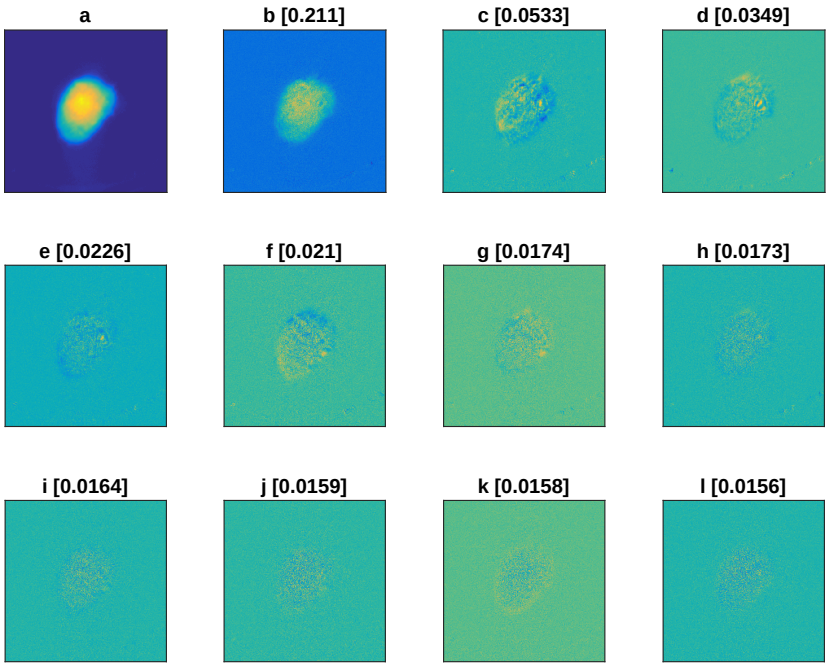

Figure 2.22: The mean image ("a") and the first PCs ("b" to "l") of a set of 50 fluorescence images stemming from our pulsed experiment described in section 2.3.1. The measurement was performed at $\delta = -3\,\Gamma$ for $\nabla B = 3$ G/cm, where the cloud was stable. The number between the brackets is the corresponding PC eigenvalue, showing the significance of the PC. The eigenvalue is written as a fraction of the total variance. The color scale is arbitrary for each image. The field of view is 5.3×5.3 cm^2.

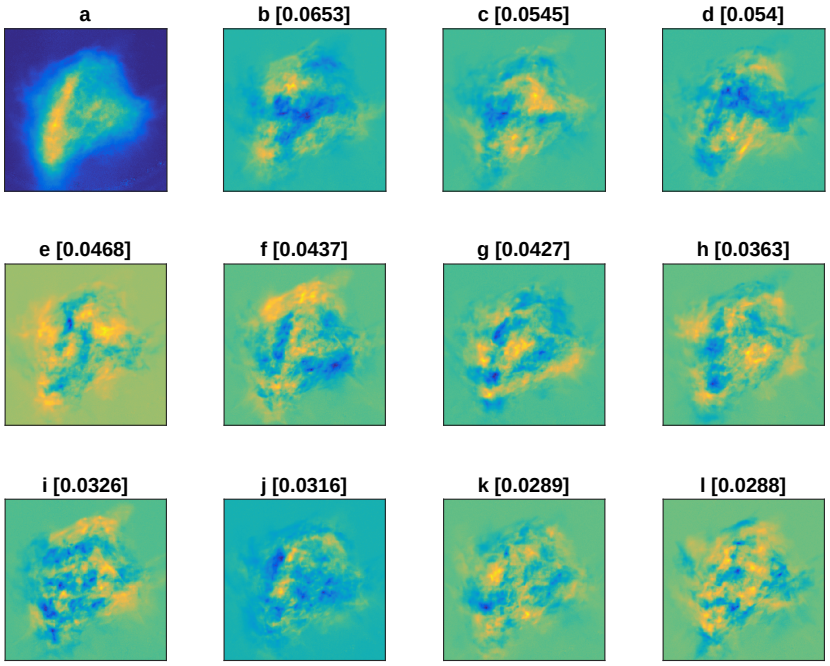

Figure 2.23: Similar depiction as in Fig. 2.22, but the fluorescence images used to produce this figure stem from the measurement performed at $\delta = -0.8\,\Gamma$ for $\nabla B = 1.2$ G/cm, where the cloud was unstable. Note that this cloud is the same one as seen in Fig. 2.16, upper row.

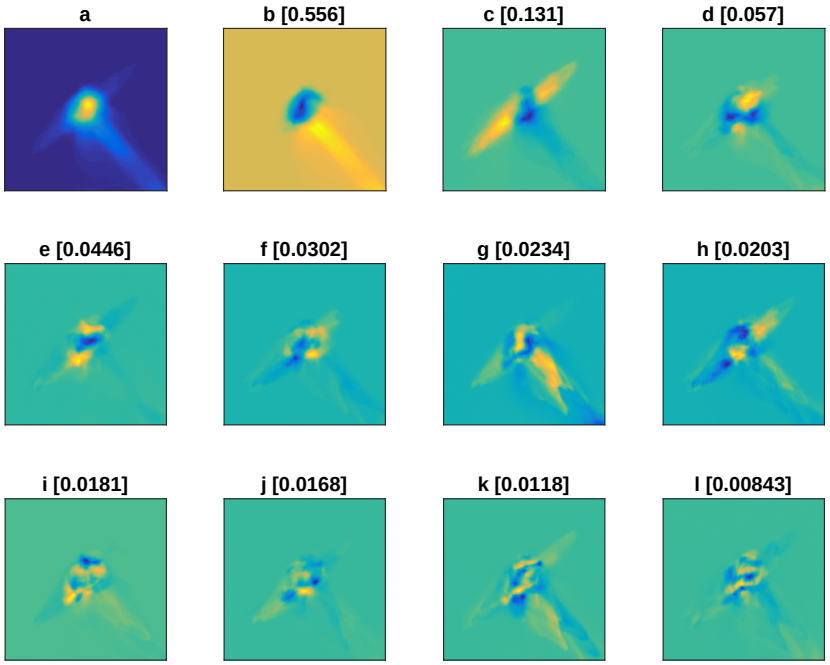

Figure 2.24: Similar depiction as in Fig. 2.22, but the fluorescence images used to produce this figure stem from the measurement performed at $\delta = -2.2\,\Gamma$ for $\nabla B = 9.6$ G/cm, where the cloud was unstable. Note that this cloud is the same one as seen in Fig. 2.16, middle row.

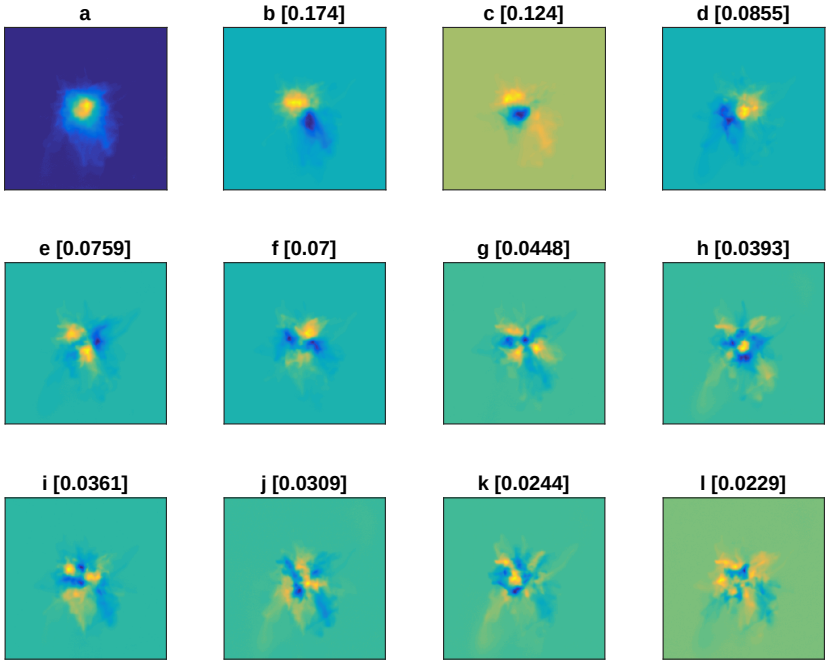

Figure 2.25: Similar depiction as in Fig. 2.22, but the fluorescence images used to produce this figure stem from the measurement performed at $\delta = -1.4\,\Gamma$ for $\nabla B = 12$ G/cm, where the cloud was unstable. Note that this cloud is the same one as seen in Fig. 2.16, lower row.

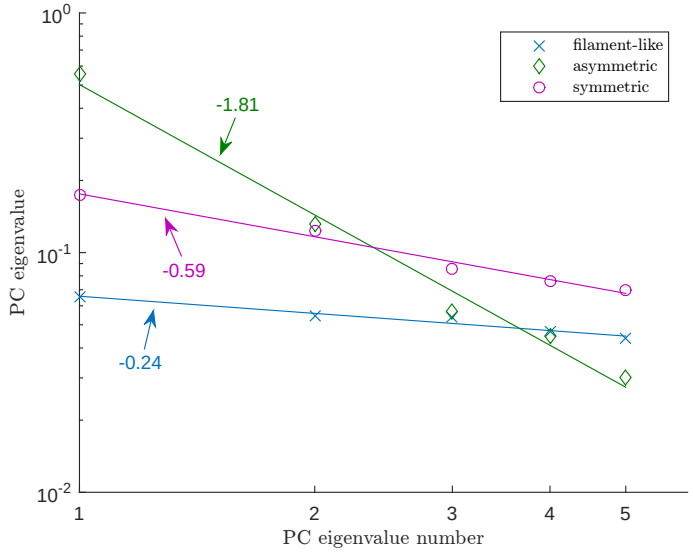

Figure 2.26: The first 5 PC eigenvalues for the filament-like (crosses; Fig. 2.23), asymmetric (diamonds; Fig. 2.24) and symmetric (circles; Fig. 2.25) regime clouds versus the PC eigenvalue number, displayed in log-log scale. The numbers next to the arrows are the scaling exponents of the power law fits (solid lines) made to the data-points corresponding to the different clouds.

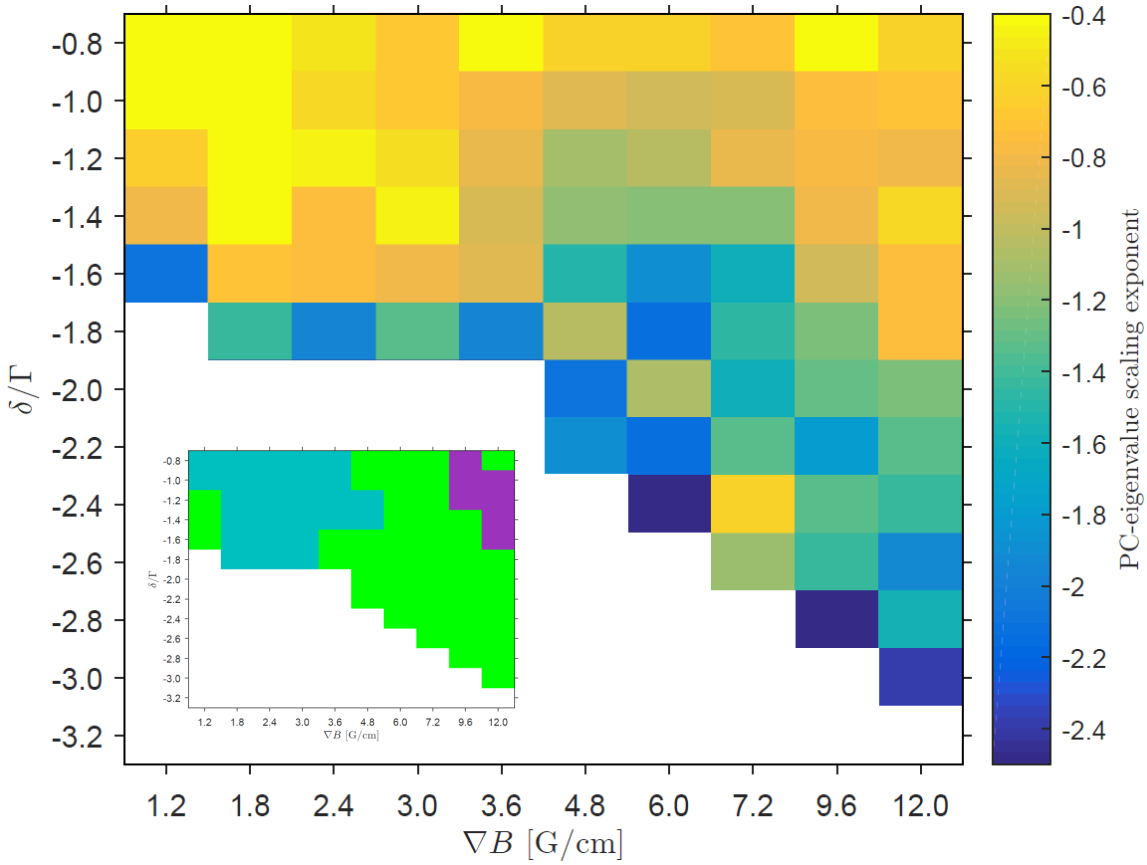

Figure 2.27: δ-∇B phase-space colormap showing the scaling exponents of PC eigenvalues (see Fig. 2.26 for the extraction procedure). The inset displays the positioning of the different instability regimes (see Fig. 2.19 for the color code used).

PCA on cloud images from the steady-state experiment

We discuss here the PCA results for a stable cloud and then an unstable cloud from our steady-state experiment. Different from before, we now have the time-connected series and access to the frequencies of the PCs. An important point to be made here is that we use δ_{inst} for the imagining, and not δ_{img}, such that we are possibly led to distortions due to the multiple-scattering (refer to section 2.2). In discussing the PCA results for the stable cloud, we see how the noise sources compare to those identified previously (Fig. 2.22). In discussing the PCA results for the unstable cloud, we see how we can relate our findings to the instability model with a Mathieu type of equation.

Let us start by commenting on the outcome of PCA seen in Fig. 2.28, where a stable cloud is considered. The first PC, "b", is seen to have a very similar shape as the mean cloud image, shown in "a", and displays the same behavior as seen last, in Fig. 2.22, such that we may associate this PC with the intensity fluctuation of the lasers. The next two and much less significant PCs, "c" and "d", have also a similar shape as the mean cloud image and, as in Fig. 2.22, these PCs may be reflecting presence of mechanical vibrations during the measurement. Finally, in the remaining PCs, we can observe that fringes are visible, indicating presence of light interference; these kind of PCs were not seen in Fig. 2.22, although can be noted to be completely negligible due to their very low significance.

Finally, let us move on to the temporal analysis part and assess the Mathieu equation model. We recall from section 1.2.3.3 that in this model, the proposed instability mechanism is driven by the coupling between two modes - the COM mode and the breathing mode. Observing the PCA outcome in Fig. 2.29, where an unstable cloud is considered, we see that the first two modes ("b", "c") resemble the dipole modes (oriented resp. along the rows and columns of the images in the movie series), while the third one ("d") is likely a combination of monopole and dipole modes. The latter judgment is based on the discussion on the result of one of our PCA examples (Fig. 2.21(a.3, b.3)). Now, the COM and breathing modes taken together ("b", "c", "d") do not account for even a half of all the variations, such that little support can be provided to the model's proposal that the instability mechanism is driven by the coupling between only these two modes. Added to that, we bear in mind that in the model, the COM mode resulted from the restoring force, with the collective interactions having no impact on the COM motion, such that direct mapping of our observed COM oscillations to the COM oscillations of the model cannot entirely be correct. Nevertheless, assuming we can do such mapping, let us now consider looking into the model's established relation between the COM and breathing oscillation frequencies, which, to recall, is $\omega_{COM} = \omega_P/\sqrt{3}$, where ω_{COM} is the COM mode frequency and ω_P is the breathing mode frequency. In Fig. 2.30(a), we plot for the COM mode "b" and the breathing (mixed with COM) mode "d" the time-dependent weights, obtained by projecting the

mean-centered images in the movie series onto the corresponding PCs[7]. As can be observed, the weights for the two modes present rather complicated sinusoidal oscillations, with Fig. 2.30(b) confirming that many frequencies are indeed involved in these oscillations. Now, while in Fig. 2.30(b) it may be reasonable to pick the COM oscillation frequency to be the frequency with the greatest Fourier amplitude due to the COM oscillation frequencies centered around this frequency, the same is not the case for the breathing oscillation frequency as the frequencies here are very spread and have comparable Fourier amplitudes. Nevertheless, because the breathing oscillation frequencies tend to peak more at larger frequencies ($\omega > 80$ Hz), we try now picking the breathing oscillation frequency to be the frequency with the greatest Fourier amplitude in the large-frequency range, and so we have $\omega_P = 109$ Hz. For the COM oscillation frequency we pick the one with the greatest Fourier amplitude, and thus we have $\omega_{COM} = 51$ Hz[8]. Applying the instability model's relation between the COM and breathing oscillation frequencies ($\omega_{COM} = \omega_P/\sqrt{3}$) we obtain $\omega_P/\sqrt{3} \approx 63$ Hz, which is not far-off from the value of ω_{COM}. This result may add some weight to the model's prediction but of course is heavily diminished, considering it is troublesome picking the correct breathing oscillation frequency. Overall, looking back at our entire discussion, the model can be judged to be too simplistic for capturing the mechanism behind the instabilities.

[7] As noted in Ref. [48], the PCs form an orthonormal basis that spans the subspace of the data set, and each original image can be represented as a sum of the mean image and the weighted contributions from each PC. The weighted contribution, or simply weight, is obtained by projecting the mean-centered image onto the PC.

[8] The fact that our ω_{COM} is close to the power-line frequency of 50 Hz is coincidental. Typically, we observe MOT oscillation frequencies in the 10-100 Hz range, mostly determined by the value of ∇B.

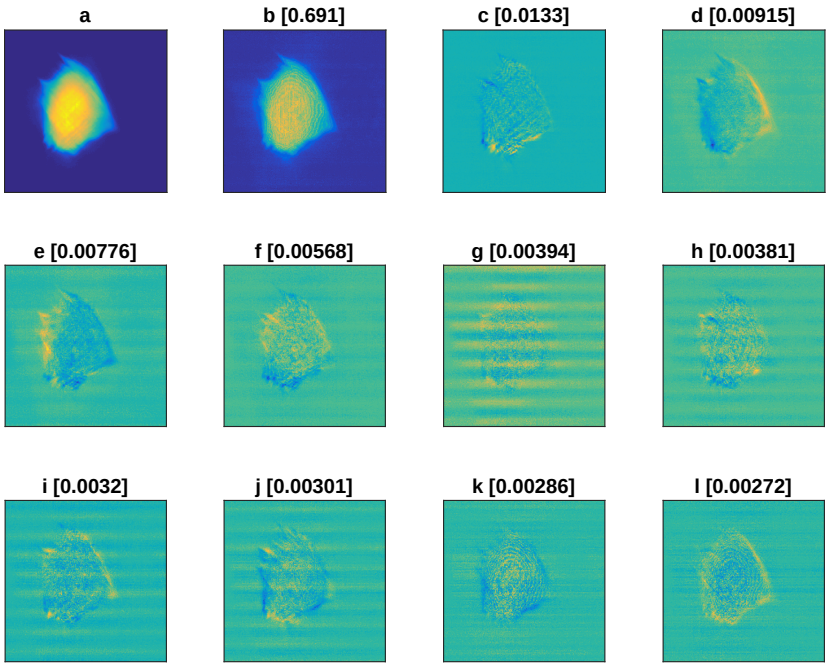

Figure 2.28: The mean image ("a") and the first PCs ("b" to "l") of a set of 200 fluorescence images (from a movie of 900 ms time length) stemming from our steady-state experiment. The measurement was performed at $\delta = -2.4\,\Gamma$ for $\nabla B = 2.4$ G/cm, where the cloud was stable. The number between the brackets is the corresponding PC eigenvalue, showing the significance of the PC. The eigenvalue is written as a fraction of the total variance. The color scale is arbitrary for each image. The field of view is 3.69×3.69 cm^2.

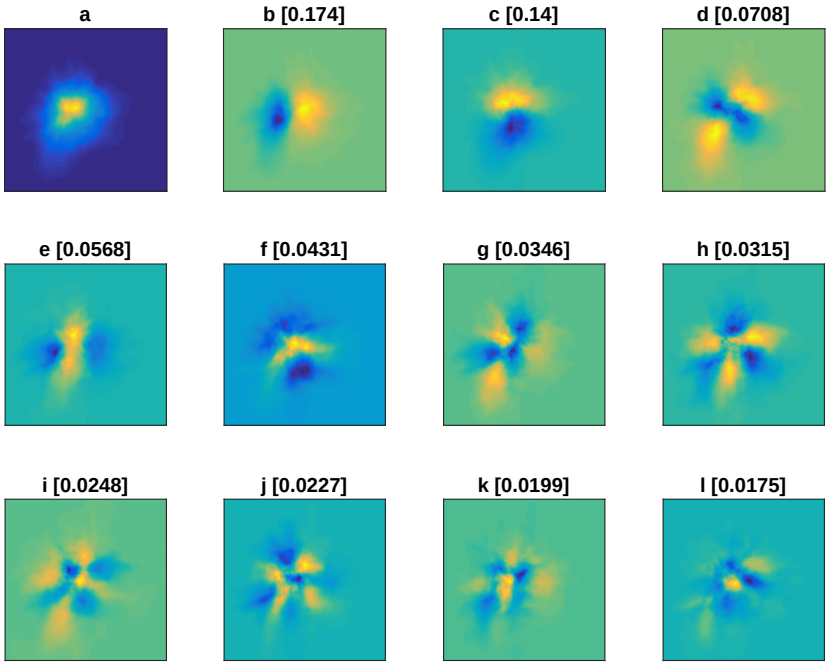

Figure 2.29: Similar depiction as in Fig. 2.28, but the fluorescence images used to produce this figure stem from the measurement performed at $\delta = -0.7\,\Gamma$ for $\nabla B = 9.6$ G/cm, where the cloud was unstable.

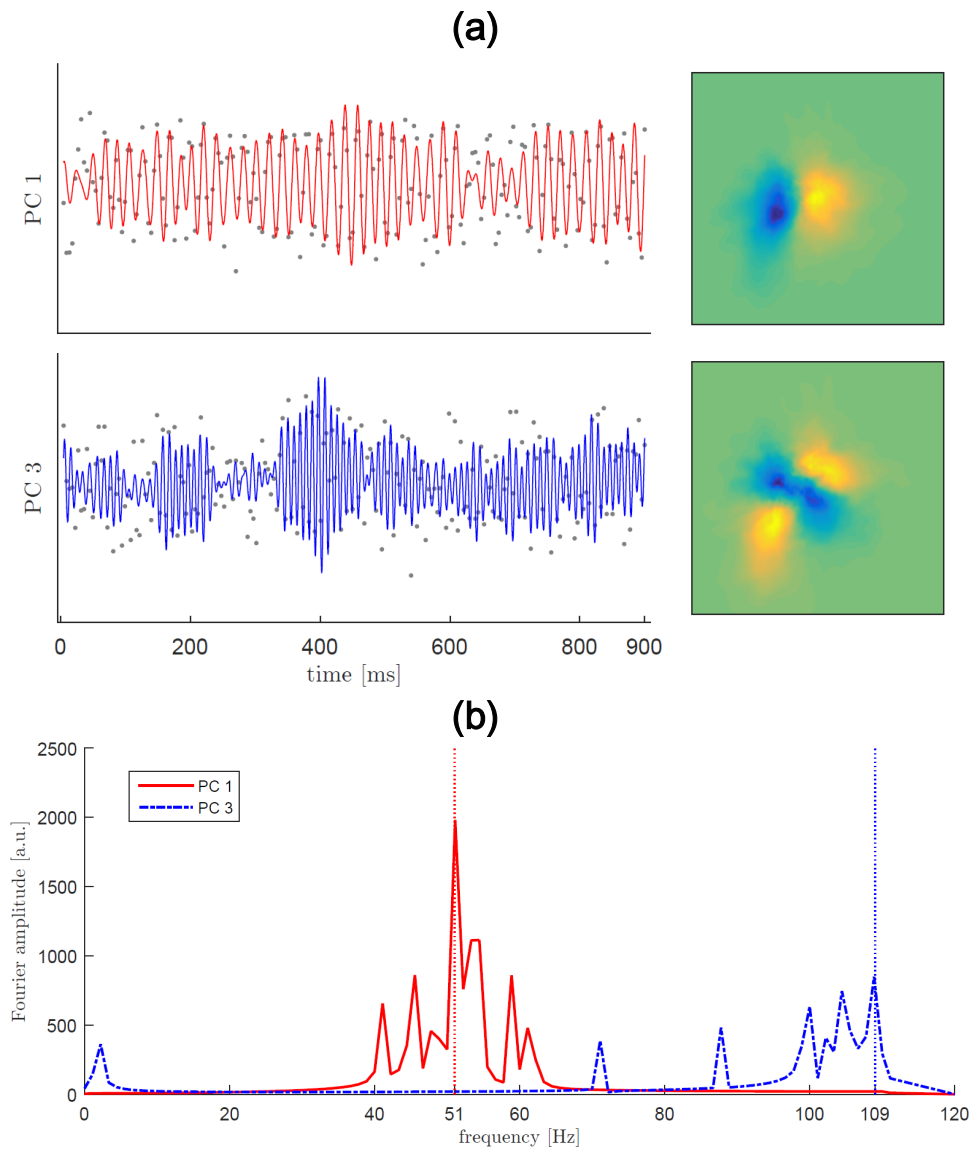

Figure 2.30: (a) The time-dependent weights (gray dots) of respectively the first and third PC seen in Fig. 2.29 and the corresponding sinusoidal fits to the weights (blue and red curves). The vertical-axes are arbitrary for each plot. (b) The single-sided Fourier amplitude spectra of the respective sinusoidal fits in (a). The vertical dotted lines indicate the frequencies of the largest peaks in the corresponding spectra.

2.4.3 Analysis of the structure sizes with spatial Fourier analysis (SFA)

In this subsection, we perform spatial Fourier analysis (SFA) on fluorescence images from the same experiment treated previously, i.e. the experiment where we varied δ and ∇B (section 2.3.1). The first motivating reason to perform such analysis is that it allows us to separate the contributions of different-sized structures developing in unstable clouds, being information that is otherwise hidden in the direct images. Moreover, this study can provide information on the physics underlying the instability phenomenon, due to the analysis yielding power spectrum scaling law exponents that are particularly relevant in the context of the photon bubble model (refer to section 1.2.3.3). We discuss first the 2D features of the structure-size distributions yielded by the analysis and, after performing angular averaging, we discuss the calculated power spectrum scaling law exponents.

We perform SFA as follows. For a given pair of δ and ∇B values, we compute the squared modulus of Fourier transforms of 50 fluorescence images and then take the mean of the results. By computing the squared modulus of Fourier transform of an image, we are computing the power spectrum, also known as the power spectral density (PSD), of that image.

In Fig. 2.31, we show in log scale the mean PSD image for a stable cloud. Dark rings can be observed in the image. Such rings appear for stable clouds and indicate that the corresponding density profiles are steeper than Gaussians[9]. The diameter of the first dark ring is inversely proportional to the size of the cloud. To calibrate the wavenumbers, we first numerically generate a sine function in 2D with a known period λ_τ in mm, then Fourier transform this function, obtaining two dots that each are placed from the image center by the amount of pixels that is equal to the wavenumber distance $k_\tau = 2\pi/\lambda_\tau$. Dividing k_τ by this pixel amount, we finally find the wavenumber k value corresponding to one pixel in the Fourier image.

We continue now with Fig. 2.32, where we show in log scale the mean PSD images for unstable clouds from the different instability regimes - the filament-like (blue enclosure), asymmetric (green enclosure) and symmetric (purple enclosure) regimes. The mean PSD images for stable clouds are also displayed. Compared to the stable cloud PSD profiles, we observe that the unstable cloud PSD profiles are broadened. This tell us us that the relative weight of small-scale structures has increased and also reflects the appearance of spatial structure smaller than the cloud size in the unstable regime. As we concentrate on the individual instability regimes, we first observe that the PSD profiles in the filament-like regime distinguish themselves by possessing dark crosses roughly along diagonal directions in the images, telling us that the weight of the structures along these directions is diminished. These directions correspond to beam directions in the direct images (refer to Fig. 2.16). We do not know the exact

[9] Computing Fourier transform of a Gaussian function yields another Gaussian function, whereas computing Fourier transform of a rectangular function yields a sinc function, which unlike the Gaussian function possesses local minima.

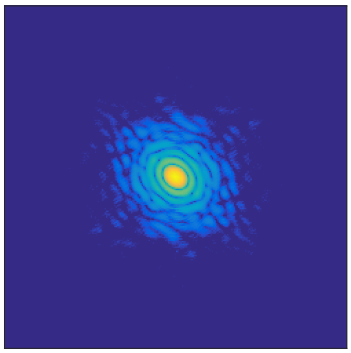

Figure 2.31: The mean PSD image for the stable cloud at the trapping detuning $\delta = -3.2\,\Gamma$ and the magnetic field gradient $\nabla B = 12$ G/cm (experiment in section 2.3.1), displayed in log scale. The intensity range is 6.5 decades. The field of view is 24.7×24.7 mm^{-2}.

origin of these crosses but exclude the possibility of the light field's interference patterns causing them, as such patterns would instead cause bright crosses, as seen for some of the stable cloud profiles in Fig. 2.32. For the asymmetric regime, we observe that the profiles distinguish themselves by being tilted. The tilt is not at all surprising, given the fact that the clouds of this regime are preferentially elongated along beam directions (see Fig. 2.20). Notice how the two upper profiles for this regime are tilted in the opposite direction compared to the two bottom ones - this is exactly the consequence of the clouds mainly elongating themselves along opposite beam directions. The angle between the beam-axis where the elongation happens and the corresponding diagonal of the PSD image is 90 °, which is imparted by the Fourier transform. For the symmetric regime, the dark crosses do not appear and the shapes are isotropic. The isotropy is well-explained by the symmetrically distributed deformations around the trap center in this regime. We next see what insights into unstable cloud structures can be gathered as we perform angular averaging of mean PSD images.

Fig. 2.33(a) displays the angular averages of mean PSD images versus the wavenumber k for the clouds in Fig. 2.32 at $\nabla B = 12$ G/cm; log-log scale is used. The dips seen in the angularly-averaged profile for the stable cloud case are indeed attributed to the fact that in the corresponding mean PSD image, the dark rings can be observed. The angular averaging confirms also the previously mentioned broadening of the PSD profiles that corresponds to the increased weight of small-scale structures. The broadening behavior is more clearly illustrated in Fig. 2.34, where ratios of angularly-averaged profiles at the small- to large-scale k are plotted versus δ/Γ for different ∇B values. The ∇B values used encompass all the instability regimes (see Fig. 2.20), such that we can observe that the broadening behavior is universal for all these regimes. From Fig. 2.34 we can clearly observe that in the unstable regime, the weight of small-scale structures gets progressively suppressed compared to larger ones

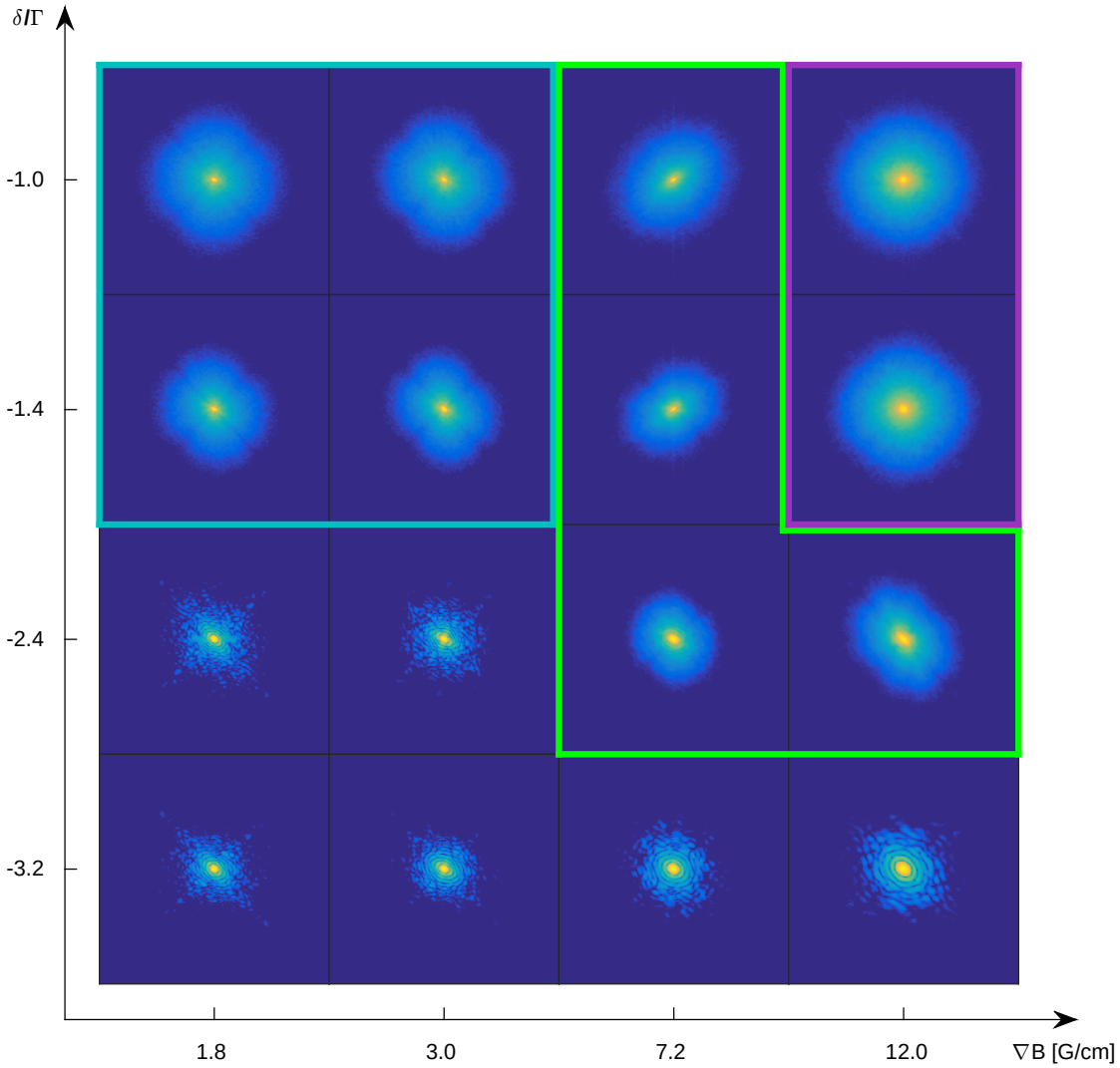

Figure 2.32: The mean PSD images for unstable clouds from the different instability regimes - the filament-like (blue enclosure), asymmetric (green enclosure) and symmetric (purple enclosure) regimes. The mean PSD images for stable clouds are also displayed. Log scale is used. The intensity range is 6.5 decades. The field of view is 24.7×24.7 mm^{-2}.

as ∇B is increased. This confirms what our eyes can see in the direct cloud-images: there are more and finer structures at lower ∇B values. The result is nevertheless counter-intuitive, due to increased ∇B implying decreased spatial scale of the cloud. The question that remains is what determines the size of the filaments.

Finally, the scaling of the PSD profiles at large wavenumbers can provide information on the physics underlying the instability phenomenon. As we recall from section 1.2.3.3, Ref. [43] reported an observation of a k^{-4} scaling at large

wavenumbers in an instability experiment with the beams tuned very close to the atomic resonance ($\delta = -0.5\,\Gamma$, for $\nabla B = 9$ G/cm), and used this observation to validate the photon bubble model. We consider extracting PSD scaling law exponents at large wavenumbers, and in Fig. 2.33(b) we illustrate our employed procedure. As can be seen, the procedure involves fitting a linear function in log-log scale to the angularly-averaged profile (of an unstable cloud) in the region immediately above the background values and yields the PSD scaling law exponent α; we note that the fitting region is selected by eye. In Fig. 2.35, we plot α versus δ/Γ for different ∇B values (encompassing all the instability regimes). The first observation that we make is that α varies quite a lot, i.e. between -3.9 to -6.4. From this finding we conclude that α is not universal for balanced MOT instabilities but rather parameter-dependent, and that caution should be applied when using a scaling exponent value to validate an instability model. Some doubt is thus cast on the conclusion of Ref. [43]. The last observation we make is that α tends to become more negative when ∇B is increased - this confirms the previous observation on the suppression of the weight of small-scale structures in Fig. 2.34.

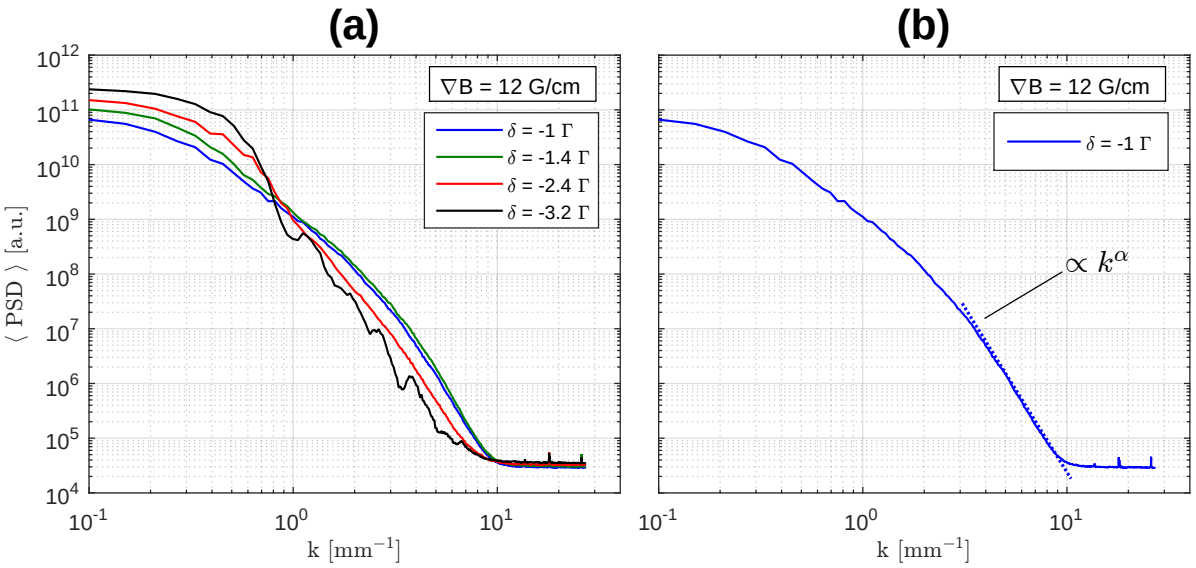

Figure 2.33: (a) The angular averages of mean PSD images versus the wavenumber k for a stable cloud ($\delta/\Gamma = -3.2$) and unstable clouds ($\delta/\Gamma = -1, -1.4, -2.4$) for $\nabla B = 12$ G/cm, displayed in log-log scale, and (b) extraction of the PSD scaling law exponent α for the angularly-averaged profile seen in (a) for one of the unstable clouds. In (b), a linear function is fitted in log-log scale to the angularly-averaged profile in the region immediately above the background values; in this example, the length of the fit (sloped dotted line) has been exaggerated for display purposes. We note that the PSD images used in the production of the angularly-averaged profiles in this figure have a greater field of view than the PSD images in Fig. 2.32.

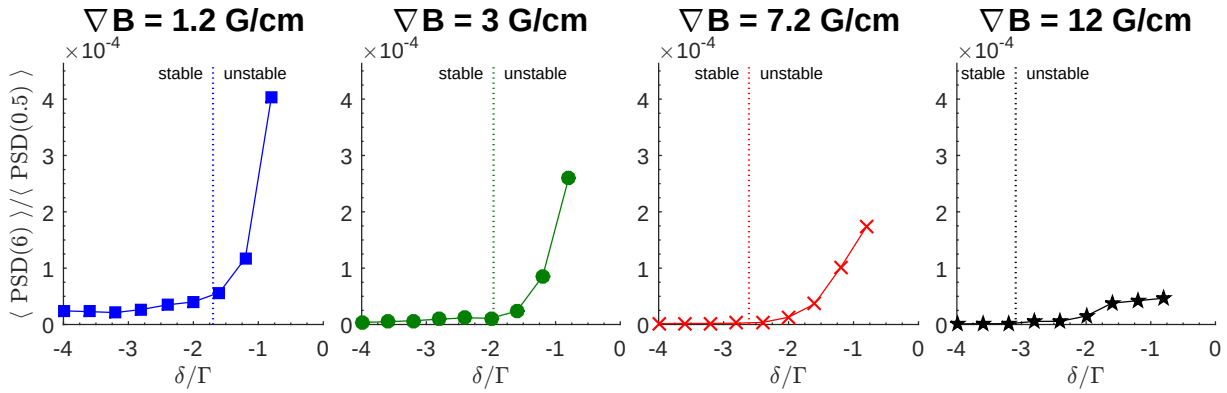

Figure 2.34: The ratio of angularly-averaged mean PSD at $k = 6$ mm^{-1} to $k = 0.5$ mm^{-1} for $\nabla B = 1.2$ G/cm (squares), 3 G/cm (dots), 7.2 G/cm (crosses) and 12 G/cm (stars). $k = 6$ mm^{-1} is in the small-scale structure range, whereas $k = 0.5$ mm^{-1} is in the large-scale structure range (see Fig. 2.33). The vertical dotted lines separate stable and unstable clouds for the different ∇B values; these lines are drawn according to the result of Fig. 2.10.

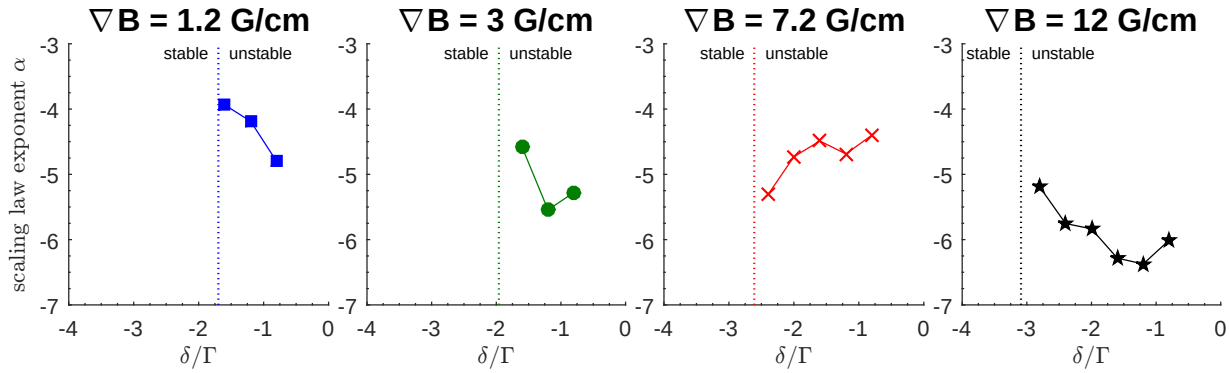

Figure 2.35: The PSD scaling law exponent α versus δ/Γ for different ∇B values. Similar notations as in Fig. 2.34 are used.

2.5 Remarks

To close this Chapter, we make some remarks by summarizing our assessment of the known analytical models of balanced MOT instabilities and providing motivation for the next course of action.

Starting with the 1-zone model [39], the assessment was done by comparing our instability threshold results with the corresponding predictions of Eq. 1.21. In section 2.3.1, studying the impact of the magnetic field gradient ∇B on the instability threshold behavior, we found a qualitative mismatch between the experiment and the theory. Thus, we were able to conclude that the physical mechanism behind the instabilities is more involved than of the 1-zone model's, where the instabilities are induced by the cloud's edge passing from a positive to negative friction. In section 2.3.2, studying the impact of the atom number N on the instability threshold behavior, we confirmed this conclusion. We suggested to turn to the two remaining alternative analytical models: (i) the Mathieu equation model, where the instability mechanism is driven by the coupling between the COM and breathing modes [41], (ii) the photon bubble model, where photon bubble structures provide a source for the unstable motion [42]. Our assessment of these two models is summarized next.

To assess the Mathieu equation model, we performed, in section 2.4.2, PCA for an unstable cloud and examined the different oscillation modes. It was shown that the COM and breathing modes did not account for even a half of all the variations, such that little support could be provided to the model's proposal that the instability mechanism is driven by the coupling between only these two modes. We raised also issues on (i) lack of direct mapping of our observed COM oscillations to the COM oscillations of the model, and (ii) lack of stringent relation between the COM and breathing oscillation frequencies in the experiment as opposed to the model. Overall, from our entire discussion, the model could be judged to be too simplistic for capturing the mechanism behind the instabilities.

To assess the photon bubble model, we performed, in section 2.4.3, SFA for unstable clouds and examined the scaling law behavior of the angularly-averaged PSD profiles in the small-scale structure range. We saw how our observations conformed to those of Ref. [43], where a k^{-4} scaling (measured at a very select set of MOT parameters) was used to validate the photon bubble model. In our broad range of MOT parameters, we observed that the PSD scaling law exponent α varied quite a lot, i.e. between -3.9 to -6.4. From this finding we concluded that α was not universal for balanced MOT instabilities but rather parameter-dependent, and that caution should be applied when using a scaling exponent value to validate an instability model. Some doubt was thus cast on the conclusion of Ref. [43].

All in all, none of the known analytical models of balanced MOT instabilities stood up to our assessment. This shows that the assumptions in these models are too crude for capturing the real physics, and thus a more involved analytical theory would have to be developed to carry out the explanations. To better

understand the instabilities, it can be highly helpful to tackle the problem first with numerical simulations, preferably in 3D, to respect the real-world scenario. As a consequence, the route of this Thesis has been to develop a kinetic 3D model for the MOT and employ it in numerical simulations. In the upcoming and final Chapter, we will describe the model as well as the simulations, and obtain qualitative agreements with the corresponding experiments.

Chapter 3

Balanced MOT instability simulations in 3D

Local table of contents

This Chapter concerns balanced MOT instability simulations in 3D. A kinetic 3D model based on a 2-level atom is first described and discussed, which is then used in the development of the $F = 0 \rightarrow F' = 1$ model, being the kinetic model employed in our simulations. The balanced MOT simulation results are compared with results of our experiments (Chapter 2). Qualitative agreements are obtained. Original studies on how the instabilities depend on implemented physical ingredients are also performed.

This Chapter is organized as follows. We start by presenting a kinetic 3D model for the MOT, based on a 2-level atom in the Doppler picture. The physical ingredients that we consider include the trapping force, diffusion, intensity attenuation and rescattering force. Next, the 2-level atom model's results are used in the construction of the corresponding forces and effects in a model based on the hyperfine transition $F = 0 \rightarrow F' = 1$. Then, we proceed explaining the algorithm and methods used in our simulations, incorporating the $F = 0 \rightarrow F' = 1$ model. Then, we cover the tests we have done in making sure that correct numerical results are obtained in our main simulations. Finally, we proceed with the main simulation results for the balanced MOT. We begin by presenting the results of simulated instability threshold versus respectively ∇B, N and I, and do comparisons with results of the corresponding experiments (sections 2.3.1, 2.3.2, 2.3.3). We then move on to studying the spatio-temporal properties of the simulated unstable regime. Here we present δ-∇B phase-space instability diagrams, found respectively by using ESA and visual inspection, and make comparisons with the experimentally obtained result (section 2.4.1). We end by investigating the impact of our simulation model's physical ingredients on the instabilities.

3.1 3D MOT forces and effects (2-level atom model)

In this section, we present a kinetic 3D model for the MOT, based on a 2-level atom. We start by obtaining expressions for this model's forces and effects - the trapping force, diffusion, intensity attenuation and rescattering force - all whose basics we have touched upon in Chapter 1. These physical ingredients are discussed within the context of balanced MOT instability simulations. At the end of this section, we provide a summary table of the obtained expressions. We note that in the next section, we will be using the 2-level atom model in the development of the $F = 0 \rightarrow F' = 1$ model, being the kinetic model employed in our simulations.

3.1.1 Trapping force

The goal of this subsection is to provide an expression for the trapping force for our 2-level atom model in 3D. As we recall from the first section of Chapter 1, trapping force is the MOT's most basic component force, responsible for the cooling and confinement of the atoms. We start by reviewing the radiation pressure and dipole forces, that arise in the case when a 2-level atom interacts with a laser electric field, following Ref. [49]. Then, we obtain an expression for the cooling force caused by radiation pressure forces due to three mutually orthogonal pairs of counter-propagating laser beams, i.e. the 3D Doppler cooling force, and, finally, extend this result to provide an expression for the 3D trapping force. The obtained trapping force is discussed within the context of balanced MOT instability simulations.

The radiation pressure and dipole forces

The laser electric field that we consider is assumed to be monochromatic with the frequency ω_L and described by a time-dependent classical field [49]:

$$\mathbf{E}_L(\mathbf{r}, t) = E_0(\mathbf{r})\boldsymbol{\epsilon}(\mathbf{r})cos(\omega_L t + \phi(\mathbf{r})) \tag{3.1}$$

where $E_0(\mathbf{r})$, $\boldsymbol{\epsilon}(\mathbf{r})$ and $\phi(\mathbf{r})$ respectively are the amplitude, polarization and phase of the field at the position $\mathbf{r}$, and t is the time.

The 2-level atom couples to the field through the atom-light coupling Hamiltonian $\hat{V}_{AL}$, which is characterized by the Rabi frequency Ω given by

$$\hbar\Omega(\mathbf{r}) = -E_0(\mathbf{r})\langle g|\hat{\mathbf{d}}|e\rangle \cdot \boldsymbol{\epsilon}(\mathbf{r}) \tag{3.2}$$

where $\langle g|\hat{\mathbf{d}}|e\rangle = \langle e|\hat{\mathbf{d}}|g\rangle$ is the dipole moment matrix element, with $|g\rangle$ and $|e\rangle$ being respectively the ground and excited state of the 2-level atom.

Since the atom also couples to the quantum vacuum field, there exists as well the atom-vacuum coupling Hamiltonian $\hat{V}_{AV}$, which is characterized by the natural linewidth Γ of the transition.

All in all, the total Hamiltonian $\hat{H}$ of the system is given by the sum of the atomic, laser (classical) and vacuum Hamiltonians, and the interaction Hamiltonians $\hat{V}_{AL}$ and $\hat{V}_{AV}$. The interaction Hamiltonians are in the following considered to be evaluated at the position operator $\hat{\mathbf{R}}$ of the atom's COM.

In order to study the dynamics of the atom's COM, one starts with the Heisenberg's equations of motion for the operators $\hat{\mathbf{R}}$ and $\hat{\mathbf{P}}$, where the latter operator denotes the momentum operator of the atom's COM. From the Heisenberg equation for $\hat{\mathbf{R}}$, i.e. $\frac{d\hat{\mathbf{R}}}{dt} = \frac{1}{i\hbar}[\hat{\mathbf{R}}, \hat{H}]$, it can be shown that $\frac{d\hat{\mathbf{R}}}{dt} = \hat{\mathbf{P}}/M$ [49], from which it follows that the force operator $\hat{\mathbf{F}}(\hat{\mathbf{R}}) = M\frac{d^2\hat{\mathbf{R}}}{dt^2} = \frac{d\hat{\mathbf{P}}}{dt}$ and so is found from the Heisenberg's equation for $\hat{\mathbf{P}}$ [49]:

$$\begin{aligned}\hat{\mathbf{F}}(\hat{\mathbf{R}}) = \frac{d\hat{\mathbf{P}}}{dt} &= \frac{1}{i\hbar}[\hat{\mathbf{P}}, \hat{H}] \\ &= -\nabla\hat{V}_{AL}(\hat{\mathbf{R}}) - \nabla\hat{V}_{AV}(\hat{\mathbf{R}})\end{aligned} \tag{3.3}$$

The mean force $\boldsymbol{\mathcal{F}}(\hat{\mathbf{R}}) = \langle\hat{\mathbf{F}}(\hat{\mathbf{R}})\rangle = -\langle\nabla\hat{V}_{AL}(\hat{\mathbf{R}})\rangle$, as the mean value of $\nabla\hat{V}_{AV}$ can be shown to vanish [49]. Proceeding to work in the semi-classical limit, where $\hat{\mathbf{R}} \to \mathbf{r}$ and $\hat{\mathbf{P}} \to \mathbf{p}$, the mean force can be written as

$$\boldsymbol{\mathcal{F}}(\mathbf{r}, t) = -\langle\nabla\hat{V}_{AL}(\mathbf{r}, t)\rangle \tag{3.4}$$

with the time-dependence reinstated.

To continue with the mean force $\boldsymbol{\mathcal{F}}$ expressed by Eq. 3.4, the rotating-wave approximation is made use of, so to neglect rapidly oscillating terms in $\hat{V}_{AL}$. $\boldsymbol{\mathcal{F}}$ can then be written as a sum of two terms [49]:

$$\boldsymbol{\mathcal{F}}(\mathbf{r}, t) = -\hbar\Omega(\mathbf{r})\left[\mathsf{b}(\mathbf{r}, t)\nabla\phi(\mathbf{r}) + \mathsf{u}(\mathbf{r}, t)\frac{\nabla\Omega(\mathbf{r})}{\Omega(\mathbf{r})}\right] \tag{3.5}$$

where $\mathsf{b}(\mathbf{r}, t) = \Im\{\sigma_{ge}(t)e^{-i(\omega_L t+\phi(\mathbf{r}))}\}$ and $\mathsf{u}(\mathbf{r}, t) = \Re\{\sigma_{ge}(t)e^{-i(\omega_L t+\phi(\mathbf{r}))}\}$ with $\sigma_{ge} = \langle\, |e\rangle\langle g|\,\rangle$ being a component of the atomic density matrix σ.

b and u are found by solving the optical Bloch equations (OBEs) for the components of σ. We are interested in the case where Ω and $\frac{d\phi}{dt}$ are time-independent, such that the OBEs admit steady-state solutions, and so b and u respectively become [49]

$$\mathsf{b}_{st}(\mathbf{r}) = \frac{\Gamma}{2\Omega(\mathbf{r})}\frac{s(\mathbf{r})}{1+s(\mathbf{r})} \quad , \quad \mathsf{u}_{st}(\mathbf{r}) = \frac{\delta}{\Omega(\mathbf{r})}\frac{s(\mathbf{r})}{1+s(\mathbf{r})} \tag{3.6}$$

where $s(\mathbf{r}) = \frac{\Omega^2(\mathbf{r})/2}{\delta^2+\Gamma^2/4}$ is the saturation parameter, and $\delta = \omega_L - \omega_0$ is the laser detuning from resonance.

Using in Eq. 3.5 the expressions for $\mathsf{b}_{st}(\mathbf{r})$ and $\mathsf{u}_{st}(\mathbf{r})$, we write the mean force as a sum of two forces:

$$\boldsymbol{\mathcal{F}}(\mathbf{r}) = \boldsymbol{\mathcal{F}}_{rp}(\mathbf{r}) + \boldsymbol{\mathcal{F}}_{dip}(\mathbf{r}) \tag{3.7}$$

$\boldsymbol{\mathcal{F}}_{rp}$ is the radiation pressure force, and $\boldsymbol{\mathcal{F}}_{dip}$ is the dipole force.

Let us examine now the two forces separately.

(a) The radiation pressure force $\boldsymbol{\mathcal{F}}_{rp}$ is given by

$$\boldsymbol{\mathcal{F}}_{rp}(\mathbf{r}) = -\hbar\nabla\phi(\mathbf{r})\frac{\Gamma}{2}\frac{s(\mathbf{r})}{1+s(\mathbf{r})} \tag{3.8}$$

The particular case that interests us is where a motionless atom at $\mathbf{r}$ is exposed to the electric field of a plane laser wave. The Rabi frequency Ω here is constant, and the phase of the wave is $\phi(\mathbf{r}) = -\mathbf{k}\cdot\mathbf{r}$, with $\mathbf{k}$ being the wavevector. The OBEs admit steady-state solutions (as Ω and $\frac{d\phi}{dt}$ are time-independent), and thus $\boldsymbol{\mathcal{F}}_{rp}$ in Eq. 3.8 can be used to give

$$\boldsymbol{\mathcal{F}}_{rp} = \hbar\mathbf{k}\frac{\Gamma}{2}\frac{s}{1+s} \quad , \quad s = \frac{I_L/I_{sat}}{1+4\frac{\delta^2}{\Gamma^2}} \tag{3.9}$$

where in the present case the Rabi frequency $\Omega = \Gamma\sqrt{\frac{I_L}{2I_{sat}}}$, with I_L being the laser intensity and $I_{sat} = \frac{\hbar\omega_L\Gamma}{2\sigma_0}$ being the saturation intensity, where $\sigma_0 = \frac{3\lambda^2}{2\pi}$ is the on-resonance scattering cross-section of the atom. Accordingly, we have the on-resonance saturation parameter $s_0 = \frac{I_L}{I_{sat}}$.

Because $\hbar\mathbf{k}$ is the momentum of the laser photon, and $\frac{\Gamma}{2}\frac{s}{1+s}$ is the scattering rate of the photons, the physical origin of $\boldsymbol{\mathcal{F}}_{rp}$ is the absorption-spontaneous emission cycling, as depicted in Fig. 1.2.

(b) The dipole force $\boldsymbol{\mathcal{F}}_{dip}$ is given by

$$\boldsymbol{\mathcal{F}}_{dip}(\mathbf{r}) = -\frac{\hbar\delta}{4}\frac{\nabla\Omega^2(\mathbf{r})}{\delta^2+\Gamma^2/4+\Omega^2(\mathbf{r})/2} \tag{3.10}$$

where the expression for $s(\mathbf{r})$ below Eq. 3.6 has been used.

In the same plane wave case as above, $\boldsymbol{\mathcal{F}}_{dip}$ is zero, because Ω is constant. For $\boldsymbol{\mathcal{F}}_{dip}$ to appear, Ω must vary in space, achieved if either or both the amplitude and polarization of the electric field vary in space (refer to Eq. 3.2). For instance, $\boldsymbol{\mathcal{F}}_{dip}$ appears when dealing with a standing laser wave [49].

For negative detunings ($\delta < 0$), the atom will be pushed towards intensity maxima of a laser field, since according to Eq. 3.10, $\boldsymbol{\mathcal{F}}_{dip}$ carries the sign of $\nabla\Omega^2$. The opposite will hold for positive detunings ($\delta > 0$). $\boldsymbol{\mathcal{F}}_{dip}$ increases indefinitely with laser intensity, which is in contrast to $\boldsymbol{\mathcal{F}}_{rp}$ that remains bounded by increased laser intensity.

$\boldsymbol{\mathcal{F}}_{dip}$ can be shown to be derivable from a potential [49], making it a conservative force and thus of a different physical origin than $\boldsymbol{\mathcal{F}}_{rp}$.

To give some insight into the physical origin of $\boldsymbol{\mathcal{F}}_{dip}$, let us consider the fact that the maximal value of $\boldsymbol{\mathcal{F}}_{dip}$ is on the order of $\sim\frac{\hbar\nabla\Omega^2(\mathbf{r})}{\nabla\Omega(\mathbf{r})} \simeq \hbar\nabla\Omega(\mathbf{r})$. In the case of a standing laser wave, $\nabla\Omega(\mathbf{r})$ can be on the order of $k_L\Omega(\mathbf{r})$ [49]. Such result corresponds to $\boldsymbol{\mathcal{F}}_{dip}$ describing transfer of the photon momentum $\hbar\mathbf{k}$ to the atom at a rate of $\Omega(\mathbf{r})$, as expected for a photon-redistribution process

involving absorption-stimulated emission cycling. Note that during the redistribution the net energy of the field does not change, as the frequency of each wave composing the standing wave is taken to be the same. The physical picture for the dipole force commonly involves the photon-redistribution process, but we bring into attention that other interpretations are also known to exist, and we will refer the reader to Ref. [49] for such alternative interpretations.

The dipole force is involved in the sub-Doppler cooling mechanism known as the Sisyphus cooling that we have mentioned in the first section of Chapter 1. To achieve the cooling effect, the Sisyphus cooling uses the decelerating effect of the dipole force combined with a dissipation of potential energy by Raman scattering processes [20].

As we will consider in the following working in the low-intensity limit, where $s_0 \ll 1$, the dipole force will be neglected. Usage of this limit will be discussed at the end of this subsection after writing down our 2-level atom model's 3D trapping force, which we will obtain by extending the result for the 3D Doppler cooling force to be presented next.

The 3D Doppler cooling force (2-level atom model)

In the first section of Chapter 1, we presented an expression for the Doppler cooling force that results from adding together the radiation pressure forces stemming from two counter-propagating beams (Eq. 1.2). We now give a more detailed explanation on how the Doppler cooling force arises in a 1D counter-propagating beam arrangement, afterwards which an expression for the Doppler cooling force in 3D is constructed.

When dealing with a moving atom in the case of a laser plane wave, we may find that Ω and $\frac{d\phi}{dt}$ are time-independent, such that the OBEs will admit steady-state solutions. The radiation pressure force will be given by the same Eq. 3.9 with the detuning $\delta \to \delta \mp \mathbf{k} \cdot \mathbf{v}$, where "$-$" is used if the laser beam is traveling in the positive direction (of an axis) with the wavevector $+\mathbf{k}$, and "$+$" is used if the laser beam is traveling in the negative direction with the wavevector $-\mathbf{k}$. This result means that the atom will see the laser beam with the Doppler shifted frequency given by Eq. 1.1. Now, if we were to consider a moving atom in the case of a laser standing wave, i.e. a superposition of two counter-propagating waves, we would find that $\Omega(\mathbf{r} = \mathbf{v}t)$ is time-dependent, and thus the OBEs would no longer admit steady-state solutions. The OBEs form here a set of coupled differential equations, whose general analytical solutions do no exist [49]. To proceed constructing an expression for the force that a moving atom feels when exposed to two counter-propagating beams, one thus resorts to using approximations. One can find that in the low-intensity limit, where $s_0 \ll 1$, the cooling force acting on a moving 2-level atom in a 1D counter-propagating beam arrangement coincides with the sum of two radiation pressure forces, one for the positively directed beam ($+\mathbf{k}$) and another one for the negatively directed beam ($-\mathbf{k}$) [49]. This cooling force is the Doppler cooling force, the name of which is attributed precisely to the fact that the cooling is achieved due to the

Doppler effect. As the intensity is increased, higher-order correctional terms to the cooling force become of importance. As shown in Ref. [53], there exists a correctional term depending on the product of the intensities of the counter-propagating beams, i.e. a term that contributes to beam cross-saturation. We note, however, that in the proceedings, we ignore the higher-order correctional terms.

In order to obtain an expression for the cooling force in the situation where the atom is exposed to three pairs of mutually orthogonal, counter-propagating beams (as in the 3D OM arrangement), we realize that the OBEs needed to be solved will be more complex compared to the one standing wave case, and it is not straightforward to justify that in the low-intensity limit, where $s_0 \ll 1$, the 3D cooling force will be given by the sum of three Doppler forces, one for each axis. Nevertheless, for mere simplicity, we assume that such addition of Doppler forces can be done as $s_0 \ll 1$ is satisfied, and we thus write down our 2-level atom model's 3D Doppler cooling force:

$$\mathbf{F}_D^{2level}(\mathbf{v}) = F_{D,\mathsf{x}}^{2level}(v_\mathsf{x})\hat{\mathbf{x}} + F_{D,\mathsf{y}}^{2level}(v_\mathsf{y})\hat{\mathbf{y}} + F_{D,\mathsf{z}}^{2level}(v_\mathsf{z})\hat{\mathbf{z}} \tag{3.11}$$

with the force's components being

$$F_{D,\alpha}^{2level}(v_\alpha) = \hbar k_L \frac{\Gamma}{2}\left(\frac{s_0}{1+6s_0+4\frac{(\delta-k_L v_\alpha)^2}{\Gamma^2}} - \frac{s_0}{1+6s_0+4\frac{(\delta+k_L v_\alpha)^2}{\Gamma^2}}\right) \tag{3.12}$$

where $\alpha = \mathsf{x},\mathsf{y},\mathsf{z}$, and $\mathbf{v} = (v_\mathsf{x}, v_\mathsf{y}, v_\mathsf{z})$ is the velocity of the atom, and we for simplicity have assumed that the wavenumber for all the beams is the same and given by $k_L = \omega_L/c$, where c is the speed of light. Note that in the denominator, we have substituted the s_0 term with $6s_0$, being a valid substitution for $s_0 \ll 1$. We allow for such substitution because the atom's transition is driven by six laser beams and, as the intensity is increased, the transition becomes more saturated, such that the cooling force exerted on the atom must go down. Such substitution implies we are introducing beam cross-saturation in our modeling. The reason we include the cross-saturation by means of the substitution, while neglecting the higher-order correctional terms that include the cross-saturation as in Ref. [53] (mentioned earlier), is because we would like to retain some character behind the physics involved, whilst reducing the overall complexity of our modeling.

In the limit of small velocities, $|v_\alpha| \ll \Gamma/k_L$ & $|\delta|/k_L$, the 3D Doppler cooling force is a friction force with the friction coefficient γ_{3D}:

$$\mathbf{F}_D^{2level}(\mathbf{v}) \approx -\gamma_{3D}\mathbf{v} \quad , \quad \gamma_{3D} = s_0\frac{-8\hbar k_L^2\delta\Gamma^3}{(\Gamma^2+6\Gamma^2 s_0+4\delta^2)^2} \tag{3.13}$$

where γ_{3D} is positive for $\delta < 0$, such that cooling is achieved, and negative for $\delta > 0$, such that heating is achieved (i.e. the atom velocities increase). Eq. 3.13 is seen to be analogous to Eq. 1.3 for the 1D Doppler cooling force in the low-velocity limit.

In what follows, we will explain how we extend the result for the 3D Doppler cooling force, Eqs. 3.11-3.12, to provide an expression for the 3D trapping force.

The 3D trapping force (2-level atom model)

To proceed obtaining an expression for the 3D trapping force, let us consider first writing down an expression for the MOT's magnetic field. In the MOT, sketched in Fig. 1.1, the coils produce a quadrupole magnetic field, whose general expression can be written in terms of elliptic integrals [54]. We consider the case where the distances from the trap center are much smaller than both the radius of the coils, R_a, and the separation length between the coils, l_a, such that the general expression for the magnetic field simplifies to [54]

$$\mathbf{B}(\mathbf{r}) = -B'\left(\frac{x}{2}\hat{\mathbf{x}} + \frac{y}{2}\hat{\mathbf{y}} - z\hat{\mathbf{z}}\right) \tag{3.14}$$

where $B' \equiv \frac{3\mu_0 I_0 l_a R_a^2}{2(R_a^2+l_a^2)^{5/2}}$, with μ_0 being the vacuum permeability and I_0 being the current flowing through the coils. $-\frac{B'}{2}$ is the magnetic field gradient respectively along the x- and y-axis, and B' is the magnetic field gradient along the z-axis; thus, the Maxwell's equation $\nabla \cdot \mathbf{B} = 0$ is correctly satisfied. The laser beam pairs in the MOT have different circular helicities depending on the axis of propagation: right-hand circular helicity for the z-axis beams and left-hand circular helicity for the x- and y-axis beams[1]. To recall (from section 2.1.3), we use the notations ∇B and B' interchangeably to denote the magnetic field gradient along the z-axis. We note that B' can be made negative by switching the directions of the currents seen in Fig. 1.1; in such a case, the handedness of the circular helicities of the laser beam pairs would have to be reversed for the MOT to work. In this Thesis, we are nevertheless sticking to the conventions of Fig. 1.1.

We recall about the 1D model of the MOT depicted in Fig. 1.5(a), where an atom with the hyperfine transition $F = 0 \rightarrow F' = 1$ is put in a counter-propagating beam arrangement, with the two beams having the respective σ^+ and σ^- polarizations, and a linearly increasing magnetic field $\mathbf{B}(z) = B'z\hat{\mathbf{z}}$ is applied, which is now seen to follow from Eq. 3.14. Due to the Zeeman interaction between the atomic total angular momentum operator $\hat{\mathbf{F}}$ and the field $\mathbf{B}(z)$, the three-fold degeneracy of the excited $F' = 1$ level is lifted, such that we may write the transition frequency between the ground Zeeman sub-level $|F = 0, m = 0\rangle$ and the excited Zeeman sub-levels $|F' = 1, m'\rangle$ as in Eq. 1.7, i.e. $\omega'(m') = \omega_{0\rightarrow 0} + m'\mu B'z$. If in the 1D model of the MOT we consider respectively the x- and y-axis, the corresponding transition frequencies are $\omega_{0\rightarrow 0} - m'\mu B'x/2$ and $\omega_{0\rightarrow 0} - m'\mu B'y/2$, as according to Eq. 3.14, the magnetic field along the x-axis is $\mathbf{B}(x) = -B'\frac{x}{2}\hat{\mathbf{x}}$ and along the y-axis it is $\mathbf{B}(y) = -B'\frac{y}{2}\hat{\mathbf{y}}$.

The Zeeman effect, which gives rise to the confinement, does not exist in our 2-level atom picture. However, we proceed adapting the *fictive* 1D MOT

[1] In the MOT, since the magnetic field gradient is opposite in sign for the z-axis, the helicity of the z-axis beams has its handedness reversed compared to the x- and y-axis beams.

arrangement approach considered previously (refer to the paragraph below Fig. 1.5) to 3D and thus assume that the six beams *themselves* are shifted in frequency according to where the atom is in what we presently consider as the fictive 3D MOT arrangement. Observing the expressions for the transition frequencies discussed in the last paragraph, we introduce the shifts $\mp\mu B' x/2$, $\mp\mu B' y/2$, $\mp\mu B' z$ for the beams traveling in the positive/negative ($\pm$) direction of the x-, y-, z-axis, respectively. Using the result for the 3D Doppler cooling force, Eqs. 3.11-3.12, with these shifts taken into account, we finally write down our 2-level atom model's 3D trapping force:

$$\boxed{\mathbf{F}_{tr}^{2level}(\mathbf{r},\mathbf{v}) = F_{tr,\mathrm{x}}^{2level}(\mathbf{r},\mathbf{v})\hat{\mathbf{x}} + F_{tr,\mathrm{y}}^{2level}(\mathbf{r},\mathbf{v})\hat{\mathbf{y}} + F_{tr,\mathrm{z}}^{2level}(\mathbf{r},\mathbf{v})\hat{\mathbf{z}}} \tag{3.15}$$

with the force's components being

$$F_{tr,\alpha}^{2level}(\mathbf{r},\mathbf{v}) = \hbar k_L \frac{\Gamma}{2I_{sat}} \left(\frac{I_\alpha^+(\mathbf{r},\mathbf{v})}{1 + \frac{I_{tot}(\mathbf{r},\mathbf{v})}{I_{sat}} + 4\frac{(\delta - k_L v_\alpha - \mu B' r'_\alpha)^2}{\Gamma^2}} - \frac{I_\alpha^-(\mathbf{r},\mathbf{v})}{1 + \frac{I_{tot}(\mathbf{r},\mathbf{v})}{I_{sat}} + 4\frac{(\delta + k_L v_\alpha + \mu B' r'_\alpha)^2}{\Gamma^2}} \right)$$

or, when compactly written,

$$\boxed{F_{tr,\alpha}^{2level}(\mathbf{r},\mathbf{v}) = \frac{1}{c}\left(I_\alpha^+(\mathbf{r},\mathbf{v})\sigma_\alpha^+(\mathbf{r},\mathbf{v}) - I_\alpha^-(\mathbf{r},\mathbf{v})\sigma_\alpha^-(\mathbf{r},\mathbf{v})\right)} \tag{3.16}$$

where

$$\boxed{\sigma_\alpha^\pm(\mathbf{r},\mathbf{v}) = \frac{\sigma_0}{1 + \frac{I_{tot}(\mathbf{r},\mathbf{v})}{I_{sat}} + 4\frac{(\delta \mp k_L v_\alpha \mp \mu B' r'_\alpha)^2}{\Gamma^2}}} \tag{3.17}$$

is the scattering cross-section corresponding to the beam with the intensity $I_\alpha^\pm$ traveling in the positive/negative ($\pm$) direction of $\hat{\boldsymbol{\alpha}} = \hat{\mathbf{x}}, \hat{\mathbf{y}}, \hat{\mathbf{z}}$. $\mathbf{r}' = (r'_\mathrm{x}, r'_\mathrm{y}, r'_\mathrm{z}) = (\frac{x}{2}, \frac{y}{2}, z)$ is the atom position with the spatial asymmetry of the magnetic field taken into account, and I_{tot} is the total beam intensity given by

$$\boxed{I_{tot}(\mathbf{r},\mathbf{v}) = \sum_{\alpha=\mathrm{x,y,z}} \left[I_\alpha^+(\mathbf{r},\mathbf{v}) + I_\alpha^-(\mathbf{r},\mathbf{v})\right]} \tag{3.18}$$

In general, the beam intensities will not be the same at a given point in the cloud, as they will be subject to attenuation, as will be covered closely in section 3.1.3. Note that presently we assume $I_\alpha^+ = I_\alpha^- = s_0 I_{sat}$, such that $\frac{I_{tot}}{I_{sat}} = 6s_0$.

In the limit of small velocities, $|v_\alpha| \ll \Gamma/k_L$ & $|\delta|/k_L$, and for positions close to the trap center, $|r'_\alpha| \ll \Gamma/(\mu B')$ & $|\delta|/(\mu B')$, the 3D trapping force describes a harmonic oscillator with the friction coefficient γ_{3D} and the spring constant κ_{3D}:

$$\mathbf{F}_{tr}^{2level}(\mathbf{r},\mathbf{v}) \approx -\gamma_{3D}\mathbf{v} - \kappa_{3D}\mathbf{r}' \quad , \quad \kappa_{3D} = \frac{\mu B'}{k_L}\gamma_{3D} \tag{3.19}$$

with γ_{3D} defined in Eq. 3.13. We observe here that the trapping force is written as a sum of the friction force $-\gamma_{3D}\mathbf{v}$ and the restoring force $-\kappa_{3D}\mathbf{r}'$. For negative detunings ($\delta < 0$) γ_{3D} is positive, such that the friction force cools

the atoms, and likewise κ_{3D} is positive, such that the restoring force pushes the atoms to center of the trap, giving rise to the confinement. Eq. 3.19 is seen to be analogous to Eq. 1.9 for a 1D trapping force in the low-velocity limit and in the vicinity of the trap center.

To end this subsection, we discuss the obtained 3D trapping force (Eqs. 3.15-3.16). Let us consider first the fact that the low-intensity limit ($s_0 \ll 1$) was imposed, which allowed for the usage of radiation pressure forces only. In our balanced MOT instability simulations, however, s_0 can be $\sim$3, essentially implying that we should be considering higher-order corrections to the trapping force. We do not consider implementing higher-order corrections merely for simplicity reasons but note that a similar kind of treatment of the trapping force was done in the past quasi-1D simulations of the balanced MOT [40], and it did not impact the ability of simulating the instabilities. Next, let us consider the relevance of sub-Doppler mechanisms for our instability simulations. The studies in Refs. [25, 59] reported that not only the velocity distribution of the atoms but also their spatial distribution involves sub-Doppler mechanisms in the balanced MOT. Concentrating on the study of Ref. [59], investigations were described where experimental techniques were applied to separate the clouds, containing $\sim 10^8$ atoms, into Doppler and sub-Doppler parts. It was shown that the sub-Doppler atoms accounted for a small fraction ($\sim 3 \cdot 10^6$ atoms) of the total and were concentrated mainly at the core of the cloud. The results were verified both experimentally and with numerical simulations. The amount of atoms used in the investigations put the clouds in the large MOT range like in the case of our studied instabilities (Chapter 2). The findings in Ref. [59] can thus affirm that our studied instabilities are mostly unaffected by sub-Doppler mechanisms, and thus great weight is provided for neglecting such mechanisms in our corresponding simulations.

3.1.2 Diffusion

The goal of this subsection is to provide an expression for the momentum diffusion coefficient for our 2-level atom model in 3D. As we recall from the first section of Chapter 1, the momentum diffusion coefficient is responsible for the diffusive heating of the atoms. The reason we want to add this effect into our instability simulations is because noise is known to play an important role in instability dynamics. For instance, we recall from section 1.2.3.2 that the erratic features in some retro-reflected MOT instabilities relied heavily on the presence of noise, and from section 1.2.3.4 we recall that parameter-modulated MOT instabilities could occupy multiple states at once due to the presence of noise. Regarding balanced MOT instabilities, noise was an important component for the observed discrepancies between experiment and theory in the instability synchronization study, as covered at the end of section 1.2.3.3.

We start with pointing out that previously we have considered only the mean part of the total force, $\boldsymbol{\mathcal{F}} = \langle \hat{\mathbf{F}} \rangle$, whilst neglecting the fluctuating part of it, commonly referred to as the Langevin force (operator), $\delta\hat{\boldsymbol{\mathcal{F}}}$, defined to be the difference between the total force and its mean value [49]:

$$\delta\hat{\boldsymbol{\mathcal{F}}} = \hat{\mathbf{F}} - \boldsymbol{\mathcal{F}} \tag{3.20}$$

It is this fluctuating part of the force gives rise to noise in atomic motion, causing the diffusive heating of the atoms. In this subsection, we first show how the Langevin force is related to the momentum diffusion coefficient, after which we provide an expression for the coefficient in the case the 2-level atom is exposed to one laser beam. We then finally provide an expression for the momentum diffusion coefficient for our 2-level atom model in 3D, by taking the six MOT beams into account, and discuss this result within the context of balanced MOT instability simulations.

Langevin force and momentum diffusion coefficient for one beam

To understand how the Langevin force is related to the momentum diffusion coefficient D, one may start with the definition relating D to the rate of change of the momentum variance $\Delta P^2(t)$:

$$2D = \frac{d}{dt}\Delta P^2(t) \tag{3.21}$$

We note that this definition is the quantized counterpart of the classical result obtainable from the Langevin equation for the momentum of a massive particle subject to a friction force and a fluctuating force [49].

The variance can be expressed as

$$\Delta P^2(t) = \langle\{\hat{\mathbf{P}}(t) - \langle\hat{\mathbf{P}}(t)\rangle\}^2\rangle$$

Differentiating the right-hand side of the above equation with respect to t and making use of the Heisenberg equation for $\hat{\mathbf{P}}$ in Eq. 3.3, i.e. $\frac{d}{dt}\hat{\mathbf{P}}(t) = \hat{\mathbf{F}}(t)$, we find with help of the product rule:

$$\frac{d}{dt}\langle\{\hat{\mathbf{P}}(t) - \langle\hat{\mathbf{P}}(t)\rangle\}^2\rangle = \langle\hat{\mathbf{F}}\cdot\hat{\mathbf{P}} + \hat{\mathbf{P}}\cdot\hat{\mathbf{F}}\rangle - 2\langle\hat{\mathbf{P}}\rangle\cdot\langle\hat{\mathbf{F}}\rangle$$

Using in the above equation the solution to the Heisenberg equation for $\hat{\mathbf{P}}$, i.e. $\hat{\mathbf{P}}(t) = \int_0^\infty d\tau\,\hat{\mathbf{F}}(t-\tau)$, we find that Eq. 3.21 tells us that

$$D = \int_0^\infty d\tau\,\langle\delta\hat{\boldsymbol{\mathcal{F}}}(t)\cdot\delta\hat{\boldsymbol{\mathcal{F}}}(t-\tau)\rangle \tag{3.22}$$

In words, we see that the momentum diffusion coefficient D is equal to the integral of the time correlation function of the Langevin force $\delta\hat{\boldsymbol{\mathcal{F}}}$.

To continue with the result of Eq. 3.22, one notices that $\delta\hat{\boldsymbol{\mathcal{F}}}$ can be written as a sum of two Langevin forces [49]: $\delta\hat{\boldsymbol{\mathcal{F}}} = \delta\hat{\boldsymbol{\mathcal{F}}}_{vac} + \delta\hat{\boldsymbol{\mathcal{F}}}_{las}$, where $\delta\hat{\boldsymbol{\mathcal{F}}}_{vac}$ and $\delta\hat{\boldsymbol{\mathcal{F}}}_{las}$ are linked to the vacuum field and the laser field, respectively. Plugging $\delta\hat{\boldsymbol{\mathcal{F}}} = \delta\hat{\boldsymbol{\mathcal{F}}}_{vac} + \delta\hat{\boldsymbol{\mathcal{F}}}_{las}$ into Eq. 3.22 it can be shown that the cross-term involving both $\delta\hat{\boldsymbol{\mathcal{F}}}_{vac}$ and $\delta\hat{\boldsymbol{\mathcal{F}}}_{las}$ vanishes [49], such that D can be written as a sum of

two momentum diffusion coefficients,

$$D = D_{vac} + D_{las} \tag{3.23}$$

where the diffusion coefficients D_{vac} and D_{las} respectively involve the vacuum field Langevin force $\delta\hat{\boldsymbol{\mathcal{F}}}_{vac}$ and the laser field Langevin force $\delta\hat{\boldsymbol{\mathcal{F}}}_{las}$.

Below we consider D_{vac} as well as D_{las} in the case the atom is exposed to the electric field of a plane laser wave, in that way staying consistent with the fact that for the mean force acting on the atom we have considered a plane wave as well - see below Eq. 3.8. Note that the saturation parameter s is hence given by the expression in Eq. 3.9.

(a) The momentum diffusion coefficient D_{vac} of the vacuum field is given by [49]

$$D_{vac} = \hbar^2 k_L^2 \frac{\Gamma}{4} \frac{s}{1+s} \tag{3.24}$$

The expression above can be interpreted in terms of randomness in the direction of the spontaneous emission. Such interpretation follows as it can be shown that the variance in the momentum due to spontaneously emitted photons, ΔP_{vac}^2, is proportional to D_{vac} and increasing linearly in time as $\Delta P_{vac}^2 = 2D_{vac}t$ [55].

(b) The momentum diffusion coefficient D_{las} of the laser field is given by [49]

$$D_{las} = \hbar^2 k_L^2 \frac{\Gamma}{4} \frac{s}{(1+s)^3} \times \left\{ 1 + \frac{12\delta^2 - \Gamma^2}{4\delta^2 + \Gamma^2} s + s^2 \right\} \tag{3.25}$$

The expression above can be interpreted to appear due to variations in the number of absorbed photons from the laser field. Such interpretation of D_{las} is supported when computing the variance in the momentum due to absorbed photons, ΔP_{las}^2, which is proportional to the variance in the number of absorbed photons, Δn_{las}^2. Having Δn_{las}^2, one can show that ΔP_{las}^2 is proportional to D_{las} and increasing linearly in time as $\Delta P_{las}^2 = 2D_{las}t$ [55].

Using Eq. 3.23 with the expressions in Eqs. 3.24, 3.25 it is possible to show that Eq. 1.4 for the finite limit temperature achievable with Doppler cooling gives the result seen in Eq. 1.5. We will show that Eq. 1.5 is obtainable with our 2-level atom model's 3D momentum diffusion coefficient written down next.

The 3D momentum diffusion coefficient (2-level atom model)

In the above, the atom was considered to be exposed to only one laser beam. When the six MOT beams are involved, we assume, similarly to the trapping force case, that each beam can be treated independently, and thus finally write

down our 2-level atom model's 3D momentum diffusion coefficient:

$$\boxed{D_{3D}^{2level}(\mathbf{r},\mathbf{v}) = D_{vac,3D}^{2level}(\mathbf{r},\mathbf{v}) + D_{las,3D}^{2level}(\mathbf{r},\mathbf{v})} \tag{3.26}$$

with

$$\boxed{D_{vac,3D}^{2level}(\mathbf{r},\mathbf{v}) = \hbar^2 k_L^2 \frac{\Gamma}{4} \frac{s_{tot}(\mathbf{r},\mathbf{v})}{1+s_{tot}(\mathbf{r},\mathbf{v})}} \tag{3.27}$$

$$\boxed{D_{las,3D}^{2level}(\mathbf{r},\mathbf{v}) = \hbar^2 k_L^2 \frac{\Gamma}{4} \frac{s_{tot}(\mathbf{r},\mathbf{v})}{(1+s_{tot}(\mathbf{r},\mathbf{v}))^3} \times \left\{1 + \frac{12\delta^2-\Gamma^2}{4\delta^2+\Gamma^2} s_{tot}(\mathbf{r},\mathbf{v}) + s_{tot}^2(\mathbf{r},\mathbf{v})\right\}} \tag{3.28}$$

being the 3D counterparts of respectively D_{vac} (Eq. 3.24) and D_{las} (Eq. 3.25) that we obtain by substituting the saturation parameter s with the total saturation parameter s_{tot}, which is a sum of the saturation parameters of the six laser beams, i.e.

$$s_{tot}(\mathbf{r},\mathbf{v}) = \sum_{\alpha=\mathsf{x},\mathsf{y},\mathsf{z}} [s_\alpha^+(\mathbf{r},\mathbf{v}) + s_\alpha^-(\mathbf{r},\mathbf{v})] \tag{3.29}$$

where

$$s_\alpha^\pm(\mathbf{r},\mathbf{v}) = \frac{I_\alpha^\pm(\mathbf{r},\mathbf{v})/I_{sat}}{1+4\frac{(\delta \mp k_L v_\alpha \mp \mu B' r'_\alpha)^2}{\Gamma^2}} \tag{3.30}$$

is the saturation parameter for the beam traveling in the positive/negative ($\pm$) direction of $\hat{\boldsymbol{\alpha}} = \hat{\mathbf{x}}, \hat{\mathbf{y}}, \hat{\mathbf{z}}$. It is obtained from the expression for the saturation parameter s given by Eq. 3.9, by taking into account the Doppler effect and the (*ad hoc*) Zeeman effect, and also the fact that the intensities of the beams may be different.

Let us now consider showing that Eq. 1.5 can be obtained with the diffusion coefficient D_{3D}^{2level}. First, in the 3D situation, an expression equivalent to Eq. 1.4 can be written, which is in terms of the 3D momentum diffusion coefficient D_{3D}^{2level} and the 3D friction coefficient γ_{3D} [55]:

$$k_B T_{lim} = \frac{D_{3D}^{2level}}{3|\gamma_{3D}|} \tag{3.31}$$

Next, we note that D_{3D}^{2level} in Eq. 3.31 involves the total saturation parameter $s_{tot} = 6s$, where s is given by Eq. 3.9. This is because γ_{3D} is derived considering the low-velocity limit and positions close to the trap center (such that the Doppler and Zeeman effects are neglected), and also because the intensities of the beams are equal to each other (s_0) in the expression for γ_{3D}. Then, by imposing the low-intensity limit condition $s_0 \ll 1$ (which holds for the trapping force), we may simplify Eqs. 3.27, 3.28 to give $D_{vac,3D}^{2level} = \frac{3\Gamma}{2}\hbar^2 k_L^2 s = D_{las,3D}^{2level}$.

From Eq. 3.26 we thus have $D_{3D}^{2level} = D_{vac,3D}^{2level} + D_{las,3D}^{2level} = 3\Gamma\hbar^2 k_L^2 s$. Observing Eq. 3.13 for γ_{3D}, we note that the term $6\Gamma s_0$ in the denominator is small compared to the sum of the remaining terms, such that we may write $\gamma_{3D} = s\frac{-8\hbar k_L^2 \delta\Gamma}{\Gamma^2+4\delta^2}$. Hence, we finally obtain

$$k_B T_{lim} = \frac{\hbar}{8}\frac{\Gamma^2 + 4\delta^2}{|\delta|} \qquad \text{(1.5 revisited)}$$

For $\delta = -\Gamma/2$ we obtain the minimum temperature, being the Doppler temperature T_D, expressed by Eq. 1.6.

To end this subsection, we discuss the obtained 3D momentum diffusion coefficient (Eqs. 3.26-3.28). In its modeling, we took into account the many-atom effect of the attenuation, although neglected the rescattering, known to cause change to the diffusion with increased number of atoms (refer to the discussion provided at the end of section 1.2.2). In principle, the modifications due to both the attenuation and rescattering should be considered, as we bear in mind that balanced MOT instabilities exist in a regime governed by many-atom physics. On one hand, one may argue that precise modeling of the diffusion is not required in our case, considering that, in the past, simulations of balanced MOT instabilities were achieved without taking into account the diffusion (refer to section 1.2.3.3). On the other hand, a detailed approach may nevertheless be required, considering that noise is known to play an important role in instability dynamics, as mentioned at the beginning of this subsection. We note that we will be investigating the impact of diffusion on the simulated instabilities in section 3.5.

3.1.3 Intensity attenuation

The goal of this subsection is to provide expressions for the MOT beam intensities with attenuation incorporated, for our 2-level atom model in 3D. As we recall from the second section of Chapter 1, intensity attenuation produces the compressional effect known as the shadow effect. The reason we want to add the attenuation into our instability simulations is because balanced MOT instabilities are known to require its inclusion to be explained (refer to section 1.2.3.3). The past quasi-1D simulations of such instabilities [40] made it specifically clear that they appear in the competition between the trapping force and the rescattering force, with intensity attenuation intricately involved. The inclusion of the attenuation is fully justified by our previous experimental result in Fig. 2.12 showing that just below the threshold the MOT is in a regime of strong attenuation. We proceed by providing the expressions for the MOT beam intensities and then finally discuss this result within the context of balanced MOT instability simulations.

Let us consider using plane MOT beams, in that way staying consistent with the treatment in the preceding subsections, where plane beams also were considered. We concentrate on the beam traveling in the positive direction of the z-axis, with the intensity I_z^+. The intensity loss that this beam will experience

as it travels through the cloud will depend on the scattering cross-section σ_z^+ of the atoms (see Eq. 3.17) and their density distribution ρ as follows:

$$\frac{d}{dz} I_z^+(\mathbf{r}, \mathbf{v}) = -I_z^+(\mathbf{r}, \mathbf{v}) \sigma_z^+(\mathbf{r}, \mathbf{v}) \rho(\mathbf{r}) \tag{3.32}$$

The general solution to the above equation is given by

$$I_z^+(\mathbf{r}, \mathbf{v}) = I_\infty e^{-\int_{-\infty}^{z} dz' \, \sigma_z^+\left(x,y,z',\mathbf{v}(x,y,z')\right)\rho(x,y,z')} \tag{3.33}$$

where I_∞ refers to the unattenuated beam intensity, and $\mathbf{v}(x, y, z')$ refers to the velocity $\mathbf{v}$ evaluated at (x, y, z'). For the remaining five MOT beams we can obtain analogous expressions to Eq. 3.33, where we note that for the beam traveling in the direction of $-\hat{\mathbf{x}}/-\hat{\mathbf{y}}/-\hat{\mathbf{z}}$, the limit of the integral is from $x/y/z$ to $+\infty$. Using obvious notations, we finally write down the full set of equations for the MOT beam intensities in our 2-level atom model:

$$\begin{aligned}
&I_x^+(\mathbf{r}, \mathbf{v}) = I_\infty e^{-\int_{-\infty}^{x} dx' \, \sigma_x^+\left(x',y,z,\mathbf{v}(x',y,z)\right)\rho(x',y,z)} \quad , \quad I_x^-(\mathbf{r}, \mathbf{v}) = I_\infty e^{-\int_{x}^{+\infty} dx' \, \sigma_x^-\left(x',y,z,\mathbf{v}(x',y,z)\right)\rho(x',y,z)} \\
&I_y^+(\mathbf{r}, \mathbf{v}) = I_\infty e^{-\int_{-\infty}^{y} dy' \, \sigma_y^+\left(x,y',z,\mathbf{v}(x,y',z)\right)\rho(x,y',z)} \quad , \quad I_y^-(\mathbf{r}, \mathbf{v}) = I_\infty e^{-\int_{y}^{+\infty} dy' \, \sigma_y^-\left(x,y',z,\mathbf{v}(x,y',z)\right)\rho(x,y',z)} \\
&I_z^+(\mathbf{r}, \mathbf{v}) = I_\infty e^{-\int_{-\infty}^{z} dz' \, \sigma_z^+\left(x,y,z',\mathbf{v}(x,y,z')\right)\rho(x,y,z')} \quad , \quad I_z^-(\mathbf{r}, \mathbf{v}) = I_\infty e^{-\int_{z}^{+\infty} dz' \, \sigma_z^-\left(x,y,z',\mathbf{v}(x,y,z')\right)\rho(x,y,z')}
\end{aligned} \tag{3.34}$$

To end this subsection, we discuss the obtained MOT intensities. Let us consider the fact that the expressions we are dealing with are very general, each found by solving an equation like Eq. 3.32. We require such general expressions in our balanced MOT instability simulations, precisely due to our previous experimental result in Fig. 2.12 showing that just below the threshold the MOT is in a regime of strong attenuation. Because the expressions are very general, the following difficulty is encountered. Each intensity requires to have the knowledge of I_{tot}, due to scattering cross-section entering into the exponential. As we know from previously (section 3.1.1), I_{tot} is included as we wish to take into account the effect of beam cross-saturation. We note that in section 3.3, we will explain the procedure used to numerically determine I_{tot}, such that we can implement beam cross-saturation. We note as well that we will be investigating the impact of attenuation on the simulated instabilities in section 3.5. Lastly, we would like to comment that plane waves of course do not exist in the MOT and, strictly speaking, our entire treatment of the forces and effects requires usage of Gaussian waves. We omit using Gaussian waves for simplicity reasons.

3.1.4 Rescattering force

The goal of this subsection is to provide an expression for the rescattering force for our 2-level atom model in 3D. As we recall from the second section of Chapter 1, the rescattering is responsible for the atoms repelling each other in the

MOT. The reason we want to add the rescattering force into our instability simulations is because this force, like the attenuation, is needed to be included to explain balanced MOT instabilities (refer to section 1.2.3.3). In this subsection, we start with the basic expression for the rescattering force, in the situation with two atoms exposed to one laser beam, as provided in section 1.2.2, and cover advanced features of this force. We then finally provide an expression for the rescattering force for our 2-level atom model in 3D, by taking the six MOT beams into account, and discuss this result within the context of balanced MOT instability simulations.

Advanced features of the rescattering force

We have in section 1.2.2 introduced to the rescattering and provided a basic expression for the force describing this effect, in the situation with two atoms exposed to one laser beam:

$$\mathbf{F}_{rsc}(\mathbf{r}_2) = \frac{I_L \sigma_L \sigma_R}{4\pi c} \frac{\hat{\mathbf{r}}_{1,2}}{|\mathbf{r}_{1,2}|^2} \qquad \text{(1.18 revisited)}$$

where $\mathbf{r}_{1,2} \equiv \mathbf{r}_2 - \mathbf{r}_1$ defines the vector pointing from atom 1 that scatters light, at $\mathbf{r}_1$, to atom 2 that rescatters the scattered light, at $\mathbf{r}_2$. $\hat{\mathbf{r}}_{1,2} = \frac{\mathbf{r}_{1,2}}{|\mathbf{r}_{1,2}|}$ is the unit vector corresponding to $\mathbf{r}_{1,2}$. σ_L is the laser scattering cross-section of atom 1, given by Eq. 1.13, and σ_R is the rescattering cross-section of atom 2, whose expression we consider writing down next.

As already mentioned in section 1.2.2, σ_R is found by evaluating an overlap integral between (i) the emission spectrum that atom 1 produces when illuminated by the laser light (of intensity I_L) and (ii) the absorption spectrum of atom 2 when illuminated by the laser light and also in presence of the weak perturbing field (of intensity I_R). Denoting the emission spectrum of atom 1 by S and the absorption spectrum of atom 2 by σ_A, we have

$$\sigma_R(\mathbf{r}_1, \mathbf{r}_2, \mathbf{v}_1, \mathbf{v}_2) = \int d\omega \; S(\omega, \mathbf{r}_1, \mathbf{v}_1) \sigma_A(\omega, \mathbf{r}_2, \mathbf{v}_2) \qquad (3.35)$$

where ω is the spectrum frequency, and the limit of the integral is from minus infinity to plus infinity.

S and σ_A can be found using different approaches. In an approach by B. R. Mollow in Refs. [56, 57], one makes use of OBEs describing the dynamics of a 2-level atom interacting with classical laser light in obtaining expressions for the respective spectra. Such approach, where the light is treated classically, is known as the 'bare atom' approach (as in our treatment for the trapping force). Another approach is the so-called 'dressed atom' approach. Here a light field that is instead quantized interacts with a 2-level atom. The dressed atom approach has been adopted by C. Tannoudji in Ref. [52], and the expressions for the properly normalized S and σ_A using this approach can be found in Ref. [58]. The expressions in Ref. [58] are, however, not valid in the limits of low

detuning (absolute value) and low intensity, being the limits that interest us. On the other hand, in Refs. [56, 57], the expressions are more general and, whilst at the same time more complicated, these are the ones we are considering in the work surrounding this Thesis.

In Appendix B, we find with help of Refs. [56, 57] the properly normalized emission and absorption spectra to be

$$S(\omega) = \left[\frac{\Gamma^2 + 4\delta^2}{\Gamma^2 + 4\delta^2 + 2\Omega^2}\right] Dirac(\omega - \delta) + \frac{\Gamma\Omega^2}{2\pi}\left(\frac{(\omega-\delta)^2 + \frac{1}{2}\Omega^2 + \Gamma^2}{\Gamma^2\left[\frac{1}{2}\Omega^2 + \delta^2 + \frac{1}{4}\Gamma^2 - 2(\omega-\delta)^2\right]^2 + (\omega-\delta)^2\left[\Omega^2 + \delta^2 + \frac{5}{4}\Gamma^2 - (\omega-\delta)^2\right]^2}\right) \tag{3.36}$$

$$\sigma_A(\omega) = \frac{\sigma_0\Gamma}{4} \times \left\{\frac{\Gamma^2 + 4\delta^2}{\Gamma^2 + 4\delta^2 + 2\Omega^2}\right\} \times \left\{\frac{(-i\omega + i\delta + \Gamma)\left(-i\omega + i2\delta + \frac{\Gamma}{2}\right) + \frac{1}{2}i\Omega^2(\omega-\delta)/\left(i\delta + \frac{\Gamma}{2}\right)}{(-i\omega + i\delta + \Gamma)\left(-i\omega + i2\delta + \frac{\Gamma}{2}\right)\left(-i\omega + \frac{\Gamma}{2}\right) + \Omega^2\left(-i\omega + i\delta + \frac{\Gamma}{2}\right)} + c.c.\right\} \tag{3.37}$$

where, since Refs. [56, 57] are considering the plane laser wave case (as we are interested in), the Rabi frequency $\Omega = \Gamma\sqrt{\frac{I_L}{2I_{sat}}}$, and we note that "$Dirac$" denotes the Dirac delta function - we use this notation so not to confuse with the notation used for the detuning, i.e. δ.

Let us comment now on features of $S(\omega)$ and $\sigma_A(\omega)$.

(a) In Eq. 3.36, we see that $S(\omega)$ is written as a sum of two contributions. The first one, which involves the Dirac delta function, gives the spectrum of light centered at a single frequency specified by the laser detuning δ and is referred to as the elastically scattered light spectrum. The second contribution possesses components of light at many different frequencies and is referred to as the inelastically scattered light spectrum. As explained by B. R. Mollow in Ref. [56], the inelastic components exist as the laser field alters the ground and excited states of the 2-level atom. We note that such view is supported in the 'bare atom' picture that the Ref. [56] adopts, though in the 'dressed atom' picture it is the dressed states, i.e. the combined states of the atom and the light, that give rise to the inelastic spectrum part.

As shown in Fig. 3.1, in the low-intensity limit, where $s_0 \ll 1$, the elastic part of the spectrum dominates over the inelastic part. In the high-intensity limit, where $s_0 \gg 1$, the situation is, however, reversed and the inelastic part dominates over the elastic part. At the same time, making $|\delta|/\Gamma$ larger will result in the elastic part remaining dominant for increased values of intensity. The ratio between the inelastic and elastic parts is equal to s. The mean of the elastic and inelastic parts is seen to be equal to 0.5, implying that the emission

spectrum's area is properly normalized to 1 (refer to Appendix B.1). From Fig. 3.1 we gain information regarding the proportion of light that is either elastically or inelastically scattered, but to know how much of each component gets rescattered, the absorption spectrum $\sigma_A(\omega)$ must be taken into account. After discussing features of $\sigma_A(\omega)$, we will turn to understanding the contributions of the elastic and inelastic parts to σ_R and see how the dynamics of the clouds are affected as the different components get rescattered.

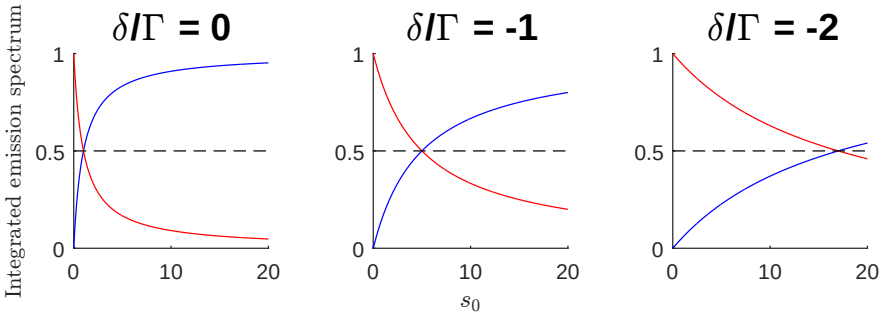

Figure 3.1: The integrated elastic (red curve) and inelastic (blue curve) parts of the emission spectrum given by Eq. 3.36 versus the on-resonance saturation parameter s_0 for different trapping detunings δ. The crossing point of the two curves corresponds to the saturation parameter s = 1. The dashed line in the middle is the mean of the two curves, equal to 0.5.

In Fig. 3.2(a), we plot the inelastic part of the emission spectrum for different δ/Γ and s_0 values. Concentrating first on the cases, where $\delta/\Gamma = 0$, we observe that as s_0 is increased, two sideband-peaks appear around the central peak. The three peaks, one in the middle surrounded by the two sideband-peaks, is famously known as the Mollow triplet. For $\delta/\Gamma = -5$ and $\delta/\Gamma = -10$, where $s_0 = 0.1$, the central peak is, however, negligibly small. For $\delta/\Gamma = -5$ and $\delta/\Gamma = -10$, where $s_0 = 10, 100$, we observe that the central feature gets shifted by the value given by δ/Γ, and, at the same time, this central feature becomes suppressed compared to the sideband features as $|\delta|/\Gamma$ gets larger. In the high-intensity limit, the central feature is peaked at δ/Γ, while the sidebands are peaked at $(\delta \pm \Omega)/\Gamma$.

(b) In Fig. 3.2(b), we plot the absorption spectrum $\sigma_A(\omega)$ of Eq. 3.37 for the same δ/Γ and s_0 values as in Fig. 3.2(a). Concentrating first again on the cases, where $\delta/\Gamma = 0$, we observe that as s_0 is increased two valleys appear with the split between them at $\omega = 0$. In the region of the two valleys, the absorption spectrum takes on negative values, representing amplification of the scattered light field, i.e. stimulated emission. Increasing s_0 results in the widening of the range of frequencies over which the stimulated emission occurs. From the $\delta/\Gamma = -5$ and $\delta/\Gamma = -10$ cases, where $s_0 = 10, 100$, we observe that further away from the resonance the dip below zero becomes insignificantly small compared to the peaked feature, such that the stimulated emission will be negligible. In the limit of high detuning (absolute value), only the peaked feature remains

and it is centered at $\omega = 0$.

Now, observing both Fig. 3.2(a) and Fig. 3.2(b), where we concentrate on the non-zero detuning cases $\delta/\Gamma = -5$ and $\delta/\Gamma = -10$, we see that the peaked feature in the absorption spectrum will overlap with one of the Mollow sidebands. The inelastically scattered light spectrum will therefore produce a significant contribution to σ_R. On the other hand, since the elastically scattered light spectrum is peaked around δ/Γ, the overlap with the absorption spectrum becomes smaller as $|\delta|/\Gamma$ gets larger. Nevertheless, since Fig. 3.1 implies that the elastic part will remain quite sizable compared to the inelastic part as $|\delta|/\Gamma$ gets larger, the elastic part can still produce a contribution to σ_R at larger $|\delta|/\Gamma$ values. We will come back to the discussion surrounding the contributions of the elastic and inelastic parts to σ_R after the discussion below on features of σ_R.

In Fig. 3.3(a), we plot the coefficient σ_R/σ_0 versus $-\delta/\Gamma$ for different s_0 values. Here we observe that as s_0 is increased, σ_R/σ_0 starts to flatten and its values near the resonance decrease and eventually become negative. The fact that the rescattering cross-section can become negative is due to the presence of gain (i.e. stimulated emission) as discussed for Fig. 3.2(b). In the gain region, the physical picture associated with scattering at atom 2 breaks down, and so the negative rescattering cross-section is meaningless. Next, in Fig. 3.3(b), we plot the coefficient σ_R/σ_0 versus s_0 for different δ/Γ values. Similarly to the case of Fig. 3.3(a), we observe that as the detuning becomes more negative, σ_R/σ_0 values get smaller in the low-intensity limit. We have also plotted σ_L/σ_0 in Fig. 3.3(b). At zero intensity we have $\sigma_R = \sigma_L$, as required by the normalization condition (refer to Appendix B.2). We observe that σ_R/σ_0 can actually be smaller than σ_L/σ_0 (see the cases with $\delta = -0.5\,\Gamma$ and $\delta = -1\,\Gamma$), such that the ratio $\sigma_R/\sigma_L < 1$ can be obtained, and thus, according to the Wieman model, there would be no equilibrium solution for the cloud (refer to Eq. 1.19).

In Fig. 3.4, we compare the parts of σ_R that result from the contribution of the elastically scattered light spectrum and the inelastically scattered light spectrum; the respective parts are denoted by $\sigma_{R,el}$ and $\sigma_{R,inel}$, and they satisfy $\sigma_R = \sigma_{R,el} + \sigma_{R,inel}$. We refer to $\sigma_{R,el}$ and $\sigma_{R,inel}$ as the elastic and inelastic part of σ_R, respectively. As can be seen from Fig. 3.4(a), for $s_0 = 1$, σ_{el}/σ_0 dominates over σ_{inel}/σ_0 over the range of detunings, but as s_0 is increased, the roles are reversed and σ_{inel}/σ_0 starts to dominate over σ_{el}/σ_0. Similar conclusions can be reached by observing Fig. 3.4(b). From this information we thus see that the elastic scattering contributes more to the rescattering force in the low-intensity limit, whereas in the high-intensity limit it is the inelastic scattering that contributes more.

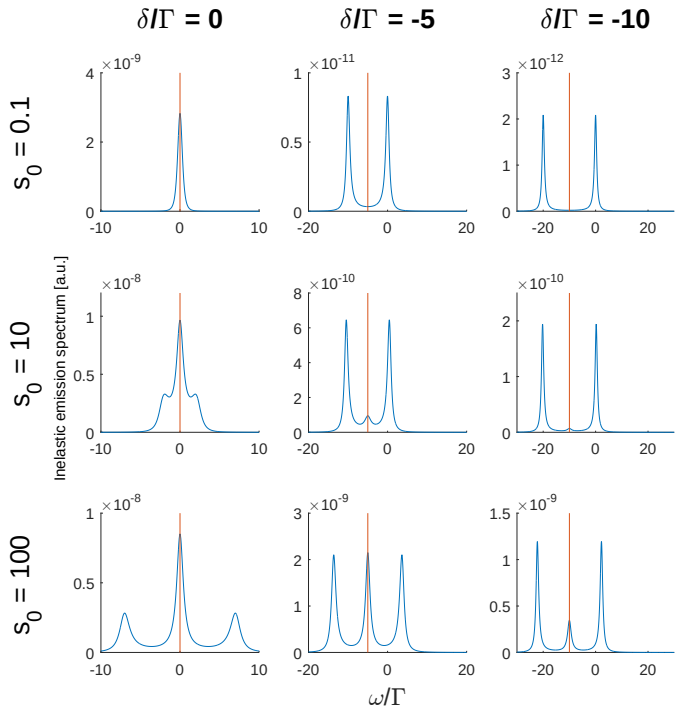

(a)

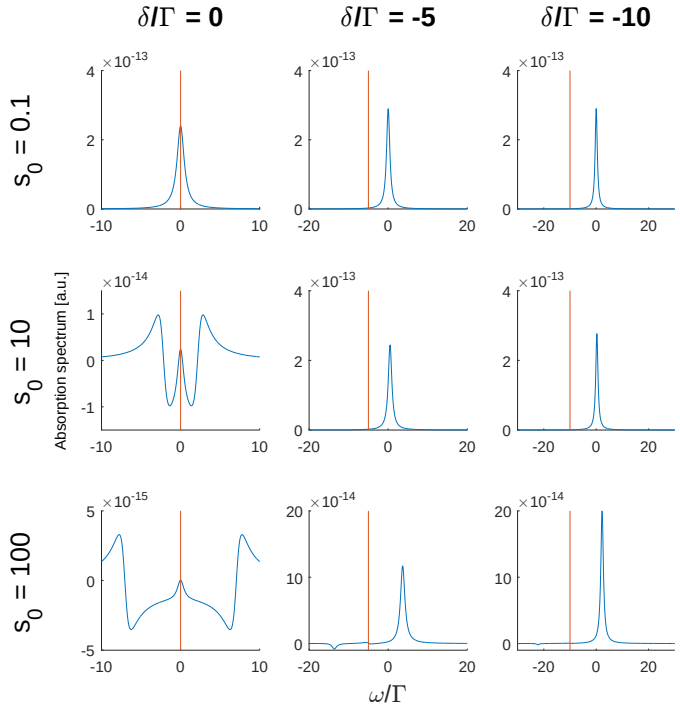

(b)

Figure 3.2: Plots displaying (a) the inelastic emission spectrum and (b) the absorption spectrum, for different trapping detunings δ (columns) and on-resonance saturation parameters s_0 (rows). The respective spectrum curves are in blue, and the vertical red lines are plotted at the values given by δ/Γ.

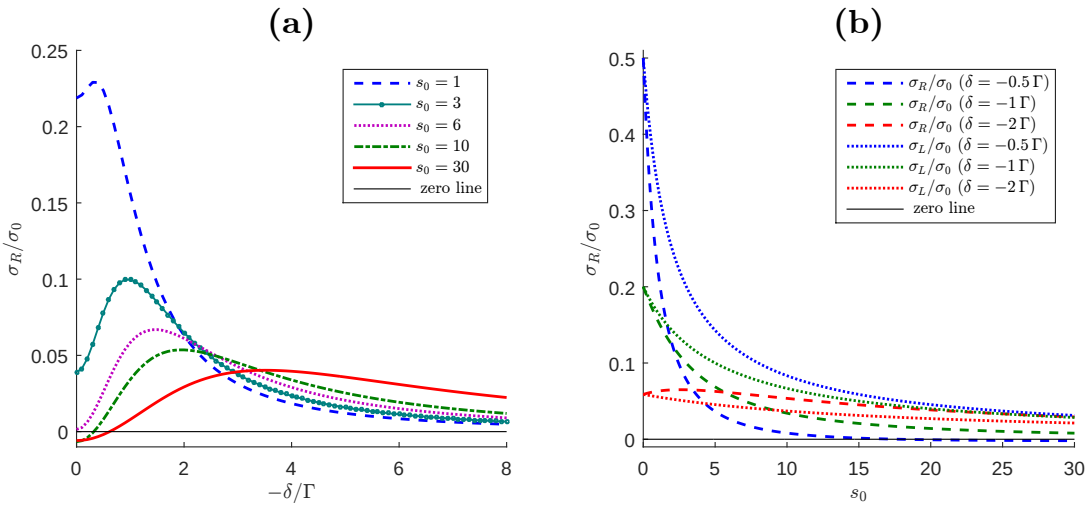

Figure 3.3: The rescattering cross-section coefficient σ_R/σ_0 plotted versus (a) $-\delta/\Gamma$ and (b) s_0. In (b), σ_L is given by Eq. 1.13.

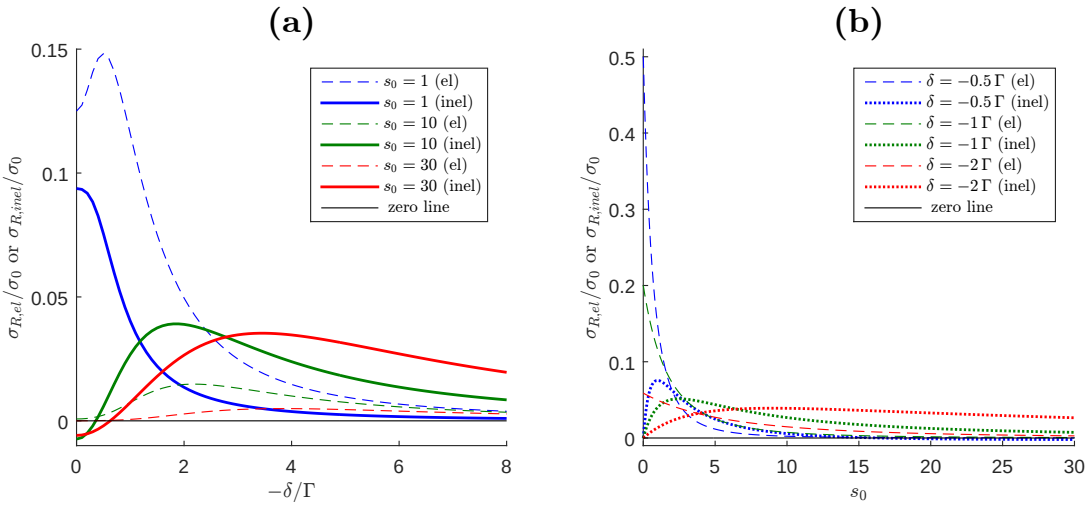

Figure 3.4: The elastic (el) and inelastic (inel) parts of the rescattering cross-section coefficient σ_R/σ_0, i.e. respectively $\sigma_{R,el}/\sigma_0$ and $\sigma_{R,inel}/\sigma_0$, plotted versus (a) $-\delta/\Gamma$ and (b) s_0.

The 3D rescattering force (2-level atom model)

We would now like to perform a generalization of the rescattering force with the six MOT beams taken into account. To do that, we assume, similarly to the trapping force case as well as the diffusion case, that each beam can be treated independently, and thus that we may add together the corresponding rescattering forces, each taking the form of Eq. 1.18. We further assume that the six rescattering forces have a common rescattering cross-section, as we proceed ignoring in it the Doppler and Zeeman effects (these effects must otherwise enter into the δ's in Eqs. 3.36, 3.37) and letting the Rabi frequency Ω involve the total beam intensity I_{tot}. We note that neither of the choices, i.e. using a common rescattering cross-section or six different ones, is fully justified. This is because, as we know from earlier, the atom is coupled to the total light field of several beams, implying that the OBEs describing the behavior of the atom are more complex than in the one beam case (where general analytical solutions do not exist), and so we may choose to resort to using approximations we deem reasonable. We will discuss the assumptions neglecting the Doppler and Zeeman effects in the rescattering cross-section after writing down this section's main result.

With the above assumptions taken into account, we finally write down our 2-level atom model's 3D rescattering force on the atom at the position $\mathbf{r}_j$ with the velocity $\mathbf{v}_j$, due to the scattering atoms at the positions $\mathbf{r}_i$ with the velocities $\mathbf{v}_i$:

$$\boxed{\mathbf{F}_{rsc}^{2level}(\mathbf{r}_j,\mathbf{v}_j) = \frac{1}{4\pi c}\times\left\{\sum_{i\neq j}\sum_{\alpha=\mathrm{x,y,z}}\left[I_\alpha^+(\mathbf{r}_i,\mathbf{v}_i)\sigma_\alpha^+(\mathbf{r}_i,\mathbf{v}_i)+I_\alpha^-(\mathbf{r}_i,\mathbf{v}_i)\sigma_\alpha^-(\mathbf{r}_i,\mathbf{v}_i)\right]\sigma_R(\mathbf{r}_i,\mathbf{r}_j\mathbf{v}_i,\mathbf{v}_j)\frac{\hat{\mathbf{r}}_{i,j}}{|\mathbf{r}_{i,j}|^2}\right\}} \tag{3.38}$$

Here $\sigma_\alpha^\pm$ is the scattering cross-section given by Eq. 3.17, and $I_\alpha^\pm$ is the laser intensity given by Eq. 3.34 (the Doppler and Zeeman effects are included in these quantities). σ_R depends on the positions and velocities of the scattering and rescattering atoms via the local laser intensities entering into the emitted and absorbed light spectra. We have defined the vector $\mathbf{r}_{i,j}\equiv\mathbf{r}_j-\mathbf{r}_i$ that points from the scattering atom at $\mathbf{r}_i$ to the rescattering atom at $\mathbf{r}_j$; the corresponding unit vector is $\hat{\mathbf{r}}_{i,j}$, found from

$$\boxed{\hat{\mathbf{r}}_{i,j}=\frac{\mathbf{r}_{i,j}}{|\mathbf{r}_{i,j}|}\quad,\quad\mathbf{r}_{i,j}=(\mathbf{x}_j-\mathbf{x}_i)+(\mathbf{y}_j-\mathbf{y}_i)+(\mathbf{z}_j-\mathbf{z}_i)} \tag{3.39}$$

where we have used $\mathbf{r}_i=\mathbf{x}_i+\mathbf{y}_i+\mathbf{z}_i$ and $\mathbf{r}_j=\mathbf{x}_j+\mathbf{y}_j+\mathbf{z}_j$. With help of Eq. 3.39 we can obtain the x-, y- and z-components of the rescattering force.

To end this subsection, we discuss the obtained 3D rescattering force (Eq. 3.38). Let us consider first the fact that special care was taken regarding the treatment of σ_R (Eq. 3.35 and Eqs. 3.36, 3.37), despite the generalization of the rescattering force involving assumptions that were primarily intuitive (commented on shortly). In particular, we wrote σ_R as an overlap integral between the emitted and absorbed light spectra and made it dependent on both the scat-

tering atom and rescattering atom positions and velocities via the local laser intensities. Such care was first of all done so to conform with the considerations made in the previous balanced MOT simulations [40], where a similar kind of treatment of σ_R was done, with the position dependence of σ_R reported to be necessary in explaining the appearance of the instabilities. Secondly, we improve the detail of the modeling of the elastic and inelastic scattering, and that can benefit our investigation on the impact of each of these components on the instability phenomenon, to be done in section 3.5. Of course, we remain aware of the fact that σ_R can become negative, which would result in an attractive rescattering force, which is an unwanted artifact. In our simulations, as we employ the $F = 0 \rightarrow F' = 1$ model described in the next section, there are three common rescattering cross-sections, and we can at most have $\frac{6}{3}s_0 \sim 6$ in these common rescattering cross-sections, and so according to Fig. 3.3(a), the rescattering force will be repulsive. Let us consider next the fact that we neglected the Doppler and Zeeman effects in the rescattering cross-section calculation. The Doppler effect can be neglected using the argument that $|\delta| \gg k_L\sqrt{\frac{3k_BT_{lim}}{M}}$ holds[2] for detunings satisfying $|\delta| \geq 1\,\Gamma$, i.e. the detunings used in our simulations. In the stable regime that we simulate, this condition remains true, although we point out that in the unstable regime, the RMS velocity v_{RMS} is larger than $\sqrt{\frac{3k_BT_{lim}}{M}}$, and the Doppler effect can actually become important (refer to section 3.5.2). Regarding the Zeeman effect, it can be neglected in the case of small magnetic field gradients, i.e. $\nabla B \lesssim 5$ G/cm. Nevertheless, in our simulations larger ∇B values are also used, and we thus have considered incorporating the Zeeman effect in the rescattering cross-section calculation - such improvement is done in our $F = 0 \rightarrow F' = 1$ model. Lastly, we bring into attention that higher-order rescattering events exist as well, and they can produce additional effects among the atoms. As implied by our previous experimental result in Fig. 2.12, we are in principle required taking into account third-order scattering (i.e. re-rescattering) in our simulations. Judging from the quite involved treatment of second-order scattering (i.e. rescattering) we just have performed, we may deem the inclusion of the higher-order rescattering events to be too complicated, but to provide an argument why neglecting them can actually be justified, we may consider the experimental findings of Ref. [24] on the cloud radius R_n scaling with the atom number N. As we have already seen in section 1.2.2, Ref. [24] observed the scaling law $R_n \propto N^{0.39}$ in the extended (and relevant to us) atom number range of $2 \cdot 10^7 \lesssim N \lesssim 10^{11}$. This observation is not far-off from the Wieman model's prediction, i.e. $R_n \propto N^{1/3}$ (Eq. 1.20), and so the Wieman model can be judged to be fairly precise in capturing the physics involved in large MOTs. As this model includes only second-order scattering events, some weight is thus provided to why we may stick to considering only such events in the study of our instabilities.

[2]The quantity $\sqrt{\frac{3k_BT_{lim}}{M}}$ is the RMS velocity of the Rb-87 atom of mass M, as found according to the equipartition theorem; T_{lim} is given by Eq. 1.5.

3.1.5 Summary table of the forces and effects

In this final subsection, we provide a summary table, Tab. 3.1, of the obtained expressions of our 2-level atom model's 3D forces and effects. We would like to make the reader aware that, although not demonstrated in this Thesis, the model can successfully be used in simulating MOT instabilities in 3D.

We recapitulate the relevant equations that lead to the obtention of the forces and effects in Tab. 3.1. The relevant equations from section 3.1.1, "Trapping force", are Eqs. 3.15, 3.16, 3.17, 3.18. From section 3.1.2, "Diffusion", they are Eqs. 3.26, 3.27, 3.28, 3.29, 3.30. From section 3.1.3, "Intensity attenuation", it is Eq. 3.34. From section 3.1.4, "Rescattering force", they are Eqs. 3.35, 3.36, 3.37, 3.38, 3.39.

We have:

$$I_{tot}(\mathbf{r},\mathbf{v}) = \sum_{\alpha=\mathrm{x,y,z}} [I_\alpha^+(\mathbf{r},\mathbf{v}) + I_\alpha^-(\mathbf{r},\mathbf{v})] \qquad \text{(3.18 revisited)}$$

$$s_{tot}(\mathbf{r},\mathbf{v}) = \sum_{\alpha=\mathrm{x,y,z}} [s_\alpha^+(\mathbf{r},\mathbf{v}) + s_\alpha^-(\mathbf{r},\mathbf{v})] \qquad \text{(3.29 revisited)}$$

$$s_\alpha^\pm(\mathbf{r},\mathbf{v}) = \frac{I_\alpha^\pm(\mathbf{r},\mathbf{v})/I_{sat}}{1 + 4\frac{(\delta \mp k_L v_\alpha \mp \mu B' r'_\alpha)^2}{\Gamma^2}} \qquad \text{(3.30 revisited)}$$

$$\sigma_\alpha^\pm(\mathbf{r},\mathbf{v}) = \frac{\sigma_0}{1 + \frac{I_{tot}(\mathbf{r},\mathbf{v})}{I_{sat}} + 4\frac{(\delta \mp k_L v_\alpha \mp \mu B' r'_\alpha)^2}{\Gamma^2}} \qquad \text{(3.17 revisited)}$$

$$\sigma_R(\mathbf{r}_i,\mathbf{r}_j,\mathbf{v}_i,\mathbf{v}_j) = \int d\omega\; S(\omega,\mathbf{r}_i,\mathbf{v}_i)\sigma_A(\omega,\mathbf{r}_j,\mathbf{v}_j) \qquad \text{(3.35 revisited)}$$

$$\hat{\mathbf{r}}_{i,j} = \frac{\mathbf{r}_{i,j}}{|\mathbf{r}_{i,j}|} \quad , \quad \mathbf{r}_{i,j} = (\mathbf{x}_j - \mathbf{x}_i) + (\mathbf{y}_j - \mathbf{y}_i) + (\mathbf{z}_j - \mathbf{z}_i) \qquad \text{(3.39 revisited)}$$

$\mathbf{r} = (x, y, z)$ and $\mathbf{v} = (v_\mathrm{x}, v_\mathrm{y}, v_\mathrm{z})$ are respectively the position and velocity of the atom. $\mathbf{r}_i$ and $\mathbf{v}_i$ are used to denote respectively the position and velocity of the atom that scatters light, while $\mathbf{r}_j$ and $\mathbf{v}_j$ are used to denote respectively the position and velocity of the atom that rescatters the scattered light.

$\mathbf{r}' = (r'_\mathrm{x}, r'_\mathrm{y}, r'_\mathrm{z}) = (\frac{x}{2}, \frac{y}{2}, z)$ is the atom position taking into account the spatial asymmetry of the magnetic field.

In Eq. 3.35, $S(\omega,\mathbf{r}_i,\mathbf{v}_i)$ and $\sigma_A(\omega,\mathbf{r}_j,\mathbf{v}_j)$ are given by Eqs. 3.36 and 3.37, respectively, with the substitution $\Omega \to \Omega_{tot}$, where Ω_{tot} is the Rabi frequency involving the sum of the intensities of the six MOT beams, i.e.

$$\Omega_{tot}(\mathbf{r},\mathbf{v}) = \Gamma\sqrt{\frac{I_{tot}(\mathbf{r},\mathbf{v})}{2I_{sat}}} \qquad (3.40)$$

Trapping force	$\mathbf{F}_{tr}^{2level}(\mathbf{r},\mathbf{v}) = F_{tr,\mathsf{x}}^{2level}(\mathbf{r},\mathbf{v})\hat{\mathbf{x}} + F_{tr,\mathsf{y}}^{2level}(\mathbf{r},\mathbf{v})\hat{\mathbf{y}} + F_{tr,\mathsf{z}}^{2level}(\mathbf{r},\mathbf{v})\hat{\mathbf{z}}$ $F_{tr,\alpha}^{2level}(\mathbf{r},\mathbf{v}) = \frac{1}{c}\left(I_{\alpha}^{+}(\mathbf{r},\mathbf{v})\sigma_{\alpha}^{+}(\mathbf{r},\mathbf{v}) - I_{\alpha}^{-}(\mathbf{r},\mathbf{v})\sigma_{\alpha}^{-}(\mathbf{r},\mathbf{v})\right) \quad , \quad \alpha = \mathsf{x},\mathsf{y},\mathsf{z}$
Rescattering force	$\mathbf{F}_{rsc}^{2level}(\mathbf{r}_j,\mathbf{v}_j) = \frac{1}{4\pi c} \times \left\{ \sum_{i\neq j} \sum_{\alpha=\mathsf{x},\mathsf{y},\mathsf{z}} \left[I_{\alpha}^{+}(\mathbf{r}_i,\mathbf{v}_i)\sigma_{\alpha}^{+}(\mathbf{r}_i,\mathbf{v}_i) + I_{\alpha}^{-}(\mathbf{r}_i,\mathbf{v}_i)\sigma_{\alpha}^{-}(\mathbf{r}_i,\mathbf{v}_i) \right] \sigma_R(\mathbf{r}_i,\mathbf{r}_j\mathbf{v}_i,\mathbf{v}_j) \frac{\hat{\mathbf{r}}_{i,j}}{|\mathbf{r}_{i,j}|^2} \right\}$
Diffusion	$D_{3D}^{2level}(\mathbf{r},\mathbf{v}) = D_{vac,3D}^{2level}(\mathbf{r},\mathbf{v}) + D_{las,3D}^{2level}(\mathbf{r},\mathbf{v})$ $D_{vac,3D}^{2level}(\mathbf{r},\mathbf{v}) = \hbar^2 k_L^2 \frac{\Gamma}{4} \frac{s_{tot}(\mathbf{r},\mathbf{v})}{1+s_{tot}(\mathbf{r},\mathbf{v})}$ $D_{las,3D}^{2level}(\mathbf{r},\mathbf{v}) = \hbar^2 k_L^2 \frac{\Gamma}{4} \frac{s_{tot}(\mathbf{r},\mathbf{v})}{(1+s_{tot}(\mathbf{r},\mathbf{v}))^3} \times \left\{ 1 + \frac{12\delta^2-\Gamma^2}{4\delta^2+\Gamma^2} s_{tot}(\mathbf{r},\mathbf{v}) + s_{tot}^2(\mathbf{r},\mathbf{v}) \right\}$
Intensity attenuation	$I_{\mathsf{x}}^{+/-}(\mathbf{r},\mathbf{v}) = I_{\infty} e^{-\int_{-\infty/x}^{x/+\infty} dx'\, \sigma_{\mathsf{x}}^{+/-}(x',y,z,\mathbf{v}(x',y,z))\rho(x',y,z)}$ $I_{\mathsf{y}}^{+/-}(\mathbf{r},\mathbf{v}) = I_{\infty} e^{-\int_{-\infty/y}^{y/+\infty} dy'\, \sigma_{\mathsf{y}}^{+/-}(x,y',z,\mathbf{v}(x,y',z))\rho(x,y',z)}$ $I_{\mathsf{z}}^{+/-}(\mathbf{r},\mathbf{v}) = I_{\infty} e^{-\int_{-\infty/z}^{z/+\infty} dz'\, \sigma_{\mathsf{z}}^{+/-}(x,y,z',\mathbf{v}(x,y,z'))\rho(x,y,z')}$

Table 3.1: 2-level atom model MOT forces and effects in 3D.

3.2 3D MOT forces and effects ($F = 0 \rightarrow F' = 1$ model)

In this section, we proceed developing a kinetic 3D model based on the hyperfine transition $F = 0 \rightarrow F' = 1$. Expressions for the forces and effects considered last (section 3.1), i.e. the trapping force, diffusion, intensity attenuation and rescattering force, are constructed. As depicted in Fig. 3.5, in the model, each of the three Zeeman transitions $m = 0 \rightarrow m' = -1, 0, +1$ between the atom's hyperfine levels $F = 0$ and $F' = 1$ is for simplicity treated as an independent 2-level system. Results of our previous 2-level atom model are going to be used here. On the other hand, a full $F = 0 \rightarrow F' = 1$ model in 3D would be far too complicated; an exhaustive kinetic model for the transition $F = 0 \rightarrow F' = 1$ has been, to the Author's knowledge, only made in 1D [53]. At the end of this section, we provide a summary table of the obtained expressions of the new model's forces and effects. Note that this new model is the kinetic model we have employed in our simulations.

Before we start, we would like to motivate the development of the $F = 0 \rightarrow F' = 1$ model. Importantly, although the hyperfine transition $F = 0 \rightarrow F' = 1$ is much simpler than compared to what we have in our experiments, i.e. $F = 2 \rightarrow F' = 3$ (Fig. 2.1), we nevertheless are adopting a more realistic approach as opposed to the fictitious approach of the single 2-level atom transition as done last. The transition $F = 0 \rightarrow F' = 1$ has been used in experiments to trap e.g. Cd [60] and Sr [61]. For the actual improvement in the physics between the $F = 0 \rightarrow F' = 1$ model and the 2-level atom model, the atoms are now polarized objects along the magnetic field direction, such that they scatter as well as rescatter light that is linear, right-hand circular or left-hand circular in different proportions depending on where in the trap they are situated.

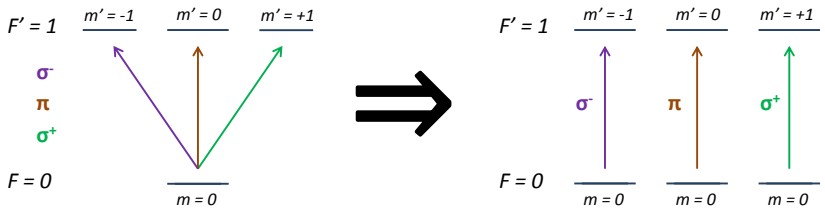

Figure 3.5: Simplification of the Zeeman sub-level structure of the hyperfine transition $F = 0 \rightarrow F' = 1$, as employed in the $F = 0 \rightarrow F' = 1$ model. Each of the three Zeeman transitions $m = 0 \rightarrow m' = -1, 0, +1$ between $F = 0$ and $F' = 1$ is treated as an independent 2-level system (right picture). The Zeeman transition $m = 0 \rightarrow m' = -1$ is induced only by left-hand circular (σ^-) polarized light, $m = 0 \rightarrow m' = +1$ only by right-hand circular (σ^+), and $m = 0 \rightarrow m' = 0$ only by linear (π).

3.2.1 Trapping force

The goal of this subsection is to provide an expression for the trapping force for our $F = 0 \to F' = 1$ model in 3D. We start by obtaining an expression for the radiation pressure force that the $F = 0 \to F' = 1$ atom experiences from one of the MOT beams. Then, we derive expressions for the fractions of MOT beam light that the atom sees respectively as linear (π), right-hand circular (σ^+) and left-hand circular (σ^-) polarized, and, finally, construct from the radiation pressure forces of each beam the model's trapping force. We note that a similar expression for this trapping force can be found in Ref. [60], although without a derivation.

Letting the $F = 0 \to F' = 1$ atom be exposed to the MOT's magnetic field $\mathbf{B}$ given by Eq. 3.14, and choosing the quantization-axis to be along the direction of $\mathbf{B}$, the Zeeman shifts introduced by $\mathbf{B}$ to the three excited levels with $m' = -1, 0, +1$ are, respectively,

$$\mu_{Z,-}(\mathbf{r}) = -\mu B(\mathbf{r}) \quad , \quad \mu_{Z,0} = 0 \quad , \quad \mu_{Z,+}(\mathbf{r}) = +\mu B(\mathbf{r}) \tag{3.41}$$

where $B(\mathbf{r}) = B'\sqrt{z^2 + \frac{1}{4}(x^2 + y^2)}$ is the magnitude of $\mathbf{B} = \mathbf{B}(\mathbf{r})$.

Concentrating for now on one of the MOT beams, say, positive z directed beam, the radiation pressure force that the $F = 0 \to F' = 1$ atom will experience from this beam will be

$$\boldsymbol{\mathcal{F}}_{\mathsf{z}}^{4level,+}(\mathbf{r}, \mathbf{v}) = \boldsymbol{\mathcal{F}}_{\mathsf{z},-}^{+}(\mathbf{r}, \mathbf{v}) + \boldsymbol{\mathcal{F}}_{\mathsf{z},0}^{+}(\mathbf{r}, \mathbf{v}) + \boldsymbol{\mathcal{F}}_{\mathsf{z},+}^{+}(\mathbf{r}, \mathbf{v}) \tag{3.42}$$

with $\boldsymbol{\mathcal{F}}_{\mathsf{z},-}^{+}$, $\boldsymbol{\mathcal{F}}_{\mathsf{z},0}^{+}$ and $\boldsymbol{\mathcal{F}}_{\mathsf{z},+}^{+}$ being the corresponding radiation pressure forces acting on the individual 2-level parts of the $F = 0 \to F' = 1$ atom that are respectively driven by σ^-, π and σ^+ polarized light (Fig. 3.5). Recall that the notation $\boldsymbol{\mathcal{F}}_{rp}$ was used in section 3.1 to denote the radiation pressure force acting on the 2-level atom. Letting $p_{\mathsf{z},-}^{+}$, $p_{\mathsf{z},0}^{+}$ and $p_{\mathsf{z},+}^{+}$ denote the fractions of the beam's light that the $F = 0 \to F' = 1$ atom will see respectively as σ^-, π and σ^+ polarized, we obtain, when observing Eq. 3.9 for $\boldsymbol{\mathcal{F}}_{rp}$ and Eq. 3.17 for σ_α^+,

$$\boldsymbol{\mathcal{F}}_{\mathsf{z},-}^{+}(\mathbf{r}, \mathbf{v}) = \frac{p_{\mathsf{z},-}^{+}(\mathbf{r})\mathcal{I}_{\mathsf{z}}^{+}(\mathbf{r}, \mathbf{v})\sigma_{\mathsf{z},-}^{+}(\mathbf{r}, \mathbf{v})}{c} \tag{3.43a}$$

$$\boldsymbol{\mathcal{F}}_{\mathsf{z},0}^{+}(\mathbf{r}, \mathbf{v}) = \frac{p_{\mathsf{z},0}^{+}(\mathbf{r})\mathcal{I}_{\mathsf{z}}^{+}(\mathbf{r}, \mathbf{v})\sigma_{\mathsf{z},0}^{+}(\mathbf{r}, \mathbf{v})}{c} \tag{3.43b}$$

$$\boldsymbol{\mathcal{F}}_{\mathsf{z},+}^{+}(\mathbf{r}, \mathbf{v}) = \frac{p_{\mathsf{z},+}^{+}(\mathbf{r})\mathcal{I}_{\mathsf{z}}^{+}(\mathbf{r}, \mathbf{v})\sigma_{\mathsf{z},+}^{+}(\mathbf{r}, \mathbf{v})}{c} \tag{3.43c}$$

where $\mathcal{I}_z^+$ is the intensity of the positive z directed beam; we note that in the $F = 0 \to F' = 1$ model case, we use another font in denoting the individual beam intensities, as in an upcoming subsection (3.2.3) we will see that they are different from the 2-level atom model intensities. $\sigma_{\mathsf{z},-}^{+}$, $\sigma_{\mathsf{z},0}^{+}$ and $\sigma_{\mathsf{z},+}^{+}$ are the scattering cross-sections for the respective σ^-, π and σ^+ polarization-driven

parts of the $F = 0 \to F' = 1$ atom, found from

$$\sigma^{\pm}_{\alpha,q}(\mathbf{r},\mathbf{v}) = \frac{\sigma_0}{1 + \frac{I_{tot,q}(\mathbf{r},\mathbf{v})}{I_{sat}} + 4\frac{(\delta \mp k_L v_\alpha - q\mu B(\mathbf{r}))^2}{\Gamma^2}} \tag{3.44}$$

where $\mathbf{v} = (v_\mathsf{x}, v_\mathsf{y}, v_\mathsf{z})$ is the velocity of the atom (as in section 3.1), $q = -, 0, +$ refers to the respective σ^-, π, σ^+ polarization-driven parts of the $F = 0 \to F' = 1$ atom, $+/-$ in the superscript refers to the laser beam propagating in the positive/negative direction of $\hat{\boldsymbol{\alpha}} = \hat{\mathbf{x}}, \hat{\mathbf{y}}, \hat{\mathbf{z}}$, respectively corresponding to $\alpha = \mathsf{x}, \mathsf{y}, \mathsf{z}$, and

$$I_{tot,q}(\mathbf{r},\mathbf{v}) = \sum_{\alpha=\mathsf{x},\mathsf{y},\mathsf{z}} [p^+_{\alpha,q}(\mathbf{r})\mathcal{I}^+_\alpha(\mathbf{r},\mathbf{v}) + p^-_{\alpha,q}(\mathbf{r})\mathcal{I}^-_\alpha(\mathbf{r},\mathbf{v})] \tag{3.45}$$

denotes the total intensity that the σ^-, π, σ^+ polarization-driven part ($q = -, 0, +$) will scatter as the atom is exposed to all six MOT beams, with $p^{\pm}_{\alpha,q}$ denoting the fraction of the positive/negative ($\pm$) $\hat{\boldsymbol{\alpha}} = \hat{\mathbf{x}}, \hat{\mathbf{y}}, \hat{\mathbf{z}}$ directed light that the atom will see as σ^-, π, σ^+ polarized ($q = -, 0, +$). There is a total of eighteen fractions, as there are three fractions corresponding to each of the six MOT beams. In this Thesis, we will refer to these fractions as the *scattering fractions*.

Finding the scattering fractions corresponding to a given beam relies on knowing what polarization state this beam has as seen by the atom. The polarization state the atom sees depends on the choice of the quantization-axis, which we have picked to be along the direction of $\mathbf{B}$. In the following, we find what polarization states the atom sees that the respective MOT beams have, and from there we find the expressions for the scattering fractions.

We will treat each MOT beam in its own separate laser basis, defined in the way seen in Fig. 3.6, depicting a situation where a MOT beam is illuminating the $F = 0 \to F' = 1$ atom. As observed in Fig. 3.6, we define the laser basis to be the orthonormal basis formed by the vectors $\hat{\mathbf{x}}_{la}, \hat{\mathbf{y}}_{la}, \hat{\mathbf{z}}_{la}$, with the z-axis vector $\hat{\mathbf{z}}_{la}$ pointing in the direction of the beam's k-vector. As also observed in Fig. 3.6, we define the atom basis to be the orthonormal basis formed by the vectors $\hat{\mathbf{x}}_{at}, \hat{\mathbf{y}}_{at}, \hat{\mathbf{z}}_{at}$, with the z-axis vector $\hat{\mathbf{z}}_{at}$ pointing in the direction of the quantization-axis, being the direction of $\mathbf{B}$.

From the Jones calculus formalism [62], we write down the respective vector representations of σ^-, π, σ^+ polarization states:

$$\boldsymbol{\epsilon}^- = \frac{1}{\sqrt{2}}\begin{bmatrix}1\\ i\\ 0\end{bmatrix} \quad , \quad \boldsymbol{\epsilon}^0 = \begin{bmatrix}0\\ 0\\ 1\end{bmatrix} \quad , \quad \boldsymbol{\epsilon}^+ = \frac{1}{\sqrt{2}}\begin{bmatrix}1\\ -i\\ 0\end{bmatrix} \tag{3.46}$$

The polarization states of the beams traveling in the positive and negative direction of $\hat{\mathbf{z}}$ are of σ^+ and represented by $\boldsymbol{\epsilon}^+$ in the corresponding laser bases, whereas the polarization states of the beams traveling in the positive and negative direction of $\hat{\mathbf{x}}, \hat{\mathbf{y}}$ are of σ^- and represented by $\boldsymbol{\epsilon}^-$ in the corresponding laser bases (refer to Fig. 1.1).

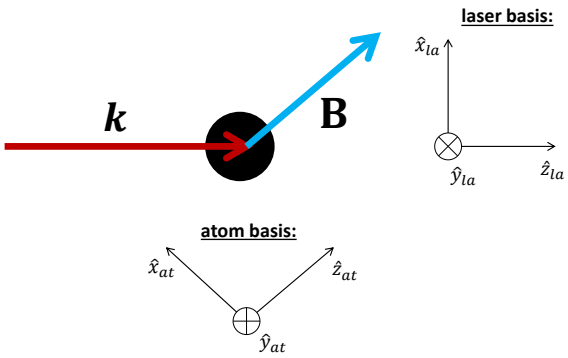

Figure 3.6: Depiction of a situation where a MOT beam is illuminating the $F = 0 \rightarrow F' = 1$ atom. Two separate orthonormal bases are defined, one of the laser beam and another one of the atom. The laser basis z-axis vector ($\hat{\mathbf{z}}_{la}$) has the same direction as the k-vector of the laser beam, while the atom basis z-axis vector ($\hat{\mathbf{z}}_{at}$) has the same direction as the quantization-axis, being the direction of the MOT's magnetic field $\mathbf{B}$.

We would like to express the polarization state vectors of the respective MOT beams in the atom basis. To make a quick sketch on how this will be done, we find, for a given MOT beam, the angle that the z-axes of the light and atom bases subtend, and then, as the choice of the x- and y-axes does not matter for these bases (as that does not affect the polarization states), we thus assume a common y-axis for both of the bases and, finally, perform a rotation of the beam's polarization state vector seen in the laser basis ($\boldsymbol{\epsilon}^-$ or $\boldsymbol{\epsilon}^+$) around this y-axis by the angle that the z-axes subtend, obtaining in this way the polarization state vector in the atom basis. Note that since the choice of the x- and y-axes does not matter, one can alternatively assume a common x-axis for both of the bases and perform the rotation around this x-axis, and obtain the same result at the end of all the calculations.

For what follows, we will assume a common y-axis for the laser and atom bases, like sketched in Fig. 3.6, and thus consider the rotation matrix

$$\mathbf{R}_{\mathsf{y}}(\theta_{\mathsf{r}}) = \begin{bmatrix} cos(\theta_{\mathsf{r}}) & 0 & -sin(\theta_{\mathsf{r}}) \\ 0 & 1 & 0 \\ sin(\theta_{\mathsf{r}}) & 0 & cos(\theta_{\mathsf{r}}) \end{bmatrix} \tag{3.47}$$

which performs y-axis rotations by the angle θ_{r}.

The angle of rotation will of course depend on which of the six MOT beams we are considering, found by writing down the dot product of the k-vector of a given beam with the B-vector. We find the six angles $\theta_{\alpha}^{\pm}$, where $+/-$ refers to the positive/negative $\hat{\boldsymbol{\alpha}} = \hat{\mathbf{x}}, \hat{\mathbf{y}}, \hat{\mathbf{z}}$ directed light, from

$$cos(\theta_{\alpha}^{\pm}) = \frac{\mathbf{k}_{\alpha}^{\pm} \cdot \mathbf{B}}{|\mathbf{k}_{\alpha}^{\pm}||\mathbf{B}|} = \frac{\pm \alpha'' B'}{2B(\mathbf{r})} \tag{3.48}$$

where $\alpha'' = -x, -y, 2z$ for respectively $\hat{\boldsymbol{\alpha}} = \hat{\mathbf{x}}, \hat{\mathbf{y}}, \hat{\mathbf{z}}$, and we have performed the dot product in the MOT basis (as the angle does not depend on the basis we are choosing), where we have used $\mathbf{k}_{\mathsf{x}}^{\pm} = (\pm k_{\mathsf{x}}, 0, 0)$, $\mathbf{k}_{\mathsf{y}}^{\pm} = (0, \pm k_{\mathsf{y}}, 0)$ and $\mathbf{k}_{\mathsf{z}}^{\pm} = (0, 0, \pm k_{\mathsf{z}})$ as the corresponding MOT basis k-vectors.

Using $\mathbf{R}_{\mathsf{y}}$ we perform next rotations of the polarization state vector seen in each of the six laser bases, $\boldsymbol{\epsilon}^-$ or $\boldsymbol{\epsilon}^+$ (where, to recall, $\boldsymbol{\epsilon}^-$ is for the positive/negative $\hat{\mathbf{x}}, \hat{\mathbf{y}}$ directed light, and $\boldsymbol{\epsilon}^+$ is for the positive/negative $\hat{\mathbf{z}}$ directed light), by the corresponding angle $\theta_\alpha^\pm$, so to obtain the respective six polarization state vectors in the atom basis:

$$\boldsymbol{\epsilon}^\pm_{\mathsf{x},la\to at} = \mathbf{R}_{\mathsf{y}}(\theta^\pm_{\mathsf{x}})\boldsymbol{\epsilon}^- = \frac{1}{\sqrt{2}}\begin{bmatrix} cos(\theta^\pm_{\mathsf{x}}) \\ i \\ sin(\theta^\pm_{\mathsf{x}}) \end{bmatrix} \tag{3.49a}$$

$$\boldsymbol{\epsilon}^\pm_{\mathsf{y},la\to at} = \mathbf{R}_{\mathsf{y}}(\theta^\pm_{\mathsf{y}})\boldsymbol{\epsilon}^- = \frac{1}{\sqrt{2}}\begin{bmatrix} cos(\theta^\pm_{\mathsf{y}}) \\ i \\ sin(\theta^\pm_{\mathsf{y}}) \end{bmatrix} \tag{3.49b}$$

$$\boldsymbol{\epsilon}^\pm_{\mathsf{z},la\to at} = \mathbf{R}_{\mathsf{y}}(\theta^\pm_{\mathsf{z}})\boldsymbol{\epsilon}^+ = \frac{1}{\sqrt{2}}\begin{bmatrix} cos(\theta^\pm_{\mathsf{z}}) \\ -i \\ sin(\theta^\pm_{\mathsf{z}}) \end{bmatrix} \tag{3.49c}$$

where "$la \to at$" in the subscripts refers to the change from the laser (la) to atom (at) basis.

By projecting $\boldsymbol{\epsilon}^\pm_{\alpha,la\to at}$ onto respectively $\boldsymbol{\epsilon}^-$, $\boldsymbol{\epsilon}^0$ and $\boldsymbol{\epsilon}^+$ and taking the absolute square of the results we can find the fractions of the positive/negative ($\pm$) $\hat{\boldsymbol{\alpha}} = \hat{\mathbf{x}}, \hat{\mathbf{y}}, \hat{\mathbf{z}}$ directed light that the atom will see respectively as σ^-, π, σ^+ polarized, i.e. the scattering fractions $p^\pm_{\alpha,-}$, $p^\pm_{\alpha,0}$ and $p^\pm_{\alpha,+}$:

$$p^\pm_{\alpha,q} = |\boldsymbol{\epsilon}^\pm_{\alpha,la\to at} \cdot \boldsymbol{\epsilon}^q|^2 \tag{3.50}$$

Note that $p^\pm_{\alpha,-} + p^\pm_{\alpha,0} + p^\pm_{\alpha,+} = 1$ because $\boldsymbol{\epsilon}^\pm_{\alpha,la\to at}$ is a unit vector and also because $\boldsymbol{\epsilon}^-$, $\boldsymbol{\epsilon}^0$ and $\boldsymbol{\epsilon}^+$ form an orthonormal basis.

Using Eqs. 3.46 and 3.49 in Eq. 3.50 we find for the MOT beam traveling in the positive/negative ($\pm$) $\hat{\boldsymbol{\alpha}} = \hat{\mathbf{x}}, \hat{\mathbf{y}}, \hat{\mathbf{z}}$ direction:

$$\boxed{p^\pm_{\alpha,q}(\mathbf{r}) = \begin{cases} \left(\frac{1}{2}\left[1 \pm \frac{\alpha' B'}{2B(\mathbf{r})}\right]\right)^2 & , \quad q = +\ (\sigma^+) \\ \left(\frac{1}{2}\left[1 \mp \frac{\alpha' B'}{2B(\mathbf{r})}\right]\right)^2 & , \quad q = -\ (\sigma^-) \\ 1 - (p^\pm_{\alpha,+} + p^\pm_{\alpha,-}) & , \quad q = 0\ \ (\pi) \end{cases}} \tag{3.51}$$

where $\alpha' = x, y, 2z$ for respectively $\hat{\boldsymbol{\alpha}} = \hat{\mathbf{x}}, \hat{\mathbf{y}}, \hat{\mathbf{z}}$. Note that if we reverse the handedness of the rotation (i.e. if $\theta^\pm_\alpha \to -\theta^\pm_\alpha$), the result for $p^\pm_{\alpha,q}$ seen in Eq. 3.51 remains the same because $cos(\theta^\pm_\alpha) = cos(-\theta^\pm_\alpha)$ and also because we perform the absolute value operation of the dot product $\boldsymbol{\epsilon}^\pm_{\alpha,la\to at} \cdot \boldsymbol{\epsilon}^q$ (see Eq. 3.50).

Finally, observing the result for the 2-level atom model trapping force in Tab. 3.1 as well as Eq. 3.42 for the radiation pressure force that the $F = 0 \to F' = 1$ atom experiences from one of the MOT beams, together with Eqs. 3.43(a-c) for the radiation pressures forces acting on the individual 2-level parts, we write down our $F = 0 \to F' = 1$ model's 3D trapping force:

$$\boxed{\mathbf{F}^{4level}_{tr}(\mathbf{r}, \mathbf{v}) = F^{4level}_{tr,\mathsf{x}}(\mathbf{r}, \mathbf{v})\hat{\mathbf{x}} + F^{4level}_{tr,\mathsf{y}}(\mathbf{r}, \mathbf{v})\hat{\mathbf{y}} + F^{4level}_{tr,\mathsf{z}}(\mathbf{r}, \mathbf{v})\hat{\mathbf{z}}} \tag{3.52}$$

with the force's components being

$$\boxed{F^{4level}_{tr,\alpha}(\mathbf{r},\mathbf{v}) = \frac{1}{c}\left(\sum_{q=-,0,+}[p^{+}_{\alpha,q}(\mathbf{r})\mathcal{I}^{+}_{\alpha}(\mathbf{r},\mathbf{v})\sigma^{+}_{\alpha,q}(\mathbf{r},\mathbf{v}) - p^{-}_{\alpha,q}(\mathbf{r})\mathcal{I}^{-}_{\alpha}(\mathbf{r},\mathbf{v})\sigma^{-}_{\alpha,q}(\mathbf{r},\mathbf{v})]\right)} \tag{3.53}$$

We note that in the limit of small velocities ($|v_\alpha| \ll \Gamma/k_L, |\delta|/k_L$) and for positions close to the trap center ($\sqrt{z^2 + \frac{1}{4}(x^2+y^2)} \ll \Gamma/(\mu B'),\ |\delta|/(\mu B')$), the $F = 0 \to F' = 1$ model's trapping force correctly describes a harmonic oscillator with the friction coefficient γ_{3D} and the spring constant κ_{3D}, as in Eq. 3.19.

3.2.2 Diffusion

The goal of this subsection is to provide an expression for the momentum diffusion coefficient for our $F = 0 \to F' = 1$ model in 3D. We make a straightforward extension of the corresponding 2-level atom model result, using results of the previous subsection.

Observing the result for the 2-level atom model's momentum diffusion coefficient in Tab. 3.1, and Eqs. 3.29 and 3.30 for respectively the 2-level atom model total saturation parameter and the 2-level atom model single-beam saturation parameter, as well as results of the previous subsection, we finally write down our $F = 0 \to F' = 1$ model's 3D momentum diffusion coefficient:

$$\boxed{D^{4level}_{3D}(\mathbf{r},\mathbf{v}) = D^{4level}_{vac,3D}(\mathbf{r},\mathbf{v}) + D^{4level}_{las,3D}(\mathbf{r},\mathbf{v})} \tag{3.54}$$

with

$$\boxed{D^{4level}_{vac,3D}(\mathbf{r},\mathbf{v}) = \hbar^2 k_L^2 \frac{\Gamma}{4}\frac{s^{4level}_{tot}(\mathbf{r},\mathbf{v})}{1+s^{4level}_{tot}(\mathbf{r},\mathbf{v})}} \tag{3.55}$$

$$\boxed{D^{4level}_{las,3D}(\mathbf{r},\mathbf{v}) = \hbar^2 k_L^2 \frac{\Gamma}{4}\frac{s^{4level}_{tot}(\mathbf{r},\mathbf{v})}{(1+s^{4level}_{tot}(\mathbf{r},\mathbf{v}))^3} \times \left\{1 + \frac{12\delta^2-\Gamma^2}{4\delta^2+\Gamma^2}s^{4level}_{tot}(\mathbf{r},\mathbf{v}) + (s^{4level}_{tot}(\mathbf{r},\mathbf{v}))^2\right\}} \tag{3.56}$$

being the $F = 0 \to F' = 1$ model's momentum diffusion coefficient of the vacuum field and laser field, respectively. s^{4level}_{tot} is the total saturation parameter that is a sum of the total saturation parameters $s_{tot,-}$, $s_{tot,0}$, $s_{tot,+}$ for the 2-level parts of the $F = 0 \to F' = 1$ atom that are driven by respectively σ^-, π, σ^+ polarized light, i.e.

$$\boxed{s^{4level}_{tot}(\mathbf{r},\mathbf{v}) = \sum_{q=-,0,+} s_{tot,q}(\mathbf{r},\mathbf{v})} \tag{3.57}$$

with

$$\boxed{s_{tot,q}(\mathbf{r},\mathbf{v}) = \sum_{\alpha=\mathrm{x,y,z}} [s^{+}_{\alpha,q}(\mathbf{r},\mathbf{v}) + s^{-}_{\alpha,q}(\mathbf{r},\mathbf{v})]} \tag{3.58}$$

where

$$\boxed{s^{\pm}_{\alpha,q}(\mathbf{r},\mathbf{v}) = \frac{p^{\pm}_{\alpha,q}(\mathbf{r})\mathcal{I}^{\pm}_{\alpha}(\mathbf{r},\mathbf{v})/I_{sat}}{1+4\frac{(\delta\mp k_L v_\alpha - q\mu B(\mathbf{r}))^2}{\Gamma^2}}} \tag{3.59}$$

denotes the saturation parameter for the 2-level part of the $F=0\rightarrow F'=1$ atom that is driven by σ^-, π, σ^+ polarized light ($q=-,0,+$) traveling in the positive/negative ($\pm$) $\hat{\boldsymbol{\alpha}}=\hat{\mathbf{x}},\hat{\mathbf{y}},\hat{\mathbf{z}}$ direction.

3.2.3 Intensity attenuation

The goal of this subsection is to provide expressions for the MOT beam intensities with attenuation incorporated, for our $F=0\rightarrow F'=1$ model in 3D. We make a straightforward extension of the corresponding 2-level atom model result, using results of the first subsection of this section.

Previously, in the 2-level atom model, we considered a plane MOT beam traveling in the positive direction of the z-axis, with the intensity I^{+}_{z} attenuated by the 2-level atoms. The attenuation of I^{+}_{z} was mentioned to depend on the scattering cross-section σ^{+}_{z} of the 2-level atoms (Eq. 3.17) as well as their density distribution ρ. The intensity loss experienced by a plane MOT beam with the intensity $\mathcal{I}^{+}_{\mathrm{z}}$ for the $F=0\rightarrow F'=1$ atom case is described by (equivalently to Eq. 3.32)

$$\frac{d}{dz}\mathcal{I}^{+}_{\mathrm{z}}(\mathbf{r},\mathbf{v}) = -\sum_{q=-,0,+} p^{+}_{\mathrm{z},q}(\mathbf{r})\mathcal{I}^{+}_{\mathrm{z}}(\mathbf{r},\mathbf{v})\sigma^{+}_{\mathrm{z},q}(\mathbf{r},\mathbf{v})\rho(\mathbf{r}) \tag{3.60}$$

where, as we recall (from section 3.2.1), $\sigma^{+}_{\mathrm{z},q}$ is the scattering cross-section for the σ^-, π, σ^+ polarization-driven part of the $F=0\rightarrow F'=1$ atom ($q=-,0,+$), and $p^{+}_{\mathrm{z},q}$ is the corresponding scattering fraction. For simplicity, we denote the density distribution of the $F=0\rightarrow F'=1$ atoms by $\rho(\mathbf{r})$, like in the case of the 2-level atom model.

The general solution to the above equation is given by (equivalently to Eq. 3.33)

$$\mathcal{I}^{+}_{\mathrm{z}}(\mathbf{r},\mathbf{v}) = I_\infty e^{-\int_{-\infty}^{z} dz' \ \sum_{q=-,0,+}\left[p^{+}_{\mathrm{z},q}(x,y,z')\sigma^{+}_{\mathrm{z},q}\left(x,y,z',\mathbf{v}(x,y,z')\right)\right]\rho(x,y,z')} \tag{3.61}$$

where, as we recall (from section 3.1.3), I_∞ refers to the unattenuated beam intensity, and $\mathbf{v}(x,y,z')$ refers to the velocity $\mathbf{v}$ evaluated at (x,y,z'). For the remaining five MOT beams we can obtain analogous expressions to Eq. 3.61, where we note that for the beam traveling in the direction of $-\hat{\mathbf{x}}/-\hat{\mathbf{y}}/-\hat{\mathbf{z}}$, the limit of the integral is from $x/y/z$ to $+\infty$. Using obvious notations, we

finally write down the full set of equations for the MOT beam intensities in our $F = 0 \rightarrow F' = 1$ model:

$$\boxed{\begin{array}{ll} \mathcal{I}^+_{\mathsf{x}}(\mathbf{r},\mathbf{v}) = I_\infty e^{-\int_{-\infty}^{x} dx' \sum\limits_{q=-,0,+} \left[p^+_{\mathsf{x},q}(x',y,z)\sigma^+_{\mathsf{x},q}\left(x',y,z,\mathbf{v}(x',y,z)\right)\right]\rho(x',y,z)} & , \ \mathcal{I}^-_{\mathsf{x}}(\mathbf{r},\mathbf{v}) = I_\infty e^{-\int_{x}^{+\infty} dx' \sum\limits_{q=-,0,+} \left[p^-_{\mathsf{x},q}(x',y,z)\sigma^-_{\mathsf{x},q}\left(x',y,z,\mathbf{v}(x',y,z)\right)\right]\rho(x',y,z)} \\ \mathcal{I}^+_{\mathsf{y}}(\mathbf{r},\mathbf{v}) = I_\infty e^{-\int_{-\infty}^{y} dy' \sum\limits_{q=-,0,+} \left[p^+_{\mathsf{y},q}(x,y',z)\sigma^+_{\mathsf{y},q}\left(x,y',z,\mathbf{v}(x,y',z)\right)\right]\rho(x,y',z)} & , \ \mathcal{I}^-_{\mathsf{y}}(\mathbf{r},\mathbf{v}) = I_\infty e^{-\int_{y}^{+\infty} dy' \sum\limits_{q=-,0,+} \left[p^-_{\mathsf{y},q}(x,y',z)\sigma^-_{\mathsf{y},q}\left(x,y',z,\mathbf{v}(x,y',z)\right)\right]\rho(x,y',z)} \\ \mathcal{I}^+_{\mathsf{z}}(\mathbf{r},\mathbf{v}) = I_\infty e^{-\int_{-\infty}^{z} dz' \sum\limits_{q=-,0,+} \left[p^+_{\mathsf{z},q}(x,y,z')\sigma^+_{\mathsf{z},q}\left(x,y,z',\mathbf{v}(x,y,z')\right)\right]\rho(x,y,z')} & , \ \mathcal{I}^-_{\mathsf{z}}(\mathbf{r},\mathbf{v}) = I_\infty e^{-\int_{z}^{+\infty} dz' \sum\limits_{q=-,0,+} \left[p^-_{\mathsf{z},q}(x,y,z')\sigma^-_{\mathsf{z},q}\left(x,y,z',\mathbf{v}(x,y,z')\right)\right]\rho(x,y,z')} \end{array}} \tag{3.62}$$

3.2.4 Rescattering force

The goal of this subsection is to provide an expression for the rescattering force for our $F = 0 \rightarrow F' = 1$ model in 3D. We start by making a sketch for the force's derivation, then write down its expression and, finally, evaluate the unknowns in this expression.

Let us consider the situation shown in Fig. 1.8, depicting the mechanism behind the rescattering, and take atom 1 and atom 2 to be the $F = 0 \rightarrow F' = 1$ atoms. As atom 1 consists of parts driven by σ^-, π, σ^+ polarized light, each of them will produce a characteristic radiation pattern of scattered light. We assume that these patterns do not to interfere and denote the intensities associated with these patterns respectively by $I_{S,-}$, $I_{S,0}$, $I_{S,+}$. At the atom 2 position $\mathbf{r}_2$, each of these intensities will be rescattered by the σ^-, π, σ^+ polarization-driven parts of this atom. The rescattered intensities by these parts will respectively be

$$\begin{aligned} I_{R,-}(\mathbf{r}_2) &= b^-_-(\mathbf{r}_2)I_{S,-}(\mathbf{r}_2) + b^0_-(\mathbf{r}_2)I_{S,0}(\mathbf{r}_2) + b^+_-(\mathbf{r}_2)I_{S,+}(\mathbf{r}_2) \\ I_{R,0}(\mathbf{r}_2) &= b^-_0(\mathbf{r}_2)I_{S,-}(\mathbf{r}_2) + b^0_0(\mathbf{r}_2)I_{S,0}(\mathbf{r}_2) + b^+_0(\mathbf{r}_2)I_{S,+}(\mathbf{r}_2) \\ I_{R,+}(\mathbf{r}_2) &= b^-_+(\mathbf{r}_2)I_{S,-}(\mathbf{r}_2) + b^0_+(\mathbf{r}_2)I_{S,0}(\mathbf{r}_2) + b^+_+(\mathbf{r}_2)I_{S,+}(\mathbf{r}_2) \end{aligned}$$

or, when compactly written,

$$\boxed{I_{R,q''}(\mathbf{r}_2) = \sum_{q'=+,0,-} b^{q'}_{q''}(\mathbf{r}_2)I_{S,q'}(\mathbf{r}_2)} \tag{3.63}$$

where $b^{q'}_{q''}$, with $q' = -, 0, +$ and $q'' = -, 0, +$, denotes the fraction of the scattered radiation pattern of intensity $I_{S,q'}$ that atom 2 will see as σ^-, π, σ^+ polarized. q' and q'' refer to the 2-level parts of respectively atom 1 and atom 2. There is a total of nine fractions, as there are three fractions corresponding to each of the three radiation patterns. In this Thesis, we will refer to these fractions as the *rescattering fractions*.

The total powers rescattered by the respective σ^-, π, σ^+ polarization-driven parts of atom 2, will, according to Eq. 1.16, be expressed by

$$P_{R,tot,q''}(\mathbf{r}_1, \mathbf{r}_2, \mathbf{v}_1, \mathbf{v}_2) = I_{R,q''}(\mathbf{r}_2)\sigma_{R,q''}(\mathbf{r}_1, \mathbf{r}_2, \mathbf{v}_1, \mathbf{v}_2) \tag{3.64}$$

where $\sigma_{R,q''}$ denotes the rescattering cross-section for the σ^-, π, σ^+ polarization-driven part of atom 2 ($q'' = -, 0, +$).

The total power rescattered by atom 2 will consequently be

$$P_R^{4level,1}(\mathbf{r}_2, \mathbf{v}_2) = \sum_{q''=+,0,-} P_{R,tot,q''}(\mathbf{r}_1, \mathbf{r}_2, \mathbf{v}_1, \mathbf{v}_2) \tag{3.65}$$

where "1" in the superscript refers to atom 1.

Observing the rescattering force's expression in Eq. 1.18, we finally write down our $F = 0 \rightarrow F' = 1$ model's 3D rescattering force on the atom at the position $\mathbf{r}_j$ with the velocity $\mathbf{v}_j$, due to the scattering atoms at the positions $\mathbf{r}_i$ with the velocities $\mathbf{v}_i$:

$$\mathbf{F}_{rsc}^{4level}(\mathbf{r}_j, \mathbf{v}_j) = \sum_{i \neq j} \frac{P_R^{4level,i}(\mathbf{r}_j, \mathbf{v}_j)}{c} \hat{\mathbf{r}}_{i,j} \tag{3.66}$$

where $\hat{\mathbf{r}}_{i,j}$ is the unit vector pointing from $\mathbf{r}_i$ to $\mathbf{r}_j$, as defined in Eq. 3.39.

In the upcoming three parts, we will respectively provide expressions for the scattered radiation pattern intensity $I_{S,q'}$, the rescattering fraction $b_{q''}^{q'}$ and the rescattering cross-section $\sigma_{R,q''}$.

Before we start, we note that in the parts surrounding respectively $I_{S,q'}$ and $b_{q''}^{q'}$, we will make use of rotation matrices so to express light polarization state vectors in different bases, similarly to what was done previously for the trapping force derivation (refer to section 3.2.1 and Fig. 3.6). The bases we will be considering are defined in the way seen in Fig. 3.7, depicting a situation where atom 1 is scattering light onto atom 2. As observed in Fig. 3.7, we define the scattered light basis to be the orthonormal basis formed by the vectors $\hat{\mathbf{x}}_l, \hat{\mathbf{y}}_l, \hat{\mathbf{z}}_l$, with the z-axis vector $\hat{\mathbf{z}}_l$ pointing in the direction of the light's k-vector $\mathbf{k}_l$. We write $\mathbf{k}_l = k_l \hat{\mathbf{r}}_{1,2}$, where $\hat{\mathbf{r}}_{1,2}$ is given by Eq. 3.39. As also observed in Fig. 3.7, we define the respective bases of atom 1 and atom 2 in accord to what was done previously, where the z-axis vector of each orthonormal atom basis points in the direction of the (local) quantization-axis, being the direction of $\mathbf{B}$. According to Eq. 3.14, the magnetic field for atom 1 is $\mathbf{B}_1 \equiv \mathbf{B}(\mathbf{r}_1) = -B'\left(\frac{x_1}{2}, \frac{y_1}{2}, -z_1\right)$, whereas for atom 2 it is $\mathbf{B}_2 \equiv \mathbf{B}(\mathbf{r}_2) = -B'\left(\frac{x_2}{2}, \frac{y_2}{2}, -z_2\right)$; thus, the x- or y-axis vector of the atom 1 basis is generally not the same as that of the atom 2 basis.

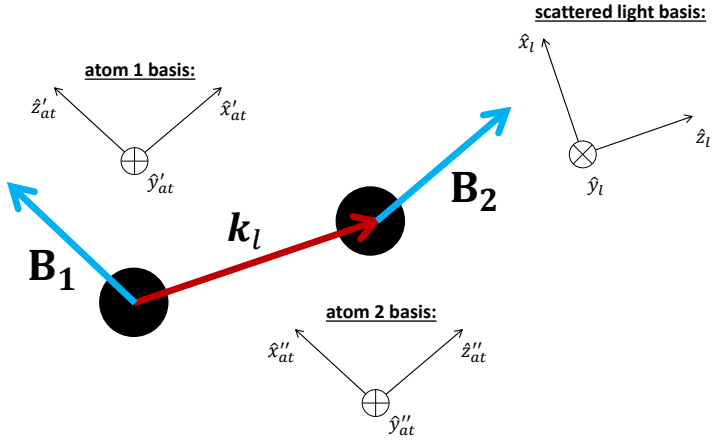

Figure 3.7: Depiction of a situation where the $F = 0 \rightarrow F' = 1$ atom 1 is scattering light onto the $F = 0 \rightarrow F' = 1$ atom 2. Three separate orthonormal bases are defined, one of the scattered light beam and another two of the respective atoms. The light basis z-axis vector ($\hat{\mathbf{z}}_l$) has the same direction as the k-vector of the scattered light beam ($\mathbf{k}_l$), while each atom basis z-axis vector ($\hat{\mathbf{z}}'_{at}$ or $\hat{\mathbf{z}}''_{at}$) has the same direction as the (local) quantization-axis, being the direction of the MOT's magnetic field $\mathbf{B}$ ($\mathbf{B}_1$ or $\mathbf{B}_2$), in accord to the sketch seen in Fig. 3.6. The x- or y-axis vector of the atom 1 basis is generally not the same as that of the atom 2 basis (see text).

The scattered radiation pattern intensity $I_{S,q'}$ $(q' = -, 0, +)$

Here we find the scattered radiation pattern intensities $I_{S,-}$, $I_{S,0}$, $I_{S,+}$ corresponding to the parts of atom 1 that are respectively driven by σ^-, π, σ^+ polarized light.

To start, let us consider the fact that the Zeeman interaction polarizes atom 1 along the direction of $\mathbf{B}_1$ and that the mentioned parts of this atom scatter light whose polarization states are represented by the respective vectors $\boldsymbol{\epsilon}^-$, $\boldsymbol{\epsilon}^0$, $\boldsymbol{\epsilon}^+$ (Eq. 3.46) in an orthonormal basis, whose z-axis vector points along the direction of $\mathbf{B}_1$. Observing Fig. 3.7, we identify such orthonormal basis with the atom 1 basis. We would like to express the polarization state vectors in the scattered light basis, seen in Fig. 3.7, where the z-axis of this basis is observed to point in the direction of the k-vector $\mathbf{k}_l$ of the scattered light. Using our previous approach (from section 3.2.1), we may assume for the atom 1 and scattered light bases a common y-axis around which the rotation will be performed so to express the polarization state vectors in the scattered light basis. The angle of rotation, denoted by $\theta_{at' \rightarrow l}$, is found through a dot product of $\mathbf{k}_l$ and $\mathbf{B}_1$:

$$cos(\theta_{at' \rightarrow l}) = \frac{\mathbf{k}_l \cdot \mathbf{B}_1}{|\mathbf{k}_l||\mathbf{B}_1|} \tag{3.67}$$

with "$at' \rightarrow l$" referring to the change from the atom 1 (at') to scattered light (l) basis.

With the use of the rotation matrix $\mathbf{R}_y$ given by Eq. 3.47, we obtain, in the scattered light basis, the polarization state vectors corresponding to the

respective σ^-, π, σ^+ polarization-driven parts of atom 1:

$$\boldsymbol{\epsilon}^{-}_{at'\to l} = \mathbf{R}_{\mathsf{y}}(\theta_{at'\to l})\boldsymbol{\epsilon}^{-} = \frac{1}{\sqrt{2}}\begin{bmatrix} cos(\theta_{at'\to l}) \\ i \\ sin(\theta_{at'\to l}) \end{bmatrix} \tag{3.68a}$$

$$\boldsymbol{\epsilon}^{0}_{at'\to l} = \mathbf{R}_{\mathsf{y}}(\theta_{at'\to l})\boldsymbol{\epsilon}^{0} = \begin{bmatrix} -sin(\theta_{at'\to l}) \\ 0 \\ cos(\theta_{at'\to l}) \end{bmatrix} \tag{3.68b}$$

$$\boldsymbol{\epsilon}^{+}_{at'\to l} = \mathbf{R}_{\mathsf{y}}(\theta_{at'\to l})\boldsymbol{\epsilon}^{+} = \frac{1}{\sqrt{2}}\begin{bmatrix} cos(\theta_{at'\to l}) \\ -i \\ sin(\theta_{at'\to l}) \end{bmatrix} \tag{3.68c}$$

Next, understanding that an electric field's direction is perpendicular to the propagation direction of the corresponding wave, we must respectively project the above vectors onto a plane orthogonal to $\mathbf{k}_l$, thus obtaining the scattered light basis vectors for the light emanating from atom 1 to atom 2:

$$\boldsymbol{\epsilon}^{proj,-}_{at'\to l} = \frac{1}{\sqrt{2}}\begin{bmatrix} cos(\theta_{at'\to l}) \\ i \\ 0 \end{bmatrix} \quad , \quad \boldsymbol{\epsilon}^{proj,0}_{at'\to l} = \begin{bmatrix} -sin(\theta_{at'\to l}) \\ 0 \\ 0 \end{bmatrix} \quad , \quad \boldsymbol{\epsilon}^{proj,+}_{at'\to l} = \frac{1}{\sqrt{2}}\begin{bmatrix} cos(\theta_{at'\to l}) \\ -i \\ 0 \end{bmatrix} \tag{3.69}$$

where "*proj*" in the superscripts refers to the projection made.

Squaring the lengths of $\boldsymbol{\epsilon}^{proj,-}_{at'\to l}$, $\boldsymbol{\epsilon}^{proj,0}_{at'\to l}$, $\boldsymbol{\epsilon}^{proj,+}_{at'\to l}$ we may learn about the shape of the radiation patterns that σ^-, π, σ^+ parts of atom 1 respectively produce. These patterns are anisotropic[3], requiring us to properly normalize the squared lengths, thus ensuring that the energy is conserved in the scattering events.

The normalized radiation patterns are

$$\eta_{q'}(\mathbf{r}_1) = \begin{cases} \frac{3}{4}\left[1 + \left(\frac{\mathbf{k}_l\cdot\mathbf{B}_1}{|\mathbf{k}_l||\mathbf{B}_1|}\right)^2\right] & , \quad q' = +\ (\sigma^+) \\ \\ \frac{3}{4}\left[1 + \left(\frac{\mathbf{k}_l\cdot\mathbf{B}_1}{|\mathbf{k}_l||\mathbf{B}_1|}\right)^2\right] & , \quad q' = -\ (\sigma^-) \\ \\ \frac{3}{2}\left[1 - \left(\frac{\mathbf{k}_l\cdot\mathbf{B}_1}{|\mathbf{k}_l||\mathbf{B}_1|}\right)^2\right] & , \quad q' = 0\ \ (\pi) \end{cases} \tag{3.70}$$

where we have used $\eta_{q'} = \frac{|\boldsymbol{\epsilon}^{proj,q'}_{at'\to l}|^2}{\frac{1}{4\pi}\int_0^{2\pi}\int_0^{\pi} d\theta_{at'\to l}\, d\phi\, |\boldsymbol{\epsilon}^{proj,q'}_{at'\to l}|^2 sin(\theta_{at'\to l})}$. The normalization is here seen to involve integration over the solid angle.

Finally, because the intensity of the light emitted by atom 1 will diminish according to the inverse-square law of propagation, we find the scattered radiation

[3] A linear (π) dipole exhibits a "doughnut-shaped" radiation pattern, whereas a circular (σ^- or σ^+) dipole exhibits a "peanut-shaped" radiation pattern [63].

pattern intensities $I_{S,-}$, $I_{S,0}$, $I_{S,+}$ from

$$I_{S,q'}(\mathbf{r}_2) = \eta_{q'}(\mathbf{r}_1) \times \frac{P_{L,tot,q'}(\mathbf{r}_1, \mathbf{v}_1)}{4\pi|\mathbf{r}_2 - \mathbf{r}_1|^2} \tag{3.71}$$

where $P_{L,tot,q'}$ denotes the total power scattered by the σ^-, π, σ^+ polarization-driven part of atom 1 ($q' = -, 0, +$) as it is exposed to all six MOT beams:

$$P_{L,tot,q'}(\mathbf{r}_1, \mathbf{v}_1) = \sum_{\alpha=\mathrm{x,y,z}} [p^+_{\alpha,q'}(\mathbf{r}_1)\mathcal{I}^+_\alpha(\mathbf{r}_1, \mathbf{v}_1)\sigma^+_{\alpha,q'}(\mathbf{r}_1, \mathbf{v}_1) + p^-_{\alpha,q'}(\mathbf{r}_1)\mathcal{I}^-_\alpha(\mathbf{r}_1, \mathbf{v}_1)\sigma^-_{\alpha,q'}(\mathbf{r}_1, \mathbf{v}_1)] \tag{3.72}$$

which is found when observing Eq. 3.53.

The rescattering fraction $b^{q'}_{q''}$ ($q' = -, 0, +$, $q'' = -, 0, +$)

Here we find the rescattering fractions $b^-_{q''}$, $b^0_{q''}$, $b^+_{q''}$. To recall, the rescattering fraction $b^{q'}_{q''}$ denotes the fraction of the scattered radiation pattern of intensity $I_{S,q'}$ ($q' = -, 0, +$) that atom 2 will see as σ^-, π, σ^+ polarized ($q'' = -, 0, +$).

As we proceed finding the rescattering fractions $b^-_{q''}$, $b^0_{q''}$, $b^+_{q''}$, we note the equivalence of the following steps of calculation to those seen when deriving the scattering fractions seen in section 3.2.1.

In the scattered light basis (Fig. 3.7), the vectors associated with the light emanating from atom 1 to atom 2 are the vectors $\boldsymbol{\epsilon}^{proj,-}_{at'\to l}$, $\boldsymbol{\epsilon}^{proj,0}_{at'\to l}$, $\boldsymbol{\epsilon}^{proj,+}_{at'\to l}$, seen in Eq. 3.69. Analogously to the scattering fractions, we want the rescattering fractions to satisfy $b^{q'}_- + b^{q'}_0 + b^{q'}_+ = 1$, and so these vectors must be unit vectors. We thus normalize $\boldsymbol{\epsilon}^{proj,-}_{at'\to l}$, $\boldsymbol{\epsilon}^{proj,0}_{at'\to l}$, $\boldsymbol{\epsilon}^{proj,+}_{at'\to l}$ by their respective lengths and obtain the corresponding unit vectors

$$\boldsymbol{\epsilon}^{u,-}_{at'\to l} = \frac{1}{h}\begin{bmatrix} cos(\theta_{at'\to l}) \\ i \\ 0 \end{bmatrix} \quad , \quad \boldsymbol{\epsilon}^{u,0}_{at'\to l} = \begin{bmatrix} -1 \\ 0 \\ 0 \end{bmatrix} \quad , \quad \boldsymbol{\epsilon}^{u,+}_{at'\to l} = \frac{1}{h}\begin{bmatrix} cos(\theta_{at'\to l}) \\ -i \\ 0 \end{bmatrix} \tag{3.73}$$

where "u" in the superscripts refers to the vectors being unit vectors and $h = \sqrt{1 + cos(\theta_{at'\to l})^2}$ is the normalization factor, common to both $\boldsymbol{\epsilon}^{u,-}_{at'\to l}$ and $\boldsymbol{\epsilon}^{u,+}_{at'\to l}$.

Next, we conveniently assume for the scattered light and atom 2 bases a common y-axis around which the rotations will be performed so to express $\boldsymbol{\epsilon}^{u,-}_{at'\to l}$, $\boldsymbol{\epsilon}^{u,0}_{at'\to l}$, $\boldsymbol{\epsilon}^{u,+}_{at'\to l}$ in the atom 2 basis. The angle of rotation, denoted by $\theta_{l\to at''}$, is found through a dot product of $\mathbf{k}_l$ and $\mathbf{B}_2$:

$$cos(\theta_{l\to at''}) = \frac{\mathbf{k}_l \cdot \mathbf{B}_2}{|\mathbf{k}_l||\mathbf{B}_2|} \tag{3.74}$$

with "$l \to at''$" referring to the change from the scattered light (l) to atom 2 (at'') basis.

With the use of the rotation matrix $\mathbf{R}_{\mathrm{y}}$ given by Eq. 3.47, we obtain, in the atom 2 basis, the (normalized) vectors associated with the scattered light emanating from atom 1 to atom 2:

$$\boldsymbol{\epsilon}^{u,-}_{l\to at''} = \mathbf{R}_{\mathrm{y}}(\theta_{l\to at''})\boldsymbol{\epsilon}^{u,-}_{at'\to l} = \frac{1}{h}\begin{bmatrix} cos(\theta_{at'\to l})cos(\theta_{l\to at''}) \\ i \\ cos(\theta_{at'\to l})sin(\theta_{l\to at''}) \end{bmatrix} \tag{3.75a}$$

$$\boldsymbol{\epsilon}^{u,0}_{l\to at''} = \mathbf{R}_{\mathrm{y}}(\theta_{l\to at''})\boldsymbol{\epsilon}^{u,0}_{at'\to l} = \begin{bmatrix} -cos(\theta_{l\to at''}) \\ 0 \\ -sin(\theta_{l\to at''}) \end{bmatrix} \tag{3.75b}$$

$$\boldsymbol{\epsilon}^{u,+}_{l\to at''} = \mathbf{R}_{\mathrm{y}}(\theta_{l\to at''})\boldsymbol{\epsilon}^{u,+}_{at'\to l} = \frac{1}{h}\begin{bmatrix} cos(\theta_{at'\to l})cos(\theta_{l\to at''}) \\ -i \\ cos(\theta_{at'\to l})sin(\theta_{l\to at''}) \end{bmatrix} \tag{3.75c}$$

We can find the rescattering fractions $b^{-}_{q''}$, $b^{0}_{q''}$, $b^{+}_{q''}$ by projecting the respective vectors $\boldsymbol{\epsilon}^{u,-}_{l\to at''}$, $\boldsymbol{\epsilon}^{u,0}_{l\to at''}$, $\boldsymbol{\epsilon}^{u,+}_{l\to at''}$ onto the vector $\boldsymbol{\epsilon}^{q''}$ (Eq. 3.46) and then squaring the absolute value of the results, i.e. by computing

$$b^{-}_{q''} = |\boldsymbol{\epsilon}^{u,-}_{l\to at''}\cdot\boldsymbol{\epsilon}^{q''}|^2 \tag{3.76a}$$

$$b^{0}_{q''} = |\boldsymbol{\epsilon}^{u,0}_{l\to at''}\cdot\boldsymbol{\epsilon}^{q''}|^2 \tag{3.76b}$$

$$b^{+}_{q''} = |\boldsymbol{\epsilon}^{u,+}_{l\to at''}\cdot\boldsymbol{\epsilon}^{q''}|^2 \tag{3.76c}$$

Note that the rescattering fractions above correctly satisfy $b^{q'}_{-} + b^{q'}_{0} + b^{q'}_{+} = 1$, analogously to the scattering fractions.

Using Eqs. 3.46 and 3.75(a-c) in Eqs. 3.76(a-c) we find

$$b^{+}_{q''}(\mathbf{r}_2) = \begin{cases} \frac{1}{2h^2}\left[\frac{\mathbf{k}_l\cdot\mathbf{B}_1}{|\mathbf{k}_l||\mathbf{B}_1|}\frac{\mathbf{k}_l\cdot\mathbf{B}_2}{|\mathbf{k}_l||\mathbf{B}_2|}+1\right]^2 & , \quad q'' = +\ (\sigma^{+}) \\ \frac{1}{2h^2}\left[\frac{\mathbf{k}_l\cdot\mathbf{B}_1}{|\mathbf{k}_l||\mathbf{B}_1|}\frac{\mathbf{k}_l\cdot\mathbf{B}_2}{|\mathbf{k}_l||\mathbf{B}_2|}-1\right]^2 & , \quad q'' = -\ (\sigma^{-}) \\ 1-(b^{+}_{+}+b^{+}_{-}) & , \quad q'' = 0\ \ (\pi) \end{cases} \tag{3.77a}$$

$$b^{-}_{q''}(\mathbf{r}_2) = \begin{cases} \frac{1}{2h^2}\left[\frac{\mathbf{k}_l\cdot\mathbf{B}_1}{|\mathbf{k}_l||\mathbf{B}_1|}\frac{\mathbf{k}_l\cdot\mathbf{B}_2}{|\mathbf{k}_l||\mathbf{B}_2|}-1\right]^2 & , \quad q'' = +\ (\sigma^{+}) \\ \frac{1}{2h^2}\left[\frac{\mathbf{k}_l\cdot\mathbf{B}_1}{|\mathbf{k}_l||\mathbf{B}_1|}\frac{\mathbf{k}_l\cdot\mathbf{B}_2}{|\mathbf{k}_l||\mathbf{B}_2|}+1\right]^2 & , \quad q'' = -\ (\sigma^{-}) \\ 1-(b^{-}_{+}+b^{-}_{-}) & , \quad q'' = 0\ \ (\pi) \end{cases} \tag{3.77b}$$

$$b^{0}_{q''}(\mathbf{r}_2) = \begin{cases} \frac{1}{2}\left[\frac{\mathbf{k}_l\cdot\mathbf{B}_2}{|\mathbf{k}_l||\mathbf{B}_2|}\right]^2 & , \quad q'' = +\ (\sigma^{+}) \\ \frac{1}{2}\left[\frac{\mathbf{k}_l\cdot\mathbf{B}_2}{|\mathbf{k}_l||\mathbf{B}_2|}\right]^2 & , \quad q'' = -\ (\sigma^{-}) \\ 1-(b^{0}_{+}+b^{0}_{-}) & , \quad q'' = 0\ \ (\pi) \end{cases} \tag{3.77c}$$

The rescattering cross-section $\sigma_{R,q''}$ $(q''=-,0,+)$

In accord to Eq. 3.35 that defines the 2-level atom model's rescattering cross-section σ_R, we write the $F=0\rightarrow F'=1$ model's rescattering cross-section $\sigma_{R,q''}$ for the σ^-, π, σ^+ polarization-driven part of atom 2 $(q''=-,0,+)$ as

$$\sigma_{R,q''}(\mathbf{r}_1,\mathbf{r}_2,\mathbf{v}_1,\mathbf{v}_2)=\int d\omega\; S_{tot,q''}(\omega,\mathbf{r}_1,\mathbf{v}_1)\sigma_{A,q''}(\omega,\mathbf{r}_2,\mathbf{v}_2) \tag{3.78}$$

where $\sigma_{A,q''}$ denotes the corresponding absorption spectrum of atom 2, and

$$S_{tot,q''}(\omega,\mathbf{r}_1,\mathbf{v}_1)=\sum_{q'=+,0,-} w_{q''}^{q'}(\mathbf{r}_1)S_{q'}(\omega,\mathbf{r}_1,\mathbf{v}_1) \tag{3.79}$$

denotes the corresponding total emission spectrum of atom 1, as seen by atom 2. $S_{tot,q''}$ is composed of the normalized emission spectra S_-, S_0, S_+ for the respective σ^-, π, σ^+ polarization-driven parts of atom 1, with $w_{q''}^{q'}$ denoting the spectrum $S_{q'}$ weight $(q'=-,0,+)$ that takes into account the anisotropy of the scattered field, as governed by $\eta_{q'}$ (Eq. 3.70), and also the different orientations of atom 1 and atom 2 along their local B-vectors, as governed by the rescattering fraction $b_{q''}^{q'}$ (Eqs. 3.77(a-c)). The weight $w_{q''}^{q'}$ is given by

$$w_{q''}^{q'}(\mathbf{r}_1)=\frac{\eta_{q'}(\mathbf{r}_1)b_{q''}^{q'}(\mathbf{r}_2)}{w_{tot,q''}(\mathbf{r}_1,\mathbf{r}_2)}\quad,\quad w_{tot,q''}(\mathbf{r}_1,\mathbf{r}_2)=\sum_{q'=+,0,-}\eta_{q'}(\mathbf{r}_1)b_{q''}^{q'}(\mathbf{r}_2) \tag{3.80}$$

where $w_{tot,q''}$ denotes the total weight corresponding to the σ^-, π, σ^+ polarization-driven part of atom 2 $(q''=-,0,+)$, such that $w_{q''}^{-}+w_{q''}^{0}+w_{q''}^{+}=1$ and $S_{tot,q''}$ (Eq. 3.79) is correctly a normalized emission spectrum.

Observing Eq. 3.36 for $S(\omega)$ and Eq. 3.37 for $\sigma_A(\omega)$, we have, when using the notations $S_{q'}(\omega,\mathbf{r}_1,\mathbf{v}_1)=S_q(\omega)$ and $\sigma_{A,q''}(\omega,\mathbf{r}_2,\mathbf{v}_2)=\sigma_{A,q}(\omega)$ $(q=-,0,+)$:

$$\begin{aligned}S_q(\omega)=&\left[\frac{\Gamma^2+4\delta_q^2}{\Gamma^2+4\delta_q^2+2\Omega_{tot,q}^2}\right]Dirac(\omega-\delta_q)\\&+\frac{\Gamma\Omega_{tot,q}^2}{2\pi}\left(\frac{(\omega-\delta_q)^2+\frac{1}{2}\Omega_{tot,q}^2+\Gamma^2}{\Gamma^2\left[\frac{1}{2}\Omega_{tot,q}^2+\delta_q^2+\frac{1}{4}\Gamma^2-2(\omega-\delta_q)^2\right]^2+(\omega-\delta_q)^2\left[\Omega_{tot,q}^2+\delta_q^2+\frac{5}{4}\Gamma^2-(\omega-\delta_q)^2\right]^2}\right)\end{aligned} \tag{3.81}$$

$$\begin{aligned}\sigma_{A,q}(\omega)=&\frac{\sigma_0\Gamma}{4}\times\left\{\frac{\Gamma^2+4\delta_q^2}{\Gamma^2+4\delta_q^2+2\Omega_{tot,q}^2}\right\}\\&\times\left\{\frac{(-i\omega+i\delta_q+\Gamma)\left(-i\omega+i2\delta_q+\frac{\Gamma}{2}\right)+\frac{1}{2}i\Omega_{tot,q}^2(\omega-\delta_q)/\left(i\delta_q+\frac{\Gamma}{2}\right)}{(-i\omega+i\delta_q+\Gamma)\left(-i\omega+i2\delta_q+\frac{\Gamma}{2}\right)\left(-i\omega+\frac{\Gamma}{2}\right)+\Omega_{tot,q}^2\left(-i\omega+i\delta_q+\frac{\Gamma}{2}\right)}+c.c.\right\}\end{aligned} \tag{3.82}$$

where

$$\Omega_{tot,q}(\mathbf{r},\mathbf{v}) = \Gamma\sqrt{\frac{I_{tot,q}(\mathbf{r},\mathbf{v})}{2I_{sat}}} \tag{3.83}$$

expresses the total Rabi frequencies for the respective σ^-, π, σ^+ polarization-driven parts of the $F = 0 \rightarrow F' = 1$ atom as they scatter the corresponding total intensities $I_{tot,-}$, $I_{tot,+}$, $I_{tot,0}$ from the laser field (Eq. 3.45), and

$$\delta_q(\mathbf{r}) = \delta - q\mu B(\mathbf{r}) \tag{3.84}$$

expresses the corresponding trapping detunings incorporating the Zeeman effect due to $\mathbf{B}$. Recall that the Zeeman effect was otherwise neglected in the 2-level atom model counterpart (refer to section 3.1.4).

3.2.5 Summary table of the forces and effects

In this final subsection, we provide a summary table, Tab. 3.2, of the obtained expressions of our $F = 0 \rightarrow F' = 1$ model's 3D forces and effects.

We recapitulate the relevant equations that lead to the obtention of the forces and effects in Tab. 3.2. The relevant equations from section 3.2.1, "Trapping force", are Eqs. 3.44, 3.45, 3.51, 3.52, 3.53. From section 3.2.2, "Diffusion", they are Eqs. 3.54, 3.55, 3.56, 3.57, 3.58, 3.59. From section 3.2.3, "Intensity attenuation", it is Eq. 3.62. From section 3.2.4, "Rescattering force", they are Eqs. 3.63, 3.64, 3.65, 3.66, 3.70, 3.71, 3.72, 3.77, 3.78, 3.79, 3.80, 3.81, 3.82, 3.83, 3.84. For convenience, we also refer to Eq. 3.39, seen in section 3.1.4.

We have:

$$\sigma^{\pm}_{\alpha,q}(\mathbf{r},\mathbf{v}) = \frac{\sigma_0}{1+\frac{I_{tot,q}(\mathbf{r},\mathbf{v})}{I_{sat}}+4\frac{(\delta\mp k_L v_\alpha - q\mu B(\mathbf{r}))^2}{\Gamma^2}} \tag{3.44 revisited}$$

$$I_{tot,q}(\mathbf{r},\mathbf{v}) = \sum_{\alpha=\mathsf{x},\mathsf{y},\mathsf{z}} \left[p^{+}_{\alpha,q}(\mathbf{r})\mathcal{I}^{+}_{\alpha}(\mathbf{r},\mathbf{v}) + p^{-}_{\alpha,q}(\mathbf{r})\mathcal{I}^{-}_{\alpha}(\mathbf{r},\mathbf{v})\right] \tag{3.45 revisited}$$

$$p^{\pm}_{\alpha,q}(\mathbf{r}) = \begin{cases} \left(\frac{1}{2}\left[1 \pm \frac{\alpha' B'}{2B(\mathbf{r})}\right]\right)^2 & , \quad q = +\ (\sigma^+) \\ \left(\frac{1}{2}\left[1 \mp \frac{\alpha' B'}{2B(\mathbf{r})}\right]\right)^2 & , \quad q = -\ (\sigma^-) \\ 1 - (p^{\pm}_{\alpha,+} + p^{\pm}_{\alpha,-}) & , \quad q = 0\ \ (\pi) \end{cases} \tag{3.51 revisited}$$

$$s^{4level}_{tot}(\mathbf{r},\mathbf{v}) = \sum_{q=-,0,+} s_{tot,q}(\mathbf{r},\mathbf{v}) \tag{3.57 revisited}$$

$$s_{tot,q}(\mathbf{r},\mathbf{v}) = \sum_{\alpha=\mathsf{x},\mathsf{y},\mathsf{z}} \left[s^{+}_{\alpha,q}(\mathbf{r},\mathbf{v}) + s^{-}_{\alpha,q}(\mathbf{r},\mathbf{v})\right] \tag{3.58 revisited}$$

$$s^{\pm}_{\alpha,q}(\mathbf{r},\mathbf{v}) = \frac{p^{\pm}_{\alpha,q}(\mathbf{r})\mathcal{I}^{\pm}_{\alpha}(\mathbf{r},\mathbf{v})/I_{sat}}{1+4\frac{(\delta\mp k_L v_\alpha - q\mu B(\mathbf{r}))^2}{\Gamma^2}} \tag{3.59 revisited}$$

$$I_{R,q''}(\mathbf{r}_j) = \sum_{q'=+,0,-} b^{q'}_{q''}(\mathbf{r}_j) I_{S,q'}(\mathbf{r}_j) \tag{3.63 revisited}$$

$$P_{R,tot,q''}(\mathbf{r}_i,\mathbf{r}_j,\mathbf{v}_i,\mathbf{v}_j) = I_{R,q''}(\mathbf{r}_j)\sigma_{R,q''}(\mathbf{r}_i,\mathbf{r}_j,\mathbf{v}_i,\mathbf{v}_j) \tag{3.64 revisited}$$

$$P^{4level,i}_{R}(\mathbf{r}_j,\mathbf{v}_j) = \sum_{q''=+,0,-} P_{R,tot,q''}(\mathbf{r}_i,\mathbf{r}_j,\mathbf{v}_i,\mathbf{v}_j) \tag{3.65 revisited}$$

$$\eta_{q'}(\mathbf{r}_i) = \begin{cases} \frac{3}{4}\left[1+\left(\frac{\mathbf{k}_l\cdot\mathbf{B}_i}{|\mathbf{k}_l||\mathbf{B}_i|}\right)^2\right] & , \quad q' = +\,(\sigma^+) \\ \frac{3}{4}\left[1+\left(\frac{\mathbf{k}_l\cdot\mathbf{B}_i}{|\mathbf{k}_l||\mathbf{B}_i|}\right)^2\right] & , \quad q' = -\,(\sigma^-) \\ \frac{3}{2}\left[1-\left(\frac{\mathbf{k}_l\cdot\mathbf{B}_i}{|\mathbf{k}_l||\mathbf{B}_i|}\right)^2\right] & , \quad q' = 0 \;\; (\pi) \end{cases} \tag{3.70 revisited}$$

$$I_{S,q'}(\mathbf{r}_j) = \eta_{q'}(\mathbf{r}_i) \times \frac{P_{L,tot,q'}(\mathbf{r}_i,\mathbf{v}_i)}{4\pi|\mathbf{r}_{i,j}|^2} \tag{3.71 revisited}$$

$$P_{L,tot,q'}(\mathbf{r}_i,\mathbf{v}_i) = \sum_{\alpha=\mathrm{x,y,z}} [p^+_{\alpha,q'}(\mathbf{r}_i)\mathcal{I}^+_\alpha(\mathbf{r}_i,\mathbf{v}_i)\sigma^+_{\alpha,q'}(\mathbf{r}_i,\mathbf{v}_i) + p^-_{\alpha,q'}(\mathbf{r}_i)\mathcal{I}^-_\alpha(\mathbf{r}_i,\mathbf{v}_i)\sigma^-_{\alpha,q'}(\mathbf{r}_i,\mathbf{v}_i)] \tag{3.72 revisited}$$

$$\hat{\mathbf{r}}_{i,j} = \frac{\mathbf{r}_{i,j}}{|\mathbf{r}_{i,j}|} \quad , \quad \mathbf{r}_{i,j} = (\mathbf{x}_j - \mathbf{x}_i) + (\mathbf{y}_j - \mathbf{y}_i) + (\mathbf{z}_j - \mathbf{z}_i) \tag{3.39 revisited}$$

$$b^+_{q''}(\mathbf{r}_j) = \begin{cases} \frac{1}{2h^2}\left[\frac{\mathbf{k}_l\cdot\mathbf{B}_i}{|\mathbf{k}_l||\mathbf{B}_i|}\frac{\mathbf{k}_l\cdot\mathbf{B}_j}{|\mathbf{k}_l||\mathbf{B}_j|}+1\right]^2 & , \quad q'' = +\,(\sigma^+) \\ \frac{1}{2h^2}\left[\frac{\mathbf{k}_l\cdot\mathbf{B}_i}{|\mathbf{k}_l||\mathbf{B}_i|}\frac{\mathbf{k}_l\cdot\mathbf{B}_j}{|\mathbf{k}_l||\mathbf{B}_j|}-1\right]^2 & , \quad q'' = -\,(\sigma^-) \\ 1-(b^+_+ + b^+_-) & , \quad q'' = 0 \;\; (\pi) \end{cases} \tag{3.77a revisited}$$

$$b^-_{q''}(\mathbf{r}_j) = \begin{cases} \frac{1}{2h^2}\left[\frac{\mathbf{k}_l\cdot\mathbf{B}_i}{|\mathbf{k}_l||\mathbf{B}_i|}\frac{\mathbf{k}_l\cdot\mathbf{B}_j}{|\mathbf{k}_l||\mathbf{B}_j|}-1\right]^2 & , \quad q'' = +\,(\sigma^+) \\ \frac{1}{2h^2}\left[\frac{\mathbf{k}_l\cdot\mathbf{B}_i}{|\mathbf{k}_l||\mathbf{B}_i|}\frac{\mathbf{k}_l\cdot\mathbf{B}_j}{|\mathbf{k}_l||\mathbf{B}_j|}+1\right]^2 & , \quad q'' = -\,(\sigma^-) \\ 1-(b^-_+ + b^-_-) & , \quad q'' = 0 \;\; (\pi) \end{cases} \tag{3.77b revisited}$$

$$b^0_{q''}(\mathbf{r}_j) = \begin{cases} \frac{1}{2}\left[\frac{\mathbf{k}_l\cdot\mathbf{B}_j}{|\mathbf{k}_l||\mathbf{B}_j|}\right]^2 & , \quad q'' = +\,(\sigma^+) \\ \frac{1}{2}\left[\frac{\mathbf{k}_l\cdot\mathbf{B}_j}{|\mathbf{k}_l||\mathbf{B}_j|}\right]^2 & , \quad q'' = -\,(\sigma^-) \\ 1-(b^0_+ + b^0_-) & , \quad q'' = 0 \;\; (\pi) \end{cases} \tag{3.77c revisited}$$

$$\sigma_{R,q''}(\mathbf{r}_i,\mathbf{r}_j,\mathbf{v}_i,\mathbf{v}_j) = \int d\omega \; S_{tot,q''}(\omega,\mathbf{r}_i,\mathbf{v}_i)\sigma_{A,q''}(\omega,\mathbf{r}_j,\mathbf{v}_j) \tag{3.78 revisited}$$

$$S_{tot,q''}(\omega, \mathbf{r}_i, \mathbf{v}_i) = \sum_{q'=+,0,-} w_{q''}^{q'}(\mathbf{r}_i) S_{q'}(\omega, \mathbf{r}_i, \mathbf{v}_i) \qquad \text{(3.79 revisited)}$$

$$w_{q''}^{q'}(\mathbf{r}_i) = \frac{\eta_{q'}(\mathbf{r}_i) b_{q''}^{q'}(\mathbf{r}_j)}{w_{tot,q''}(\mathbf{r}_i, \mathbf{r}_j)} \quad , \quad w_{tot,q''}(\mathbf{r}_i, \mathbf{r}_j) = \sum_{q'=+,0,-} \eta_{q'}(\mathbf{r}_i) b_{q''}^{q'}(\mathbf{r}_j)$$

(3.80 revisited)

$\mathbf{r} = (x, y, z)$ and $\mathbf{v} = (v_\mathrm{x}, v_\mathrm{y}, v_\mathrm{z})$ are respectively the position and velocity of the atom. $\mathbf{r}_i$ and $\mathbf{v}_i$ are used to denote respectively the position and velocity of the atom that scatters light, while $\mathbf{r}_j$ and $\mathbf{v}_j$ are used to denote respectively the position and velocity of the atom that rescatters the scattered light.

$B(\mathbf{r}) = B'\sqrt{z^2 + \frac{1}{4}(x^2 + y^2)}$ is the magnitude of the magnetic field $\mathbf{B}(\mathbf{r})$ (Eq. 3.14). $\mathbf{B}_i \equiv \mathbf{B}(\mathbf{r}_i)$ and $\mathbf{B}_j \equiv \mathbf{B}(\mathbf{r}_j)$ refer to the magnetic field at the position of respectively the scattering atom and the rescattering atom.

$q = -, 0, +$ refers to the respective σ^-, π, σ^+ polarization-driven parts of the $(F = 0 \to F' = 1)$ atom, with $q' = -, 0, +$ and $q'' = -, 0, +$ referring to such parts of respectively the scattering atom and the rescattering atom.

In Eq. 3.51, $\alpha' = x, y, 2z$ for respectively $\hat{\boldsymbol{\alpha}} = \hat{\mathbf{x}}, \hat{\mathbf{y}}, \hat{\mathbf{z}}$.

In Eqs. 3.77(a, b), $h = \sqrt{1 + \left(\frac{\mathbf{k}_l \cdot \mathbf{B}_i}{|\mathbf{k}_l||\mathbf{B}_i|}\right)^2}$ (see below Eq. 3.73, with Eq. 3.67 being used).

In Eq. 3.78, $\sigma_{A,q''}(\omega, \mathbf{r}_j, \mathbf{v}_j)$ is given by Eq. 3.82, and, in Eq. 3.79, $S_{q'}(\omega, \mathbf{r}_i, \mathbf{v}_i)$ is given by Eq. 3.81. Here we use

$$\Omega_{tot,q}(\mathbf{r}, \mathbf{v}) = \Gamma\sqrt{\frac{I_{tot,q}(\mathbf{r}, \mathbf{v})}{2I_{sat}}} \qquad \text{(3.83 revisited)}$$

$$\delta_q(\mathbf{r}) = \delta - q\mu B(\mathbf{r}) \qquad \text{(3.84 revisited)}$$

Trapping force	$\mathbf{F}_{tr}^{4level}(\mathbf{r},\mathbf{v}) = F_{tr,\mathsf{x}}^{4level}(\mathbf{r},\mathbf{v})\hat{\mathbf{x}} + F_{tr,\mathsf{y}}^{4level}(\mathbf{r},\mathbf{v})\hat{\mathbf{y}} + F_{tr,\mathsf{z}}^{4level}(\mathbf{r},\mathbf{v})\hat{\mathbf{z}}$ $F_{tr,\alpha}^{4level}(\mathbf{r},\mathbf{v}) = \frac{1}{c}\left(\sum_{q=-,0,+}[p_{\alpha,q}^{+}(\mathbf{r})\mathcal{I}_{\alpha}^{+}(\mathbf{r},\mathbf{v})\sigma_{\alpha,q}^{+}(\mathbf{r},\mathbf{v}) - p_{\alpha,q}^{-}(\mathbf{r})\mathcal{I}_{\alpha}^{-}(\mathbf{r},\mathbf{v})\sigma_{\alpha,q}^{-}(\mathbf{r},\mathbf{v})]\right) \quad , \quad \alpha = \mathsf{x},\mathsf{y},\mathsf{z}$
Rescattering force	$\mathbf{F}_{rsc}^{4level}(\mathbf{r}_j,\mathbf{v}_j) = \sum_{i\neq j}\frac{P_R^{4level,i}(\mathbf{r}_j,\mathbf{v}_j)}{c}\hat{\mathbf{r}}_{i,j}$
Diffusion	$D_{3D}^{4level}(\mathbf{r},\mathbf{v}) = D_{vac,3D}^{4level}(\mathbf{r},\mathbf{v}) + D_{las,3D}^{4level}(\mathbf{r},\mathbf{v})$ $D_{vac,3D}^{4level}(\mathbf{r},\mathbf{v}) = \hbar^2 k_L^2 \frac{\Gamma}{4}\frac{s_{tot}^{4level}(\mathbf{r},\mathbf{v})}{1+s_{tot}^{4level}(\mathbf{r},\mathbf{v})}$ $D_{las,3D}^{4level}(\mathbf{r},\mathbf{v}) = \hbar^2 k_L^2 \frac{\Gamma}{4}\frac{s_{tot}^{4level}(\mathbf{r},\mathbf{v})}{(1+s_{tot}^{4level}(\mathbf{r},\mathbf{v}))^3} \times \left\{1 + \frac{12\delta^2-\Gamma^2}{4\delta^2+\Gamma^2}s_{tot}^{4level}(\mathbf{r},\mathbf{v}) + (s_{tot}^{4level}(\mathbf{r},\mathbf{v}))^2\right\}$
Intensity attenuation	$\mathcal{I}_{\mathsf{x}}^{+/-}(\mathbf{r},\mathbf{v}) = I_\infty e^{-\int_{-\infty/x}^{x/+\infty} dx' \sum_{q=-,0,+}\left[p_{\mathsf{x},q}^{+/-}(x',y,z)\sigma_{\mathsf{x},q}^{+/-}(x',y,z,\mathbf{v}(x',y,z))\right]\rho(x',y,z)}$ $\mathcal{I}_{\mathsf{y}}^{+/-}(\mathbf{r},\mathbf{v}) = I_\infty e^{-\int_{-\infty/y}^{y/+\infty} dy' \sum_{q=-,0,+}\left[p_{\mathsf{y},q}^{+/-}(x,y',z)\sigma_{\mathsf{y},q}^{+/-}(x,y',z,\mathbf{v}(x,y',z))\right]\rho(x,y',z)}$ $\mathcal{I}_{\mathsf{z}}^{+/-}(\mathbf{r},\mathbf{v}) = I_\infty e^{-\int_{-\infty/z}^{z/+\infty} dz' \sum_{q=-,0,+}\left[p_{\mathsf{z},q}^{+/-}(x,y,z')\sigma_{\mathsf{z},q}^{+/-}(x,y,z',\mathbf{v}(x,y,z'))\right]\rho(x,y,z')}$

Table 3.2: $F = 0 \rightarrow F' = 1$ model MOT forces and effects in 3D.

3.3 The simulation algorithm and methods

In this section, we explain the algorithm and methods used in our simulations, incorporating the $F = 0 \rightarrow F' = 1$ model (section 3.2). The algorithm that we use is the Leapfrog algorithm, while the methods that we use include the super-particle method and the tube method. The Leapfrog algorithm allows us to propagate the MOT cloud in time, while the super-particle method yields great improvement in the simulation speed and with the tube method we are able to evaluate beam intensity attenuation.

3.3.1 The Leapfrog algorithm

In this subsection, we begin by providing the basics of the numerical algorithm known as the Leapfrog algorithm. It allows us to propagate the MOT cloud in time. The strengths of the Leapfrog algorithm are stated and other, commonly used numerical algorithms, i.e. the Euler and Runge-Kutta (RK) algorithms, are very briefly mentioned and compared to the Leapfrog algorithm. Finally, we explain how the Leapfrog algorithm is implemented in our simulations. We note that in-depth treatments of all these algorithms can be found in e.g. Refs. [64, 65, 66].

Basics of the Leapfrog algorithm

The Leapfrog algorithm is used to numerically integrate differential equations that have the form of the Newton's equations

$$\begin{aligned} \frac{d\mathbf{v}}{dt} &= \frac{\mathbf{F}_{tot}(\mathbf{r})}{M} \\ \frac{d\mathbf{r}}{dt} &= \mathbf{v} \end{aligned} \tag{3.85}$$

where $\mathbf{v}$ and $\mathbf{r}$ are respectively the velocity and position of the particle, M is the mass of the particle, and $\mathbf{F}_{tot}(\mathbf{r})$ is the position-dependent total force acting on the particle. (The total force in our simulations is also velocity-dependent, and the consequence of this will be seen shortly.)

The Leapfrog algorithm employs the following iterative scheme for updating the velocity and position in time:

1. Compute the force $\mathbf{F}_{tot}(t_n) = \mathbf{F}_{tot}(\mathbf{r}(t_n))$.
2. Update the velocity $\mathbf{v}(t_{n+1/2}) = \mathbf{v}(t_{n-1/2}) + \frac{\mathbf{F}_{tot}(t_n)}{M}\Delta t$.
3. Update the position $\mathbf{r}(t_{n+1}) = \mathbf{r}(t_n) + \mathbf{v}(t_{n+1/2})\Delta t$.

where the integer $n = 0, 1, 2, \ldots$ marks the iteration step, with $n = 0$ used when initiating the scheme, and Δt is the size of the time-step. The velocities and

positions are updated at interleaved time points, and thus the velocities and positions are said to *leapfrog* over each other, as Fig. 3.8 illustrates. When the scheme is initiated ($n = 0$), the position $\mathbf{r}(t_0)$ and velocity $\mathbf{v}(t_{-1/2})$ must be specified. Because at the beginning one only has $\mathbf{r}(t_0)$ and $\mathbf{v}(t_0)$, to obtain $\mathbf{v}(t_{-1/2})$ one can make use of the approximation $\mathbf{v}(t_{-1/2}) \approx \mathbf{v}(t_0) - \frac{1}{2}\frac{\mathbf{F}_{tot}(t_0)}{M}\Delta t$ [67]. Alternatively (and this is what we use, as seen shortly), $\mathbf{v}(t_{-1/2}) \approx \mathbf{v}(t_0)$.

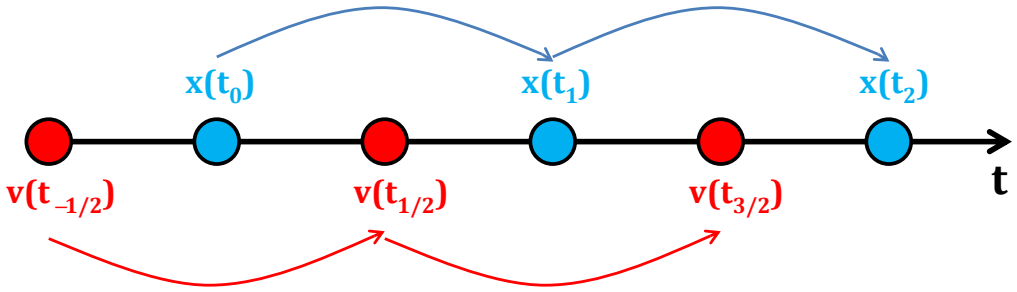

Figure 3.8: Illustration of the Leapfrog algorithm. Specifying the initial velocity $\mathbf{v}(t_{-1/2})$ and initial position $\mathbf{r}(t_0)$ of the particle, the subsequent velocities and positions are updated at interleaved time points, and thus the velocities and positions are said to *leapfrog* over each other.

The Leapfrog algorithm is a second-order algorithm, meaning that the global error, i.e. error at a given point in time, is proportional to Δt^2. The Euler algorithm and Runge-Kutta 2 (RK2) are commonly used numerical algorithms for solving ordinary differential equations, where the Euler algorithm is a first-order algorithm and RK2 is of the same order as Leapfrog, i.e. second-order. Another commonly employed algorithm, Runge-Kutta 4 (RK4), has an improved accuracy compared to RK2 and is a fourth-order algorithm. The Leapfrog algorithm, although being second-order, requires the same number of function evaluations per iteration step as the first-order Euler algorithm. The RK algorithms are, on the other hand, more computationally expensive compared to the Leapfrog algorithm.

The main strengths of the Leapfrog algorithm come from it being a time-reversible and symplectic algorithm. These numerical properties are highly desirable as they guarantee that the physical aspects of simulation problems are respected. With a time-reversible algorithm one can perform any amount of iteration steps forward in time, then do the same amount of steps backwards in time, and arrive at one's starting point. Symplectic algorithms preserve the total energy in the simulated system over time. For algorithms that are not symplectic, a numerical drift in the total energy builds up over a long period of simulation, compromising the long-term stability of the problem. Due to their energy-preserving property, symplectic algorithms are said to be *globally stable* [67]. The Euler and RK algorithms are neither time-reversible nor symplectic.

Implementing the Leapfrog algorithm in MOT simulations

In our simulations of the MOT, we consider simulating particle dynamics governed by Newton's equations of the form seen in Eq. 3.85. The Leapfrog algorithm is used to numerically integrate the equations, providing us with knowledge of the positions and velocities of the particles at points in time. As will be explained in the next subsection, we make use of the so-called super-particles for representing collections of regular particles in order to reduce the numerical effort of the simulations. For now, we assume we are dealing with regular particles, such that the total force acting on the particle at the position $\mathbf{r}_\mathrm{i}$ with the velocity $\mathbf{v}_\mathrm{i}$, will be, within our $F = 0 \rightarrow F' = 1$ model,

$$\mathbf{F}_{tot}^{4level}(\mathbf{r}_\mathrm{i}, \mathbf{v}_\mathrm{i}) = \mathbf{F}_{tr}^{4level}(\mathbf{r}_\mathrm{i}, \mathbf{v}_\mathrm{i}) + \mathbf{F}_{rsc}^{4level}(\mathbf{r}_\mathrm{i}, \mathbf{v}_\mathrm{i}) + \mathbf{D}^{4level}(\mathbf{r}_\mathrm{i}, \mathbf{v}_\mathrm{i}) \tag{3.86}$$

where $\mathbf{F}_{tr}^{4level}$ and $\mathbf{F}_{rsc}^{4level}$ are respectively the trapping force and the rescattering force acting on the particle, with the expressions for these forces found in Tab. 3.2, and $\mathbf{D}^{4level}$ is the force on the particle induced by the diffusion processes, with the momentum diffusion coefficient given by D_{3D}^{4level} and found in Tab. 3.2. D_{3D}^{4level} can be simulated by introduction of Gaussian white noise, such that $\mathbf{D}^{4level}$ will take the form [68]

$$\mathbf{D}^{4level} = \sqrt{\frac{2D_{3D}^{4level}}{3\Delta t}} \times (Gaussian\ \ white\ \ noise) \tag{3.87}$$

with Δt being the size of the time-step in the Leapfrog algorithm.

In the computation of $\mathbf{F}_{tot}^{4level}$ at a given iteration step (refer to the gray box in the introduction of the Leapfrog algorithm), we use cloud particle positions and velocities at interleaved time points: at the first iteration step ($n = 0$) we use $\mathbf{r}(t_0)$ and $\mathbf{v}(t_{-1/2})$, at the second step ($n = 1$) we use $\mathbf{r}(t_1)$ and $\mathbf{v}(t_{1/2})$, at the third step ($n = 2$) we use $\mathbf{r}(t_2)$ and $\mathbf{v}(t_{3/2})$, etc. To obtain $\mathbf{v}(t_{-1/2})$, we make use of the approximation $\mathbf{v}(t_{-1/2}) \approx \mathbf{v}(t_0)$ (noted upon in the introduction of the Leapfrog algorithm); the x-, y-, z-components of $\mathbf{v}(t_0)$ are random between 0 and 0.01 m/s (much less than the RMS velocity at the Doppler temperature, $\sim$0.2 m/s). We assume such approximation (i.e. $\mathbf{v}(t_{-1/2}) \approx \mathbf{v}(t_0)$) to be valid for a small enough simulation time-step Δt used. We note that in the next section, surrounding the simulations tests, we will explain how Δt is picked. We also note that, apart from $\mathbf{D}^{4level}$, the velocity-dependence in our total force $\mathbf{F}_{tot}^{4level}$ makes the Leapfrog algorithm to no longer be time-reversible.

Before presenting our employed simulation methods (the super-particle method and the tube method), we sketch how the whole simulation is implemented:

1. At t_0, a Gaussian cloud is generated, composed of super-particles.
2. Beam intensity attenuation is then evaluated at the positions of the super-particles, with help of the tube method.
3. Forces acting on each super-particle are then found.
4. Having the forces, the Leapfrog algorithm propagates the cloud forward in time by one Δt.
5. At the new positions, the intensity attenuation is first evaluated, then the forces are found, and then the Leapfrog algorithm propagates the cloud forward in time by one Δt. This cycle is repeated until the simulation end time t_{end}.

3.3.2 The super-particle method

In this subsection, we begin by providing the basics of the numerical method known as the super-particle method. Its purpose is to increase the simulation speed. Finally, we explain how this method is implemented in our simulations. We note that the super-particle method stems from the broader numerical method known as the Particle-In-Cell method [69, 70, 71], commonly employed in plasma physics simulations.

Basics of the super-particle method

The super-particle method involves utilization of the so-called super-particle, which is a particle that represents a collection of regular particles (atoms). Having a regular particle amount N and a super-particle amount N_{sup}, the regular particle amount that a single super-particle represents is $\frac{N}{N_{sup}}$. A single super-particle represents often a vast amount of regular particles, for instance, hundreds of billion in magnetopause simulations [70], yielding a dramatic increase in the simulation speed, although at the trade-off of accuracy. Closer to our topic, the super-particle method was used in the quasi-1D simulations of balanced MOT instabilities [40].

Implementing the super-particle method in MOT simulations

The justification of using super-particles in our simulations is obviously similar to that in Ref. [40]. As we saw from our experiments (Chapter 2), the instabilities could contain an excess of $\sim 10^{10}$ atoms. Because the rescattering force leads to an N^2 problem (refer to Eq. 3.66), the computation of this one force with 10^{10} particles would require no less than $(10^{10})^2$ operations. Such an impressive number of operations is further magnified by the fact that our simulations require typically several thousands of iteration steps to be completed. Indeed, simulating the behavior of the real number of particles would be impractical to do on a desktop computer[4]. In our simulations, we therefore choose to replace the regular particles with the super-particles.

As we implement the super-particle method in our simulations, we scale the mass and scattering cross-section of each super-particle according to how many regular particles the super-particle represents, as specified by the ratio $\frac{N}{N_{sup}}$. The mass of the super-particle is $\frac{N}{N_{sup}}M$, and its on-resonance scattering cross-section is $\frac{N}{N_{sup}}\sigma_0$. Observing Eq. 3.86 for the total force on the regular particle, we then write the total force on the super-particle at the position $\mathbf{r}_\mathrm{i}$ with the velocity $\mathbf{v}_\mathrm{i}$ as

$$\mathbf{F}^{4level}_{tot,sup}(\mathbf{r}_\mathrm{i},\mathbf{v}_\mathrm{i}) = \frac{N}{N_{sup}}\mathbf{F}^{4level}_{tr}(\mathbf{r}_\mathrm{i},\mathbf{v}_\mathrm{i}) + \left(\frac{N}{N_{sup}}\right)^2 \mathbf{F}^{4level}_{rsc}(\mathbf{r}_\mathrm{i},\mathbf{v}_\mathrm{i}) + \frac{N}{N_{sup}}\mathbf{D}^{4level}(\mathbf{r}_\mathrm{i},\mathbf{v}_\mathrm{i}) \tag{3.88}$$

[4] As of 2020, one of the fastest computer processors, AMD Ryzen Threadripper 3990X, can perform just over 10^{12} operations per second at 4.35 GHz; see `https://www.amd.com`.

$\mathbf{F}_{tr}^{4level}$ carries the $\frac{N}{N_{sup}}$ scaling because $\mathbf{F}_{tr}^{4level}$ (Eq. 3.53) is written as a sum of terms that contain the scattering cross-section $\sigma_{\alpha,q}^{\pm} \propto \sigma_0$. $\mathbf{F}_{rsc}^{4level}$ carries the $\left(\frac{N}{N_{sup}}\right)^2$ scaling because $\mathbf{F}_{rsc}^{4level}$ (Eq. 3.66) is written as a sum of terms that contain a product of the scattering cross-section $\sigma_{\alpha,q}^{\pm} \propto \sigma_0$ and the rescattering cross-section $\sigma_{R,q} \propto \sigma_0$ (refer to Eqs. 3.63, 3.64, 3.65, 3.71, 3.72). $\mathbf{D}^{4level}$ carries the $\frac{N}{N_{sup}}$ scaling for the following reasons. According to Eq. 3.31, we have $D_{3D}^{4level} \propto \gamma_{3D} T_{lim}$, where the trapping force's friction coefficient γ_{3D} carries the $\frac{N}{N_{sup}}$ scaling as $\mathbf{F}_{tr}^{4level}$ carries the same scaling, and the limit temperature T_{lim} carries the $\frac{N}{N_{sup}}$ scaling, as according to the equipartition theorem, we have $T_{lim} \propto M$; moreover, according to Eq. 3.87, $\mathbf{D}^{4level}$ involves a square root of D_{3D}^{4level}. Taking everything into account, the scaling of $\mathbf{D}^{4level}$ is thus $\frac{N}{N_{sup}}$.

We note that in the upcoming simulation-testing section, we will explain how the super-particle number is picked.

3.3.3 The tube method

In this subsection, we begin by providing the basics of the numerical method that we refer to as the tube method, devised with the purpose of evaluating beam intensity attenuation at the positions of the super-particles. Then, we explain how this method is implemented in our simulations and, finally, explain what is done so to additionally implement the effect of beam cross-saturation.

Basics of the tube method

Fig. 3.9 displays the first part of an illustration of the tube method in 2D, and Fig. 3.10 displays the second part. Starting with Fig. 3.9, the upper two drawings depict the same cloud composed of super-particles, shown as black dots, and it is imagined that each beam is segmented into rectangular tubes oriented parallel to the beam's propagation direction. During the cloud's evolution, the tubes remain at fixed positions, with the width of all the tubes being of a set size. The lower drawing displays the same cloud, with the green dots indicating the positions of the points where intensity of each beam is calculated first. The green dots are placed at grid-point positions located through the center of the tubes. As Fig. 3.10 displays, in the calculation of e.g. the $+\hat{\mathbf{x}}$ directed beam's intensity at the position of a given green dot, the super-particles that contribute are only those that are within the tube associated with this green dot and, at the same time, are positioned at x-values smaller than of this green dot. Once the intensities of each beam at the positions of the green dots are calculated, the intensities at the positions of the super-particles are found by means of interpolation.

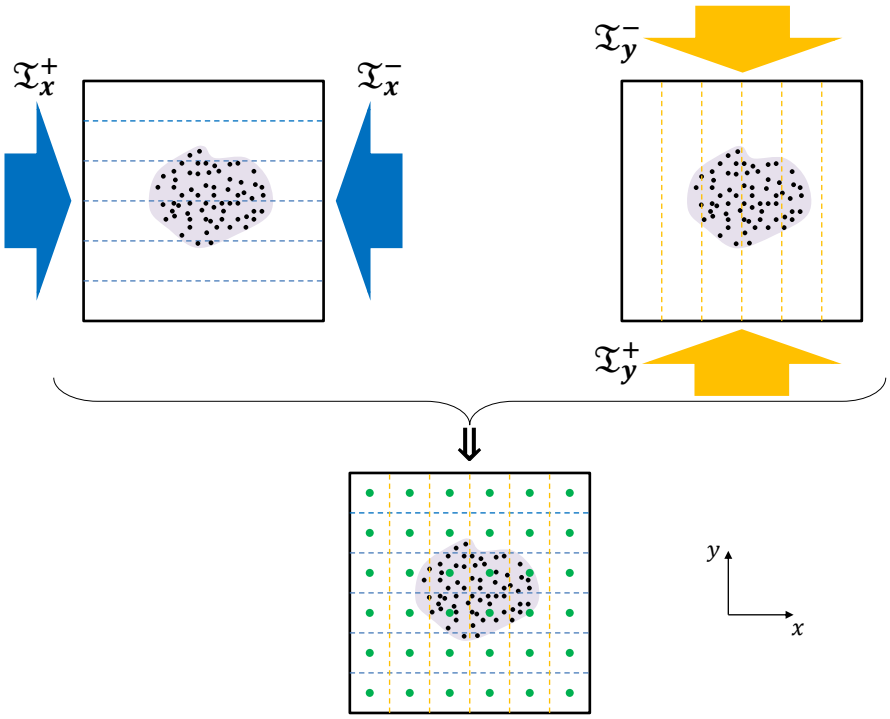

Figure 3.9: Part one of a 2D illustration of the tube method used for evaluating beam intensity attenuation at super-particle positions. The upper two drawings depict the same cloud composed of super-particles, shown as black dots, where it is imagined that each beam (of respective intensity $\mathcal{I}_x^+$, $\mathcal{I}_x^-$, $\mathcal{I}_y^+$, $\mathcal{I}_y^-$) is segmented into rectangular tubes oriented parallel to the beam's propagation direction (dashed blue and orange lines indicate the segmentation). The lower drawing displays the same cloud, with the green dots indicating the positions of the points where intensity of each beam is calculated first. The green dots are placed at grid-point positions located through the center of the tubes. Part two of the illustration is displayed in Fig. 3.10.

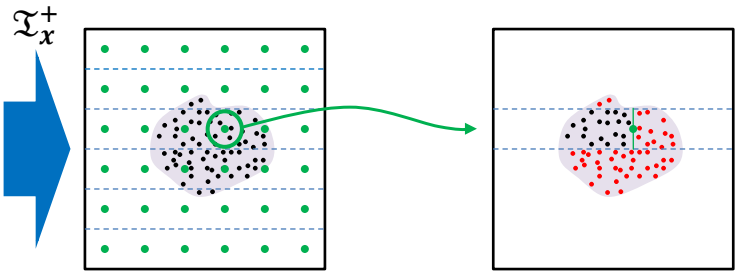

Figure 3.10: Part two of a 2D illustration of the tube method used for evaluating beam intensity attenuation at super-particle positions. In the calculation of e.g. the $+\hat{\mathbf{x}}$ directed beam's intensity at the position of a green dot encircled in green on the left drawing, the super-particles that contribute are only those that are within the tube associated with this green dot and, at the same time, are positioned at x-values smaller than of this green dot. The red dots seen on the right drawing are the super-particles that are excluded from the intensity calculation for the selected green dot. Once the intensities of each beam at the positions of the green dots are calculated, the intensities at the positions of the super-particles are found by means of interpolation.

Implementing the tube method in MOT simulations

We implement the tube method in our 3D simulations. To evaluate beam intensity attenuation at the super-particle positions, a fixed grid of points is created in the 3D space and intensity of each beam is calculated at the positions of the grid-points that encapsulate the super-particles (overspilled grid-points are neglected), after which the intensity at each super-particle position is found by means of interpolation. The interpolated intensity values are then used in the calculation of the forces (Eq. 3.88). Note that if there are super-particles appearing outside the grid, which can happen in the unstable regime, additional grid-points are created that encapsulate these super-particles and the interpolation proceeds as usual.

The numerical calculation of a beam's intensity at a given green dot position involves the assumption that a given super-particle at $\mathbf{r}_\mathsf{i}$ is represented by a Dirac delta function $\delta(\mathbf{r}-\mathbf{r}_\mathsf{i})$, allowing to write the density of the cloud as $\rho(\mathbf{r}) = \sum_\mathsf{i}\delta(\mathbf{r}-\mathbf{r}_\mathsf{i}) = \sum_\mathsf{i}\delta(x-x_\mathsf{i})\delta(y-y_\mathsf{i})\delta(z-z_\mathsf{i})$. As an example, concentrating on the $+\hat{\mathbf{x}}$ directed beam, the integral appearing in the expression of the beam's intensity $\mathcal{I}_x^+$ (see Tab. 3.2) is numerically determined from

$$
\begin{aligned}
&\int_{-\infty}^{x} dx' \sum_{q=-,0,+} \left[p^+_{\mathsf{x},q}(x',y,z)\sigma^+_{\mathsf{x},q}\left(x',y,z,\mathbf{v}(x',y,z)\right)\right]\rho(x',y,z)\\
&= \int_{-\infty}^{x} dx' \sum_{q=-,0,+} \left[p^+_{\mathsf{x},q}(x',y,z)\sigma^+_{\mathsf{x},q}\left(x',y,z,\mathbf{v}(x',y,z)\right)\right]\sum_\mathsf{i}\delta(x'-x_\mathsf{i})\delta(y-y_\mathsf{i})\delta(z-z_\mathsf{i})\\
&= \sum_{x_\mathsf{i}<x}\left\{\sum_{q=-,0,+}\left[p^+_{\mathsf{x},q}(x_\mathsf{i},y,z)\sigma^+_{\mathsf{x},q}\left(x_\mathsf{i},y,z,\mathbf{v}(x_\mathsf{i},y,z)\right)\right]\delta(y-y_\mathsf{i})\delta(z-z_\mathsf{i})\right\}\\
&\approx \frac{1}{W^2}\times\sum_{\substack{x_\mathsf{i}<x\\ |y_\mathsf{i}-y|<W/2\\ |z_\mathsf{i}-z|<W/2}}\left\{\sum_{q=-,0,+}\left[p^+_{\mathsf{x},q}(x_\mathsf{i},y_\mathsf{i},z_\mathsf{i})\sigma^+_{\mathsf{x},q}\left(x_\mathsf{i},y_\mathsf{i},z_\mathsf{i},\mathbf{v}(x_\mathsf{i},y_\mathsf{i},z_\mathsf{i})\right)\right]\right\}
\end{aligned}
\tag{3.89}
$$

where W is the width of the tube, and W^2 is thus the transverse area of the tube. We note that in the upcoming simulation-testing section, we will explain how W is picked.

With the above expression, the intensity $\mathcal{I}_x^+$ at a given green dot position is therefore numerically calculated from

$$
\mathcal{I}_x^+(\mathbf{r}) = I_\infty exp\left(-\frac{N}{N_{sup}}\frac{1}{W^2}\times\sum_{\substack{x_\mathsf{i}<x\\ |y_\mathsf{i}-y|<W/2\\ |z_\mathsf{i}-z|<W/2}}\left\{\sum_{q=-,0,+}\left[p^+_{\mathsf{x},q}(x_\mathsf{i},y_\mathsf{i},z_\mathsf{i})\sigma^+_{\mathsf{x},q}\left(x_\mathsf{i},y_\mathsf{i},z_\mathsf{i},\mathbf{v}(x_\mathsf{i},y_\mathsf{i},z_\mathsf{i})\right)\right]\right\}\right)
\tag{3.90}
$$

where the multiplication by the ratio $\frac{N}{N_{sup}}$ is done because the scattering cross-section $\sigma^+_{\mathsf{x},q} \propto \sigma_0$, with σ_0 carrying the $\frac{N}{N_{sup}}$ scaling (refer to section 3.3.2).

Now, as we recall the full expression $\sigma^+_{\mathsf{x},q} = \frac{\sigma_0}{1+\frac{I_{tot,q}}{I_{sat}}+4\frac{(\delta-k_L v_{\mathsf{x}}-q\mu B(\mathbf{r}))^2}{\Gamma^2}}$ (see Eq. 3.44), we observe that to calculate $\mathcal{I}^+_x$ we need to have the knowledge of $I_{tot,q} = \sum_{\alpha=\mathsf{x},\mathsf{y},\mathsf{z}}[p^+_{\alpha,q}\mathcal{I}^+_\alpha + p^-_{\alpha,q}\mathcal{I}^-_\alpha]$ (see Eq. 3.45), which includes all the intensities $\mathcal{I}^\pm_\alpha$, $\alpha = \mathsf{x},\mathsf{y},\mathsf{z}$, at a given green dot position. We have previously introduced the term $\frac{I_{tot,q}}{I_{sat}}$ into scattering cross-sections to take into account the effect of beam cross-saturation. We proceed next outlining how we numerically determine $I_{tot,q}$, such that beam cross-saturation can be implemented.

Implementing the beam cross-saturation effect in MOT simulations

As we wish to implement the beam cross-saturation effect, the calculation of beam intensities at the grid-point positions (green dots in the tube method illustrations) involves usage of a while-loop. To start this loop, one must specify initial values for the intensities (discussed in the next paragraph), which are used to calculate $I_{tot,q}$. Having this $I_{tot,q}$, new beam intensities can be found (as in Eq. 3.90). These new intensities are then used to construct intensities that are equal mixtures of new and old (last step) intensities, i.e. we construct "[{New intensities} + {Old intensities}]×1/2". The constructed intensities are compared to the old intensities, and if the constructed intensities are not convergent, these are fed back into the loop. The loop terminates when the constructed intensities are convergent. (The convergent intensities are then used in the interpolation of the intensities at the super-particles positions, after which the forces acting on the super-particles are found.)

At the first Leapfrog algorithm iteration step, we start the while-loop with the beam intensities picked to be I_∞ (the unattenuated intensity value). Note that any initial values can in principle work, due to the convergent intensities being independent of such choice. At the second Leapfrog algorithm iteration step, we start the while-loop with the convergent beam intensities found in the last iteration step, and so on for the remaining iteration steps. Note that the convergent solutions (of the intensities) for the iteration steps that follow after the first iteration step are found faster than for the first iteration step, because of the super-particle distribution at the new step being relatively close to the distribution of the previous step.

Of course, we have no reason to believe that we implement beam cross-saturation correctly with the six beams involved, as no analytical results exist to be compared with the numerical results. Nevertheless, in the upcoming simulation-testing section we will demonstrate that the procedure involving the while-loop works correctly when one beam is considered, where we can compare with iteratively computed results.

3.4 The simulation tests

In this section, we cover the tests we have done in making sure that correct numerical results are obtained in our main simulations (section 3.5). Following a logical order, we cover first the tests of the simulation algorithm and methods (section 3.3), and then the tests of the $F = 0 \rightarrow F' = 1$ model's forces and effects (section 3.2). We start off by explaining how we pick the time-step in the Leapfrog algorithm, after which we explain how we pick the number of super-particles and then how the tube-width is picked in the tube method. Afterwards, we show the test for the implementation of the beam cross-saturation effect, where the beam transmissions found using the employed while-loop when only one beam is considered are compared with the corresponding iteratively computed results. Next, we show the tests for the trapping force plus diffusion, where the numerically determined limit temperatures and cloud densities in the temperature-limited regime are compared with the corresponding analytical predictions. Then, we show the test for the rescattering force involving its symmetry, where it is checked that for a pair of motionless particles the ratio of the rescattering force's magnitude between them remains at unity when they are mirrored through the trap center. Finally, we show the test for the simulated stable cloud size versus the atom number N, where a comparison with the Wieman model's $N^{1/3}$ scaling is made.

Before we start, we bring into attention that in the tests where the diffusion is turned on, we neglect the Doppler and Zeeman effects in the momentum diffusion coefficient D_{3D}^{4level} (Eq. 3.54), in that way respecting this same choice as in our main simulations (the choices in the main simulations are elaborated more in section 3.5). Also, we set the gyromagnetic ratio $\mu = 2\pi \times 1.4 \times 10^6$ Hz/G, as we do in our main simulations. Moreover, for the atom mass M, it is picked to be that used in our main simulations - of the atomic species Rb-87 (see footnote 1 in section 2.1.1 for the value of M).

3.4.1 Picking the time-step in the Leapfrog algorithm

In this subsection, we explain how we pick the time-step Δt in the Leapfrog algorithm (section 3.3.1) employed in simulating cloud evolution. The numerically and analytically found particle trajectories are first compared and then used to support a devised *rule of thumb* for picking Δt.

Let us examine Fig. 3.11, where we compare the single particle z-trajectories that are numerical (solid blue curves) and analytical (dotted red curves). Different ∇B and Δt values are considered at fixed values of δ and s_0. In obtaining the numerical results, we have turned off the diffusion and used the full expression of the trapping force (Tab. 3.2). For our picked initial velocity and position, the trapping force approximately describes a damped harmonic oscillator (Eq. 3.19), which has the analytical solution (with $x(t) = y(t) = 0$)

$$z(t) = \mathcal{A}_0 e^{-\frac{\gamma_{3D}}{2M}t} sin(\omega'_{tr,3D}t + \phi_0) \tag{3.91}$$

where $\omega'_{tr,3D} = \sqrt{\omega^2_{tr,3D} - \frac{\gamma^2_{3D}}{4M^2}}$ is the damped trapping frequency, with $\omega_{tr,3D} = \sqrt{\kappa_{3D}/M}$ being the (undamped) trapping frequency, $\mathcal{A}_0 = \sqrt{\mathsf{a}_0^2 + \mathsf{b}_0^2}$ and $\phi_0 = tan^{-1}(\mathsf{a}_0/\mathsf{b}_0)$ are respectively the initial amplitude and phase offset of the oscillator, with the constants $\mathsf{a}_0 = z(0)$ and $\mathsf{b}_0 = \frac{v_z(0) + \frac{\gamma_{3D}}{2M} z(0)}{\omega'_{tr,3D}}$, with $z(0)$ and $v_z(0)$ being respectively the initial position and initial velocity of the particle.

As seen in Fig. 3.11, when $\Delta t > 1/\omega_{tr,3D}$ (first column) and $\Delta t = 1/\omega_{tr,3D}$ (second column), the numerical solutions can diverge at long times, whereas for $\Delta t \ll 1/\omega_{tr,3D}$ (third column) the numerical and analytical solutions match almost perfectly. It may be surprising that the divergence can occur for $\Delta t = 1/\omega_{tr,3D}$, because $\omega_{tr,3D} \gtrapprox \omega'_{tr,3D}$, such that Δt is smaller than the damping period. However, we must bear in mind that we are bounded by the numerical error, and when we work very near the largest frequency in the system (notice the approximate-sign in $\omega_{tr,3D} \gtrapprox \omega'_{tr,3D}$), this error can be significant enough to produce the divergence. Naturally, this error becomes insignificant as Δt is much smaller than the inverse of the largest frequency in the system, in which case an almost exact match between numerical and analytical solutions can be obtained, like e.g. in Fig. 3.11 (third column).

We use the results in Fig. 3.11 to support our devised *rule of thumb* for picking Δt in the main simulations (section 3.5). In particular, this rule tells us that for a given set of MOT parameters, we use $\Delta t < 1/\omega_{tr,3D} \cdot 0.1$. Due to the presence of many-atom effects in our main simulations we remain aware that the largest frequency in the system may be larger than $\omega_{tr,3D}$, and so we have considered to manually adjust Δt (with the *rule of thumb* of course satisfied). In the main simulation section, we will be presenting the results of a *field test* with Δt picked to be smaller than $1/\omega_{tr,3D} \cdot 0.1$ and, for the sake of completeness, also larger than $1/\omega_{tr,3D} \cdot 0.1$.

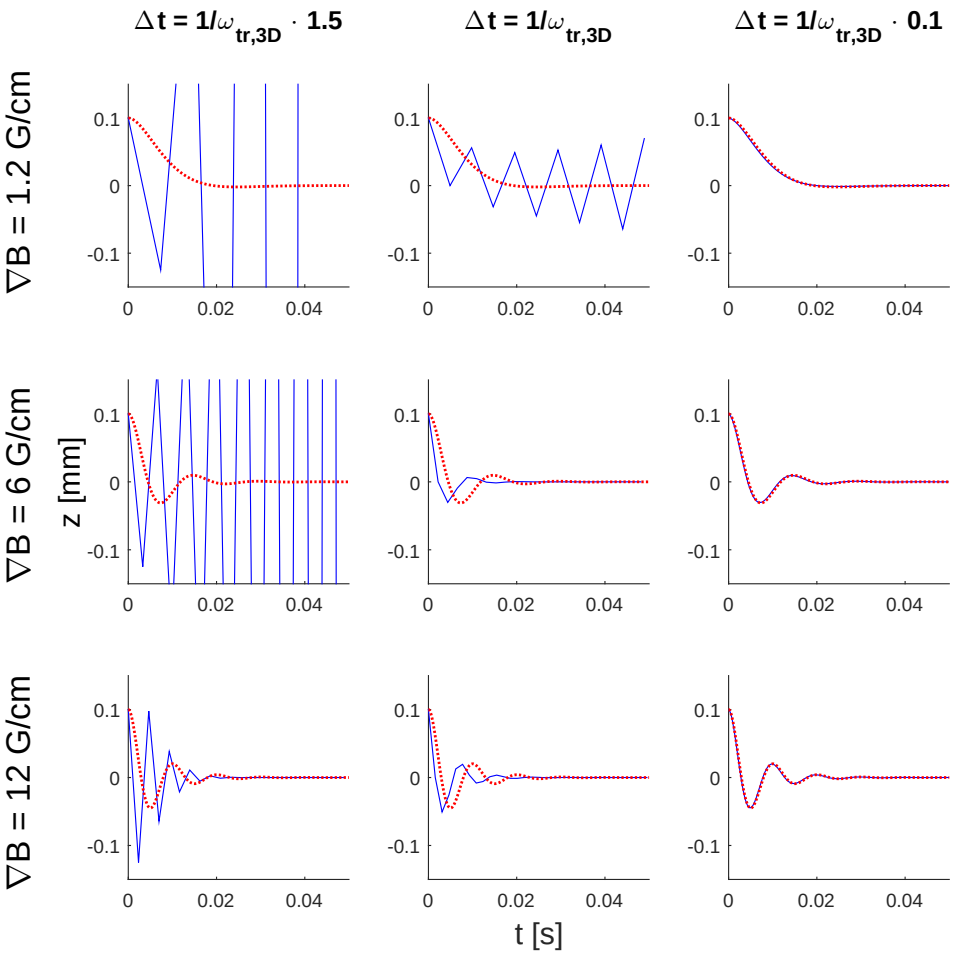

Figure 3.11: Comparisons of the single particle z-trajectories that are numerical (solid blue curves) and analytical (dotted red curves). Different magnetic field gradients ∇B (rows) and simulation time-steps Δt (columns) are considered at the trapping detuning $\delta = -5.5\,\Gamma$ and the on-resonance saturation parameter $s_0 = 3$. $\Delta t \propto 1/\omega_{tr,3D}$, where $\omega_{tr,3D}$ is the trapping frequency. The analytical results are found using Eq. 3.91, with the initial position $z(0) = 0.1$ mm and the initial velocity $v_z(0) = 0$. Note that the analytical curves are repeated at each ∇B value.

3.4.2 Picking the super-particle number

When employing the super-particle method (section 3.3.2) and picking the super-particle number N_{sup}, our first and foremost concern is that this number is large enough for us to actually be able to simulate the instabilities, and for that we are required to do *field tests*. Once we have determined the lowest N_{sup} value at which we can simulate the instabilities, the next logical step is to find the N_{sup} value at which the simulation outcome becomes independent of N_{sup}. In the main simulation section (3.5), we will report the lowest N_{sup} value needed to simulate the instabilities and will also present the results of a *field test* for the N_{sup} convergence for the instabilities. In what follows, in the next subsection, we will be comparing the numerically and analytically found beam transmissions, and will see how the coarse-graining in the intensity attenuation evaluation diminishes as N_{sup} is increased.

3.4.3 Picking the tube-width in the tube method

In this subsection, we explain how we pick the tube-width W in the tube method (section 3.3.3) employed in evaluating beam intensity attenuation. The numerically and analytically found beam transmissions are first compared and then used to support a devised *rule of thumb* for picking W. Note that motionless particles are considered and that the beam cross-saturation effect is neglected (its implementation test is seen in the next subsection).

Let us examine first Figs. 3.12 and 3.13, where we compare the numerically and analytically found transmissions for a beam traveling in the positive z direction (resp. blue dots, red curves) and the negative z direction (resp. green dots, black curves) through the center of respectively a Gaussian and uniform cubical cloud with fixed N and size. Different N_{sup} and optimal tube-width W_0 values are considered at fixed values of δ, ∇B and s_0. In the numerics, it is the tube center that passes through the cloud center. The next paragraph will clarify how W_0 is picked. To find the analytical results, we plug in respectively uniform and Gaussian densities in the full expressions of $\mathcal{I}_z^+$ and $\mathcal{I}_z^-$ (see Tab. 3.2). As seen in the figures, the numerical results lie close to the analytical ones, with the coarse-graining in the attenuation evaluation diminishing as N_{sup} is increased, despite the fact that W_0 at the same time gets smaller. This diminishing happens because more super-particles nevertheless are captured inside the thinner tubes. Choosing a smaller or larger W than W_0 for a given N_{sup} will result in respectively more coarsening and finer detail in the intensity attenuation evaluation. As discussed in the next paragraph, counterintuitively, picking such smaller or larger W can respectively be advantageous and disadvantageous.

Moving on to Figs. 3.14 and 3.15, we compare the numerically and analytically found transmissions for a beam traveling in the positive z direction (resp. blue dots, red curves) and the negative z direction (resp. green dots, black curves) through different positions of respectively a Gaussian and uniform cubical cloud with the fixed N and size as last. Different W values are considered for a fixed N_{sup} value at the previously used MOT parameter values. We ob-

serve from the figures that for smaller or larger W than W_0, respectively more coarsening and finer detail in the attenuation evaluation is expectedly obtained. Also, as the tube center approaches the cloud edge, for the smaller-W case the numerical results are seen to still lie close to the analytical result, but a clear deviation is seen for the larger-W case. This deviation is due to a decreased ratio of the super-particle amount captured inside the tube versus the area of the tube; for instance, using W much larger than the cloud size, the attenuation curve obtained with the tube method would be almost flat as the mentioned ratio would be very small. In summary, decreasing W comes at a trade-off of overall diminished detail in the attenuation evaluation, whereas increasing W comes at a trade-off of underestimation of the attenuation, especially when closer to the cloud edge. Therefore, in order to balance the different trade-offs, an optimal tube-width must be picked. As implied by the figures seen here, the optimal tube-width is such that the deviations from the analytical results are first noticeable when the tube center is $\sim$10 % away from the cloud edge.

We use the results in Figs. 3.12, 3.13, 3.14, 3.15 to support our devised *rule of thumb* for picking W in the main simulations (section 3.5). In particular, this rule tells us that for the N_{sup} value of 10^2, 10^3, 10^4 and 10^5 super-particles we use respectively $W/\sigma = 3/4,\ 1/4,\ 1/10$ and $1/20$, where σ is the RMS width of the Gaussian cloud (of super-particles) that we generate at the starting point of our simulations, and for all the intermediate values of N_{sup} we use the interpolated W/σ values. Note that the smallest N_{sup} value we have considered is 10^2 super-particles and we have not exceeded $1.9 \cdot 10^4$ super-particles. The initial Gaussian cloud's σ is picked such that it is as close as possible to the RMS radius $r_{RMS} \equiv \sqrt{\langle |\mathbf{r} - \mathbf{r}_{COM}|^2 \rangle}$ of the cloud after the transient behavior ends; here $\mathbf{r}_{COM}$ is the COM position of the cloud. The transient behavior will be discussed more in the final testing subsection as well as in the main simulation section. In the latter, we will also be presenting the results of a *field test* with W picked to be smaller as well as larger than what is set by the *rule of thumb*, and will discuss the tube method's numerical performance in the unstable regime, where sizable fluctuations in r_{RMS} can occur.

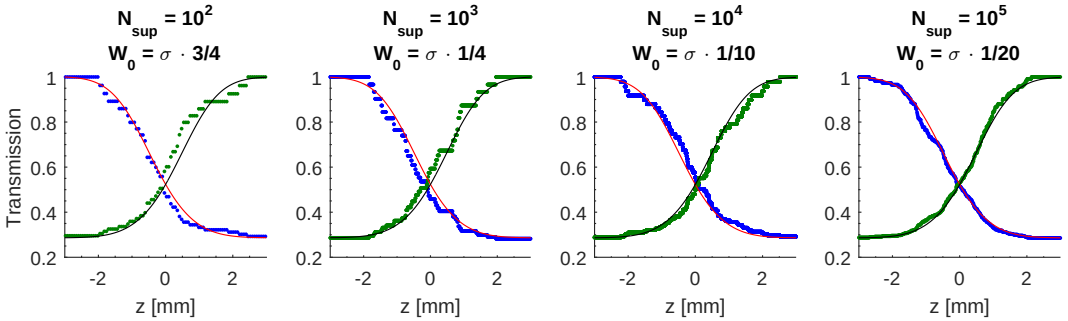

Figure 3.12: Comparisons of the numerically and analytically found transmissions for a beam traveling in the positive z direction (resp. blue dots, red curves) and the negative z direction (resp. green dots, black curves) through the center of a 3D Gaussian cloud with the atom number $N = 10^9$ and the RMS width $\sigma = 1$ mm. Different super-particle numbers N_{sup} and optimal tube-widths W_0 are considered at the trapping detuning $\delta = -3\,\Gamma$, the magnetic field gradient $\nabla B = 6$ G/cm and the on-resonance saturation parameter $s_0 = 1$. Note that the analytical curves are repeated for each new plot.

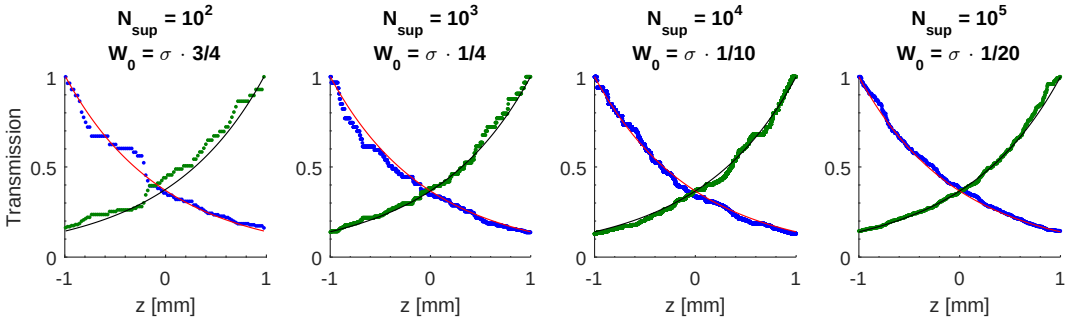

Figure 3.13: Similar depiction as in Fig. 3.12, but a 3D uniform cubical cloud is considered, with σ equal to half the cloud's extent (in each dimension), which is equal to the RMS width of the Gaussian cloud considered in Fig. 3.12.

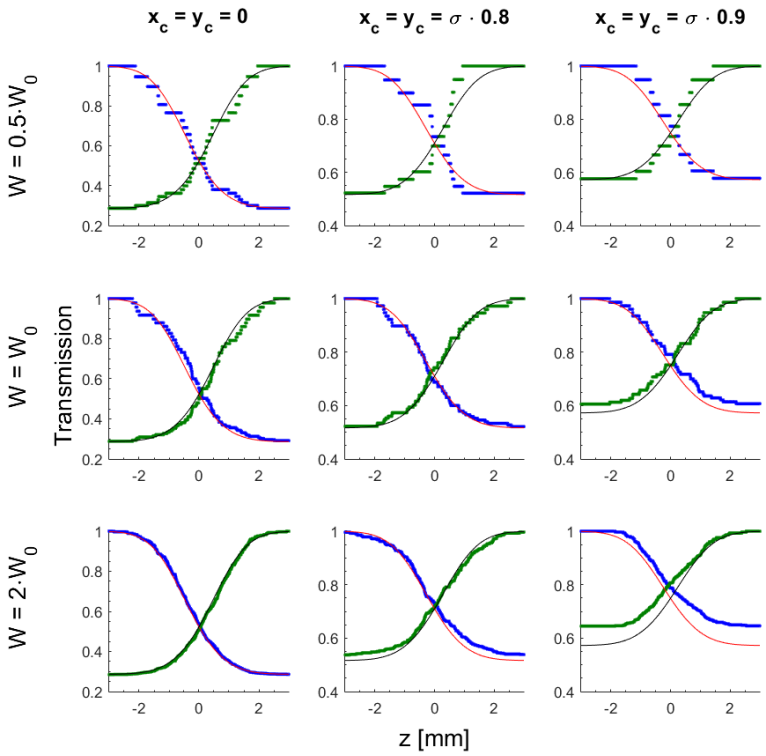

Figure 3.14: Comparisons of the numerically and analytically found transmissions for a beam traveling in the positive z direction (resp. blue dots, red curves) and the negative z direction (resp. green dots, black curves) through different positions (columns) of a 3D Gaussian cloud with the atom number N and the RMS width σ as in Fig. 3.12. x_c and y_c are the respective x- and y-positions of the tube center. Different tube-widths W (rows) are considered for $N_{sup} = 10^4$ super-particles at the MOT parameter values used in Fig. 3.12. W_0 is the optimal tube-width (see Fig. 3.12, third plot title). Note that the analytical curves are repeated at each $x_c = y_c$ value.

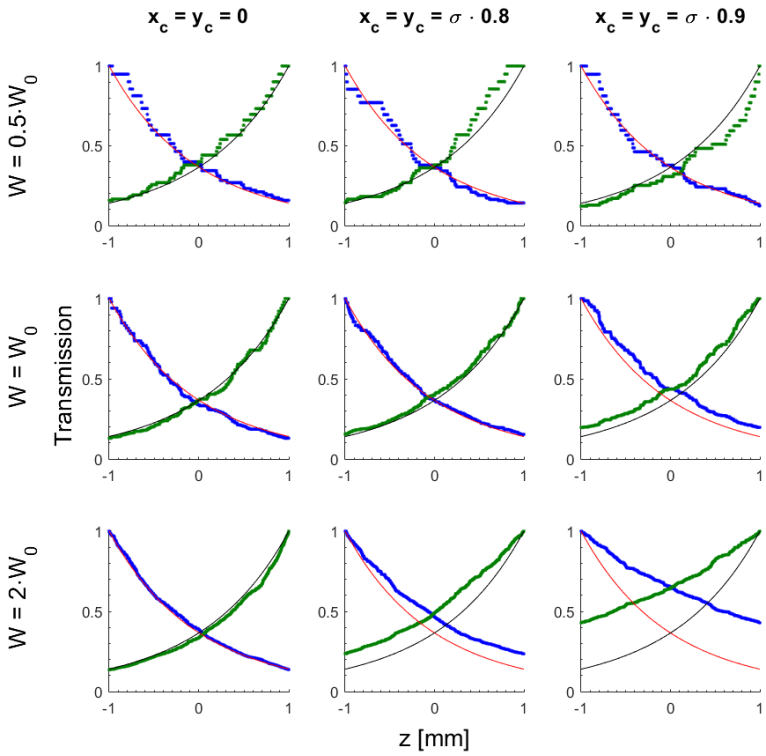

Figure 3.15: Similar depiction as in Fig. 3.14, but a 3D uniform cubical cloud is considered, with σ being half the cloud's extent (in each dimension), which is equal to the RMS width of the Gaussian cloud considered in Fig. 3.12.

3.4.4 Testing of the beam cross-saturation implementation

In this subsection, we show the test for the implementation of the beam cross-saturation effect (section 3.3.3), where the beam transmissions found using the employed while-loop when only one beam is considered are compared with the corresponding iteratively computed results. Because only one beam is considered to be illuminating the cloud, the total intensity appearing in the denominator of the scattering cross-section is that of this one beam. Note that motionless particles are considered.

Let us examine Fig. 3.16, where we compare the numerically and iteratively found transmissions for a beam traveling in the positive z direction (resp. blue dots, solid red curves) through the center of a uniform cubical cloud with fixed N and size, when beam intensity appears in the scattering cross-section. Different ∇B and δ values are considered at fixed values of N_{sup} and s_0. The results in the case where no intensity appears in the scattering cross-section are also provided in the figure (dashed black curves) - these are purely analytical, as found using the procedure in the previous subsection (3.4.3). In obtaining the numerical results, the earlier described while-loop is employed (section 3.3.3). To find the iterative results, we start with Eq. 3.32 for the beam's attenuation in the 2-level atom case (it is valid here since the beam traverses through the center of the cloud). We first compute the quantity $\Delta I_z^+ = I_z^+ \sigma_z^+ \rho \Delta z$, which is the intensity loss that the beam experiences as it traverses an increment Δz through the cloud of the uniform density ρ containing atoms with the scattering cross-section σ_z^+, whose denominator includes the unattenuated intensity I_∞ value. We subtract then ΔI_z^+ from I_∞ to find the beam's intensity after traversing one Δz, and then proceed computing a new ΔI_z^+, with the intensity in the denominator of σ_z^+ being equal to the beam's intensity after traversing one Δz. We continue doing the iterative calculation until the cloud has been finally traversed. Note that the results in the case where no intensity appears in the scattering cross-section can be obtained by applying an equivalent iterative procedure. As seen in the figure, the numerical results lie close to the iterative ones (intensity included in the scattering cross-section) and, very importantly, when at near-resonance (first column), where the curves with intensity included and intensity excluded are clearly different. We deem therefore the beam cross-saturation test a success and so proceed including in our main simulations (section 3.5) the effect of beam cross-saturation with all six MOT beams taken into account (as described in section 3.3.3).

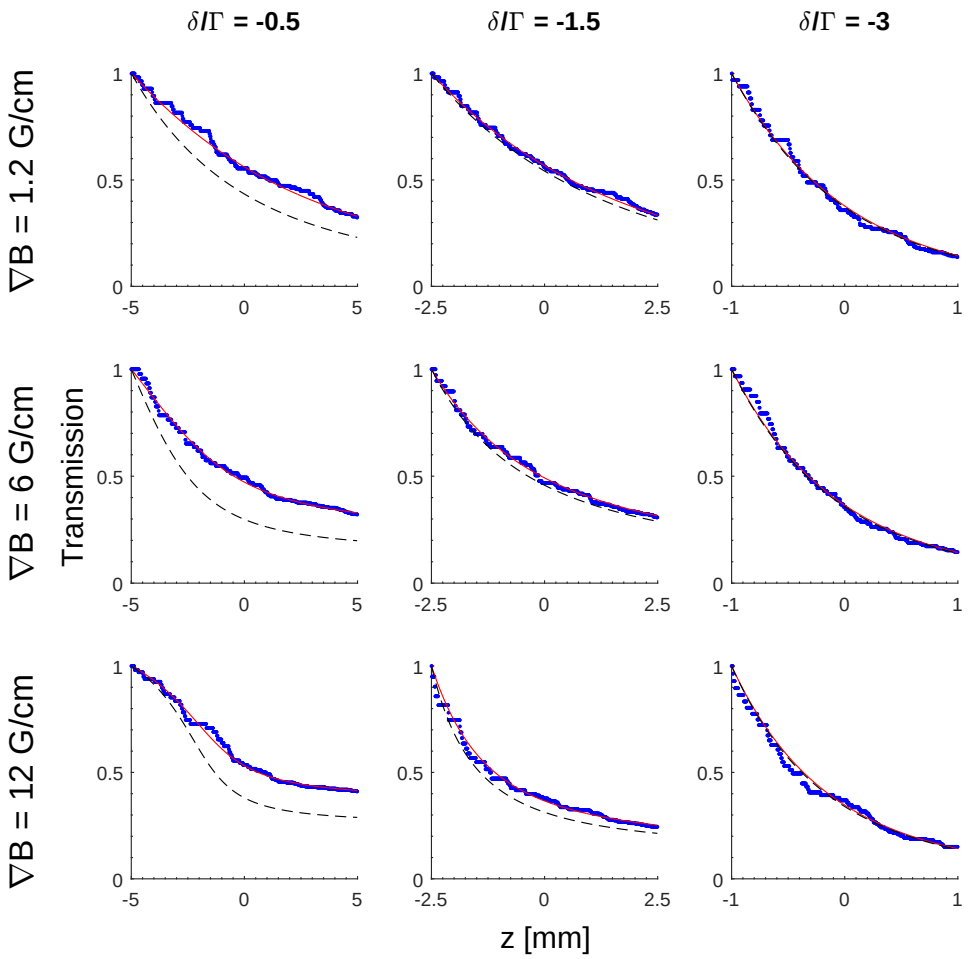

Figure 3.16: Comparisons of the numerically and iteratively found transmissions for a beam traveling in the positive z direction (resp. blue dots, solid red curves) through the center of a 3D uniform cubical cloud with the atom number $N = 10^9$ and the extent (in each dimension) equal to the length of the position-axis (see plots), when beam intensity appears in the scattering cross-section. Different magnetic field gradients ∇B (rows) and trapping detunings δ (columns) are considered for $N_{sup} = 10^3$ super-particles at the on-resonance saturation parameter $s_0 = 1$. The analytical results in the case where no intensity appears in the scattering cross-section are also provided (dashed black curves).

3.4.5 Testing of the trapping force plus diffusion

In this subsection, we show the tests for the trapping force plus diffusion (Tab. 3.2), where the numerically determined limit temperatures and cloud densities in the temperature-limited regime are compared with the corresponding analytical predictions. Note that the intensity attenuation and the rescattering force are turned off so to impose the temperature-limited regime.

Limit temperature test

Let us examine first Fig. 3.17, where we compare, for different s_0 and δ values, the evolutions of the numerically determined average kinetic energies of the cloud particles, i.e. $\frac{1}{2}M\langle|\mathbf{v}|^2\rangle$ (solid blue curves), with the analytically found values of $\frac{3}{2}k_BT_{lim} = \frac{1}{2}\frac{D_{3D}^{4level}}{|\gamma_{3D}|}$ (dotted red lines), where the equality is due to Eq. 3.31. The magnetic field is turned off in the test here, and we note therefore to manually pick the time-step Δt, which is small enough for the numerical results to be independent of Δt. Since we are dealing with single-atom physics (of the temperature-limited regime), the particle number here is not important, but we pick a large $N = N_{sup}$ value so to smooth the numerical solutions. As seen in the figure, when the steady-state is reached (set by γ_{3D}^{-1}), the average kinetic energies lie close to $\frac{3}{2}k_BT_{lim}$, being the consequence of the equipartition theorem. By computing the mean of the average kinetic energy values after the steady-state is reached and equating this mean to $\frac{3}{2}k_BT_{lim}$ (application of the equipartition theorem), we can obtain the numerically determined limit temperature.

Moving on to Fig. 3.18, we compare, for the s_0 values in Fig. 3.17, the numerically determined limit temperatures (blue crosses) with the analytical predictions, where (i) the general equation $\frac{3}{2}k_BT_{lim} = \frac{1}{2}\frac{D_{3D}^{4level}}{|\gamma_{3D}|}$ is used (dotted red curves), and (ii) the low-intensity limit ($s_0 \ll 1$) is imposed on D_{3D}^{4level} so that Eq. 1.5 is used (dashed black curves). We observe, most importantly, that the numerically determined temperatures lie on the analytical curves found using the general equation, and we deem therefore the limit temperature test a success. Moreover, we observe that the two analytical curves correctly match each other in the low-intensity limit (refer to section 3.1.2 for the derived proof).

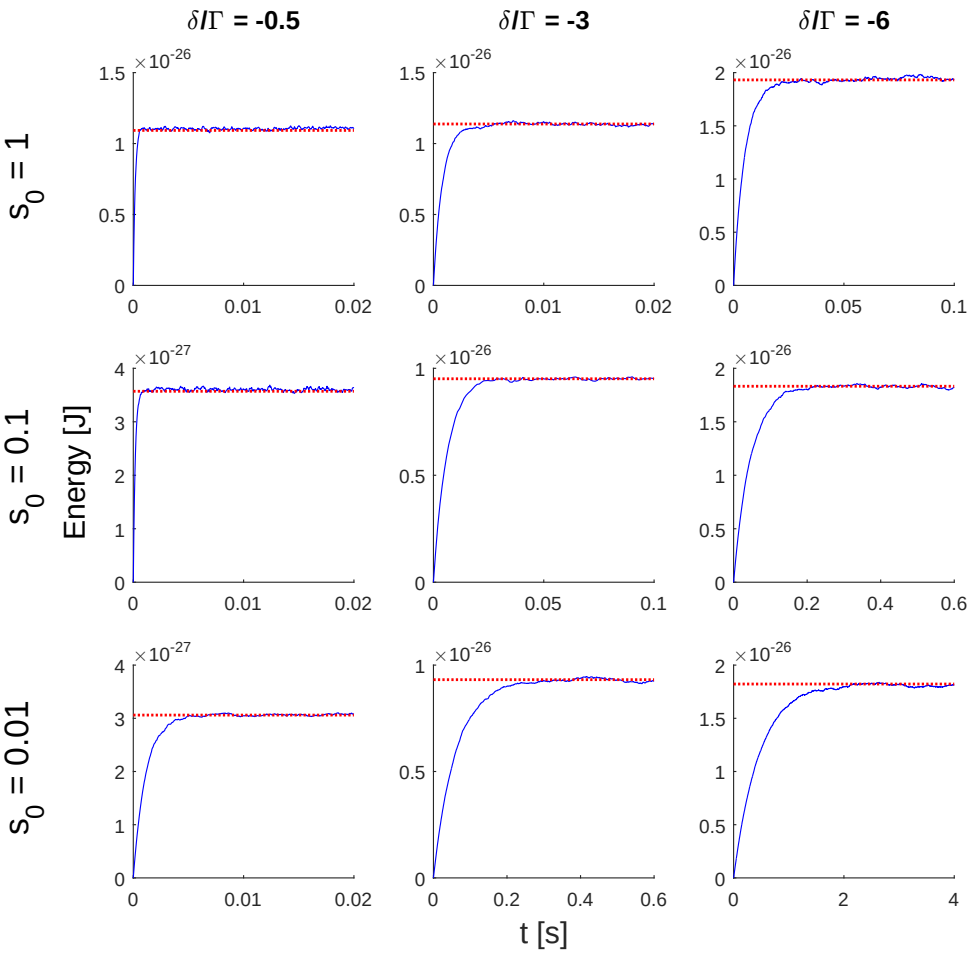

Figure 3.17: Comparisons of the evolutions of the numerically determined average kinetic energies of the cloud particles (solid blue curves) with the analytically found values of $\frac{3}{2}k_B T_{lim}$ (dotted red lines). Different on-resonance saturation parameters s_0 (rows) and trapping detunings δ (columns) are considered. The atom number is $N = 10^4$, equal to the super-particle number N_{sup}; picking a large particle number smoothes the numerical results.

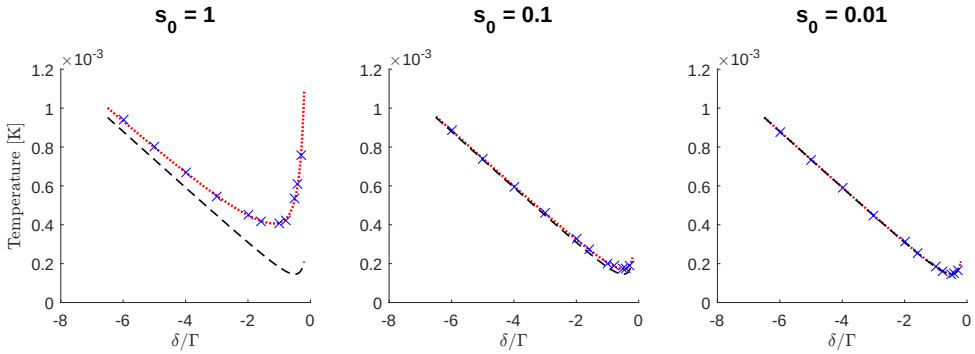

Figure 3.18: Comparisons, for the s_0 values in Fig. 3.17, of the numerically determined limit temperatures (blue crosses) with the analytical predictions (dotted red and dashed black curves) commented in the text.

Density test

Let us proceed examining Fig. 3.19, where we compare the numerically determined cloud densities (blue crosses) and the corresponding analytical predictions (dotted red lines) for different ∇B and δ values at fixed values of s_0 and $N = N_{sup}$. The results are angular averages of the 3D densities. In obtaining the numerical results, we have set the time-step Δt according to the devised rule of thumb (refer to section 3.4.1), and the density was extracted after the average kinetic energy of the particles has reached the steady-state. To find the analytical results, we have considered the fact that we are dealing with small particle velocities ($|v_\alpha| \ll |\delta|/k_L$) and remain close to the trap center ($|r'_\alpha| \ll |\delta|/(\mu B')$), such that the particle dynamics obey Langevin equations of motion involving a sum of the approximated trapping force given by Eq. 3.19 and the Langevin force seen in Eq. 3.20. These Langevin equations reproduce the Boltzmann distribution for the particle probability density for the x-, y-, z-axis, respectively

$$\rho_{\mathsf{x}}(x) = \frac{1}{\rho_{0,\mathsf{x}}} e^{\frac{-U_{tr,\mathsf{x}}(x)}{k_B T_{lim}}} \quad , \quad \rho_{\mathsf{y}}(y) = \frac{1}{\rho_{0,\mathsf{y}}} e^{\frac{-U_{tr,\mathsf{y}}(y)}{k_B T_{lim}}} \quad , \quad \rho_{\mathsf{z}}(z) = \frac{1}{\rho_{0,\mathsf{z}}} e^{\frac{-U_{tr,\mathsf{z}}(z)}{k_B T_{lim}}} \tag{3.92}$$

where $\rho_{0,\mathsf{x}} = \int_{-\infty}^{+\infty} dx\, e^{\frac{-U_{tr,\mathsf{x}}(x)}{k_B T_{lim}}}$, $\rho_{0,\mathsf{y}} = \int_{-\infty}^{+\infty} dy\, e^{\frac{-U_{tr,\mathsf{y}}(y)}{k_B T_{lim}}}$, $\rho_{0,\mathsf{z}} = \int_{-\infty}^{+\infty} dz\, e^{\frac{-U_{tr,\mathsf{z}}(z)}{k_B T_{lim}}}$ are the normalization constants, $k_B T_{lim}$ is related to D_{3D}^{4level} through Eq. 3.31 (as previously), and $U_{tr,\mathsf{x}}, U_{tr,\mathsf{y}}, U_{tr,\mathsf{z}}$ are the trapping potentials that satisfy

$$\mathbf{F}_{rest,3D}(\mathbf{r}) = -\left(\frac{dU_{tr,\mathsf{x}}(x)}{dx}\hat{\mathbf{x}} + \frac{dU_{tr,\mathsf{y}}(y)}{dy}\hat{\mathbf{y}} + \frac{dU_{tr,\mathsf{z}}(z)}{dz}\hat{\mathbf{z}} \right) \tag{3.93}$$

where $\mathbf{F}_{rest,3D}(\mathbf{r}) = -\kappa_{3D}\left(\frac{x}{2}\hat{\mathbf{x}} + \frac{y}{2}\hat{\mathbf{y}} + z\hat{\mathbf{z}}\right)$ is the restoring force in Eq. 3.19.

From Eq. 3.93 we find

$$U_{tr,\mathsf{x}}(x) = \frac{1}{4}\kappa_{3D}x^2 \quad , \quad \rho_{0,\mathsf{x}} = \sqrt{\frac{4\pi k_B T_{lim}}{\kappa_{3D}}} \tag{3.94a}$$

$$U_{tr,\mathsf{y}}(y) = \frac{1}{4}\kappa_{3D}y^2 \quad , \quad \rho_{0,\mathsf{y}} = \sqrt{\frac{4\pi k_B T_{lim}}{\kappa_{3D}}} \tag{3.94b}$$

$$U_{tr,\mathsf{z}}(z) = \frac{1}{2}\kappa_{3D}z^2 \quad , \quad \rho_{0,\mathsf{z}} = \sqrt{\frac{2\pi k_B T_{lim}}{\kappa_{3D}}} \tag{3.94c}$$

The density in 3D is $\rho(\mathbf{r}) = \rho_{\mathsf{x}}(x)\rho_{\mathsf{y}}(y)\rho_{\mathsf{z}}(z)$. Switching from the Cartesian coordinates x, y, z to the spherical ones r, θ, φ, where $x = r\,sin(\theta)cos(\varphi)$, $y = r\,sin(\theta)sin(\varphi)$, $z = r\,cos(\theta)$, and integrating over the angles $\theta \in [0, \pi], \varphi \in [0, 2\pi)$, we obtain finally the angularly-averaged density

$$\rho(r) = N \times \frac{1}{2}\frac{\kappa_{3D}}{\sqrt{8}\pi\frac{D_{3D}}{3|\gamma_{3D}|}} \times e^{\frac{-\kappa_{3D}r^2}{4\frac{D_{3D}}{3|\gamma_{3D}|}}} \times \frac{erf\left(\sqrt{\frac{\kappa_{3D}r^2}{4\frac{D_{3D}}{3|\gamma_{3D}|}}}\right)}{r} \tag{3.95}$$

which we note correctly satisfies $\int_0^\infty dr\, r^2\rho(r) = N$.

As seen in Fig. 3.19, the large variety of numerically determined densities lie close to the analytically predicted ones using Eq. 3.95, allowing us to deem the density test a success.

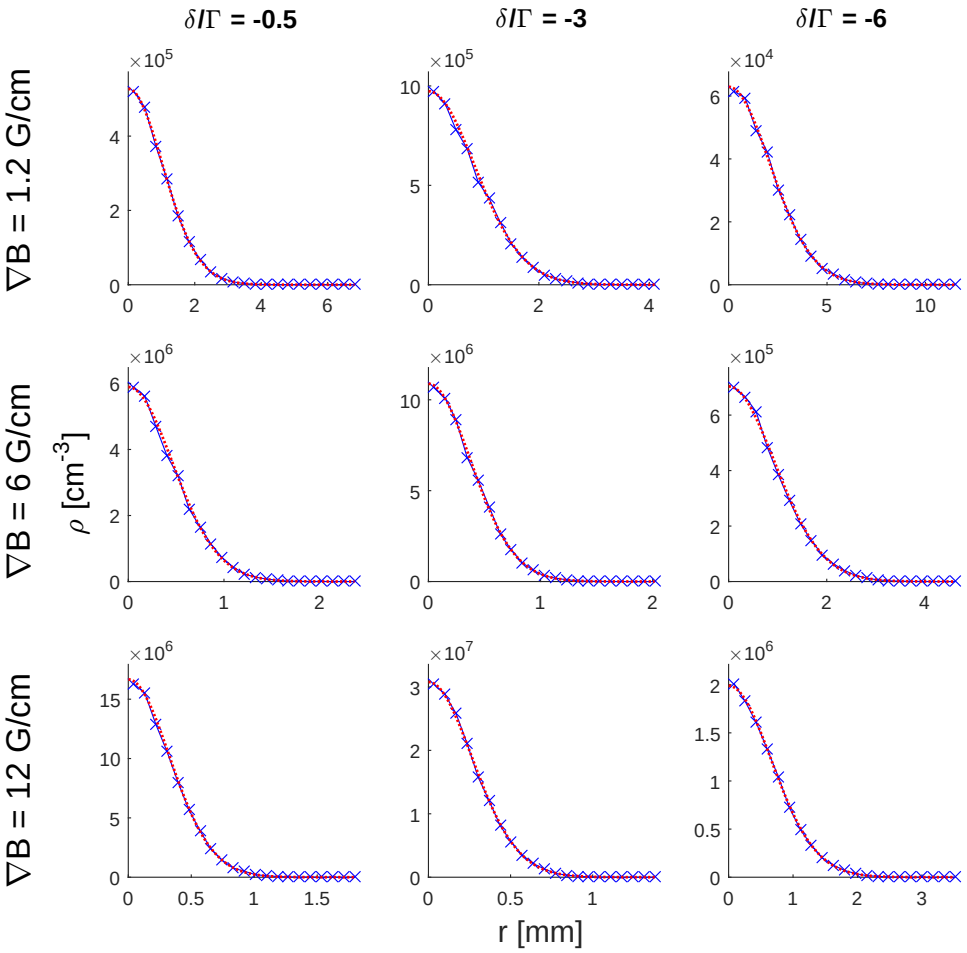

Figure 3.19: Comparisons of the numerically determined cloud densities (blue crosses) with the corresponding analytical predictions (dotted red curves). Different magnetic field gradients ∇B (rows) and trapping detunings δ (columns) are considered at the on-resonance saturation parameter $s_0 = 3$ and the atom number $N = 10^4$, equal to the super-particle number N_{sup}. The lines connecting the numerical data-points are drawn as a visual aid. The results are angular averages of the 3D densities. The analytical results are found using Eq. 3.95.

3.4.6 Testing of the rescattering force

In this subsection, we show the test for the rescattering force (Tab. 3.2) involving its symmetry, where it is checked that for a pair of motionless particles the ratio of the rescattering force's magnitude between them remains at unity when they are mirrored through the trap center. We keep only the rescattering force in this test and expect the computed ratio to remain the same due to the magnitude of the magnetic field, $B(\mathbf{r} = x, y, z) = B'\sqrt{z^2 + \frac{1}{4}(x^2 + y^2)}$, remaining the same for mirrored particles ($B(x, y, z) = B(-x, -y, -z)$). Although this test is rather simple, it helps to increase our confidence in that the rescattering force's implementation is done correctly, which we realize involves a lot of detail due to the force's complicated expression.

Let us examine Fig. 3.20, where we display pairs of particles (blue squares, red dots, green diamonds, black crosses) that are mirrored through the trap center at different radii and locations. Employing the notations $F_{rsc,12}$ and $F_{rsc,21}$ for the magnitude of the rescattering force respectively on one particle due to the second one and the other way around, we find for the different pairs in the figure the ratio $F_{rsc,12}/F_{rsc,21}$ correctly remaining at unity. The ratio of unity is obtained for whichever new positions of the mirrored particles we have tried picking, and we deem therefore the rescattering force's symmetry test a success.

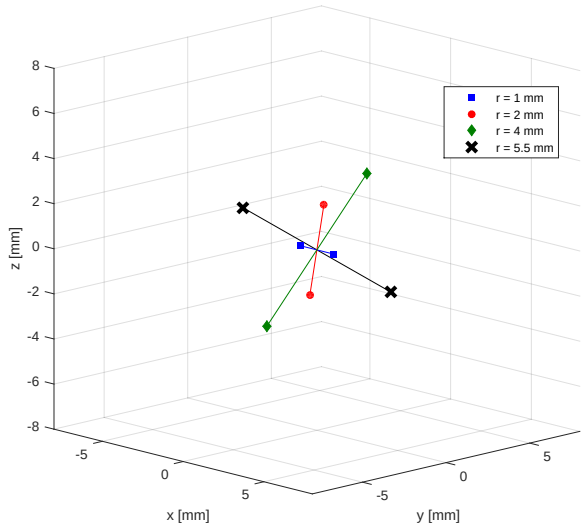

Figure 3.20: Pairs of particles (blue squares, red dots, green diamonds, black crosses) that are mirrored through the trap center at different radii and locations, used for the discussion of the rescattering force's symmetry test as seen in the text. The lines connecting the particles are drawn as a visual aid.

3.4.7 Testing of the stable cloud size versus N

In this final subsection, we show the test for the simulated stable cloud size versus the atom number N, where a comparison with the Wieman model's $N^{1/3}$ scaling is made. We include all the forces and effects (Tab. 3.2) in this test, with an expectation that these reproduce the $N^{1/3}$ scaling in the large stable MOT case. This test is able to give a strong indicator that our model reproduces the known physics of the MOT in the multiple-scattering limit, greatly increasing our confidence in embarking on the instability simulations that we will be describing after this test. We start off by checking the N_{sup} convergence for the stable cloud size, so we could pick N_{sup} that is large enough for the numerical results to be independent of N_{sup}, and afterwards present the main result of this subsection. We note that in the next section, we will prove that the clouds dealt with here indeed are stable.

N_{sup} convergence for the stable cloud size

Let us examine first Fig. 3.21, where we plot the RMS radius r_{RMS} evolution for the simulated stable clouds with different N_{sup} values at fixed values of N, δ, ∇B, I_∞ and I_{sat}. The time-step Δt of the simulations has been set according to the devised *rule of thumb* (refer to section 3.4.1). The initial r_{RMS} value is the same for all the N_{sup} values and does not deviate more than 10 % from the r_{RMS} value after the transient behavior ends, and so the tube-width used in the attenuation evaluation is of optimal size at a given N_{sup} value (refer to section 3.4.3). Notice how the transient behavior makes an abrupt change as N_{sup} passes a certain point: for $N_{sup} \leq 5 \cdot 10^3$ super-particles it results in damping oscillations in the r_{RMS} evolution, whereas for $N_{sup} \geq 7 \cdot 10^3$ super-particles it results in damping oscillations followed up by a rise in the r_{RMS} evolution. The first damping oscillations are well-explained by single-atom physics, whereas the rise is due to many-atom physics. The change in the transient behavior indicates thus that the coarse-graining below $N_{sup} = 7 \cdot 10^3$ super-particles prevents some new feature due to many-atom physics from appearing. Specifically, we report that the clouds undergo a change in shape with the rise in the r_{RMS} evolution. The subsequent fluctuations in the r_{RMS} evolution (after the transient) occur because of the diffusion and diminish in amplitude as N_{sup} is increased due to the averaging effect of the increase in N_{sup}.

In Fig. 3.22, we proceed plotting, for the simulated clouds considered in Fig. 3.21, the averaged r_{RMS} values after the initial transient behavior ends versus N_{sup}. We observe that both below and above $N_{sup} = 5 \cdot 10^3$ super-particles the r_{RMS} values are larger, and as soon as $N_{sup} = 10^4$ super-particles, the change in the averaged r_{RMS} value levels off. However, throughout all of the considered range of N_{sup}, the size deviation is within $\sim$10%, and so it is reasonable to pick any used N_{sup} value to obtain the main result of this section. Nevertheless, we choose to continue with $N_{sup} = 7 \cdot 10^3$ super-particles, as we intend also to show density profiles, which are more correctly represented for this N_{sup} value (and above), due to the change in cloud shape.

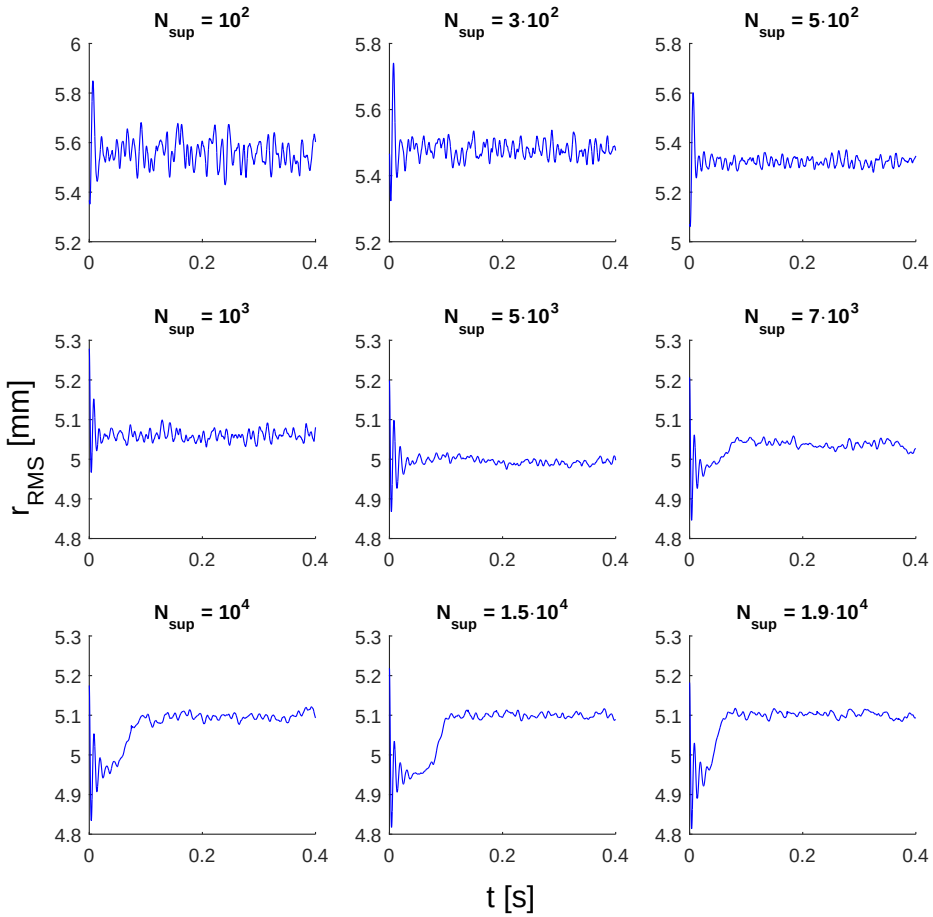

Figure 3.21: The RMS radius r_{RMS} evolution for the simulated stable clouds with different super-particle numbers N_{sup} at the atom number $N = 10^{11}$, the trapping detuning $\delta = -6\,\Gamma$, the magnetic field gradient $\nabla B = 7.2$ G/cm, the unattenuated intensity $I_\infty = 5$ mW/cm^2 and the saturation intensity $I_{sat} = 1.67$ mW/cm^2. The initial r_{RMS} value is 5.1 mm, for all the N_{sup} values. Note that the usage of the particular I_{sat} value is explained at the start of section 3.5.

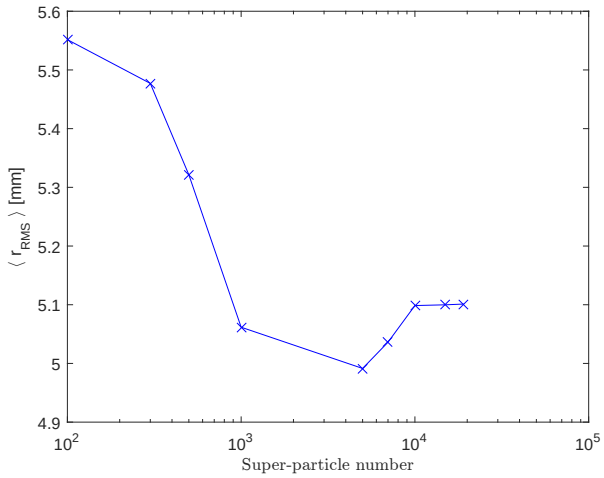

Figure 3.22: The averaged RMS radius $\langle r_{RMS} \rangle$ for the simulated stable clouds considered in Fig. 3.21 after the initial transient behavior ends (see text) versus the super-particle number N_{sup}. The blue crosses are the simulation results, and the solid line connecting them is drawn as a visual aid.

Simulated stable cloud size versus N

We present now the main result of this subsection, displayed in Fig. 3.23, where we plot the averaged RMS radius $\langle r_{RMS} \rangle$ (after the transient) of the simulated stable clouds versus N. The remaining MOT parameters and Δt are the same as last, and the initial r_{RMS} value is adjusted as usual. The super-particle number $N_{sup} = 7 \cdot 10^3$, in accord to the previous discussion. The insets in the figure display examples of the cloud density profiles: the numerical results (solid curves), obtained by first integrating along the z-axis and then using the points along the x-axis ($y = 0$), together with the corresponding Gaussian fits (dotted curves). The figure tells us that below 10^7 atoms the cloud size is independent of N and the cloud density profile is Gaussian, as expected in the temperature-limited regime. Above 10^8 atoms, the cloud size increases according to the Wieman model's $N^{1/3}$ scaling. Such increase is a clear signature of the multiple-scattering regime, and here we observe variations occurring in the cloud density profile. Around 10^9 atoms, the profile is closely flat-top. At even higher atom numbers, the top of the profile rounds off and a development of a central feature with enhanced density appears. The behaviors are overall consistent with the observations in Ref. [24], as described above Fig. 1.9; however, the development of the central feature was linked in Ref. [24] to the MOT entering the two-component regime, where sub-Doppler effects are important. As sub-Doppler mechanisms are neglected in our case, we link the appearance of the central feature to the nonlinearities in the implemented physical ingredients. We deem the test for the cloud size versus N a success.

For the last remark, we mention here that clouds are systematically larger in the simulations versus the experiments, roughly by a factor of 2. This discrepancy between the cloud sizes and its implications will be discussed in the following section, where simulations of the unstable MOT are finally presented.

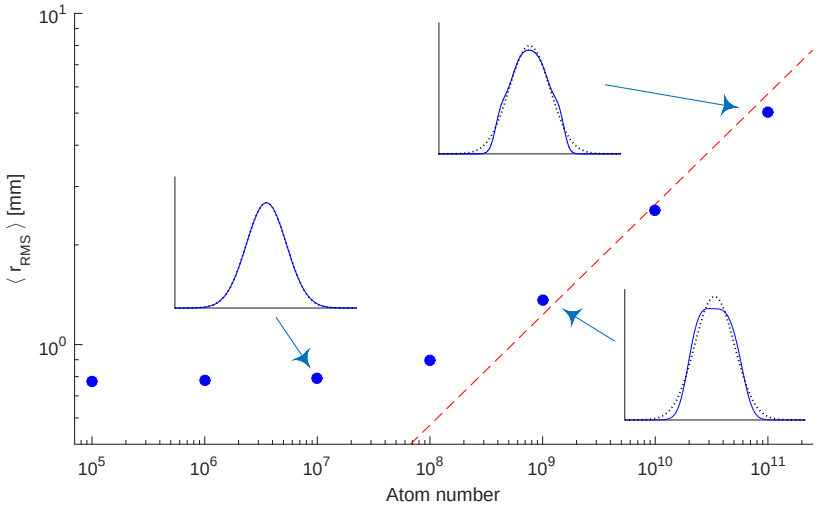

Figure 3.23: The averaged RMS radius $\langle r_{RMS} \rangle$ (after the transient) of the simulated stable clouds versus the atom number N. The remaining MOT parameters are the same as in Fig. 3.21. The super-particle number $N_{sup} = 7 \cdot 10^3$. The dots are the simulation results, and the dashed line corresponds to the Wieman model's $N^{1/3}$ scaling. The insets show examples of the cloud density profiles which have been spatially rescaled. The solid curves are the numerically obtained density profiles (see text), while the dotted curves correspond to the Gaussian fits. The solid curves have been smoothed.

3.5 The balanced MOT simulation results

In this section, we present the main results of the balanced MOT simulations in 3D. We begin by presenting the results of simulated instability threshold versus respectively ∇B, N and I, and do comparisons with results of the corresponding experiments (sections 2.3.1, 2.3.2, 2.3.3). Next, we move on to studying the spatio-temporal properties of the simulated unstable regime. Here we present δ-∇B phase-space instability diagrams, found respectively by using ESA and visual inspection, and make comparisons with the experimentally obtained result (section 2.4.1). Lastly, we investigate the impact of our simulation model's ingredient forces and effects on the instabilities; in particular, we investigate the impact of diffusion, then intensity attenuation, and then elastically as well as inelastically scattered light spectrum.

Before we start, we bring into attention the following:

1. We neglect the Doppler and Zeeman effects in the momentum diffusion coefficient D_{3D}^{4level} (Eq. 3.54). This choice is done in order to simplify the implementation of the diffusion, although we must point out that it is not fully justifiable physically, as we will show in this section that both of these effects can be quite significant. Also, we set the gyromagnetic ratio $\mu = 2\pi \times 1.4 \times 10^6$ Hz/G, as used in the original study of balanced MOT instabilities [39]. Also, for the atom mass M, it is picked to be that of the atomic species used in our experiments, i.e. Rb-87 (see footnote 1 in section 2.1.1 for the value of M). Moreover, we set the saturation intensity $I_{sat} = 1.67$ mW/cm^2 (as in Fig. 3.23). This value of I_{sat} is found for Rb-87 in cases where σ^+ and σ^- polarized light transfers the atomic population into the respective cycling transitions $m = 2 \rightarrow m' = 3$ and $m = -2 \rightarrow m' = -3$ of $F = 2 \rightarrow F' = 3$ of the D2 line (Fig. 2.1(b)) [14]. Of course, such population transfer does not occur in a real MOT as the atoms at different locations see the beam light to be polarized differently, and the I_{sat} value will consequently change according to the atom location. Nevertheless, for mere simplicity, we work under the assumption that the I_{sat} value does not vary and proceed using $I_{sat} = 1.67$ mW/cm^2.

2. The lowest amount of super-particles needed to simulate the instabilities is $N_{sup} = 10^3$. However, we use $N_{sup} = 7 \cdot 10^3$ super-particles in simulating them. This N_{sup} value coincides with the convergent one seen in section 3.4.7 for the stable cloud size; however, here the choice is based on the test we have done surrounding the N_{sup} convergence for instability threshold, as presented in the first subsection, where we also present instability threshold's dependence on the simulation time-step Δt as well as the tube-width W.

3. On a desktop computer, a single simulation run with $N_{sup} = 7 \cdot 10^3$ super-particles takes us 1-2 weeks to complete (MATLAB), depending on the other parameters used in the simulation. To increase our efficiency, we thus made use

of a computer cluster, allowing us to do many simulation runs at the same time.

3.5.1 The instability threshold behaviors

In this subsection, we present the results of simulated instability threshold versus respectively ∇B, N and I, and do comparisons with results of the corresponding experiments (sections 2.3.1, 2.3.2, 2.3.3). We make general considerations for finding simulated instability threshold in the first sub-subsection (surrounding threshold versus ∇B), where we also present instability threshold's dependence on the super-particle number N_{sup}, the simulation time-step Δt and the tube-width W.

3.5.1.1 Instability threshold versus ∇B

In this sub-subsection, we start by providing the parameters used in the simulation of instability threshold versus ∇B. Next, we make general considerations for finding simulated instability threshold. Then, we present the simulated threshold versus ∇B and compare its behavior with that from the corresponding experiment (section 2.3.1). Finally, we present the results of *field tests* for instability threshold's dependence on the super-particle number N_{sup}, the simulation time-step Δt and the tube-width W. A discussion of the results is provided. We note that results seen here are part of the publication in Ref. [72].

Simulation parameters, finding simulated instability threshold, and instability threshold versus ∇B

We proceed here to provide the parameters used in the simulation of instability threshold versus ∇B, followed up by making general considerations for finding simulated instability threshold and presenting the simulated instability threshold versus ∇B together with a comparison with threshold in the corresponding experiment (section 2.3.1).

Like in the experiment, we have here in the simulation $N = 1.5 \cdot 10^{10}$ atoms, $I_\infty = 5$ mW/cm^2 per MOT beam and the same ∇B values in the range from 1.2 to 12 G/cm. As mentioned in the introduction of this section, we use $N_{sup} = 7 \cdot 10^3$ super-particles. The remaining simulation parameters, at the different ∇B values, are summarized in Tab. 3.3. The simulation end time t_{end} seen in Tab. 3.3 is discussed in the next paragraph, surrounding the general considerations for finding simulated instability threshold.

To find simulated instability threshold, we mimic the experimental threshold-determination procedure (section 2.3.1), which, to briefly recall, involves comparisons of images for quantifying the amount of cloud spatial fluctuation, after which plots are made of the fluctuations in the working range of δ values, and, finally, the threshold detuning δ_{thr} is extracted by means of extrapolation. In gathering the imagery in the simulations, we select 50 random time instances in the cloud evolution after the transient behavior ends and integrate the corresponding 3D cloud densities along the z-axis. Note that by employing

∇B [G/cm]	$-\delta/\Gamma$ (step of 0.05)	$r_{RMS}(t=0)$ [mm]	t_{end} [s]	Δt [s]
1.2	2.1 to 2.35 2.4 to 2.8	6	1.2 2.4	10^{-4}
1.8	2.1 to 2.9	5.3	1.2	10^{-4}
2.4	2.1 to 3	4.7	1.2	10^{-4}
3	2.2 to 3.1	4.2	1.2	10^{-4}
3.6	2.3 to 3.2	4	0.9	$8 \cdot 10^{-5}$
4.8	2.6 to 3.5	3.6	2.4	$6 \cdot 10^{-5}$
6	2.6 to 3.6	3.3	2.1	$4 \cdot 10^{-5}$
7.2	2.6 to 3.7	3	1.8	$2 \cdot 10^{-5}$
9.6	3.3 to 4.1	2.7	1.2	10^{-5}
12	3.5 to 4.35	2.4	0.7	$8 \cdot 10^{-6}$

Table 3.3: Parameters used at the different magnetic field gradients ∇B in the simulation of instability threshold versus ∇B, with the atom number $N = 1.5 \cdot 10^{10}$, the unattenuated intensity $I_\infty = 5$ mW/cm^2 per MOT beam and the super-particle number $N_{sup} = 7 \cdot 10^3$. The displayed parameters are the trapping detuning δ, the simulation end time t_{end}, the simulation time-step Δt and the RMS radius r_{RMS} of the 3D Gaussian cloud generated at the simulation start ($t = 0$). Note that each Δt value satisfies the devised *rule of thumb* for picking Δt (section 3.4.1), and the initial value of r_{RMS} determines the fixed tube-width W (section 3.4.3).

the random selection procedure we respect the experimental temporal sequence that randomly probes the cloud dynamics, and by performing integration of the cloud densities along the z-axis, analogous kind of imagery to that of the experiments is obtained (refer to section 2.2.2). To know the starting point for the selection, we examine evolutions of (i) r_{RMS} and (ii) N_{sup} in one octant. In Figs. 3.24-3.26, we plot such evolutions for different δ values at three values of ∇B. As we concentrate on the r_{RMS} evolution plots, we observe that for all the cases there is a first transient ($\lesssim 0.1$ s duration) corresponding to position damping of the MOT. We note that this transient is somewhat different from the one seen previously in Fig. 3.21 ($N_{sup} \geq 7 \cdot 10^3$), but that is explained by the cloud undergoing different cloud shapes changes, due to a lower atom number now used ($N = 10^{11}$ versus $N = 1.5 \cdot 10^{10}$); stable cloud shapes will be discussed shortly. As next observed, once a certain δ value is passed, characteristic to the ∇B value, spontaneous oscillations occur after some period in time after the first transient. The total transient time before the onset of the oscillations is seen to shorten as $|\delta|$ gets smaller; we report that this shortening indeed continues the closer to the resonance one gets. We mention that the existence of a second transient before the spontaneous oscillations was not observed in the past quasi-1D simulations of balanced MOT instabilities [40]. Now, for the δ values where the oscillations do not occur, we perform the random selection of the images after the first transient, while for the δ values where the oscillations occur, the selection is done after the onset of the instability (ex.: at $\nabla B = 3.6$ G/cm (Fig. 3.25), we use the images with $t > 0.5$ s and $t > 0.3$ s for respec-

tively $\delta/\Gamma = -3$ and -2.9). The oscillations in the N_{sup} evolution are observed to be more pronounced than in the r_{RMS} evolution, and this can help us to easier determine the point in time after which the selection of the cloud images is done. The r_{RMS} evolution is complementary to the N_{sup} evolution and is useful at higher ∇B values, where the variations in N_{sup} can be great enough for the underlying oscillations to look washed out (see Fig. 3.26). Note that the simulation end time t_{end} is adjusted to be longer for smaller ∇B values, due to the period of the oscillations observed to become longer in such a case - this is related to the fact that the trapping frequency correspondingly becomes smaller. After gathering the 2D density images, we perform Gaussian filtering. The filter's standard deviation is fixed at 2 sigma. In essence, the need of filtering is due to the coarse-graining due to the limited N_{sup} in the simulations. Without the filtering, the cloud fluctuation for the unstable clouds near the threshold can be found to be as low as for the stable clouds, resulting in the underestimation of the δ_{thr} value. In Fig. 3.27, we demonstrate this for the previous case ∇B values. The most prominent example in this figure is for $\nabla B = 3.6$ G/cm, where δ_{thr} is seen to shift by more than $0.2\,\Gamma$ further from the resonance due to the filtering; observing the oscillations in the corresponding Fig. 3.25, we can confirm that without the filtering, δ_{thr} is clearly underestimated.

Before moving on to presenting the simulated threshold versus ∇B, we would like to point out in Figs. 3.24-3.26 and 3.27 some additional things, which a careful reader could be wondering about. Starting with Figs. 3.24-3.26, it may be surprising that the percentage of N_{sup} can exceed $\frac{100}{8}\,\% = 12.5\,\%$ in a single octant for the stable clouds (see the first two columns of the lower rows in these figures). This is explained by the fact that simulated stable clouds can be observed to be in a twisted petal shape; we will touch more upon this behavior in the following subsection, presenting the instability diagram simulation results. Next, we note about the case in Fig. 3.27 with $\nabla B = 9.6$ G/cm, where it is observed that with the image filtering employed, there is a sudden drop in the spatial fluctuation for $\delta/\Gamma > -3.55$, whereas there is no such drop without the filtering. This drop is related to the fact that one passes from one instability regime to another, where some clouds fluctuate on a smaller spatial scale; the following subsection will show these regimes.

In Fig. 3.28, we plot the measured and simulated δ_{thr} values versus ∇B (see the black dots and blue circles, resp.). As in the experiment, δ_{thr} in the simulation is observed to decrease with ∇B, with a similar linear slope - the slopes are $-0.13\,\Gamma$ and $-0.14\,\Gamma$ per 1 G/cm for the experiment and simulation, respectively (see the solid black and blue line, resp.). This indicates that our simulation model (the $F = 0 \rightarrow F' = 1$ model, section 3.2) efficiently captures the physical ingredients involved in the threshold determination versus ∇B. The threshold-offset of around $-1\,\Gamma$ for the simulation is probably linked to the larger cloud size versus the experiment (as first noted to exist at the end of section 3.4.7). The mismatch in sizes is not surprising, considering the simplified nature of our model. Most prominently, the model deals with a less involved transition than what we have in the experiment ($F = 0 \rightarrow F' = 1$ versus $F = 2 \rightarrow F' = 3$), possibly yielding a different effective Zeeman shift. The size can also be impacted

by the usage of common rescattering cross-sections for each of the three Zeeman transitions of our model (see Eq. 3.78), instead of six separate rescattering cross-sections (one for each beam) for each of these transitions (we have three rescattering cross-sections, instead of eighteen). According to Fig. 3.3(a), a common rescattering cross-section is larger in value for $-\delta/\Gamma \gtrsim 2$, compared to if six separate rescattering cross-sections are used. Technically, this results in the simulated cloud being larger (as the rescattering force is proportional to the rescattering cross-section). For detunings closer to the resonance, $-\delta/\Gamma \lesssim 2$, the situation regarding the sizes is reversed.

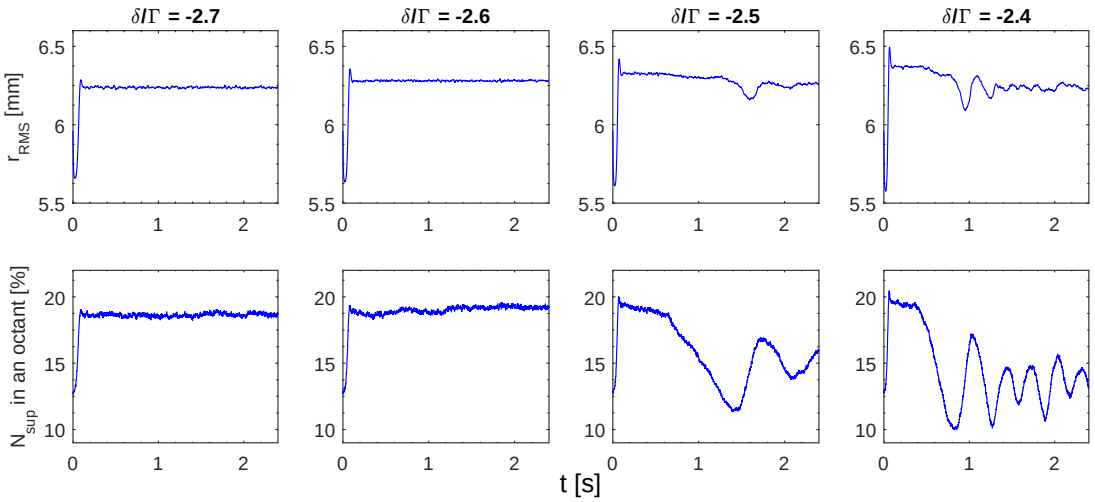

Figure 3.24: The RMS radius r_{RMS} evolution and the super-particle number N_{sup} in one octant $(x, y, z > 0)$ evolution for the simulated clouds (resp. upper and lower row) for different trapping detunings δ (columns) at the magnetic field gradient $\nabla B = 1.2$ G/cm. The simulation parameters can be found in Tab. 3.3.

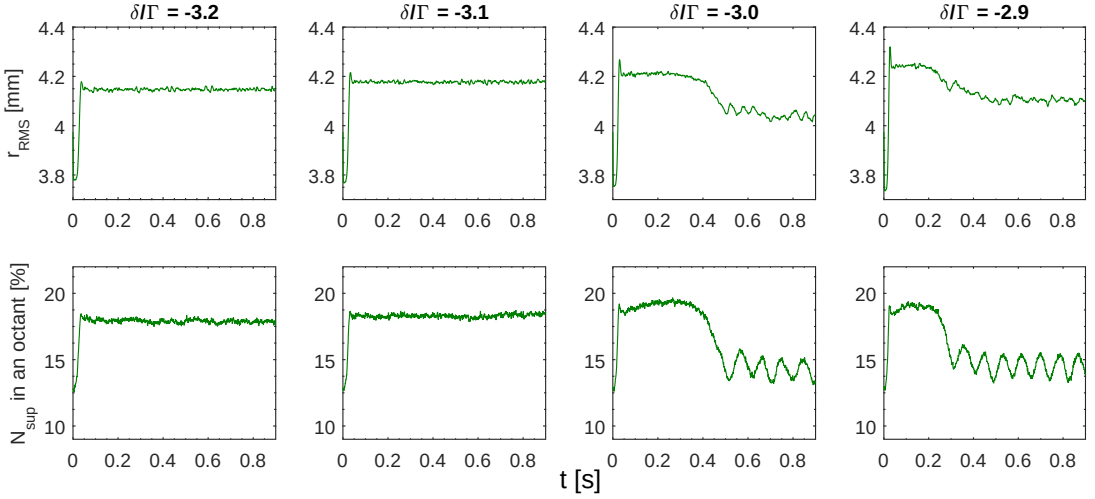

Figure 3.25: Similar depiction as in Fig. 3.24, but $\nabla B = 3.6$ G/cm.

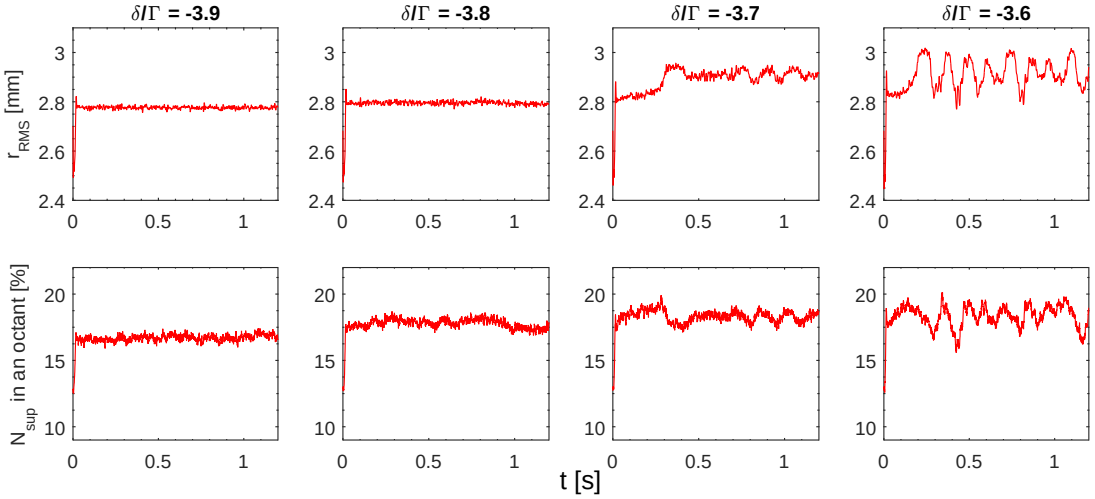

Figure 3.26: Similar depiction as in Fig. 3.24, but $\nabla B = 9.6$ G/cm.

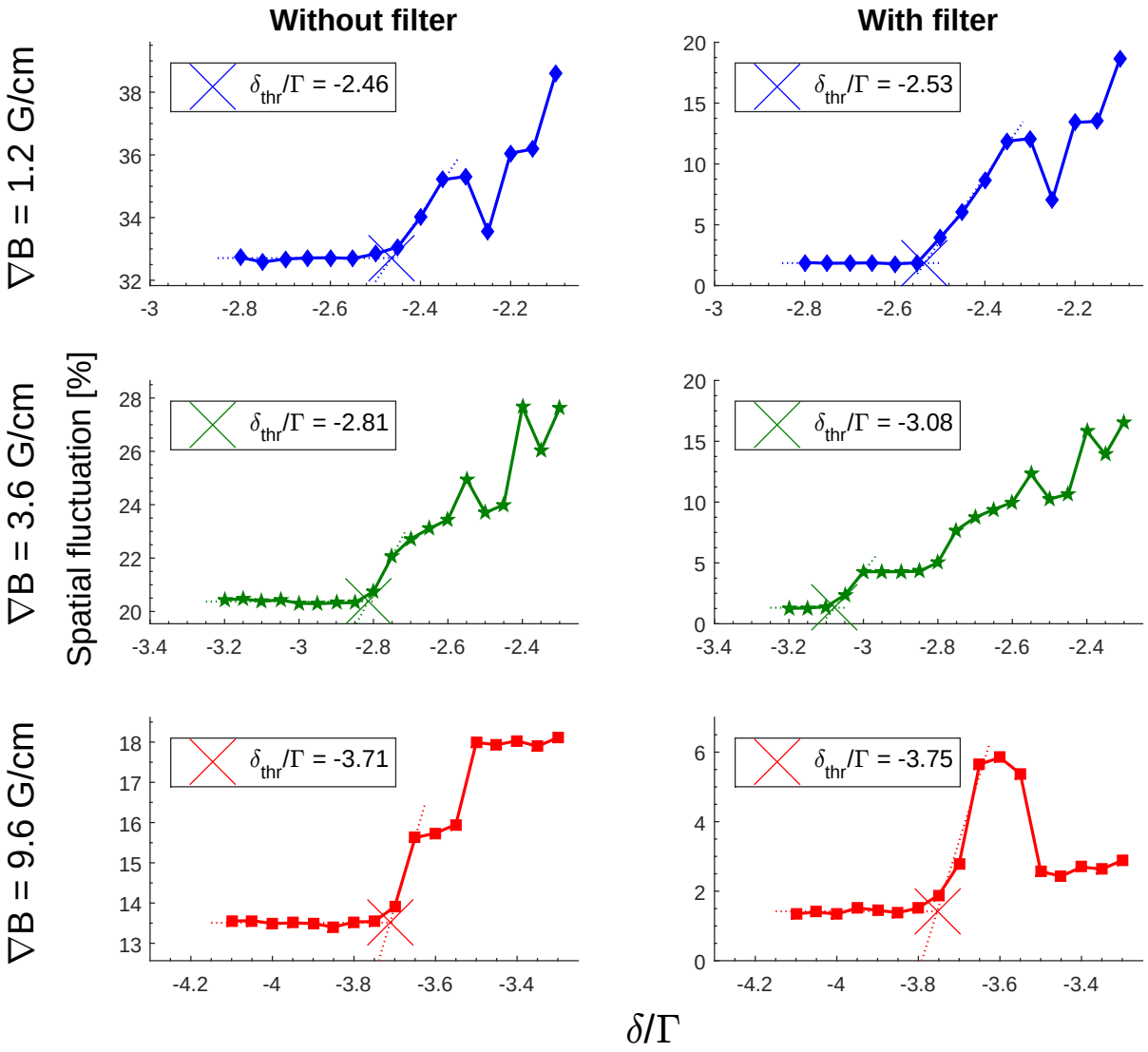

Figure 3.27: Determination of the instability threshold detuning δ_{thr} without Gaussian filtering (left column) and with Gaussian filtering (right column) performed on the simulated cloud images for different magnetic field gradients ∇B (rows). See the text for more details on the filtering, and see Fig. 2.9 for the different notations used in this figure.

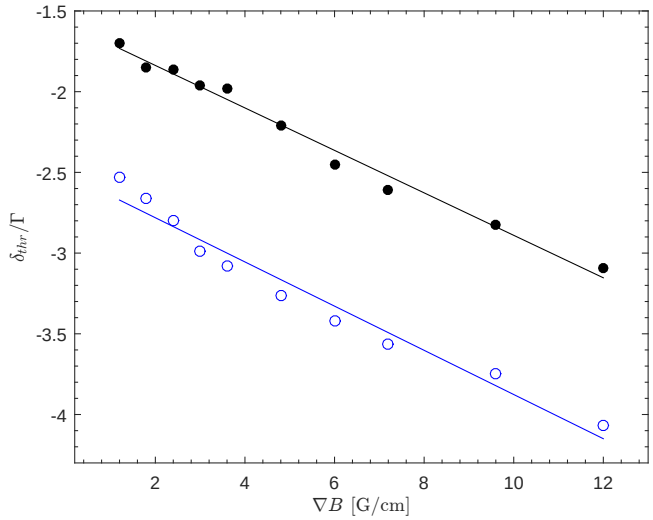

Figure 3.28: The threshold detuning δ_{thr} in units of Γ versus the magnetic field gradient ∇B. The black dots are the experimental results, and the blue circles are the simulated results. The solid black and blue lines are linear fits to the corresponding data-points. The experimental results are also displayed in Fig. 2.10. The simulation parameters can be found in Tab. 3.3.

Testing of instability threshold's dependence on N_{sup}, Δt and W

Here we present the results of *field tests* for instability threshold's dependence on the super-particle number N_{sup}, the simulation time-step Δt and the tube-width W. The purpose of these tests is to discuss the error produced with our choices of N_{sup}, Δt, W in the main simulation. We concentrate on the case with $\nabla B = 3$ G/cm, with the remaining parameters (not varied in a given test) being the same as previously (Tab. 3.3), with the exceptions being that in the N_{sup} convergence test, we use the $-\delta/\Gamma$ values from 2.5 to 3.3 (step of 0.05), while in the remaining tests we use the $-\delta/\Gamma$ values from 2.65 to 3.3.

Let us start with Fig. 3.29, displaying the outcome for the threshold's dependence on the super-particle number N_{sup}. The boundary at $N_{sup} = 10^3$ super-particles (vertical dotted line) indicates the lowest amount of super-particles needed to simulate the instabilities. Indeed, here the coarse-graining becomes too great for capturing the necessary detail for the instabilities to appear. We stress that this boundary is not limited to the simulation parameters in the test and is observed to be general. We observe that at $N_{sup} = 10^4$ super-particles the convergence in δ_{thr} is reached ($\delta_{thr}/\Gamma = -3.13$). With our current choice of $N_{sup} = 7 \cdot 10^3$ super-particles the underestimation in $|\delta_{thr}|$ is, however, less than 5 % ($\frac{3.13}{2.99} = 4.68\,\%$) (see the large cross), which we deem to be acceptable. Moreover, by sticking to our current choice of N_{sup}, we save a lot of simulation time, as with an increase to $N_{sup} = 10^4$ super-particles we observe a two-fold increase in the time consumption, which is significant given that a single simulation run with $N_{sup} = 7 \cdot 10^3$ super-particles takes us 1-2 weeks to complete (see the introduction to this section).

Next, let us consider Fig. 3.30, displaying the outcome for the threshold's dependence on the simulation time-step Δt. As we first observe from the figure, in our main simulation we indeed used a convergent Δt value (see the filled diamond). As Δt is increased, error is produced in the threshold determination and, eventually, a boundary is reached at which the simulated clouds disperse due to the numerical solutions becoming divergent (see the vertical solid line). Bear in mind that this boundary is limited to the simulation parameters in the test. Notice as well the preceding boundary (vertical dashed line), drawn using $\Delta t = 1/\omega_{tr,3D} \cdot 0.1$, evaluated at δ_{thr} of the main simulation ($\delta_{thr}/\Gamma = -2.99$). As observed in the figure, this Δt value is very close to being a convergent one. Considering the results leading up to the devised *rule of thumb* for picking Δt and this rule's discussion (section 3.4.1), this observation indicates that many-atom effects do not introduce here frequencies larger than the trapping frequency $\omega_{tr,3D}$. Note that this test does not exclude the possibility that deeper in the unstable regime frequencies larger than $\omega_{tr,3D}$ are introduced, and thus, as will be seen in the next subsection (surrounding the instability diagram simulation), we have considered to further reduce Δt.

Finally, let us consider Fig. 3.31, displaying the outcome for the threshold's dependence on the the tube-width W. As we first observe from the figure, since in our main simulation the W value is set by the devised *rule of thumb* (refer to section 3.4.3), we are led to an underestimation in $|\delta_{thr}|$ (see the filled

square), and the convergent W value is 25 % smaller in size. The underestimation is, however, by around 4 % ($\frac{3.11}{2.99} = 4.01\,\%$), and when taking into account the underestimation produced due our choice of N_{sup}, we thus have an overall underestimation of around 9 %, which we deem to be acceptable. Moreover, by sticking to our current choice of W, we save some simulation time, because a larger W value implies less grid-points at which the intensity is first evaluated (refer to Figs. 3.9, 3.10). Next, the two boundaries in the figure (vertical solid lines) tell us that by making W either twice as large or four times as small as set by the *rule of thumb*, we no longer can simulate the instabilities. This is related to the respective facts that the attenuation gets underestimated, especially when closer to the cloud edge, and that the detail of the attenuation evaluation gets too coarse (refer to section 3.4.3 and Figs. 3.14, 3.15). We stress, however, that these boundaries are limited to the simulation parameters in the test. We note that in the next subsection (surrounding the instability diagram simulation), we will show how large the cloud-size fluctuations can become when deeply in the unstable regime and comment on the tube method's corresponding numerical performance.

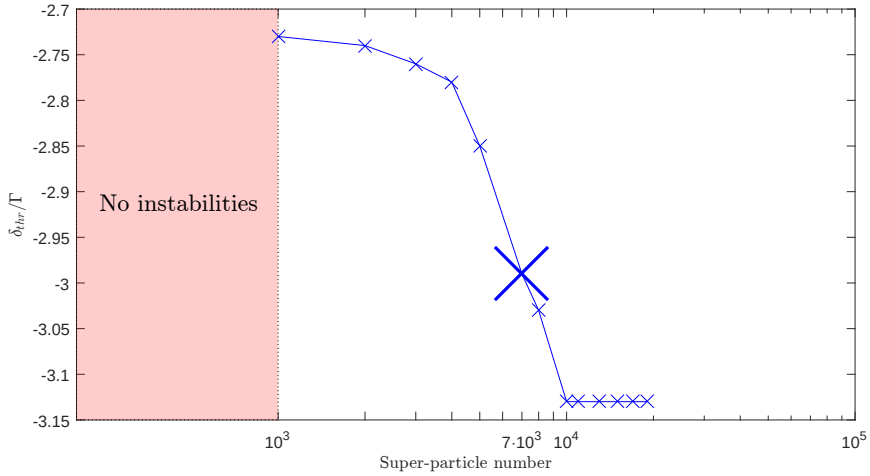

Figure 3.29: Test for the instability threshold's at $\nabla B = 3$ G/cm dependence on the super-particle number N_{sup}. The small crosses are the test results, and the large cross is the result of the main simulation (see Fig. 3.28). The solid line connecting the data-points is drawn as a visual aid. The vertical dotted line is the boundary indicating the lowest N_{sup} value needed to simulate the instabilities (see text).

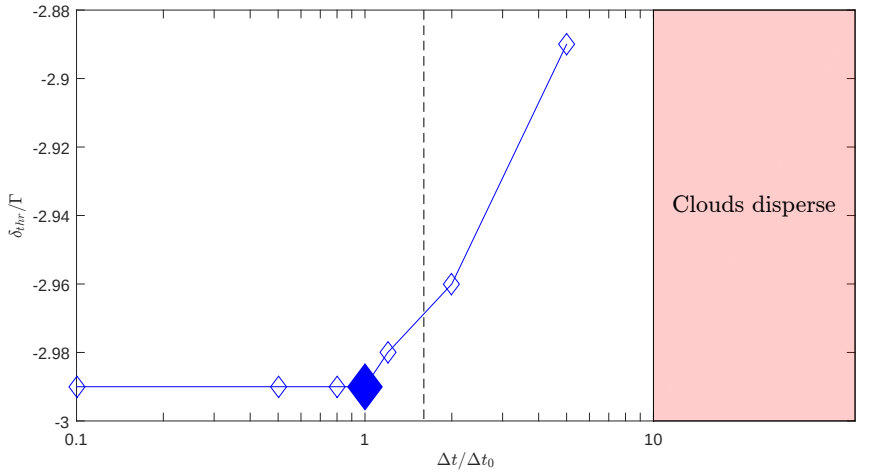

Figure 3.30: Test for the instability threshold's at $\nabla B = 3$ G/cm dependence on the simulation time-step Δt. The empty diamonds are the test results, and the filled diamond is the result of the main simulation (see Fig. 3.28). The solid line connecting the data-points is drawn as a visual aid. Δt_0 is the simulation-time step used in the main simulation (see Tab. 3.3). The vertical dashed line is the boundary drawn using $\Delta t = 1/\omega_{tr,3D} \cdot 0.1$, evaluated at δ_{thr} of the main simulation ($\omega_{tr,3D}$ is the trapping frequency, see below Eq. 3.91). The vertical solid line is the boundary indicating the largest Δt value at which the simulated clouds disperse (see text).

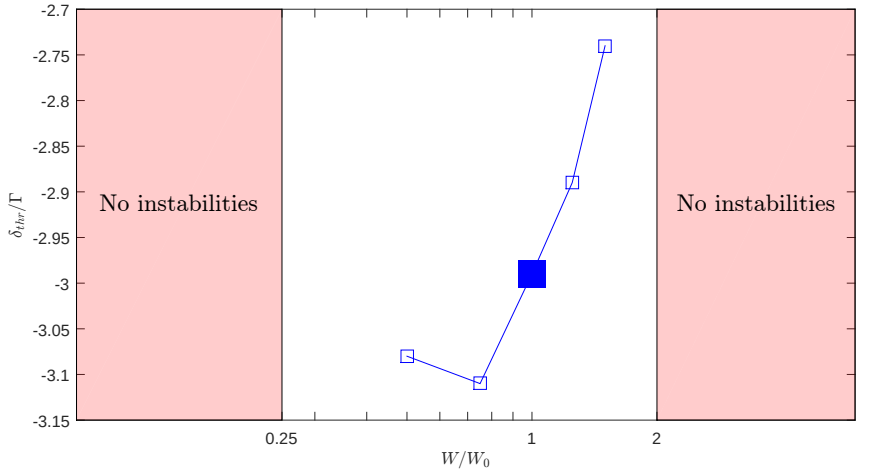

Figure 3.31: Test for the instability threshold's at $\nabla B = 3$ G/cm dependence on the tube-width W. The empty squares are the test results, and the filled square is the result of the main simulation (see Fig. 3.28). The solid line connecting the data-points is drawn as a visual aid. W_0 is the tube-width set according to the devised *rule of thumb* (refer to section 3.4.3): we have $W_0 = 0.15 \cdot r_{RMS}(t = 0)$, with $r_{RMS}(t = 0)$ being the initial cloud radius. The vertical solid lines are the boundaries indicating the smallest (left) and largest (right) W values at which the instabilities can no longer be simulated (see text).

3.5.1.2 Instability threshold versus N

In this sub-subsection, we present the simulated instability threshold versus N and compare its behavior with that from the corresponding experiment (section 2.3.2). We, moreover, present the simulated maximal optical depths b_{MOT}^{max} as seen by a MOT beam when in presence of the other MOT beams versus N, for the stable clouds just below the threshold, and compare them (b_{MOT}^{max}) with their counterpart from the same experiment. The simulation parameters are first provided, followed up by a presentation of the results with their discussion. We note that results seen here are part of the publication in Ref. [72].

Like in the experiment, we have here in the simulation $I_\infty = 5$ mW/cm^2 per MOT beam, and $\nabla B = 7.2$ G/cm. As mentioned in the introduction of this section, we use $N_{sup} = 7 \cdot 10^3$ super-particles. The remaining simulation parameters, at the different N values, are summarized in Tab. 3.4. The N values are close to the experimental ones.

N	$-\delta/\Gamma$ (step of 0.05)	$r_{RMS}(t=0)$ [mm]	t_{end} [s]	Δt [s]
$5 \cdot 10^8$	2.2 to 2.8	1	1.8	$2 \cdot 10^{-5}$
10^9	2.2 to 2.8	1.4	—//—	—//—
$1.5 \cdot 10^9$	2.5 to 2.9	1.6	—//—	—//—
$3 \cdot 10^9$	2.8 to 3.2	1.9	—//—	—//—
$5 \cdot 10^9$	2.5 to 3.3	2.2	—//—	—//—
10^{10}	2.9 to 3.5	2.8	—//—	—//—
$1.5 \cdot 10^{10}$ (*)	2.6 to 3.7	3	—//—	—//—
$3 \cdot 10^{10}$	3.8 to 4.2	3.8	—//—	—//—
$5 \cdot 10^{10}$	3.95 to 4.45	4.4	—//—	—//—
$8 \cdot 10^{10}$	4.4 to 5	4.8	—//—	—//—
10^{11}	4.8 to 5.3	5.2	—//—	—//—
$1.5 \cdot 10^{11}$	5.3 to 5.8	6	—//—	—//—

Table 3.4: Parameters used at the different atom numbers N in the simulation of instability threshold versus N, with the unattenuated intensity $I_\infty = 5$ mW/cm^2 per MOT beam, the magnetic field gradient $\nabla B = 7.2$ G/cm and the super-particle number $N_{sup} = 7 \cdot 10^3$. The displayed parameters are the trapping detuning δ, the simulation end time t_{end}, the simulation time-step Δt and the RMS radius r_{RMS} of the 3D Gaussian cloud generated at the simulation start ($t = 0$). Note that each Δt value satisfies the devised *rule of thumb* for picking Δt (section 3.4.1), and the initial value of r_{RMS} determines the fixed tube-width W (section 3.4.3). (*) stems from Tab. 3.3, at $\nabla B = 7.2$ G/cm.

In Fig. 3.32, we plot the measured and simulated δ_{thr} values versus N (see the black dots and blue circles, resp.). As in the experiment, δ_{thr} in the simulation is observed to decrease with N, with similar power law scaling - the scalings are $-0.17\,\Gamma$ and $-0.14\,\Gamma$ for the experiment and simulation, respectively (see the solid black and blue line, resp.). Again, similarly to the previous case of the simulated threshold versus ∇B (section 3.5.1.1), this indicates that

our simulation model (the $F = 0 \rightarrow F' = 1$ model, section 3.2) efficiently captures the physical ingredients involved in the threshold determination versus N. The threshold-offset existing between the simulated and experimental results is, as previously (section 3.5.1.1), probably linked to the larger cloud size in the simulation.

We remind that in section 3.4.7, it was said we will prove that the clouds dealt with there are stable. The simulated threshold result at $N = 10^{11}$ atoms in Fig. 3.32 serves as the proof. Note that Fig. 3.29 suggests that the simulated results in Fig. 3.32 are underestimated (in absolute value) by $\sim$5 % as we use $N_{sup} = 7 \cdot 10^3$ super-particles, although by taking into account this underestimation, it is nevertheless true that the clouds which contain more than $N_{sup} = 7 \cdot 10^3$ super-particles in section 3.4.7 are stable (as $\delta_{thr}/\Gamma = -5.12$ at $N = 10^{11}$ for $N_{sup} = 7 \cdot 10^3$).

Finally, let us consider Fig. 3.33, where we display the simulated maximal optical depths b_{MOT}^{max} as seen by a MOT beam when in presence of the other MOT beams versus N, for the stable clouds just below the threshold, together with their experimental counterpart (see the purple diamonds and green crosses, resp.). We remind (from section 2.3.2) that the experimental outcome had diminished quality, such that we discussed only its general features. In obtaining the simulated results, we simply perform 1D Gaussian fitting to averaged (after the transient) optical depth profile (2D) on a line of points on the x-axis ($y = 0$), and take the peak-value of the fit as b_{MOT}^{max}. Firstly, we observe that b_{MOT}^{max} remains on average around 1, which contrasts the experiment where b_{MOT}^{max} is consistently above 1. We link the offset to the larger cloud size in the simulation and to the implementation of beam cross-saturation (section 3.3.3) considering it enhances the beam transmission through the clouds (see Fig. 3.16). Secondly, we observe that b_{MOT}^{max} in the simulation increases as N is increased, which may not be as clear-cut from the experimental counterpart due to the diminished quality. This observation suggests that, as the atom number is increased, the instabilities are induced for increasingly larger beam attenuations and, in turn, for increasingly larger compressional shadow forces.

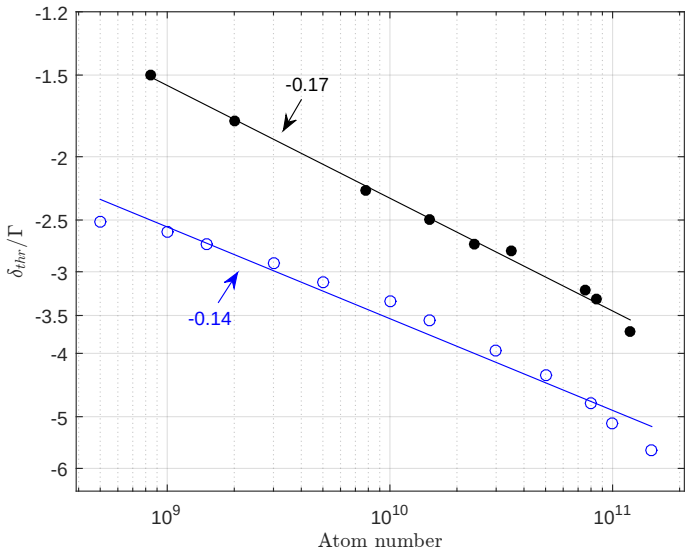

Figure 3.32: The threshold detuning δ_{thr} in units of Γ versus the atom number N, displayed in log-log scale. The black dots are the experimental results, and the blue circles are the simulated results. The solid black and blue lines are the power law fits to the corresponding data-points. The numbers next to the arrows are the scaling exponents of the corresponding power law fits. The experimental results are also displayed in Fig. 2.11. The simulation parameters can be found in Tab. 3.4.

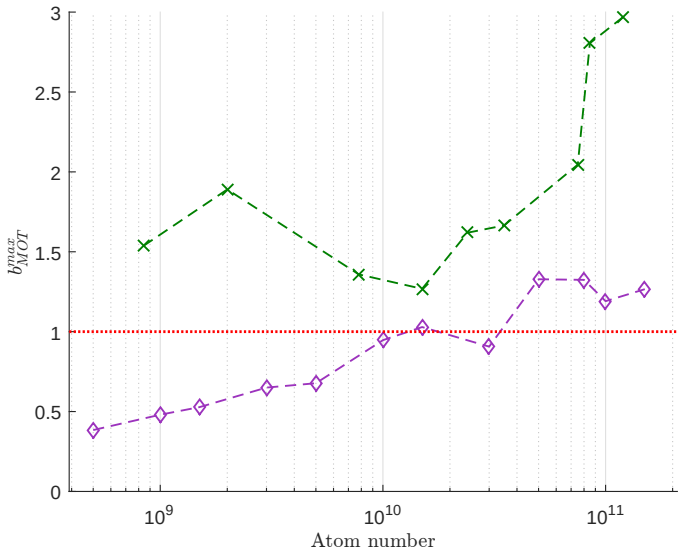

Figure 3.33: The maximal optical depth b_{MOT}^{max} as seen by a MOT beam when in presence of the other MOT beams versus the atom number N, for the stable clouds just below the threshold. The green crosses are the experimental results, and the purple diamonds are the simulated results. The dashed lines connecting the data-points are drawn as a visual aid. The horizontal dotted line indicates the rough boundary near which the multiple-scattering regime occurs. The experimental results are also displayed in Fig. 2.12. The simulation parameters can be found in Tab. 3.4.

3.5.1.3 Instability threshold versus I

In this sub-subsection, we present the simulated instability threshold versus I and compare its behavior with that from the corresponding experiment (section 2.3.3). The simulation parameters are first provided, followed up by a presentation of the results with their discussion. Note that throughout this sub-subsection I refers to the unattenuated intensity I_∞ per MOT beam.

Unlike in the experiment, where we considered three different ∇B values at three respective N values, we have here in the simulation considered a single ∇B and N value. We have here $\nabla B = 3$ G/cm at $N = 1.5 \cdot 10^{10}$ atoms - a unique pair of parameters, not used in the experiment. (We wanted first to do a simulation with the same N value as for the simulated threshold versus ∇B (section 3.5.1.1) and intended to later use the parameters as in the experiment.) As mentioned in the introduction of this section, we use $N_{sup} = 7 \cdot 10^3$ super-particles. The remaining simulation parameters, at the different I values, are summarized in Tab. 3.5. The I values are close to the experimental ones.

I [mW/cm^2]	$-\delta/\Gamma$ (step of 0.05)	$r_{RMS}(t=0)$ [mm]	t_{end} [s]	Δt [s]
0.05	2.6 to 3.2	3.6	1.2	10^{-4}
0.1	3.1 to 3.7	3.4	—//—	—//—
0.2	3.6 to 4.2	3.2	—//—	—//—
0.3	3.9 to 4.5	3.1	—//—	—//—
0.4	4.1 to 4.7	3	—//—	—//—
0.5	4.4 to 5	3.1	—//—	—//—
0.6	4.5 to 5.1	3.1	—//—	—//—
0.7	4.7 to 5.3	3.1	—//—	—//—
0.8	4.7 to 5.3	3.1	—//—	—//—
0.9	4.9 to 5.5	3.1	—//—	—//—
1	4.9 to 5.5	3.1	—//—	—//—
2	4.3 to 4.9	3.5	—//—	—//—
3	3.4 to 4	4	—//—	—//—
4	3.1 to 3.6	4.2	—//—	—//—
5 (*)	2.2 to 3.1	4.2	—//—	—//—

Table 3.5: Parameters used at the different values of the unattenuated intensity I (I_∞) per MOT beam in the simulation of instability threshold versus I, with the atom number $N = 1.5 \cdot 10^{10}$, the magnetic field gradient $\nabla B = 3$ G/cm and the super-particle number $N_{sup} = 7 \cdot 10^3$. The displayed parameters are the trapping detuning δ, the simulation end time t_{end}, the simulation time-step Δt and the RMS radius r_{RMS} of the 3D Gaussian cloud generated at the simulation start ($t = 0$). Note that each Δt value satisfies the devised *rule of thumb* for picking Δt (section 3.4.1), and the initial value of r_{RMS} determines the fixed tube-width W (section 3.4.3). (*) stems from Tab. 3.3, at $\nabla B = 3$ G/cm.

In Fig. 3.34, we plot the measured δ_{thr} values at $\nabla B = 4.8$ G/cm and

simulated δ_{thr} values divided by 1.7 versus I (see the black dots and blue circles, resp.). Note that $\nabla B = 4.8$ G/cm is selected and the division by 1.7 is done, as that allows us for a better side-to-side comparison of the threshold behavior characteristic to both the experiment and the simulation. Thus, we can easier observe that, similarly to the experiment, the simulated threshold behavior versus I is non-monotonous and divided into two regimes: first a sharp decrease at lower I, with a slower increase at higher I (note the log horizontal-axis). Such similarity indicates that our simulation model (the $F = 0 \rightarrow F' = 1$ model, section 3.2) is capable of capturing the physical ingredients involved in the threshold determination versus I.

To continue with trying to understand the threshold behavior versus I, we may resort to removing one by one the implemented physical ingredients or replacing them with something else and simpler. This would be a valid approach in understanding the threshold behavior versus ∇B and N, too. Now, since our simulation of threshold versus I confirms the experimental observation that the instabilities exist for MOT parameters where the elastic scattering dominates over the inelastic scattering, we have been motivated to perform an investigation on the impact of elastically and inelastically scattered light spectrum on the instabilities. In the last subsection (3.5.3), the results of this investigation will be presented.

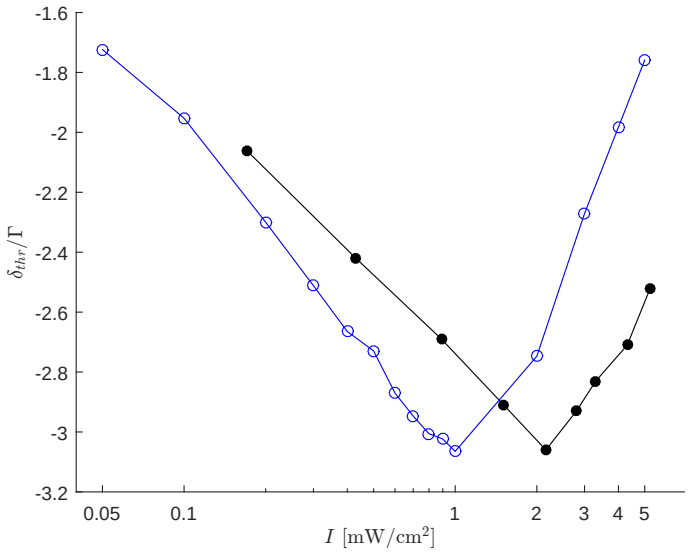

Figure 3.34: The threshold detuning δ_{thr} in units of Γ versus the peak intensity per MOT beam, I. The black dots are the experimental results, and the blue circles are the simulated results divided by 1.7 (i.e. $\delta_{thr}/1.7$). The solid lines connecting the data-points are drawn as a visual aid. The experimental results are also displayed in Fig. 2.13 ($\nabla B = 4.8$ G/cm). The simulation parameters can be found in Tab. 3.5.

3.5.2 The spatio-temporal properties of the unstable regime: δ-∇B phase-space instability diagram

In this subsection, we study the spatio-temporal properties of the simulated unstable regime. δ-∇B phase-space instability diagrams are here obtained, using respectively ESA and visual inspection, and comparisons are made with the experimentally obtained result (section 2.4.1). We start by providing the simulation parameters, after which we present imagery of simulated clouds that have been visually identified to belong to distinct instability regimes in the δ-∇B phase-space. Next, we analyze these clouds using ESA and apply the previous instability regime criteria based on this analysis to create a δ-∇B phase-space instability diagram, which we then compare with the experimentally obtained result. Another diagram of the same kind is afterwards created but using visual inspection, and then also compared with the experimentally obtained result. The stable cloud shape is briefly addressed at the end. A discussion of the results is provided. We note that results seen here are part of the publication in Ref. [73].

Simulation parameters

The simulation considered here is an extension of the one surrounding the simulated instability threshold versus ∇B (section 3.5.1.1), as clouds deeper in the unstable regime were simulated. The simulation parameters, at the different ∇B values, are summarized in Tab. 3.6. Note first from this table that deeper in the unstable regime (i.e. in the extension) we have picked shorter simulation end time t_{end} as well as smaller simulation time-step Δt. Shorter t_{end} is picked as the time before the instability sets in is shorter than t_{end}. Smaller Δt is picked to further ensure that we are working with convergent Δt (refer to Fig. 3.30 and its discussion). Note also that we have picked larger initial r_{RMS} value deeper in the unstable regime, due to greater cloud size fluctuations. Cloud size fluctuations are discussed in the next part of this subsection, where we start by presenting imagery of simulated clouds that have been visually identified to belong to distinct instability regimes in the δ-∇B phase-space.

∇B [G/cm]	$-\delta/\Gamma$ (step of 0.1)	$r_{RMS}(t=0)$ [mm]	t_{end} [s]	Δt [s]
1.2	1 to 2	6.5	0.4	10^{-5}
	2.1 to 2.3	6	1.2	10^{-4}
	2.4 to 2.8	6	2.4	10^{-4}
1.8	1 to 2	5.6	0.4	10^{-5}
	2.1 to 2.9	5.3	1.2	10^{-4}
2.4	1 to 2	5	0.4	10^{-5}
	2.1 to 3	4.7	1.2	10^{-4}
3	1 to 2.1	4.6	0.4	10^{-5}
	2.2 to 3.1	4.2	1.2	10^{-4}
3.6	1 to 1.5	4.3	0.2	$8 \cdot 10^{-6}$
	1.6 to 1.9	4.3	0.3	$8 \cdot 10^{-6}$
	2 to 2.2	4.3	0.7	$8 \cdot 10^{-6}$
	2.3 to 3.2	4	0.9	$8 \cdot 10^{-5}$
4.8	1 to 1.8	3.9	0.2	$6 \cdot 10^{-6}$
	1.9 to 2.5	3.9	0.5	$6 \cdot 10^{-6}$
	2.6 to 3.5	3.6	2.4	$6 \cdot 10^{-5}$
6	1 to 1.8	3.6	0.1	$4 \cdot 10^{-6}$
	1.9 to 2.5	3.6	0.3	$4 \cdot 10^{-6}$
	2.6 to 3.6	3.3	2.1	$4 \cdot 10^{-5}$
7.2	1 to 1.4	3.3	0.02	$2 \cdot 10^{-6}$
	1.5 to 1.9	3.3	0.04	$2 \cdot 10^{-6}$
	2 to 2.5	3.3	0.3	$2 \cdot 10^{-6}$
	2.6 to 3.7	3	1.8	$2 \cdot 10^{-5}$
9.6	1 to 1.8	3	0.02	10^{-6}
	1.9 to 2.5	3	0.16	10^{-6}
	2.6 to 4.1	2.7	1.2	10^{-5}
12	1 to 1.9	2.7	0.02	$8 \cdot 10^{-7}$
	2 to 2.5	2.7	0.1	$8 \cdot 10^{-7}$
	2.6 to 4.3	2.4	0.7	$8 \cdot 10^{-6}$

Table 3.6: Parameters used at the different magnetic field gradients ∇B in the instability diagram simulation, with the atom number $N = 1.5 \cdot 10^{10}$, the unattenuated intensity $I_\infty = 5$ mW/cm^2 per MOT beam and the super-particle number $N_{sup} = 7 \cdot 10^3$. The displayed parameters are the trapping detuning δ, the simulation end time t_{end}, the simulation time-step Δt and the RMS radius r_{RMS} of the 3D Gaussian cloud generated at the simulation start ($t = 0$). Note that each Δt value satisfies the devised *rule of thumb* for picking Δt (section 3.4.1), and the initial value of r_{RMS} determines the fixed tube-width W (section 3.4.3). Note as well that a part of the parameters seen here stem from Tab. 3.3.

Visual identification of distinct instability regimes

We next present imagery of simulated clouds that we have visually identified to belong to distinct instability regimes in the δ-∇B phase-space. Also, we show how the various properties, including the size, COM position, velocity and expelled super-particle number, evolve in time for these clouds.

In Figs. 3.35 and 3.36, we display imagery of simulated clouds in 2D and 3D, respectively, that we have visually identified to belong to distinct instability regimes in the δ-∇B phase-space. The six different example cases, at $[\delta,\ \nabla B] = [-1.3\,\Gamma,\ 1.2\ \text{G/cm}]$, $[-1.8\,\Gamma,\ 3.6\ \text{G/cm}]$, $[-2.6\,\Gamma,\ 12\ \text{G/cm}]$, $[-3.3\,\Gamma,\ 6\ \text{G/cm}]$, $[-2.9\,\Gamma,\ 9.6\ \text{G/cm}]$ and $[-1.1\,\Gamma,\ 7.2\ \text{G/cm}]$, are respectively referred to as A, B, C, D, E and F. Let us concentrate first on the case-A, -B and -C clouds, which are reminiscent of those observed in the experiment. We observe in Fig. 3.35 that the case-A cloud possesses complex-looking structures fluctuating inside a roughly fixed envelope, similarly to the experiment, in the *filament-like* regime; the structures are not as small and numerous as in the experiment, which we attribute to the coarse-graining due to the limited N_{sup} in the simulation. The case-B cloud in this figure is seen to exhibit intermittent elongations along beam directions (diagonals in the images), like in the *asymmetric* regime; note that we are thus provided strong evidence that our experimental observations of such symmetry-breaking behavior are not due to some experimental artifact (e.g. residual intensity imbalance). For the case-C cloud in the same figure, we observe large deformations in arbitrary directions but on average roughly isotropically distributed around the trap center, like in the *symmetric* regime. Fig. 3.36 illustrates the fact that large deformations of the case-B and -C clouds primarily occur in the xy-plane (the image-plane in Fig. 3.35), which is the plane of lowest magnetic field gradient; this was reported to happen in the experiment, too. Hence, in addition to being able to reproduce different threshold behaviors (refer to section 3.5.1), our simulation model is seen to also predict instability regimes obtained experimentally. The simulation, however, produces unstable clouds that do not occur in the experiment - the case-D, -E and -F clouds. The case-D cloud is observed in Fig. 3.35 to possesses a squarish elliptical shape oriented 45° with respect to a beam direction (horizontally in the image-plane) while being nearly static. The case-E cloud is seen to have a twisted elliptical shape along a beam direction while being nearly static as the case-D cloud. For the case-F cloud, two components are exhibited: a fluctuating central core and a fluctuating cross of atoms formed along beam directions. Fig. 3.36 illustrates the fact that the case-D cloud is twisted when observed in a different plane from the xy-plane, and that large deformations of the case-E and -F clouds primarily occur in the xy-plane.

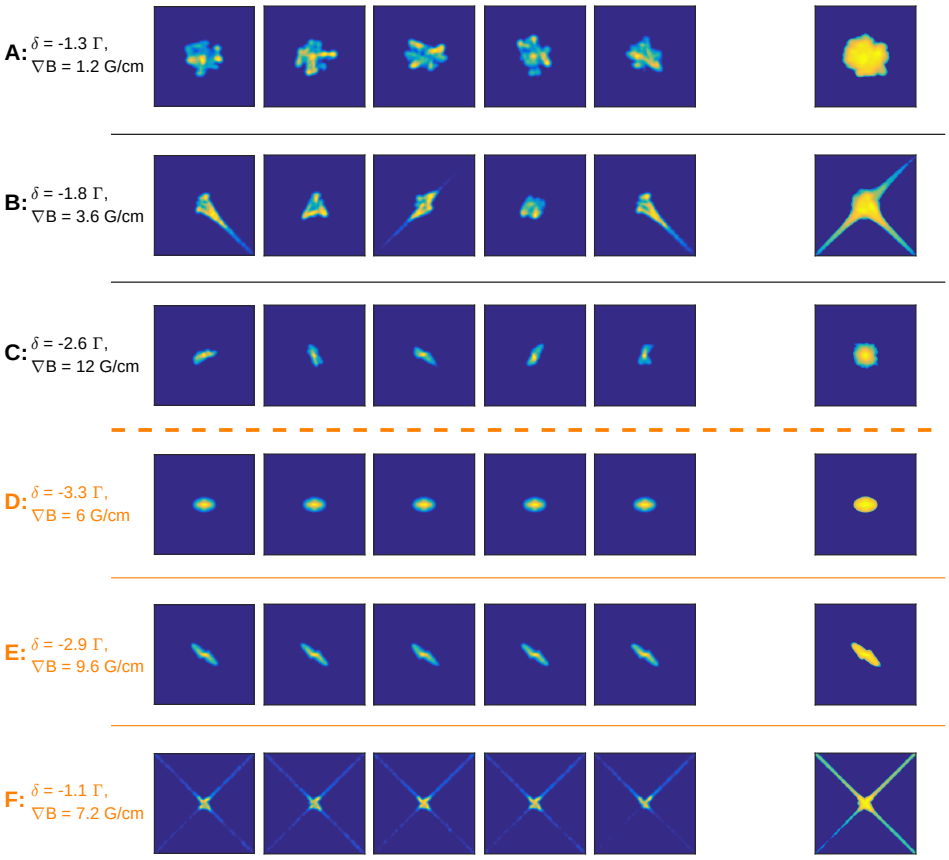

Figure 3.35: Display of 2D images of simulated clouds belonging to the distinct instability regimes discussed in the text. Each image in the five leftmost columns is a single-shot image (density integrated along the z-axis; Gaussian-filtered, standard deviation of 2 sigma) showing a random instance of the cloud dynamics, and each image in the rightmost column is a log-scaled average of 50 single-shot images. 5 % of the lowest intensity has been removed from the single-shot images in the construction of each average image (for display purposes only). The diagonals in the images correspond to the directions of two pairs of MOT beams. The field of view is 9.6×9.6 cm^2. Note that the case-A, -B and -C clouds visually resemble the same case experimental clouds in Fig. 2.16.

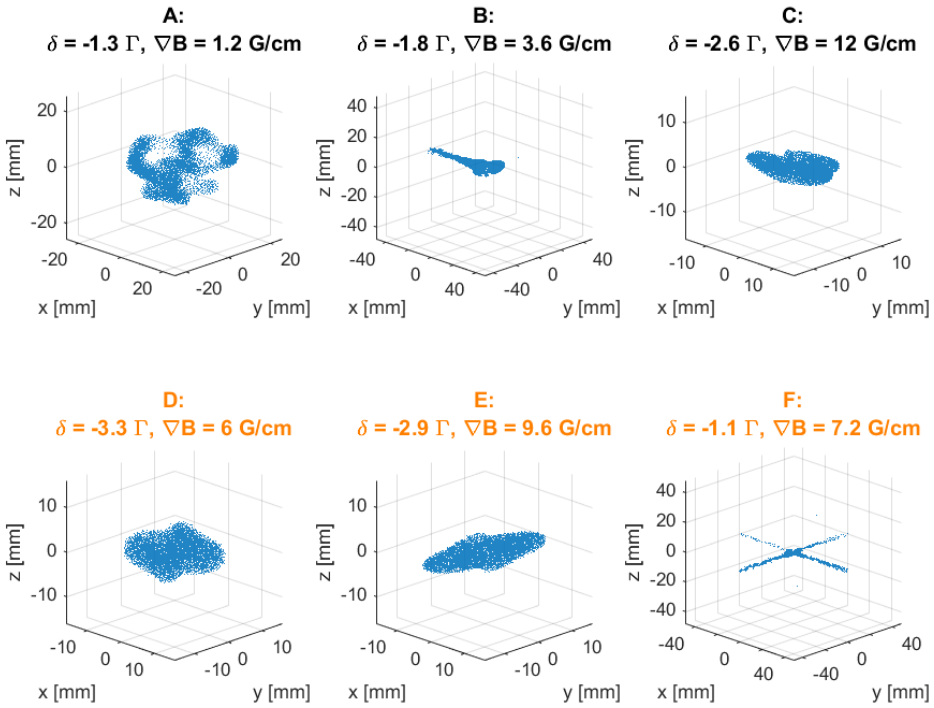

Figure 3.36: Display of 3D images of the simulated clouds in Fig. 3.35. Each image is a single-shot image. The individual dots are super-particles.

In Fig. 3.37, we display, for the simulated unstable clouds in Fig. 3.35, the evolutions of the RMS radius $r_{RMS} \equiv \sqrt{\langle |\mathbf{r} - \mathbf{r}_{COM}|^2 \rangle}$ (defined in section 3.4.3), the COM radius r_{COM} scaled by r_{RMS}, the RMS velocity $v_{RMS} \equiv \sqrt{\langle |\mathbf{v}|^2 \rangle}$ and the super-particle number N_{sup} beyond a cubic frame with the center of the MOT's and the edge length of the image frame's in Fig. 3.35. The r_{RMS}, r_{COM}/r_{RMS} and v_{RMS} evolutions neglect N_{sup} beyond this cubic frame. Note that such expelled super-particles are not excluded in the simulation (refer to section 3.3.3, the part for the tube method implementation). From the r_{RMS} evolution plots we observe that for the case-A, -B and -C clouds the fluctuations (oscillations) are more significant than compared to the case-D, -E and -F clouds - as apparent from the corresponding single-shot images in Fig. 3.35. Notice that the case-C cloud distinguishes itself due to its size fluctuations reaching amplitudes up to $\sim$50 % of the initial size - this nevertheless should not compromise the numerical performance of the tube method, as indicated by the result in Fig. 3.31. Therefore, we may deem the tube method to perform fairly accurately when simulating the unstable regime. From the r_{COM}/r_{RMS} evolution plots we observe that, with an exception of the case-B cloud, the COM of the clouds remains close to the MOT center - again, as apparent from the corresponding single-shot images in Fig. 3.35. From the v_{RMS} evolution plots we notice that some cloud cases - B, E and F - have the median velocity (after the transient) exceeding 4 m/s, implying that the Doppler effect, which we have neglected in the rescattering cross-section calculation, can be important for these clouds (for 4 m/s the Doppler width is $\sim\Gamma$). Note that the momentum diffusion coefficient calculation is here also compromised, due to us choosing to neglect in it the Doppler effect (see the introduction of this section); this calculation is, moreover, affected by the fact that we have neglected in it the Zeeman effect (for example, for the case-E cloud, with the median radius of $\sim$4.5 mm, the Zeeman width is $\sim\Gamma$). From the evolution plots for N_{sup} beyond the cubic frame we observe that for all the clouds, with an exception of the case-F cloud, no super-particles or a negligible amount go beyond that frame; there are great spikes in the N_{sup} evolution plot for the case-B cloud, but that is explained by the severe intermittent deformations that the cloud undergoes along beam directions (see Fig. 3.35). For the case-F cloud, more than 2/3 of all the super-particles go beyond the cubic frame in only 0.02 seconds. The expulsion occurs along beam directions (see Fig. 3.35). This case cloud is close to the resonance, but the fact that the trap here becomes narrow (refer to Fig. 1.6) is clearly not enough to explain such dramatic as well as highly-directional expulsion. If the expulsion did not have preferred directions, we could probably relate it to the numerical artifact of a too large simulation time-step. However, given the high directionality, we have a good reason to believe that the observed behavior is in fact genuine. We are going to refrain from more speculation surrounding causes of this expulsion.

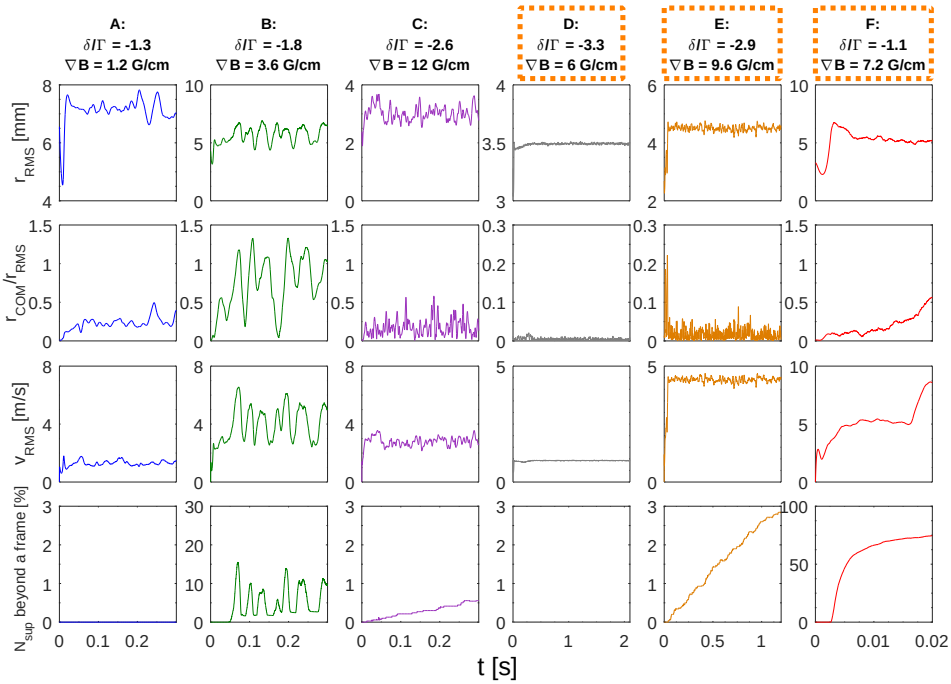

Figure 3.37: A display, for the simulated unstable clouds in Fig. 3.35, of the evolutions (rows) of the RMS radius r_{RMS} ($\equiv \sqrt{\langle |\mathbf{r} - \mathbf{r}_{COM}|^2 \rangle}$), the COM radius r_{COM} scaled by r_{RMS}, the RMS velocity v_{RMS} ($\equiv \sqrt{\langle |\mathbf{v}|^2 \rangle}$) and the super-particle number N_{sup} beyond a cubic frame with the center of the MOT's and the edge length of the image frame's in Fig. 3.35. The r_{RMS}, r_{COM}/r_{RMS} and v_{RMS} evolutions neglect N_{sup} beyond this cubic frame. Note that the time-axis is the same for the case-A, -B and -C clouds, for a better comparison (total evolution time can be found in Tab. 3.6).

δ-∇B phase-space instability diagram based on ESA

We here continue by providing the ESA results for the simulated unstable clouds in Fig. 3.35 and apply the previous instability regime criteria (from section 2.4.1) based on this analysis to create a δ-∇B phase-space instability diagram. This diagram is compared with the experimental one in Fig. 2.19.

In Fig. 3.38, we display the histograms obtained using ESA for the simulated unstable clouds in Fig. 3.35. To stay consistent with the image treatment done when determining instability threshold (refer to section 3.5.1.1), we note to use the same Gaussian filtering (standard deviation of 2 sigma). Let us start with the cloud cases not occurring in the experiment - D, E and F. The case-D and -E clouds are seen to posses very narrow histograms, most of them with either one or two bins (the bin size is 0.025) and only once with three bins (in E, S4), with different means, too, which vary from $\sim$1/16 to $\sim$1/4. This corresponds to what can be discerned visually in Fig. 3.35: the narrow width of the histograms is due to the clouds being almost static, with the off-centering of the mean of the histograms (from 1/8) being due to the clouds assuming anisotropic distributions. The case-F cloud is seen to possess narrow, two-bin wide histograms for the odd-numbered sectors, while twice and up to almost four times as wide for the even-numbered sectors, and with the means of the histograms being four

times larger for the even-numbered sectors compared to the odd-numbered sectors, $\sim 1/4$ versus $\sim 1/16$. This result of the greater widths and means of the histograms for the even-numbered sectors tells us that in these sectors, the cloud undergoes more profound anisotropic deformations, with all such deformations on average preferentially distributed among these sectors. Such behavior is well-explained by the formation of the cross of atoms as they are expelled from the cloud core along beam directions, as seen in Fig. 3.35. We move on now to the remaining cases - A, B and C. Compared to the previous cases, they are seen to possess greater histogram-widths, indicative of the clouds undergoing greater anisotropic deformations. More importantly, they present close similarities with the ESA results of the corresponding experimental cases (see Fig. 2.17). As in the experiment, the case-A cloud possesses histograms with width of ~ 0.2 and centering at $\sim 1/8$, which tell us that the cloud undergoes small anisotropic deformations that are on average almost isotropically-distributed. Such behavior of the cloud may also be judged from its single-shot and average images in Fig. 3.35. The case-B cloud bears as well resemblance with the experimental result. First of all, we observe that the histogram-widths increase in comparison to the case-A cloud: they are here from ~ 0.2 to ~ 0.5 with the average of ~ 0.3. Secondly, we observe that the histogram-means vary by a lot, here from ~ 0.05 to ~ 0.25, and imply anisotropic cloud distribution on average. Thirdly, we observe a similar double-peak/bimodal structure appearing for one of the sectors (S8), indicative of intermittent behavior. Indeed, such intermittent behavior may also be discerned from the single-shot images of the cloud in Fig. 3.35. Regarding the case-C cloud, we observe that, similarly to the experiment, the histogram-widths are increased in comparison to the case-A cloud, here close to their average of ~ 0.3, while the histogram-means remain at $\sim 1/8$, overall telling us that the cloud undergoes greater anisotropic deformations that are on average almost isotropically-distributed. Such behavior of the cloud may also be judged from its single-shot and average images in Fig. 3.35. Moreover, as in the experiment, the histograms for the case-C cloud show, like for the case-A cloud, no signs of intermittent behavior as exhibited by the case-B cloud. Note that the histograms for the case-C cloud are, however, on average less wide than for the case-B cloud and do not reach the average widths of the experimental counterpart. As we will see next, all the case-C clouds do not reach the large average histograms-widths observed in the experiment, and this has an important consequence on the instability diagram result, when based on ESA.

We consider now constructing an instability diagram, drawn using our previous criteria (for separating the case-A, -B and -C instability regimes) that we recall (from section 2.4.1) involve knowledge of the average histogram-width and the average of the largest-to-individual histogram-width ratios, calculated from ESA. In Fig. 3.39(a), we display the δ-∇B phase-space colormap showing the average histogram-width for the simulated unstable clouds. We take notice of the stand-out region in the colormap for low ∇B values ($\nabla B \leq 4.8$ G/cm), where the average histogram-width exceeds 1/3, which, as previously written (in section 2.4.1), is indicative of the clouds undergoing sizable anisotropic deformations. The case-C clouds in the simulation do not, however, fall into

this category of clouds, as they otherwise did in the experiment. Also, the stand-out region in the corresponding experimental colormap in Fig. 2.18(a) is positioned very differently, for high ∇B values ($\nabla B \geq 9.6$ G/cm), and already suggests a different-looking simulated instability diagram. In Fig. 3.39(b), we display the average of the largest-to-individual histogram-width ratios for the simulated unstable clouds. We take notice of the stand-out region stretching out across the whole of the ∇B-range, where the average of the largest-to-individual histogram-width ratios exceeds 1.8, which, as previously written, implies that some cloud parts undergo much greater anisotropic deformations than other parts. The case-B clouds in the simulation fall into this category of clouds, like their experimental counterpart. However, the stand-out region in the corresponding experimental colormap in Fig. 2.18(b) occurs for intermediate and high ∇B values ($\nabla B \geq 6$ G/cm). Furthermore, the stand-out region in Fig. 3.39(b) completely overlaps with the one in Fig. 3.39(a), which is not the case in the experiment.

In Fig. 3.40, we show the simulated δ-∇B phase-space colormap diagram that is drawn according to the devised instability regime criteria. We use the previous color code to indicate the different kinds of unstable clouds: blue, green and purple for respectively the case-A, -B and -C clouds. We observe that the case-C region is missing from the diagram, indeed being the consequence of the stand-out region in Fig. 3.39(b) completely overlapping with the one in Fig. 3.39(a). Concentrating on the case-A and -B regions, we observe that the diagram anyhow does not show good resemblance with the corresponding experimental one in Fig. 2.19. For low ∇B values, the simulated diagram predicts existence of the case-B clouds closer to the resonance, whereas in the experimental one this part is dominated by the case-A clouds. Moving on to the intermediate and high ∇B-range, the simulated diagram predicts existence of both case-A and -B clouds, whereas the experimental one shows that the case-A clouds do not appear in this ∇B-range. Apart from the case-C clouds possessing insufficiently wide histograms, another important factor contributing to the discrepancy between the simulation and experiment is the prediction of the instability regimes not occurring in the experiment (D, E and F). These factors motivate us to next create another instability diagram, and, to keep it simple as well as fairly robust, we will do so by using visual inspection.

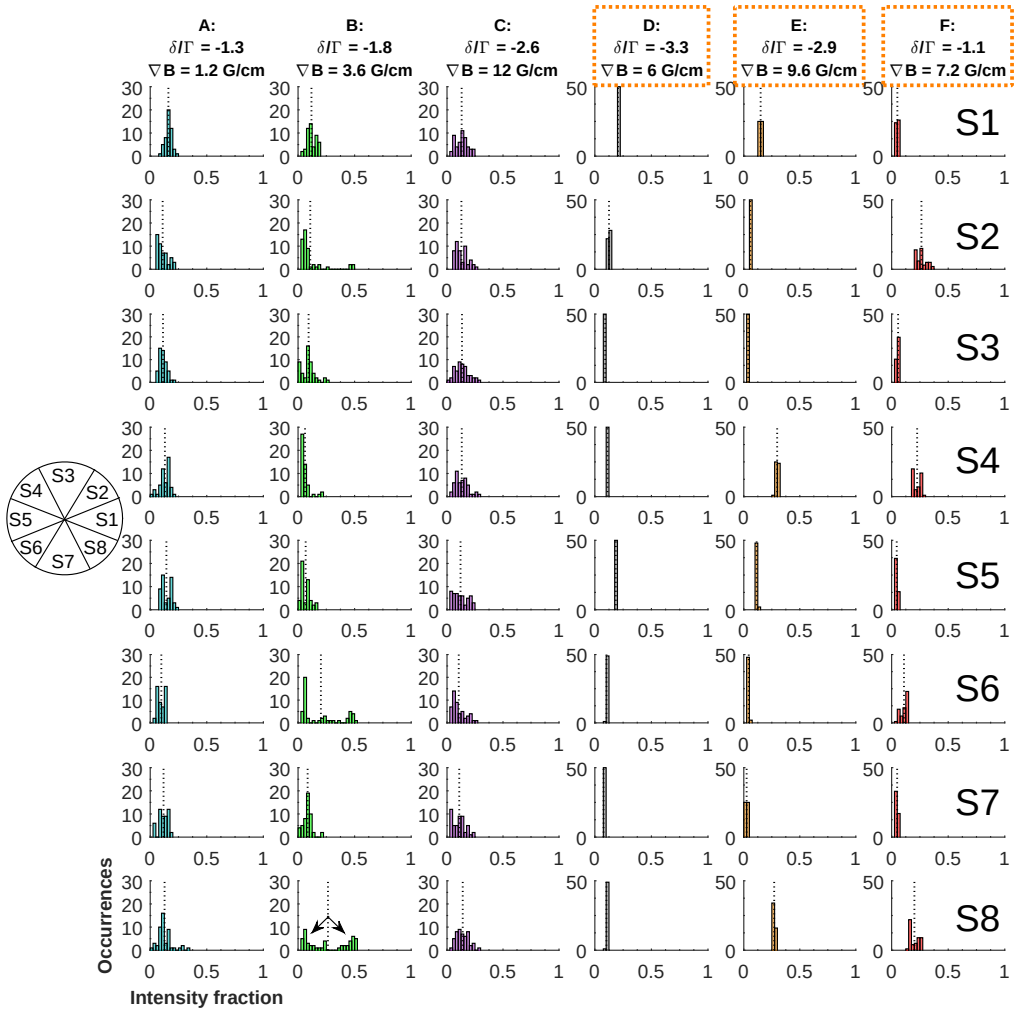

Figure 3.38: The ESA results for the simulated unstable clouds in Fig. 3.35. The histograms show the statistics on the intensity fractions in each sector (S1-8, rows). The arrows reflect intermittent behavior of one of the clouds as discussed in the text. The vertical dotted lines indicate the means of the data used in the construction of the corresponding histograms. Note the similarities of the case-A, -B and -C results with the corresponding experimental ones in Fig. 2.17.

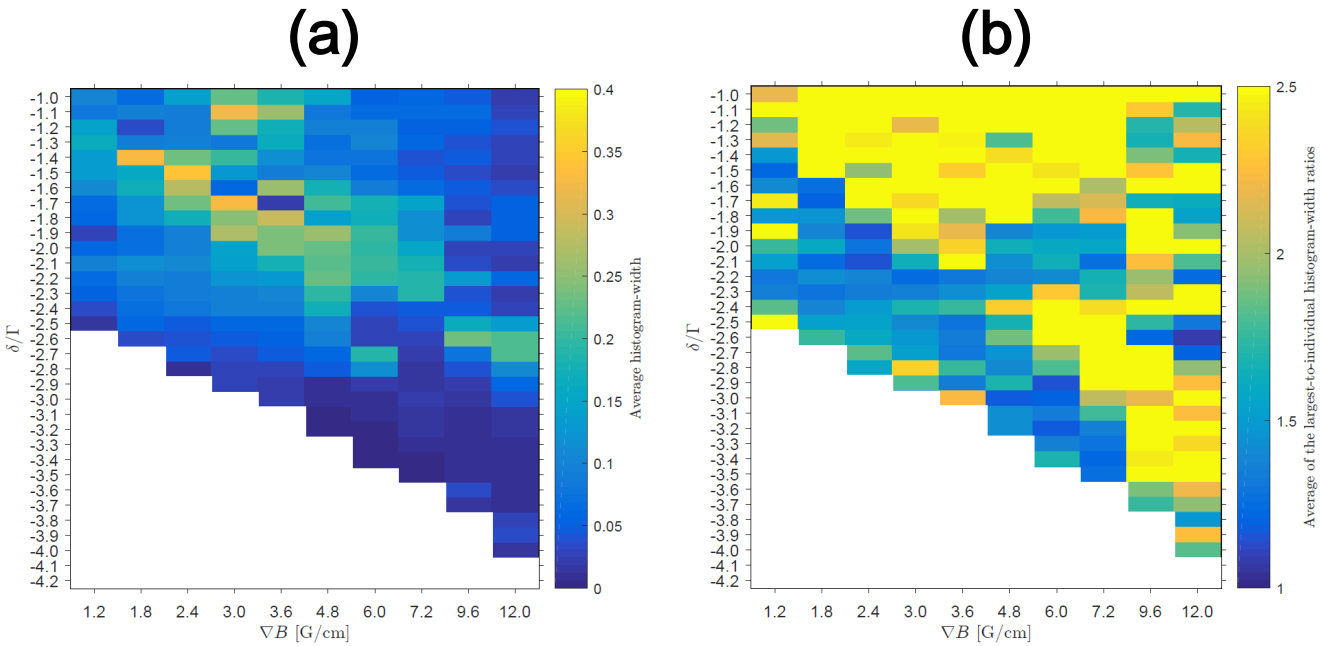

Figure 3.39: Simulated δ-∇B phase-space colormaps showing (a) the average histogram-width and (b) the average of the largest-to-individual histogram-width ratios, calculated from ESA. White color is used for stable clouds, determined by the simulated result in Fig. 3.28. The simulation parameters can be found in Tab. 3.6. Note the corresponding experimental results in Fig. 2.18.

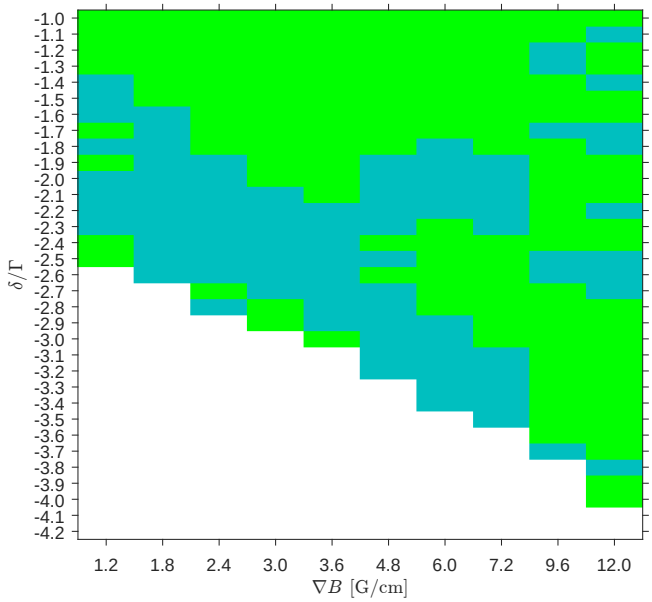

Figure 3.40: Simulated δ-∇B phase-space colormap diagram that is drawn according to the instability regime criteria seen in section 2.4.1. The following color code is used for the unstable clouds: blue, green and purple for respectively the case-A, -B and -C clouds (the last case is missing from the diagram; see text). White color is used for stable clouds, determined by the simulated result in Fig. 3.28. The simulation parameters can be found in Tab. 3.6. Note the corresponding experimental result in Fig. 2.19.

δ-∇B phase-space instability diagram based on visual inspection

We here finally provide the simulated δ-∇B phase-space instability diagram that is produced using visual inspection of the clouds. This diagram is compared with the experimental one in Fig. 2.20 (produced using ESA). The stable cloud shape is briefly addressed at the end.

In Fig. 3.41, we show the simulated δ-∇B phase-space instability diagram that is produced using visual inspection of the clouds. It includes unstable cloud imagery, like in the experimental instability diagram in Fig. 2.20. From this imagery we can observe features characteristic to each regime (six in total). Let us start by commenting on the regime cases resembling well those occurring in the experiment - A, B and C. The case-A regime (blue enclosure) occurs in the low ∇B-range and from the threshold to roughly the middle of the simulated unstable δ-range. This regime is seen to possess average features similar to those of the example case-A cloud at [$\delta = -1.3\,\Gamma$, $\nabla B = 1.2$ G/cm], as roughly isotropic distribution of deformations can be discerned. Moving on to the case-B regime (green enclosure), it stretches out across the whole of the ∇B-range and above the middle of the simulated unstable δ-range while being further from the resonance in the intermediate and high ∇B-range. The clouds here are seen to be elongated along beam directions (diagonals in the images). We report that the clouds here, like the example case-B cloud at [$\delta = -1.8\,\Gamma$, $\nabla B = 3.6$ G/cm], show the same kind of intermittency, where the cloud undergoes elongations along beam directions. Regarding the case-C regime (purple enclosure), occurring in the high ∇B-range and roughly at the middle of the simulated unstable δ-range, the average features display isotropic distribution of deformations, similarly to the example case-C cloud at [$\delta = -2.6\,\Gamma$, $\nabla B = 12$ G/cm]. Larger portions of the cloud can in this regime shift away from the MOT center compared to the case-A regime. Also, the case-C regime, similarly to the case-A regime, does not exhibit intermittent behavior as the case-B regime. Next, let us move on to commenting the regime cases not occurring in the experiment - D, E and F. The case-D regime (gray enclosure), occurring after the mid-low ∇B value ($\nabla B > 3$ G/cm) and close to the threshold, displays squarish elliptical shapes oriented 45 ° with respect to one or other beam direction (horizontally or vertically in the image-plane), similarly to the example case-D cloud at [$\delta = -3.3\,\Gamma$, $\nabla B = 6$ G/cm]. The clouds here remain nearly static. For the case-E regime (brown enclosure), occurring for intermediate and high ∇B values between the case-C and -D regimes in δ, the clouds appear in a twisted elliptical shape oriented along one or other beam direction, similarly to the example case-E cloud at [$\delta = -2.9\,\Gamma$, $\nabla B = 9.6$ G/cm]. Most of the clouds here remain nearly static, similarly to the case-D clouds. Finally, for the case-F regime, occurring closer to the resonance for intermediate and high ∇B values, we observe each cloud to be composed of a central core with a cross of atoms along beam directions, similarly to the example case-F cloud at [$\delta = -1.1\,\Gamma$, $\nabla B = 7.2$ G/cm]. In this regime, the cross of atoms is formed as the clouds expel the atoms from the core; this expulsion is very dramatic as more than 2/3 of all the super-particles are expelled (beyond a 3D frame with the edges of size

of an image in the diagram) in merely 0.02 seconds of simulation start. Concerning the 3D features of the different regime clouds, they are similar to the corresponding ones in Fig. 3.36, with the case-D regime clouds being twisted when observed in a different plane from the xy-plane (the image-plane in the diagram), and with large deformations of the case-B, -C, -E and -F regime clouds occurring primarily in the xy-plane; no new notable information is gathered for the case-A regime from the 3D features.

We consider now comparing the simulated instability diagram in Fig. 3.41 with the experimental instability diagram in Fig. 2.20. Of course, no one-to-one comparison can be made, due to the different amount of instability regimes presented in the simulated diagram versus the experimental diagram. Nevertheless, because the case-D, -E and -F regime clouds break the trap symmetry in a close fashion to the case-B regime clouds, let us for now assume that all these regimes form a common regime. Under this assumption, such common regime presents itself across the whole of the ∇B-range and is overall more expansive than in the experiment. Regarding the case-A and -C regimes, these are positioned in the same ∇B ranges in both diagrams, i.e. the case-A regime for low ∇B values and the case-C regime for high ∇B values, but are less expansive in the simulation compared to the experiment. Next, let us consider the fact that the simulated threshold is offset by around $-1\,\Gamma$ from the experimental threshold. Thus, it may be speculated that in the simulation, we are exploring the part of the unstable regime deeper than in the experiment, and new physics is being shown for $\delta \gtrsim -2\,\Gamma$ in the simulated diagram. Assuming new physics indeed is being shown for $\delta \gtrsim -2\,\Gamma$, the simulated diagram becomes more alike with the experimental diagram, as the common regime together with the case-A and -C regimes are then positioned similarly in both diagrams. More interestingly, the simulated diagram thus predicts existence of the quite dramatic case-F regime. By performing experiments deeper in the unstable regime, it may be checked whether such regime indeed exists.

We would like to give names to the instability regimes not occurring in the experiment according to their most characteristic features observed in Figs. 3.35, 3.37 and 3.41. The case-D regime, due to the clouds being oriented $45\,^\circ$ with respect to one or other beam direction, we call it the *anti-aligned* regime. The case-E regime, due to the clouds being oriented along one or other beam direction, we call it the *aligned* regime. The case-F regime, due to the dramatic particle expulsion, we call it the *explosive* regime.

We close this sub-subsection by briefly addressing the stable cloud shape. In Fig. 3.41, it is observed to not be round, as otherwise ideally expected. In Fig. 3.42, we display 2D and 3D imagery showing how stable cloud shape changes as one moves further away from the threshold for $\nabla B = 3.6$ G/cm; the remaining simulation parameters are mentioned in the figure text. At $\delta/\Gamma = -3.5$, being near the threshold ($\delta_{thr}/\Gamma \approx -3$), the shape in the 2D image is seen to not be round and to possess features of a petal, as can also be observed for the stable clouds in Fig. 3.41, and the 3D image reveals this petal to be twisted. As one moves further away from the threshold, the 2D cloud shape is seen to turn rounder, with the twist in 3D diminishing; at more than $1.5\,\Gamma$ away

from the threshold (in absolute value), the 2D shape becomes round, with the twisting having disappeared. The fact that the twisting disappears when far from the threshold is supported by Fig. 3.43, where the N_{sup} evolution, in all the respective eight octants (in 3D), is plotted for the clouds in Fig. 3.42. From Fig. 3.43 we are told that when less than $1.5\,\Gamma$ away from the threshold, the amount of N_{sup} in each octant is unequal (see after the transient, of course), indicating existence of the twisting. However, when more than $1.5\,\Gamma$ away from the threshold, the amount of N_{sup} in each octant is the same, indicating that the twisting has disappeared. We note to not have observed experimentally the petal shapes discussed here, which we believe ultimately appear due to the simplicity of our simulation model. We link their observation in the simulated environment to the intensity attenuation. This has to do with the fact that the cloud compression should be maximal along the beam-axes, due to the optical depth there being the highest. Thus, the cloud should appear as a flattened ellipsoid pinched along the beam-axes, with this effect being more pronounced for smaller absolute values of detuning, because the optical depth is higher. However, the cloud also twists in 3D, which is not clear to us why.

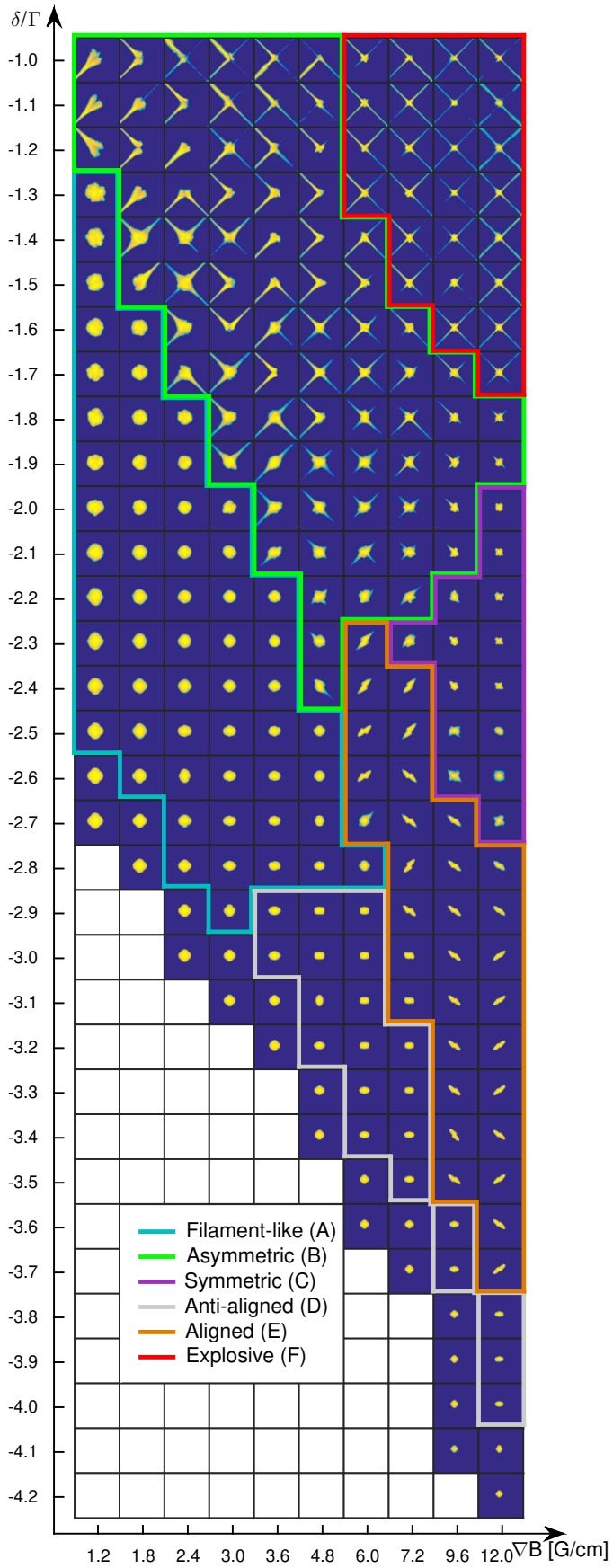

Figure 3.41: Simulated δ-∇B phase-space instability diagram that is produced using visual inspection of clouds. Each image is a log-scaled average of 50 single-shot images (densities integrated along the z-axis; Gaussian-filtered, standard deviation of 2 sigma), which had 5 % of their lowest intensity removed (for display purposes only). The blue, green, purple, gray, brown and red lines enclose respectively the filament-like (A), asymmetric (B), symmetric (C), anti-aligned (D), aligned (E) and explosive (F) regimes. The diagonals in the images correspond to the directions of two pairs of MOT beams. The field of view is 9.6×9.6 cm^2. The simulation parameters can be found in Tab. 3.6. Note the experimental result in Fig. 2.20 (produced using ESA).

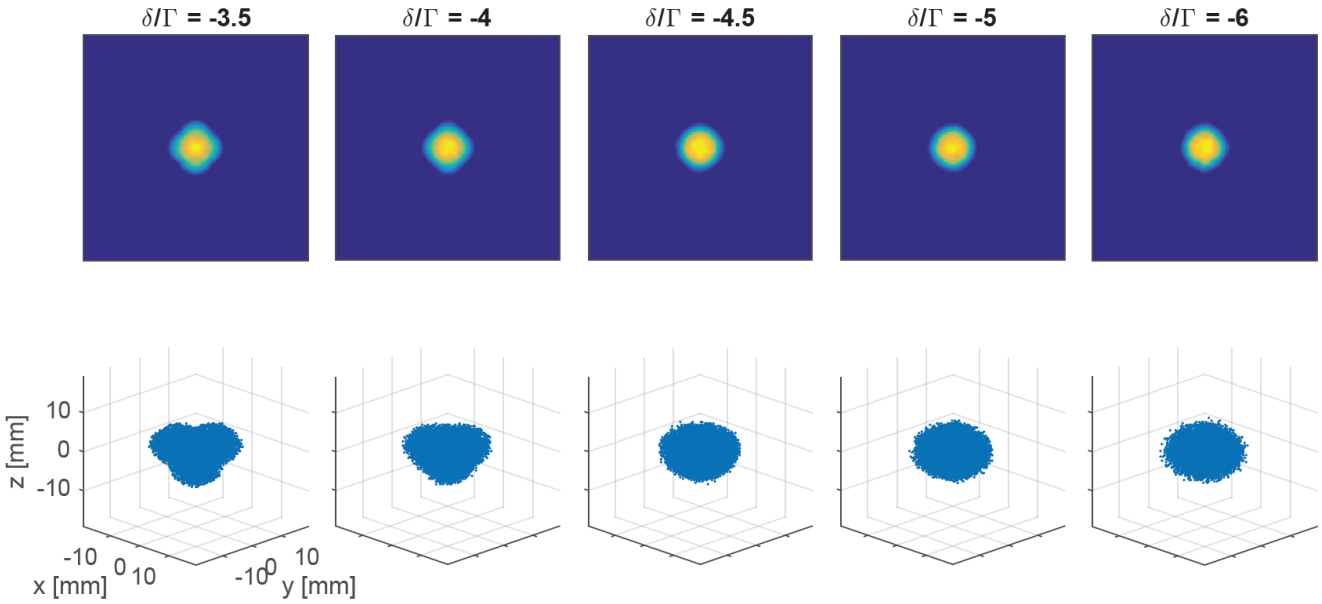

Figure 3.42: Display of 2D images (first row) and 3D images (second row) of the simulated stable clouds for different trapping detunings δ (columns) at the magnetic field gradient $\nabla B = 3.6$ G/cm. Each image is a single-shot image. The 2D images are the cloud densities integrated along the z-axis that are Gaussian filtered (standard deviation of 2 sigma); the diagonals correspond to the directions of two pairs of MOT beams; the field of view is 9.6×9.6 cm^2. In the 3D images, the individual dots are super-particles; the axes of the plots are the same for each image. The remaining simulation parameters are the same as in Tab. 3.3, but the simulation end time $t_{end} = 0.9$ s.

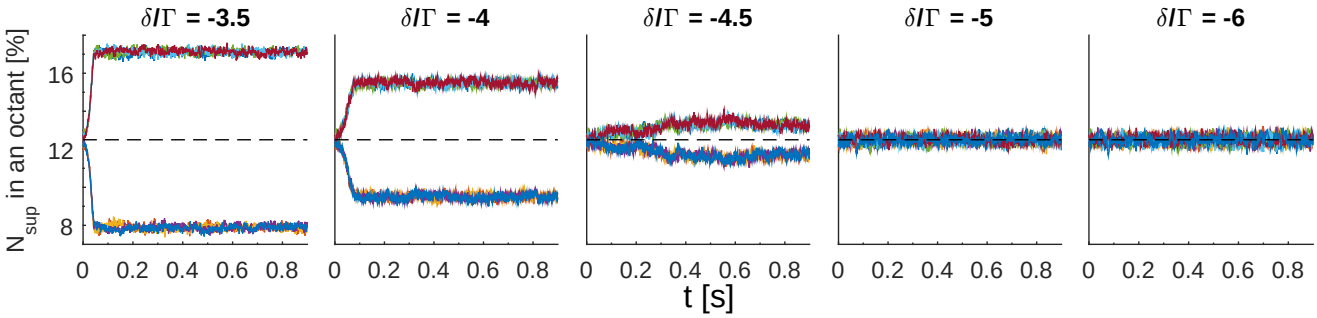

Figure 3.43: The super-particle number N_{sup} in an octant evolution for the simulated stable clouds in Fig. 3.42. There are eight different-colored solid curves that correspond to the N_{sup} evolution in one of the respective eight octants in 3D. When all the solid curves are on the dashed black line at 12.5 %, the amount of N_{sup} in each octant is the same.

3.5.3 The impact of different physical ingredients on the instabilities

Our interest in doing the numerical simulations is to allow for inclusion of fairly complex effects, though we will not be provided with a straightforward understanding of the physics at work. We can, however, improve the understanding by varying the different ingredients in the simulation and assess their impact on the instabilities. In this subsection, we investigate first the impact of diffusion on the instabilities, then do it for intensity attenuation and, finally, for elastically and inelastically scattered light spectrum. The motivating reasons for the particular investigations are given in the following sub-subsections.

3.5.3.1 The impact of diffusion on the instabilities

In this sub-subsection, we investigate the impact of diffusion on the instabilities. The investigation is motivated by the fact that noise is known to play an important role in instability dynamics, as we already have mentioned in section 3.1.2. We describe first how this investigation proceeds and then discuss its results.

The investigation here involves checking instability threshold's dependence on the scaling factor of $\mathbf{D}^{4level}$, the force due to the diffusion (see Eq. 3.87). Denoting the scaling factor by c_d, the scaled force due to the diffusion is $\mathbf{D}' = c_d \cdot \mathbf{D}^{4level}$. We use $c_d = 0, 0.5, 2, 5, 10$ and concentrate on the case with $\nabla B = 3$ G/cm, with the remaining parameters being the same as in Tab. 3.3.

In Fig. 3.44, we show the outcome of the investigation. As can be seen, with no diffusion ($c_d = 0$), the same threshold is obtained as in our main simulation ($c_d = 1$; $\delta_{thr}/\Gamma = -2.99$). Importantly, because the instabilities exist without the diffusion, this shows that it is not an essential effect in triggering them. Note that such conclusion is in an agreement with the quasi-1D simulations of balanced MOT instabilities in Ref. [40], as the diffusion there was neglected. When the diffusion is larger than usual ($c_d > 1$), the threshold is seen to shift towards the resonance, with the change being $\sim 0.6\,\Gamma$ per decade. The fact that the threshold shifts, shows that the diffusion, while not being essential in triggering the instabilities, nevertheless affects their mechanics. As the mechanics are affected, this suggests that the instability simulations may benefit from more precise modeling of the diffusion than in our quite simplistic case (refer to section 3.2.2). The reason for the shift and why it is positive we, however, do not know.

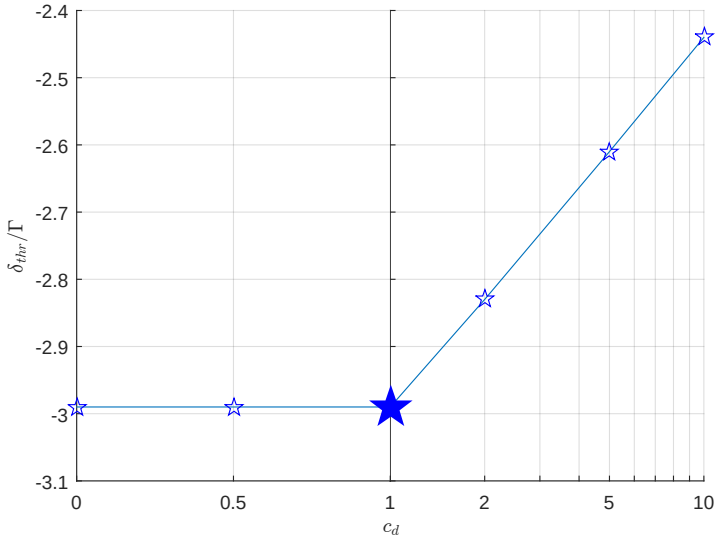

Figure 3.44: Test for the instability threshold's at $\nabla B = 3$ G/cm dependence on the scaling factor c_d of $\mathbf{D}^{4level}$, the force due to the diffusion (Eq. 3.87). The empty stars are the test results, and the filled star is the result of the main simulation (see Fig. 3.28). The solid line connecting the data-points is drawn as a visual aid. Notice the horizontal-axis being half-linear, half-log.

3.5.3.2 The impact of intensity attenuation on the instabilities

In this sub-subsection, we investigate the impact of intensity attenuation on the instabilities. The investigation involves checking whether the instabilities can be observed as we remove the intensity attenuation, i.e. as we set intensity to be constant in the cloud. It is natural to do this kind of investigation, as the intensity attenuation is understood to be a necessary effect for the instabilities to appear (refer to section 1.2.3.3). We next present and discuss the results of this investigation.

In Fig. 3.45, we display 2D and 3D imagery of clouds for $\nabla B = 3$ G/cm at different δ values in the previous range of unstable and stable clouds (see Fig. 3.41), as the intensity attenuation is removed; the remaining simulation parameters are mentioned in the figure text. The shapes in 2D are stable and round, with no sign of twisting in 3D, just like for the clouds in Fig. 3.42 when far from the threshold ($\delta/\Gamma \leq -5$). We see thus, in the explored parameter range, the instabilities cannot be obtained when the intensity attenuation is removed. The necessity of the attenuation confirms similar observations reported in Ref. [40] (the quasi-1D simulations of balanced MOT instabilities). We do not know yet the details of the physics involved, but we can guess that the shadow effect (produced by the attenuation) plays the role in a feedback mechanism, where this effect works against the cloud expansion due to the rescattering. Depending on parameters, systems with feedback are prone to spontaneous oscillation.

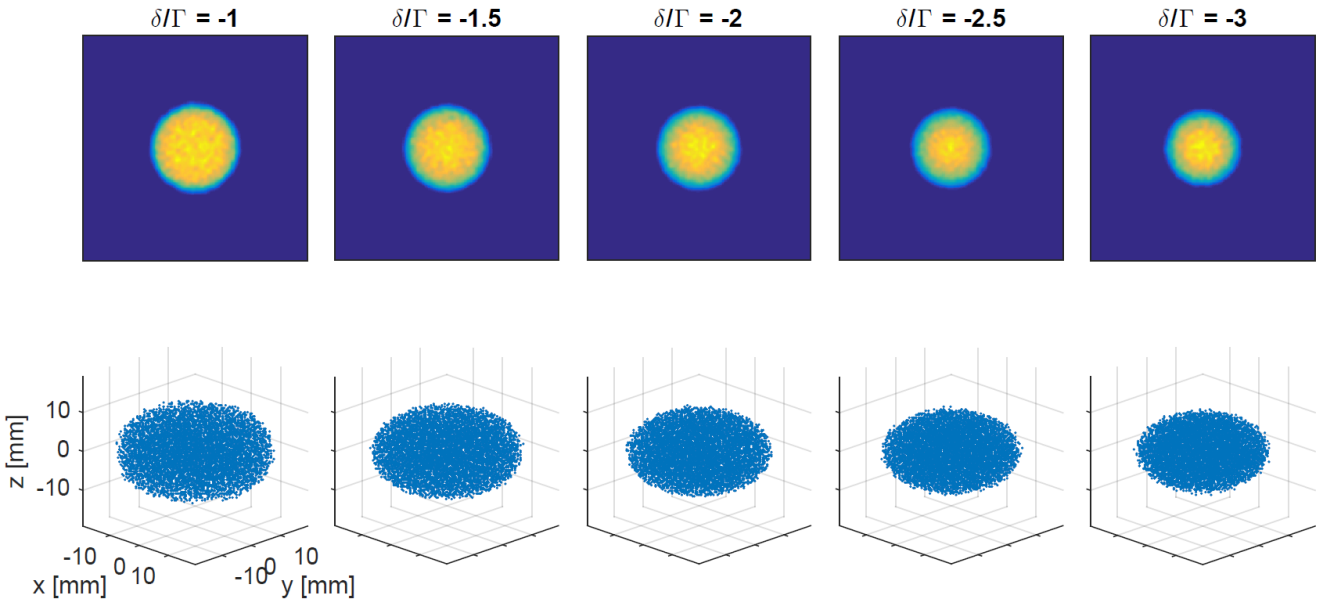

Figure 3.45: Display of 2D images (first row) and 3D images (second row) of the simulated stable clouds for different trapping detunings δ (columns) at the magnetic field gradient $\nabla B = 3$ G/cm, as obtained after removal of the intensity attenuation (i.e. intensity is set to be constant in the cloud). Each image is a single-shot image. The 2D images are the cloud densities integrated along the z-axis that are Gaussian filtered (standard deviation of 2 sigma); the diagonals correspond to the directions of two pairs of MOT beams; the field of view is 9.6×9.6 cm^2. In the 3D images, the individual dots are super-particles; the axes of the plots are the same for each image. The remaining simulation parameters are the same as in Tab. 3.6 at the corresponding $-\delta/\Gamma$ values, but the initial RMS radius $r_{RMS}(t = 0) = 7.3$, 7.3, 7, 6.7, 6.7 mm for respectively $-\delta/\Gamma = 1$, 1.5, 2, 2.5, 3.

3.5.3.3 The impact of elastically and inelastically scattered light spectrum on the instabilities

In this sub-subsection, we investigate the impact of elastically and inelastically scattered light spectrum on the instabilities. The investigation involves checking whether the instabilities can be observed as we remove either of the two parts of the rescattering cross-section that result from the contribution of the elastically and inelastically scattered light spectrum; we adopt here the same notations as in section 3.1.4 for these parts: $\sigma_{R,el}$ for the elastic part and $\sigma_{R,inel}$ for the inelastic part. This investigation is motivated by the fact that inelastic scattering is responsible, in the Wieman model, for σ_R being larger than σ_L and thus for the collective behavior of the cloud. However, we have observed that the instabilities survive at low saturation (refer to sections 2.3.3 and 3.5.1.3), which seems contradictory with this *naive* picture. We next present and discuss the results of this investigation.

It is found that we still obtain the instabilities in the simulation when either $\sigma_{R,el}$ or $\sigma_{R,inel}$ are set to zero, which indicates that none of these parts alone is

necessary. In Fig. 3.46(a), we display the result of a test on how the threshold at $\nabla B = 3$ G/cm is affected after removing either $\sigma_{R,el}$ or $\sigma_{R,inel}$; the remaining simulation parameters are mentioned in the figure text. The thresholds are seen to be shifted further away from the resonance compared to our main simulation result ($\delta_{thr}/\Gamma = -2.99$), roughly by 2.5 times ($\delta_{thr}/\Gamma = -7.22$ for $\sigma_{R,el} = 0$ and $\delta_{thr}/\Gamma = -8.12$ for $\sigma_{R,inel} = 0$). It is not clear to us why the thresholds shift further away from the resonance, considering the rescattering force becomes weaker after the removal of either $\sigma_{R,el}$ or $\sigma_{R,inel}$. We observe in Fig. 3.46(b) that the size of the cloud is smaller when the value of rescattering cross-section is reduced, which is consistent with the Wieman model. However, the fact that the threshold detuning becomes more negative as the cloud size decreases is quite puzzling.

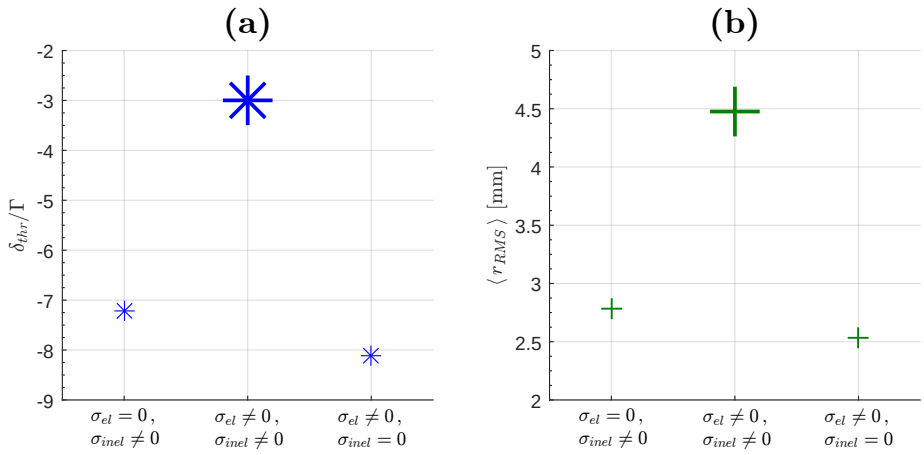

Figure 3.46: (a) Test on how the instability threshold at $\nabla B = 3$ G/cm is affected after removing either $\sigma_{R,el}$ or $\sigma_{R,inel}$, being the parts of the rescattering cross-section that result from the contribution of respectively the elastic part and inelastic part of the emission spectrum (refer to section 3.1.4). The small asterisks are the test results, and the large asterisk is the result of the main simulation (see Fig. 3.28). The remaining simulation parameters for the test are the same as in Tab. 3.3, but the initial RMS radius $r_{RMS}(t = 0) = 2.8$ mm and the $-\delta/\Gamma$ values range from 6.5 to 8.5 (step of 0.1). (b) The averaged RMS radius $\langle r_{RMS} \rangle$ (after the transient) of the stable clouds just below the threshold for the cases in (a).

Conclusion and Outlook

This Thesis investigated the fundamental aspects of self-oscillating atomic clouds in a large, balanced MOT. There were three main Chapters: Chapter 1 concerned basic working principles of the MOT and a presentation of different MOT regimes, Chapter 2 concerned our balanced MOT experiments and an assessment of the known analytical models of balanced MOT instabilities, and Chapter 3 concerned our balanced MOT numerical simulations in 3D and a comparison of their results with results of the corresponding experiments. Below we write the important lessons learned in each of these Chapters, give conclusions and outlook for the future research.

In Chapter 1, we saw that in three of the four MOT configurations, where self-oscillating clouds existed, such instabilities first appeared when the MOT entered a regime governed by many-atom physics. To recall, the configurations were respectively misaligned, retro-reflected and balanced. In the remaining MOT configuration, i.e. the parameter-modulated configuration, where resonant phenomena existed, such instabilities exhibited collective phenomena when the MOT entered a regime governed by many-atom physics. The past theoretical models could explain the appearance of retro-reflected and balanced MOT instabilities as well as the collective phenomena that parameter-modulated MOT instabilities exhibited, but not the appearance of misaligned MOT instabilities. Note that the models that attempted to explain misaligned MOT instabilities had all in common that they neglected the intensity attenuation, which otherwise was shown to play a crucial role for instabilities in other MOT configurations. Thus, it could be naturally speculated that the intensity attenuation is a necessary effect for misaligned MOT instabilities to be explained. As we recall, such speculation was also made in the original Ref. [30]. As our simulation model includes the intensity attenuation, we have considered checking if we could simulate unstable motion in the misaligned MOT, with the incorporation of the misalignment done according to Appendix C. In Fig. 3.47, we proceed showing a sequence of images of a simulated misaligned MOT instability - an orbiting clump, known to experimentally exist (see Fig. 1.10); the simulation parameters are mentioned in the figure text. We note that the result in Fig. 3.47 is only preliminary and we have not studied it in detail, but with the tests that have been done, we found the rescattering as well as the intensity attenuation to be crucial in obtaining the instability. It thus seems that the intensity attenuation was the missing ingredient. The instability was obtained for the beam misalignment l_s satisfying $\frac{1}{6}w_d \leq l_s < \frac{1}{5}w_d$, with w_d being the beam waist diameter. Smaller and higher misalignments yield the results shown in Fig. 3.48, where the same simulation parameters as in Fig. 3.47 have been used. As displayed in Fig. 3.48, for $l_s < \frac{1}{6}w_d$ a uniform structure forms, while for $\frac{1}{5}w_d \leq l_s < \frac{1}{3.75}w_d$ a stable ring structure is obtained, and for even higher l_s the cloud escapes the trap. The results are in a close agreement with the experimental ones in Ref. [30] (see Fig. 1.10 and the paragraph above this figure). Overall, the simulation model developed in this Thesis thus shows a good potential for future studies of both stable and unstable structures in the misaligned MOT. Our

simulation model could benefit future studies of retro-reflected and parameter-modulated instabilities, too. For the retro-reflected MOT case, we recall that the past models were not designed to go beyond the temporal description that otherwise was required in explaining the observed complex spatio-temporal features of the instabilities [38]. With some straightforward modifications to our model, one could be enabled to do studies of such spatio-temporal features. For the parameter-modulated MOT case, we recall that more diverse complex dynamical behaviors could be investigated when magnetic field gradient or laser detuning modulation was in place instead of intensity modulation [46], and this could be done with our model, again, after introducing some straightforward modifications.

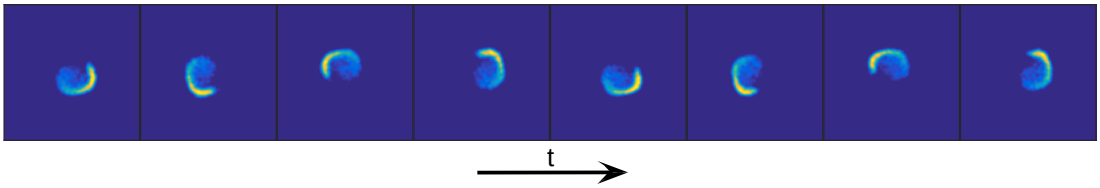

Figure 3.47: Display of a sequence of 2D images of a simulated misaligned MOT instability - an orbiting clump. The images are the cloud densities integrated along the z-axis that are Gaussian filtered (standard deviation of 2 sigma). The diagonals correspond to the directions of two pairs of MOT beams. The time-separation between each image is 2 ms. The field of view is 3.2×3.2 cm^2. The simulation was performed for $N = 5 \cdot 10^8$ atoms using $N_{sup} = 10^3$ super-particles, at the magnetic field gradient $\nabla B = 7.2$ G/cm, the trapping detuning $\delta = -2.8\,\Gamma$, the intensity per MOT beam of $I = 5$ mW/cm^2, the initial radius $r_{RMS}(t = 0) = 1.5$ mm, the simulation end time $t_{end} = 0.5$ s, the simulation time-step $\Delta t = 10^{-4}$ s, and the beam misalignment $l_s = \frac{1}{6} w_d$, with $w_d = 6$ mm being the beam waist diameter.

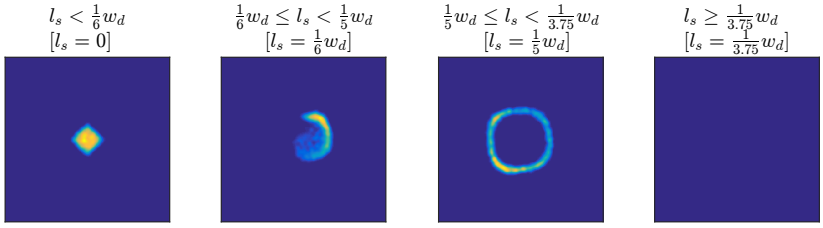

Figure 3.48: Display of 2D images of simulated clouds in a misaligned MOT. Each image is a single-shot image (densities integrated along the z-axis; Gaussian-filtered, standard deviation of 2 sigma). From left to right: a uniform stable cloud, an orbiting clump (in Fig. 3.47), a stable ring-structure, an empty trap. The first row above each image shows the range of the beam misalignment l_s where each structure occurs, in terms of the beam waist diameter w_d, and the second row shows l_s used in the actual simulation. The diagonals correspond to the directions of two pairs of MOT beams. The field of view is 3.2×3.2 cm^2. The same simulation parameters as for the orbiting clump are used (refer to Fig. 3.47 text). Note the similarities with the experimental result in Fig. 1.10.

Moving on to the balanced MOT instability experiments in Chapter 2, we looked first at the threshold behavior versus respectively the magnetic field gradient ∇B, the atom number N and the intensity I per MOT beam. Unique behaviors were exhibited in each respective case. We saw that the threshold versus ∇B showed a linear behavior (see Fig. 2.10), the threshold versus N yielded a power law behavior (see Fig. 2.11), and the threshold versus I exhibited a non-monotonous behavior (see Fig. 2.13). We saw that the 1-zone model [39] was not successful in explaining our observations. Thus, the mechanism behind the instabilities was deemed to be more involved than of this model's, where the instabilities are induced by the cloud's edge passing from a positive to negative friction. Threshold behaviors could be experimentally studied in the future, in extended ranges of parameters. Regarding the ∇B and N thresholds, as we have observed monotonous behaviors, it would interesting knowing whether (or when) different behaviors could be obtained with e.g. increased ∇B and N values for the respective thresholds. For the I threshold, it would be interesting knowing whether the instabilities could be found to persist until zero intensity and also be extinguished at larger intensities.

In the next part of Chapter 2, surrounding the spatio-temporal properties of the unstable regime, we first made a visual identification of three distinct instability regimes and used ESA to produce a diagram showing their location in the δ-∇B phase-space (see Fig. 2.20). The regimes were (i) the filament-like regime, where the clouds possessed complex-looking, filamentary structures, (ii) the asymmetric regime, where the clouds broke the symmetry of the trap in a striking fashion by intermittently elongating themselves along beam directions, and (iii) the symmetric regime, where the deformations were remarkably symmetrically distributed around the trap center. For the future experimental research, it would be interesting knowing how robust the observed regimes are versus changes in parameters and whether other, unique regimes could also be found.

We proceeded examining the identified regimes using other tools of analysis - PCA and SFA - to see what complementary information could be gathered about these regimes. Using PCA we learned about the oscillation modes of clouds of these regimes, while using SFA we learned about the size distribution of the structures developing in clouds of these regimes. Using these tools we were also able to assess the remaining alternative analytical instability-models: (i) the Mathieu equation model, where the instability mechanism is driven by the coupling between the COM and breathing modes [41], (ii) the photon bubble model, where photon bubble structures provide a source for the unstable motion [42]. These models did not stand up to our assessment, such that we concluded that the assumptions in all the known analytical models (the 1-zone model, the Mathieu equation model and the photon bubble model) were too crude for capturing the real physics and that a more involved analytical theory would have to be developed to carry out the explanations.

In our final Chapter, Chapter 3, we constructed a 3D kinetic model based on the hyperfine transition $F = 0 \rightarrow F' = 1$, and employed this model in our balanced MOT instability simulations. We saw first that the simulated threshold behaviors yielded qualitative agreements with the corresponding experimental behaviors, indicating that our simulation model captured well the physics involved in the threshold determination (see Figs. 3.28, 3.32 and 3.34). To continue with trying to understand different threshold behaviors, we proposed to remove one by one the implemented physical ingredients or to replace them with something else and simpler.

In the next part of Chapter 3, surrounding the spatio-temporal properties of the simulated unstable regime, we first made a visual identification of six distinct instability regimes in the δ-∇B phase-space (see Fig. 3.35). Three of these regimes corresponded well to the experimentally observed ones, which told us that our simulation model could go beyond predictions of threshold behaviors. The simulation, however, yielded regimes not observed experimentally, and this was a contributing factor to why we could not obtain a similar instability diagram as in the experiment when employing ESA (see Fig. 3.40). We continued thus creating an instability diagram using visual inspection (see Fig. 3.41). Of course, we could not make a one-to-one comparison with the experimental instability diagram, due to the difference in the amount of instability regimes. To proceed with the comparison, we considered assuming that the regimes not observed in the experiment formed a part of a common regime, to which the asymmetric regime also belonged. This was owed to the fact that these other regimes broke the trap symmetry in a close fashion to the asymmetric regime. Next, we considered the fact that the simulated threshold was offset by around $-1\,\Gamma$ from the experimental threshold. With such consideration in mind, we speculated that new physics was being shown closer to the resonance as set by the size of the offset. In this way, the simulated diagram could be deemed to be more alike to the experimental one and, more interestingly, it predicted a regime in which the clouds expelled particles along beam directions in a very dramatic fashion. Due to the dramatic particle expulsion, we later called this regime the explosive regime. We mentioned that, by performing experiments deeper in the unstable regime, it could be checked whether such regime indeed exists.

We proceeded at the end to investigate the impact of our simulation model's physical ingredients on the instabilities. We investigated first the impact of diffusion on the instabilities, then did it for intensity attenuation and, finally, for elastically and inelastically scattered light spectrum. Many similar kinds of investigations could be done in the future, to aid the understanding of the instability phenomenon. For instance, one could investigate the impact of beam cross-saturation on the instabilities as it is removed, as well as what happens as one varies the strength of the rescattering or neglects the rescattering cross-section position dependence (stemming from the intensity attenuation or the Zeeman effect, or both). The last-mentioned investigation was considered in Ref. [40], although that was in quasi-1D.

From the results of the last Chapter, we make the final conclusion that this Thesis has led to the development of a powerful numerical tool for studying self-oscillating clouds of the balanced MOT in a full-blown 3D environment. We wish for it to inspire a creation of an analytical theory that could predict the behaviors that our simulations were successful at predicting. In that task, it would be useful to first understand if our simulation model could be simplified. For instance, as we mentioned in section 3.1.5, the 2-level atom version of our model could be used in simulating the instabilities. It would thus be instrumental to check whether this much simpler version could yield similar predictions. Besides, studies of instabilities in other MOT configurations could also be enabled by introducing straightforward modifications to our simulation model, as we already exemplified earlier for the misaligned MOT case (see Figs. 3.47, 3.48). Thus, our developed numerical tool furthermore offers great versatility, with promising future results beyond the balanced MOT.

Appendices

Appendix A

2-level atom elastic and inelastic scattering rates

In this Appendix, we write down expressions for the elastic and inelastic scattering rates for a 2-level atom as well as make a graphical representation of these expressions.

The elastic and inelastic scattering rates for a 2-level atom are respectively given by [51]

$$\Gamma_{el} = \frac{\Gamma}{2}\frac{s}{(1+s)^2} \tag{A.1a}$$

$$\Gamma_{inel} = \frac{\Gamma}{2}\frac{s^2}{(1+s)^2} \tag{A.1b}$$

where $s = \frac{s_0}{1+4\frac{\delta^2}{\Gamma^2}}$ is the saturation parameter (see below Eq. 1.2).

The above expressions are graphically represented in Fig. A.1.

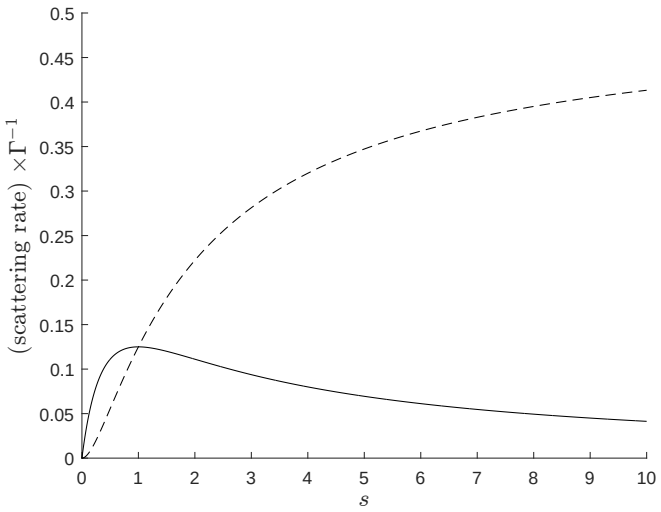

Figure A.1: The elastic and inelastic scattering rates for a 2-level atom in units of Γ versus the saturation parameter s, shown respectively as solid and dashed curves. The expressions for the rates are given by Eq. A.1.

Appendix B

Emission and absorption

In this Appendix, we explain how to obtain the normalized emission spectrum $S(\omega)$, given by Eq. 3.36, and the normalized absorption spectrum $\sigma_A(\omega)$, given by Eq. 3.37. Appendix B.1 concerns $S(\omega)$, and Appendix B.2 concerns $\sigma_A(\omega)$. Refs. [56] and [57] are respectively made use of.

B.1 Normalized emission spectrum $S(\omega)$

Eq. 4.15 in Ref. [56] provides us with an expression for the non-normalized emission spectrum for a 2-level atom. Using our notations, we write the expression for the spectrum given by this equation as

$$\begin{aligned} S^{non}(\omega) = &\left[\frac{8\pi\overline{n}_\infty^2\left(\frac{1}{4}\Gamma^2+\delta^2\right)}{\Omega^2}\right] Dirac(\omega-\delta) \\ &+\overline{n}_\infty\Gamma\Omega^2\left(\frac{(\omega-\delta)^2+\frac{1}{2}\Omega^2+\Gamma^2}{\Gamma^2\left[\frac{1}{2}\Omega^2+\delta^2+\frac{1}{4}\Gamma^2-2(\omega-\delta)^2\right]^2+(\omega-\delta)^2\left[\Omega^2+\delta^2+\frac{5}{4}\Gamma^2-(\omega-\delta)^2\right]^2}\right) \end{aligned} \tag{B.1}$$

where the constant $\overline{n}_\infty = \frac{\Omega^2}{\Gamma^2+4\delta^2+2\Omega^2}$ is the steady-state occupation number for the upper state, and we note to have referenced the frequency ω with respect to the atomic transition frequency ω_0.

As the total emitted power by the atom must be same as the power the atom receives (law of energy conservation), we must ensure that integration of the emission spectrum with respect to ω yields an area of 1. In Ref. [56], plugging Eq. 2.16 into Eq. 2.20 and making use of Eq. 2.21, yields the normalization condition for the emission spectrum. Using our notations, this condition reads as

$$\begin{aligned} \int_{-\infty}^{+\infty} d\omega\, S^{non}(\omega) &= 2\pi\overline{n}_\infty \\ &= 2\pi\left[\frac{\Omega^2}{\Gamma^2+4\delta^2+2\Omega^2}\right] \end{aligned} \tag{B.2}$$

The properly normalized emission spectrum will be equal to $S^{non}(\omega)$ divided by the right-hand side of Eq. B.2. After some math, we obtain the normalized emission spectrum:

$$\begin{aligned} S(\omega) = &\left[\frac{\Gamma^2+4\delta^2}{\Gamma^2+4\delta^2+2\Omega^2}\right] Dirac(\omega-\delta) \\ &+\frac{\Gamma\Omega^2}{2\pi}\left(\frac{(\omega-\delta)^2+\frac{1}{2}\Omega^2+\Gamma^2}{\Gamma^2\left[\frac{1}{2}\Omega^2+\delta^2+\frac{1}{4}\Gamma^2-2(\omega-\delta)^2\right]^2+(\omega-\delta)^2\left[\Omega^2+\delta^2+\frac{5}{4}\Gamma^2-(\omega-\delta)^2\right]^2}\right) \end{aligned} \tag{3.36 revisited}$$

B.2 Normalized absorption spectrum $\sigma_A(\omega)$

Eq. 3.8 in Ref. [57] provides us with an expression for the rate of absorption of photons from a weak perturbing field by a 2-level atom driven by a strong laser field. Using our notations, we write the expression for the rate given by this equation as

$$\widetilde{g}_A(\omega) = \frac{\Omega_R^2}{4} \times \left\{ \frac{\Gamma^2 + 4\delta^2}{\Gamma^2 + 4\delta^2 + 2\Omega^2} \right\} \times \left\{ \frac{(-i\omega + i\delta + \Gamma)\left(-i\omega + i2\delta + \frac{\Gamma}{2}\right) + \frac{1}{2}i\Omega^2(\omega - \delta)/\left(i\delta + \frac{\Gamma}{2}\right)}{(-i\omega + i\delta + \Gamma)\left(-i\omega + i2\delta + \frac{\Gamma}{2}\right)\left(-i\omega + \frac{\Gamma}{2}\right) + \Omega^2\left(-i\omega + i\delta + \frac{\Gamma}{2}\right)} + c.c. \right\} \tag{B.3}$$

where Ω_R is the Rabi frequency of the weak perturbing field, defined from Eqs. 2.12(a), 3.1, 3.4 in Ref. [57], and we note to have referenced the frequency ω with respect to the atomic transition frequency ω_0.

As the laser intensity I_L approaches 0, Eq. B.3 reduces to

$$\widetilde{g}_A(\omega) \to \frac{\Omega_R^2}{4}\frac{4\Gamma}{\Gamma^2 + 4\omega^2} = \frac{\Gamma}{2}\frac{I_R/I_{sat}}{1 + 4\frac{\omega^2}{\Gamma^2}} \qquad for \quad \Omega \to 0 \tag{B.4}$$

where we have assumed that we are dealing with a plane wave perturbing field, such that $\Omega_R = \Gamma\sqrt{\frac{I_R}{2I_{sat}}}$, with I_R being the intensity of the weak perturbing field.

The expression in Eq. B.4 is equivalent to the expression for the scattering rate of the photons from the laser field for $I_L \ll 1$, i.e. $\frac{\Gamma}{2}\frac{I_L/I_{sat}}{1+4\frac{\delta^2}{\Gamma^2}}$. The equivalence allows us to identify the rescattering cross-section of the atom in presence of the weak perturbing field, for I_L approaching 0, as

$$\sigma_R \to \sigma_L \qquad for \quad \Omega \to 0 \tag{B.5}$$

where σ_L is the scattering cross-section, given by Eq. 1.13, with $s_0 = 0$ in the denominator.

Eq. B.5 provides us with the normalization condition for the absorption spectrum. Using Eq. B.3, the normalized absorption spectrum is readily identified as

$$\sigma_A(\omega) = \frac{\sigma_0\Gamma}{4} \times \left\{ \frac{\Gamma^2 + 4\delta^2}{\Gamma^2 + 4\delta^2 + 2\Omega^2} \right\} \times \left\{ \frac{(-i\omega + i\delta + \Gamma)\left(-i\omega + i2\delta + \frac{\Gamma}{2}\right) + \frac{1}{2}i\Omega^2(\omega - \delta)/\left(i\delta + \frac{\Gamma}{2}\right)}{(-i\omega + i\delta + \Gamma)\left(-i\omega + i2\delta + \frac{\Gamma}{2}\right)\left(-i\omega + \frac{\Gamma}{2}\right) + \Omega^2\left(-i\omega + i\delta + \frac{\Gamma}{2}\right)} + c.c. \right\}$$

(3.37 revisited)

Note that using Eqs. 3.36 and 3.37 in the definition for σ_R given by Eq. 3.35, we correctly obtain $\sigma_R \to \sigma_L$ for $\Omega \to 0$ (i.e. Eq. B.5).

Appendix C

Beam intensities in the misaligned MOT

In this Appendix, we write down the modifications in Eq. 3.62 for the MOT beam intensities in the $F = 0 \rightarrow F' = 1$ model (section 3.2), so to incorporate the beam misalignment.

Gaussian beams are considered. This respects the choice of the past theoretical models of the misaligned MOT (see the references in section 1.2.3.1). We consider the beam misalignment is introduced in the xy-plane and thus finally write the following modifications in Eq. 3.62:

$$\boxed{\begin{array}{ll} For\ \mathcal{I}_{\mathsf{x}}^{+}(\mathbf{r}) : I_\infty \rightarrow I_\infty e^{-\frac{(y-l_s)^2+z^2}{2w_0^2}} & , \quad For\ \mathcal{I}_{\mathsf{x}}^{-}(\mathbf{r}) : I_\infty \rightarrow I_\infty e^{-\frac{(y+l_s)^2+z^2}{2w_0^2}} \\ For\ \mathcal{I}_{\mathsf{y}}^{+}(\mathbf{r}) : I_\infty \rightarrow I_\infty e^{-\frac{(x+l_s)^2+z^2}{2w_0^2}} & , \quad For\ \mathcal{I}_{\mathsf{y}}^{-}(\mathbf{r}) : I_\infty \rightarrow I_\infty e^{-\frac{(x-l_s)^2+z^2}{2w_0^2}} \\ For\ \mathcal{I}_{\mathsf{z}}^{+}(\mathbf{r}) : I_\infty \rightarrow I_\infty e^{-\frac{x^2+y^2}{2w_0^2}} & , \quad For\ \mathcal{I}_{\mathsf{z}}^{-}(\mathbf{r}) : I_\infty \rightarrow I_\infty e^{-\frac{x^2+y^2}{2w_0^2}} \end{array}} \tag{C.1}$$

where l_s is the beam misalignment, and w_0 is the beam waist radius. We define $w_d \equiv 2w_0$ as the beam waist diameter.

Bibliography

[1] A. Jenkins. *Self-oscillation.* Physics Reports, vol. 525, no. 2, pp. 167-222, 2013.

[2] G. Karreman, and C. Prood. *Heart muscle contraction oscillation.* International Journal of Bio-Medical Computing, vol. 38, no. 1, pp. 49-53, 1995.

[3] R. F. Christy. *The theory of Cepheid variability.* Quarterly Journal of the Royal Astronomical Society, vol. 9, pp. 13-39, 1968.

[4] A. B. Pippard. *The physics of vibration, omnibus ed.* Cambridge University Press, Cambridge, 1989.

[5] K. Ida, T. Kobayashi, T. E. Evans, S. Inagaki, M. E. Austin, M. W. Shafer, S. Ohdachi, Y. Suzuki, S.-I. Itoh, and K. Itoh. *Self-regulated oscillation of transport and topology of magnetic islands in toroidal plasmas.* Scientific Reports, vol. 5, no. 16165, 2015.

[6] R. Huß, R. Wilhelm, C. Kolleck, J. Neumann, and D. Kracht. *Suppression of parasitic oscillations in a core-doped ceramic Nd:YAG laser by Sm:YAG cladding.* Optics Express, vol. 18, no. 12, pp. 13094-13101, 2010.

[7] E. Flores-Garcia, M. Ponce-Silva, L. G. Vela-Valdes, M. A. Juarez, and L. Hernandez-Gonzalez. *Analysis and design method for high-frequency self-oscillating electronic ballasts.* IEEE Transactions on Industry Applications, vol. 47, no. 6, pp. 2430-2436, 2011.

[8] G. S. Nusinovich, R. Pu, and V. L. Granatstein. *Suppression and nonlinear excitation of parasitic modes in second harmonic gyrotrons operating in a very high order mode.* Applied Physics Letters, vol. 107, no. 1, 2015.

[9] D. Bohm, and M. Weinstein. *The self-oscillations of a charged particle.* Physical Review, vol. 74, no. 12, pp. 1789-1798, 1948.

[10] H. Zeng, M. Lahikainen, L. Liu, Z. Ahmed, O. M. Wani, M. Wang, H. Yang, and A. Priimagi. *Light-fuelled freestyle self-oscillators.* Nature Communications, vol. 10, no. 5057, 2019.

[11] S. K. Zhdanov, M. Schwabe, R. Heidemann, R. Sütterlin, H. M. Thomas, M. Rubin-Zuzic, H. Rothermel, T. Hagl, A. V. Ivlev, G. E. Morfill, V. I. Molotkov, A. M. Lipaev, O. F. Petrov, V. E. Fortov, and T. Reiter. *Auto-oscillations in complex plasmas.* New Journal of Physics, vol. 12, no. 4, 2010.

[12] E. L. Raab, M. Prentiss, A. Cable, S. Chu, and D. E. Pritchard. *Trapping of neutral sodium atoms with radiation pressure.* Physical Review Letters, vol. 59, no. 23, pp. 2631-2634, 1987.

[13] N. F. Ramsey. *Molecular beams.* Oxford University Press, Oxford, 1956.

[14] D. A. Steck. *Rubidium 87 D line data.* `https://steck.us/alkalidata/rubidium87numbers.1.6.pdf` Note: link entered in 2020.

[15] T. W. Hänsch, and A. L. Schawlow. *Cooling of gases by laser radiation.* Optics Communications, vol. 13, no. 1, pp. 68-69, 1975.

[16] D. Lucas, P. Horak, and G. Grynberg. *Sisyphus cooling of rubidium atoms on the D2 line: the role of the neighbouring transitions.* The European Physical Journal D - Atomic, Molecular, Optical and Plasma Physics, vol. 7, pp. 261–267, 1999.

[17] N. Kostylev, E. Ivanov, M. E. Tobar, and J. J. McFerran. *Sub-Doppler cooling of ytterbium with the* $^1S_0{-}^1P_1$ *transition including* ^{171}Yb *(*$I = 1/2$*).* Journal of the Optical Society of America B, vol. 31, no. 7, pp. 1614-1620, 2014.

[18] C. Salomon, J. Dalibard, W. D. Phillips, A. Clairon, and S. Guellati. *Laser cooling of cesium atoms below 3* μK*.* Europhysics Letters, vol. 12, no. 8, 1990.

[19] P. D. Lett, W. D. Phillips, S. L. Rolston, C. E. Tanner, R. N. Watts, and C. I. Westbrook. *Optical molasses.* Journal of the Optical Society of America B, vol. 6, no. 11, pp. 2084-2107, 1989.

[20] D. J. Wineland, J. Dalibard, and C. Cohen-Tannoudji. *Sisyphus cooling of a bound atom.* Journal of the Optical Society of America B, vol. 9, no. 1, pp. 32-42, 1992.

[21] R. Chang, A. L. Hoendervanger, Q. Bouton, Y. Fang, T. Klafka, K. Audo, A. Aspect, C. I. Westbrook, and D. Clément. *Three-dimensional laser cooling at the Doppler limit.* Physical Review A, vol. 90, no. 6, pp. 063407 (7), 2014.

[22] C. D. Wallace, T. P. Dinneen, K. Y. N. Tan, A. Kumarakrishnan, P. L. Gould, and J. Javanainen. *Measurements of temperature and spring constant in a magneto-optical trap.* Journal of the Optical Society of America B, vol. 11, no. 5, pp. 703-711, 1994.

[23] J. Dalibard. *Laser cooling of an optically thick gas: the simplest radiation pressure trap?* Optics Communications, vol. 68, no. 3, pp. 203-208, 1988.

[24] A. Camara, R. Kaiser, and G. Labeyrie. *Scaling behavior of a very large magneto-optical trap.* Physical Review A, vol. 90, no. 6, pp. 063404 (8), 2014.

[25] C. G. Townsend, N. H. Edwards, C. J. Cooper, K. P. Zetie, C. J. Foot, A. M. Steane, P. Szriftgiser, H. Perrin, and J. Dalibard. *Phase-space density in the magneto-optical trap.* Physical Review A, vol. 52, no. 2, pp. 1423-1440, 1995.

[26] G. Hillenbrand, C. J. Foot, and K. Burnett. *Heating due to long-range photon exchange interactions between cold atoms.* Physical Review A, vol. 50, no. 2, pp. 1479-1489, 1994.

[27] M. Drewsen, Ph. Laurent, A. Nadir, G. Santarelli, A. Clairon, Y. Castin, D. Grison, and C. Salomon. *Investigation of sub-Doppler cooling effects in a cesium magneto-optical trap.* Applied Physics B, vol. 59, pp. 283–298, 1994.

[28] C. J. Cooper, G. Hillenbrand, J. Rink, C. G. Townsend, K. Zetie, and C. J. Foot. *The temperature of atoms in a magneto-optical trap.* Europhysics Letters, vol. 28, no. 6, 1994.

[29] S. Pradhan, and B. N. Jagatap. *Measurement of temperature of laser cooled atoms by one-dimensional expansion in a magneto-optical trap.* Review of Scientific Instruments, vol. 79, pp. 013101 (4), 2008.

[30] D. W. Sesko, T. G. Walker, and C. E. Wieman. *Behavior of neutral atoms in a spontaneous force trap.* Journal of the Optical Society of America B, vol. 8, no. 5, pp. 946-958, 1991.

[31] V. S. Bagnato, L. G. Marcassa, M. Oria, G. I. Surdutovich, R. Vitlina, and S. C. Zilio. *Spatial distribution of atoms in a magneto-optical trap.* Physical Review A, vol. 48, no. 5, pp. 3771-3775, 1993.

[32] M. T. de Araujo, L. G. Marcassa, S. C. Zilio, and V. S. Bagnato. *Double-ring structure: another variant in the spatial distribution of cold sodium atoms.* Physical Review A, vol. 51, no. 5, pp. 4286-4288, 1995.

[33] D. Felinto, L. G. Marcassa, V. S. Bagnato, and S. S. Vianna. *Influence of the number of atoms in a ring-shaped magneto-optical trap: observation of bifurcation.* Physical Review A, vol. 60, no. 3, pp. 2591-2594, 1999.

[34] D. Wilkowski, J. Ringot, D. Hennequin, and J. C. Garreau. *Instabilities in a magneto-optical trap: noise-induced dynamics in an atomic system.* Physical Review Letters, vol. 85, no. 9, pp. 1839-1842, 2000.

[35] A. di Stefano, M. Fauquembergue, Ph. Verkerk, and D. Hennequin. *Giant oscillations in a magneto-optical trap.* Physical Review A, vol. 67, no. 3, pp. 033404 (4), 2003.

[36] D. Hennequin. *Stochastic dynamics of the magneto-optical trap.* The European Physical Journal D - Atomic, Molecular, Optical and Plasma Physics, vol. 28, pp. 135–147, 2004.

[37] A. di Stefano, Ph. Verkerk, and D. Hennequin. *Deterministic instabilities in the magneto-optical trap.* The European Physical Journal D - Atomic, Molecular, Optical and Plasma Physics, vol. 30, pp. 243–258, 2004.

[38] R. Romain, A. Jallageas, Ph. Verkerk, and D. Hennequin. *Spatial instabilities in a cloud of cold atoms.* Physical Review E, vol. 94, no. 5, pp. 052212 (6), 2016.

[39] G. Labeyrie, F. Michaud, and R. Kaiser. *Self-sustained oscillations in a large magneto-optical trap.* Physical Review Letters, vol. 96, no. 2, pp. 023003 (4), 2006.

[40] T. Pohl, G. Labeyrie, and R. Kaiser. *Self-driven nonlinear dynamics in magneto-optical traps.* Physical Review A, vol. 74, no. 2, pp. 023409 (4), 2006.

[41] H. Terças, J. T. Mendonça, and R. Kaiser. *Driven collective instabilities in magneto-optical traps: a fluid-dynamical approach.* Europhysics Letters, vol. 89, no. 5, 2010.

[42] J. T. Mendonça, and R. Kaiser. *Photon bubbles in ultracold matter.* Physical Review Letters, vol. 108, no. 3, pp. 033001 (5), 2012.

[43] J. D. Rodrigues, J. A. Rodrigues, A. V. Ferreira, H. Terças, R. Kaiser, and J. T. Mendonça. *Photon bubble turbulence in cold atomic gases.* `arXiv:1604.08114`, 2016.

[44] H. Heimonen, L. C. Kwek, R. Kaiser, and G. Labeyrie. *Synchronization of a self-sustained cold-atom oscillator.* Physical Review A, vol. 97, no. 4, pp. 043406 (5), 2018.

[45] K. Kim, H.-R. Noh, Y.-H. Yeon, and W. Jhe. *Observation of the Hopf bifurcation in parametrically driven trapped atoms.* Physical Review A, vol. 68, no. 3, pp. 031403 (4), 2003.

[46] G. Moon, M.-S. Heo, Y. Kim, H.-R. Noh, and W. Jhe. *Nonlinear, nonequilibrium and collective dynamics in a periodically modulated cold atom system.* Physics Reports, vol. 698, pp. 1-30, 2017.

[47] G. Labeyrie, D. Delande, C.A. Müller , C. Miniatura, and R. Kaiser. *Multiple scattering of light in a resonant medium.* Optics Communications, vol. 243, no. 1–6, pp. 157-164, 2004.

[48] R. Dubessy, C. De Rossi, T. Badr, L. Longchambon, and H. Perrin. *Imaging the collective excitations of an ultracold gas using statistical correlations.* New Journal of Physics, vol. 16, no. 12, 2014.

[49] C. Cohen-Tannoudji. *Atomic motion in laser light.* Elsevier Science Publishers B. V., 1992.

[50] J. Dalibard, and C. Cohen-Tannoudji. *Laser cooling below the Doppler limit by polarization gradients: simple theoretical models.* Journal of the Optical Society of America B, vol. 6, no. 11, pp. 2023-2045, 1989.

[51] C. Cohen-Tannoudji, J. Dupont-Roc, and G. Grynberg. *Atom-photon interactions: basic processes and applications.* Wiley-VCH, New York, 1998.

[52] C. Cohen-Tannoudji. *Cargese lectures in physics.* Edited by M. Levy. Gordon and Breach Science Publishers, New York, 1968.

[53] R. Romain, D. Hennequin, and Ph. Verkerk. *Phase-space description of the magneto-optical trap.* The European Physical Journal D - Atomic, Molecular, Optical and Plasma Physics, vol. 61, pp. 171–180, 2011.

[54] I. R. Berkman. *The elliptical lead zeppelin.* BSc thesis, Leiden University, 2015.

[55] H. Perrin. *Les Houches lectures on laser cooling and trapping, October 2012.* `http://www-lpl.univ-paris13.fr/bec/bec/Teaching/lecture2_2012.pdf` Note: link entered in 2020.

[56] B. R. Mollow. *Power spectrum of light scattered by two-level systems.* Physical Review, vol. 188, no. 5, pp. 1969-1975, 1969.

[57] B. R. Mollow. *Stimulated emission and absorption near resonance for driven systems.* Physical Review A, vol. 5, no. 5, pp. 2217-2222, 1972.

[58] L. Pruvost, I. Serre, H.-T. Duong, and J. Jortner. *Expansion and cooling of a bright rubidium three-dimensional optical molasses.* Physical Review A, vol. 61, no. 5, pp. 053408 (9), 2000.

[59] K. Kim, H.-R. Noh, H.-J. Ha, and W. Jhe. *Direct observation of the sub-Doppler trap in a parametrically driven magneto-optical trap.* Physical Review A, vol. 69, no. 3, pp. 033406 (5), 2004.

[60] K.-A. Brickman, M.-S. Chang, M. Acton, A. Chew, D. Matsukevich, P. C. Haljan, V. S. Bagnato, and C. Monroe. *Magneto-optical trapping of cadmium.* Physical Review A, vol. 76, no. 4, pp. 043411 (8), 2007.

[61] X. Xu, T. H. Loftus, J. L. Hall, A. Gallagher, and J. Ye. *Cooling and trapping of atomic strontium.* Journal of the Optical Society of America B, vol. 20, no. 5, pp. 968-976, 2003.

[62] S. N. Savenkov. *Jones and Mueller matrices: structure, symmetry relations and information content.* In: A. Kokhanovsky (Ed.) Light Scattering Reviews 4. Springer Praxis Books. Springer, Berlin, Heidelberg, 2009.

[63] D. A. Steck. *Quantum and atom optics.* `http://steck.us/teaching` Note: link entered in 2020 (revision 0.13.4).

[64] C. Y. Kaya, and L. Noakes. *The leapfrog algorithm: background and demonstration.* In: Proceedings of the International Conference on Optimization Techniques and Applications, vol. 1. Curtin University, Perth, 1998.

[65] C. A. Silebi, and W. E. Schiesser. *Dynamic modeling of transport process systems - 1st edition.* Academic Press, 2012.

[66] L. Zheng, and X. Zhang. *Modeling and analysis of modern fluid problems.* Academic Press, 2017.

[67] P. Young. *Leapfrog method and other "symplectic" algorithms for integrating Newton's laws of motion.* `https://courses.physics.ucsd.edu/2018/Winter/physics141/Assignments/leapfrog.pdf` Note: link entered in 2020.

[68] M. Sachs, B. Leimkuhler, and V. Danos. *Langevin dynamics with variable coefficients and nonconservative forces: from stationary states to numerical methods.* Entropy, vol. 19, no. 12, 2017.

[69] C. K. Birsdall, and A. B. Langdon. *Plasma physics via computer simulation.* CRC Press, 2004.

[70] M. Melzani, R. Walder, D. Folini, and C. Winisdoerffer. *Differences between real and Particle-In-Cell plasmas: effects of coarse-graining.* International Journal of Modern Physics: Conference Series, vol. 28, id. 1460194, 2014.

[71] T. D. Arber, K. Bennett, C. S. Brady, A. Lawrence-Douglas, M. G. Ramsay, N. J. Sircombe, P. Gillies, R. G. Evans, H. Schmitz, A. R. Bell, and C. P. Ridgers. *Contemporary Particle-In-Cell approach to laser-plasma modelling.* Plasma Physics and Controlled Fusion, vol. 57, no. 11, 2015.

[72] M. Gaudesius, R. Kaiser, G. Labeyrie, Y.-C. Zhang, and T. Pohl. *Instability threshold in a large balanced magneto-optical trap.* Physical Review A, vol. 101, no. 5, pp. 053626 (7), 2020.

[73] M. Gaudesius, Y.-C. Zhang, T. Pohl, R. Kaiser, and G. Labeyrie. *Phase diagram of spatiotemporal instabilities in a large magneto-optical trap.* Physical Review A, vol. 103, no. 4, pp. L041101 (5), 2021.

Acknowledgments

I would like to first of all thank to my supervisors, Robin Kaiser and Guillaume Labeyrie; it was my utmost pleasure working with you for the last three years. I thank you a lot for the many fruitful and insightful discussions we had throughout my PhD studies. I also appreciate a lot that you took the time to give comments on my Thesis manuscript.

I am thankful to Thomas Pohl for welcoming me to Aarhus University on my secondment and for providing valuable inputs for the numerical simulations. I am very grateful to Yong-Chang Zhang, who was always responsive (even on Saturdays and Sundays) and made the computer cluster work tirelessly; I thank you for the valuable inputs for the simulations.

I am thankful to Thorsten Ackemann for welcoming me to Strathclyde University on my secondment and for letting me work on his experiment. I am as well happy for your role as leader of the ColOpt network, where I met many rich personalities, to whom I thank for enhancing my PhD experience: James, Ángel, Antonello, Adrián, Giuseppe, both Francescos, Valeria, Elmer, Arthur, Aleksei, Adam and Xianliang.

I thank to Nathalie Hamel, Isabelle Larochette, Sanaë Mahir, and Nicola McRobbie for being fantastic secretaries and for making the life easier regarding the paperwork.

Last but not least, I thank to the researchers and PhD students that made my time more memorable and cheerful at our institute, INPHYNI. Ana for being a kind, caring person and for helping with various formalities. Antonin and Florent for being very French and for the hikes. Julián for being a fun, enjoyable person ... and for the run in Nice that destroyed our knees (it rhymes, but ouch!). And, of course: señorissimo Jesús, Loïc the memelord, both Pierres, Alexis, Patrice, Aurélien, Jean, Vittorio, Paolo, Amy, Hector, Álvaro, Adrián, William, Mathilde, both Mathiases and Christophe.

Formally, I acknowledge the funding support from the European Union's Horizon 2020 research and innovation programme under the Marie Skłodowska-Curie grant agreement no. 721465.